

---

# Characterisation of III-V semiconductor hybrid systems for spinorbitronic functionality

---



DISSERTATION

*zur Erlangung des  
Doktorgrades der Naturwissenschaften (Dr. rer. nat.)  
der Fakultät für Physik der Universität Regensburg*

*vorgelegt von*

**Michaela Trottmann**

*aus Regensburg*

2020

Das Promotionsgesuch wurde eingereicht am 22.01.2020.

Die Arbeit wurde angeleitet von Prof. Dr. Dominique Bougeard.

Prüfungsausschuss:

Vorsitzende:	Prof. Dr. Magdalena Marganska-Lyzniak
Erstgutachter:	Prof. Dr. Dominique Bougeard
Zweitgutachter:	Prof. Dr. Dieter Weiss
Weiterer Prüfer:	Prof. Dr. Christian Schüller

# Contents

1	Introduction .....	1
---	--------------------	---

## I Theoretical background

2	Fundamental concepts of 2D and 1D electric transport .....	7
2.1	The two-dimensional electron gas .....	7
2.1.1	Drude model .....	8
2.1.2	The quantum Hall effect .....	10
2.1.3	The field-effect .....	15
2.2	Ballistic electron transport in a 1D channel .....	16
2.2.1	Conductance quantization in an ideal 1D wire structure .....	17
2.2.2	Electron transmission in the adiabatic approximation .....	18
2.2.3	Non-ideal 1D transport .....	20
2.2.4	1D transport in a perpendicular magnetic field .....	21
3	Fundamental concepts of spin-orbit interaction .....	23
3.1	SOI in 2D systems .....	24
3.1.1	Bulk inversion asymmetry (BIA) .....	24
3.1.2	Structure inversion asymmetry (SIA) .....	25
3.1.3	Combination of SIA and BIA .....	26
3.2	Evaluation of SOI strength .....	27
3.2.1	FFT analysis of the magnetooscillations .....	27
3.2.2	Beating-node analysis of the magnetooscillations .....	30
3.3	SOI in 1D systems .....	31

<b>II</b>	<b>Epitaxy and methods</b>	
<b>4</b>	<b>Experimental methods</b>	<b>37</b>
<b>4.1</b>	<b>Molecular-beam epitaxy</b>	<b>37</b>
4.1.1	The MBE system	37
4.1.2	Calibration of the In cell	38
<b>4.2</b>	<b>Postgrowth crystal characterisation methods</b>	<b>39</b>
4.2.1	Secondary ion mass spectroscopy	39
4.2.2	Transmission electron microscopy	39
4.2.3	Atomic force microscopy	40
<b>4.3</b>	<b>Electric transport measurements</b>	<b>40</b>
4.3.1	Device design	40
4.3.2	Measurement setups	44
<b>5</b>	<b>Design and characterisation of InGaAs/InAlAs systems</b>	<b>45</b>
<b>5.1</b>	<b>Buffer layer growth</b>	<b>45</b>
<b>5.2</b>	<b>Design of InGaAs/InAlAs active layer systems</b>	<b>49</b>
<b>5.3</b>	<b>Discussion and conclusion</b>	<b>55</b>
<b>5.4</b>	<b>Comment on other material systems</b>	<b>57</b>
<b>III</b>	<b>Study of 1D and 2D transport characteristics</b>	
<b>6</b>	<b>Realization of conductance quantization in InGaAs/InAlAs</b>	<b>61</b>
<b>6.1</b>	<b>Finger-gate layout</b>	<b>61</b>
<b>6.2</b>	<b>2D and 1D transport in the model system GaAs/AlGaAs</b>	<b>64</b>
6.2.1	2D magnetotransport properties	64
6.2.2	1D transport in SG-defined QPCs	66
6.2.3	Conclusion	72
<b>6.3</b>	<b>1D transport in InGaAs/InAlAs systems</b>	<b>73</b>
6.3.1	1D transport in SG-defined QPCs	73
6.3.2	1D transport in TrG-defined QPCs	79
<b>6.4</b>	<b>Conclusion and discussion</b>	<b>87</b>
<b>7</b>	<b>Gating response of various III-V heterostructures</b>	<b>89</b>
<b>7.1</b>	<b>Sample fabrication and MT measurement sequence</b>	<b>90</b>
<b>7.2</b>	<b>Chemical treatment and different surface terminations</b>	<b>91</b>
7.2.1	5nm In <sub>0.75</sub> Ga <sub>0.25</sub> As cap	91
7.2.2	2.5nm In <sub>0.75</sub> Ga <sub>0.25</sub> As cap	94
7.2.3	Charge transfer model	101
7.2.4	In <sub>0.75</sub> Al <sub>0.25</sub> As surface termination	112
7.2.5	Conclusion	115
<b>7.3</b>	<b>Post-deposition thermal annealing</b>	<b>117</b>
7.3.1	Gating responses of annealed samples I - L	117



<b>7.4</b>	<b>Variation of the dielectric material</b>	<b>121</b>
<b>7.5</b>	<b>Charge carrier mobility and scattering sources</b>	<b>124</b>
7.5.1	The charge carrier mobility	125
7.5.2	The elastic mean free path	128
<b>7.6</b>	<b>Towards the reduction of InAlAs deep level donor states</b>	<b>130</b>
<b>7.7</b>	<b>Conclusion</b>	<b>131</b>
<b>8</b>	<b>Ballistic conductance in InGaAs/InAlAs-based systems</b>	<b>135</b>
<b>8.1</b>	<b>Realization of robust ballistic 1D conductance</b>	<b>136</b>
8.1.1	Reproducibility	136
8.1.2	Time stability	138
8.1.3	Conclusion	139
<b>8.2</b>	<b>Tuning the ballistic conductance</b>	<b>139</b>
8.2.1	Variation of $V_{CG}$	139
8.2.2	Asymmetric biasing $V_{SG1} \neq V_{SG2}$	141
8.2.3	Conclusion	143
<b>8.3</b>	<b>1D conductance in alternative heterostructures</b>	<b>143</b>
<b>8.4</b>	<b>Conclusion</b>	<b>146</b>
<b>9</b>	<b>Signatures of Rashba-type spin-orbit interaction</b>	<b>147</b>
<b>9.1</b>	<b>Gating response of undoped InGaAs/InAlAs heterostructure</b>	<b>147</b>
<b>9.2</b>	<b>FFT of magnetooscillations</b>	<b>148</b>
9.2.1	Exemplary FFT in gating regime III	149
9.2.2	Large magnetic field limit	150
9.2.3	Semi-classical simulation of the magnetoresistivity	152
9.2.4	Gate voltage dependence of FFT spectra	155
<b>9.3</b>	<b>Double-peak generation in FFT</b>	<b>156</b>
9.3.1	Size-quantization effects	156
9.3.2	SOI effect	159
<b>9.4</b>	<b>SOI in undoped InGaAs/InAlAs systems</b>	<b>159</b>
9.4.1	SOI effects in magnetooscillations	159
9.4.2	Evaluation of SOI strength	160
9.4.3	FFT analysis	160
9.4.4	Beating-node analysis	162
9.4.5	Discussion	163
9.4.6	Comparison to literature	167
<b>9.5</b>	<b>Conclusion</b>	<b>168</b>
<b>10</b>	<b>Conclusion and outlook</b>	<b>169</b>

## IV

## Appendix

<b>A</b>	<b>Sample fabrication</b>	<b>177</b>
----------	---------------------------	------------

## Contents

---

<b>B</b>	<b>Supplementary measurements .....</b>	<b>181</b>
<b>B.1</b>	<b>1D and 2D transport measurements .....</b>	<b>181</b>
<b>B.2</b>	<b>Estimation of the quantum lifetime .....</b>	<b>185</b>
<b>B.3</b>	<b>Determination of SOI strength .....</b>	<b>186</b>
	 <b>Bibliography .....</b>	 <b>187</b>
	<b>Acknowledgments .....</b>	<b>203</b>

# Introduction

In 1988, two groups from Delft [1] and Cambridge [2] reported their historical discovery that the resistance of a Sharvin-type point contact, which they both implemented in a GaAs/AlGaAs heterostructure, does not change continuously when the width of the constriction is reduced. Instead, they found distinct steps in the resistance and conductance curves to appear. Van Wees et al. [1] concluded their publication with the solemn words: *"A novel quantum effect is found: The conductance is quantized in units of  $e^2/\pi\hbar$ ."* This finding constitutes a profound experimental confirmation of the Landauer formula, already suggested in 1957 by Rolf Landauer [3], which was later generalized to the Landauer-Büttiker formula [4]. Since then, in addition to GaAs-based electron systems [5–9], conductance quantization has been realized in many other material systems as, e.g., GaN/AlGaN heterostructures [10], AlAs [11], InGaAs [12–16], InAs [17–20], InSb [21] and Si/SiGe systems [22–24].

When considering such quantization effects in 1D in the context of materials with strong spin-orbit interaction, new research fields have opened up as, for example, the high-topical field of topological quantum computation [25–29]. Therein, the coupling of a high-mobility 2D electron gas with large spin-orbit interaction to an s-wave superconductor presents a fundamental part. In these experiments, quantum point contacts are employed to measure the quantized conductance doubling - a manifestation of proximity-induced superconductivity in the 2D electron system [30, 31]. To follow the theoretical recipe for the creation of a spinless p-wave superconductor in which a single isolated Majorana state arises [27, 28], quantum point contacts generate the required 1D subband structure [30, 31].

As a second example, the physics of quantum point contacts has fueled a variety of device applications and concepts [13, 16, 19, 32, 33], merging under the roof of spinorbitronics [34]. One goal is the realization of a spin-transistor. This requires the implementation of three key components to yield a fully functional system, i.e. a spin injector, a spin detector and a tuning knob to manipulate the spin current between injection and

detection. Realizing the proposed spin-transistor generally entails two main manufacturing challenges: Firstly, using ferromagnetic electrodes for the generation and read-out of the spin-polarized current, one is usually subjected to the conductance mismatch. Secondly, spin-dephasing mechanisms inside the transistor channel impede a loss-free transmission of spin-information. In an elegant, ballistic and all-electric spin-transistor concept presented by Chuang et al. [13], these obstacles are readily eliminated. Therein, two serial quantum point contacts, which are implemented in a 2D electron gas, are employed as a spin injector and spin detector by adjusting the strength of lateral spin-orbit coupling inside the 1D channel. By exploiting Rashba-type spin-orbit interaction, the spin precession between spin injector and detector can be manipulated with an external electric field, applied via a middle-gate electrode.

Given the examples outlined above, it is interesting to note that the key requirements for topological quantum computation and the spinorbitronic device application are very similar: Achieving large spin-orbit coupling in a highly mobile electron system with a clean semiconductor surface. In this regard, InAs/InGaAs-based heterostructures offer inherent advantages in their material properties, like a low effective mass, a large Landé g-factor, as well as large Rashba spin-orbit interaction, making them attractive candidates for these device applications. In addition to all of that, the absence of a Schottky barrier for sufficiently large indium concentrations enables the fabrication of metal-semiconductor interfaces with unique transparency. To harvest the undeniable potential of this semiconductor system, material specific challenges have to be met. This thesis focuses on those perspectives of the InAs-based material system which would qualify it as a reliable platform for the realization of reliable 1D spinorbitronic devices.

Due to the lack of a lattice-matched substrate for InAs and InGaAs with arbitrary indium concentration, sophisticated buffer layer concepts have to be implemented during the molecular beam epitaxy to achieve highly mobile electron systems [35–38]. Furthermore, InAlAs, which is commonly applied as a high-band gap material in InAs/InGaAs layer structures, introduces a significant arsenic-related background impurity density into the system, which at the same time provides free charge carriers for the InAs/InGaAs 2D system and thereby acts as an intrinsic dopant [37, 39]. On the upside, this yields the advantage that the epitaxial incorporation of a modulation doping layer into the system, which generally impedes the ballisticity of a 2D electron system, is not mandatory. On the downside, the doping-providing and thus ionized InAlAs defect states introduce a Coulombic disorder potential in the barrier layers surrounding the 2D electron gas, whereby 1D transport is likely to be affected. Except for their doping properties, InAlAs defect states have been scarcely addressed in the literature so far. Evaluating their impact on the implementation of 1D spinorbitronic devices in these material systems is a central part of this thesis, since a holistic study is not available yet.

Last but not least, a very elementary manufacturing challenge has to be met in III-V systems: GaAs and InAs, as well as their ternary compound systems  $\text{In}_x\text{Ga}_{1-x}\text{As}$  lack an electrically stable and defect-free oxide, which forms at the surface and influences the gating response of the system [40, 41]. This entails the need for elaborated device fabrication processes to avoid opacity of the semiconductor interface, being severely

---

detrimental for 2D electron systems proximitized to a superconductor, as well as to prevent hysteretic effects when the material system is gated.

From the above considerations it is apparent that a profound and comprehensive understanding of the electrostatic properties of the employed hybrid semiconductor/insulator/metal system is essential en route to spinorbitronic and topological applications. With our work, we intend to contribute to the current investigations in this quite extensive field of research.

This thesis is organized as follows:

In chapter 2, we briefly introduce the fundamental concepts of the herein analysed 2D and 1D transport characteristics in external electric and magnetic fields.

Chapter 3 summarizes relevant aspects of band-related spin-orbit interaction, especially in 2D electron systems. Furthermore, we address the spin-transistor concept as presented in [13].

The structural and electrical characterisation methods used in this thesis are shortly introduced in chapter 4.

In chapter 5, we summarize the key results of our epitaxial study, where we growth-engineer our active layer system. The heterostructures are structurally analysed and their magnetotransport properties are then tested with respect to their suitability for spinorbitronic device application.

Chapter 6 is devoted to the realization of quantized conductance in the  $\text{In}_{0.75}\text{Ga}_{0.25}\text{As}/\text{In}_{0.75}\text{Al}_{0.25}\text{As}$  layer system. Thereby, we test a split-gate design on the model system  $\text{GaAs}/\text{Al}_{0.31}\text{Ga}_{0.69}\text{As}$ . We then provide a thorough study of the transport in electrically defined quantum point contacts in the non-illuminated and illuminated state in the material system  $\text{InGaAs}$ .

Based on the experimental results of the preceding chapter, we discuss the gate response of several different metal/dielectric/semiconductor material combinations in the top-gated Hall bar measurements in chapter 7. We introduce a holistic charge transfer model, which is able to describe the electric transport properties under gating over a wide bias and electron density range.

At this point, our detailed understanding of the material system allows us to demonstrate the realization of robust ballistic conductance in different  $\text{In}_{0.75}\text{Ga}_{0.25}\text{As}/\text{In}_{0.75}\text{Al}_{0.25}\text{As}$  active layer systems in chapter 8.

Chapter 9 addresses the peculiar magnetooscillations, which appear when we gate our system. From these experiments, we are able to estimate the strength of Rashba spin-orbit interaction in our heterostructures.

Chapter 10 concludes and evaluates the experimental results by means of their implications on device applications.

The appendix IV yields supplementary information to sample fabrication and auxiliary transport measurements in one and two dimensions.





# Theoretical background

<b>2</b>	<b>Fundamental concepts of 2D and 1D electric transport .....</b>	<b>7</b>
2.1	The two-dimensional electron gas .....	7
2.2	Ballistic electron transport in a 1D channel.....	16
<b>3</b>	<b>Fundamental concepts of spin-orbit interaction.....</b>	<b>23</b>
3.1	SOI in 2D systems .....	24
3.2	Evaluation of SOI strength .....	27
3.3	SOI in 1D systems .....	31





# Fundamental concepts of 2D and 1D electric transport

This chapter briefly introduces the fundamental concepts of electric transport in band structure-engineered semiconductor heterostructures in external electric and magnetic fields. Therein, we give the relevant expressions for 2D and 1D electric transport, which we will utilise in the course of this thesis.

## 2.1 The two-dimensional electron gas

The dispersion relation of an electron in a crystal lattice can be derived by means of  $\mathbf{k} \cdot \mathbf{p}$ -perturbation theory from the Bloch equation. By introducing the electron effective mass  $m^*$  as

$$\frac{1}{m^*} = \frac{1}{m_e} \left( 1 + \frac{2m_e P^2}{\hbar^2} \right),$$

with  $\hbar = h/2\pi$  being the reduced Planck constant, the dispersion relation of the *nearly free electron* in a bulk crystal near the  $\Gamma$ -point can be described with

$$E_c(\mathbf{k}) \approx E_c + \frac{\hbar^2 k^2}{2m^*}, \quad (2.1)$$

where  $E_c$  is the lower edge of the conduction band. The band edge parameter  $P$  can be considered as the expectation value of the momentum in the vicinity of the  $\Gamma$ -point.

In the course of this thesis, we will analyse the electric transport in band structure-engineered semiconductor heterostructures. The thereby introduced band discontinuities, which present a perturbation to the periodic lattice potential, enable the confinement of the electron's motion in the semiconductor crystal. This perturbation of the translational invariance in one direction, for example the  $z$ -direction, can be treated in the framework of the envelope function approximation (EPA). Due to the still maintained translational invariance in the directions  $x$  and  $y$  perpendicular to the confinement direction, the wave function  $\Psi(\mathbf{r})$  of the electron can be decomposed into  $\Psi(\mathbf{r}) = \psi(x, y)\chi(z)$ . By means of

## 2 Fundamental concepts of 2D and 1D electric transport

---

this ansatz and the appropriate boundary conditions, one finds that the energy spectrum in the  $z$ -direction is quantized and can be described via discrete subband states  $\chi_n(z)$ , where  $n$  is the corresponding quantum number. The total energy dispersion relation then reads as

$$E = E_n(k_{\parallel}) + \frac{\hbar^2 k_{\parallel}^2}{2m^*}, \quad (2.2)$$

where  $k_{\parallel} = \sqrt{k_x^2 + k_y^2}$  is the in-plane wave vector. If only the lowest subband is occupied one commonly refers to the system as a *two-dimensional electron gas (2DEG)*. The resulting density of states (DOS) of the 2DEG is

$$\mathcal{D}_{2D}(E) = \frac{g_s g_v m^*}{\pi \hbar^2},$$

with  $g_s$  being the degree of spin degeneracy and  $g_v$  represents the valley degeneracy. For  $\text{In}_{0.75}\text{Ga}_{0.25}\text{As}/\text{In}_{0.75}\text{Al}_{0.25}\text{As}$  heterostructures, we generally apply  $g_s = 2$  and  $g_v = 1$ . The sheet carrier density  $n_s$  of the 2DEG can be expressed as

$$n_s = \mathcal{D}_{2D}(E) \cdot E_F,$$

where  $E_F$  is the Fermi energy, referring to the highest occupied energy state of the system. Thus, the corresponding Fermi wave vector  $k_F$  is given by

$$k_F = \sqrt{\frac{2m^* E_F}{\hbar^2}} = \sqrt{2\pi n_s}. \quad (2.3)$$

### 2.1.1 Drude model

A basic theoretical model for the description of the motion of electrons in a crystal is provided by the Drude model [42, 43]. In this semiclassical description, the electrons are described as classical particles, that undergo collisions inside the crystal after an average scattering time  $\tau_{tr}$  when moving in an external electric field. In between two subsequent scattering events, an electron gains on average the so-called drift velocity  $\mathbf{v}_D$ . The current density  $\mathbf{j}$  is determined as

$$\mathbf{j} = \sigma \mathbf{E} = -en_s \mu \mathbf{E} = -en_s \mathbf{v}_D, \quad (2.4)$$

with  $\sigma$  being the conductivity and  $\mu = \frac{|e|\tau_{tr}}{m^*}$  is the electron mobility.

The motion of an electron, which is subjected to an additional magnetic field, is described by

$$\frac{m^*}{\tau_{tr}} \mathbf{v}_D = -e(\mathbf{E} + \mathbf{v}_D \times \mathbf{B}). \quad (2.5)$$

In the case of  $|\mathbf{B}| \neq 0$ ,  $\sigma$  transforms into a tensor. By choosing  $\mathbf{B} = (0, 0, B)$ , we can

write the current density as

$$\begin{pmatrix} j_x \\ j_y \end{pmatrix} = \begin{pmatrix} \sigma_{xx} & \sigma_{xy} \\ \sigma_{yx} & \sigma_{yy} \end{pmatrix} \cdot \begin{pmatrix} E_x \\ E_y \end{pmatrix} = \frac{\sigma_0}{1 + \omega_c^2 \tau_{tr}^2} \cdot \begin{pmatrix} 1 & -\omega_c \tau_{tr} \\ \omega_c \tau_{tr} & 1 \end{pmatrix} \cdot \begin{pmatrix} E_x \\ E_y \end{pmatrix}, \quad (2.6)$$

with the Drude conductivity

$$\sigma_0 = n_s e^2 \frac{\tau_{tr}}{m^*} = n_s e \mu$$

and the cyclotron frequency

$$\omega_c = \frac{eB}{m^*}.$$

By tensor inversion of the conductivity tensor, we gain the corresponding resistivity tensor:  $\sigma = \rho^{-1}$ . It can be shown that the components yield the following form:

$$\rho_{xx} = \rho_{yy} = \frac{\sigma_{xx}}{\sigma_{xx}^2 + \sigma_{yy}^2} = \frac{m^*}{e^2 n_s \tau_{tr}} \quad (2.7)$$

$$\rho_{xy} = -\rho_{yx} = \frac{\sigma_{xy}}{\sigma_{xx}^2 + \sigma_{yy}^2} = \frac{B}{|e| n_s}. \quad (2.8)$$

Measuring  $\rho_{xx}$  and  $\rho_{xy}$  independently from each other in a magnetotransport (MT) measurement thus yields the sheet carrier density  $n_s$  and the corresponding charge carrier mobility  $\mu$ , which characterise the transport properties of a 2DEG:

$$n_s = \left( e \cdot \frac{\partial \rho_{xy}}{\partial B} \Big|_{B=0} \right)^{-1} \quad (2.9)$$

$$\mu = \left( e \cdot n_s \rho_{xx}(B=0) \right)^{-1}. \quad (2.10)$$

Different device geometries can be employed to determine  $n_s$  and  $\mu$  in a MT measurement. This will be subject of section 4.3. Depending on the sample geometry and also on the applied evaluation method, we will distinguish between  $n_{vdP}$ ,  $n_{Hall}$  and  $n_{SDH}$  as introduced in the following sections.

An important length scale in the regime of diffusive - and also ballistic - transport is the elastic mean free path  $l_{mfp}$ , which can be expressed as

$$l_{mfp} = v_F \tau_{tr} = \frac{\hbar}{e} \sqrt{2\pi n_s} \mu, \quad (2.11)$$

where  $v_F = \frac{\hbar k_F}{m^*}$  is the Fermi velocity.

### Parallel transport

In the Drude model multisubband occupation and parallel conduction can be described as a sum of the currents of all participating transport channels [44, 45]. Thus, the total

## 2 Fundamental concepts of 2D and 1D electric transport

conductivity  $\sigma_{tot}$  of the system can be expressed in the form of a summation over all contributing sheet conductivities  $\sigma_i$ , where  $i$  labels the individual transport channel:

$$\sigma_{tot} = \sigma_1 + \sigma_2 + \dots = \sum \sigma_i , \quad (2.12)$$

with

$$\sigma_i = \frac{n_i e^2 \tau_{tr,i}}{m_i^*} \cdot \frac{1}{1 + \omega_c^2 \tau_{tr,i}^2} \cdot \begin{pmatrix} 1 & -\omega_c \tau_{tr,i} \\ \omega_c \tau_{tr,i} & 1 \end{pmatrix} . \quad (2.13)$$

Inversion of the expression (2.12) for the total conductivity  $\sigma_{tot}$  yields the corresponding term for the total resistivity  $\rho_{tot}$  of the system.

The case of two non-interacting transport channels, labeled with the indices 1 and 2, yields in the limit of small magnetic fields when following simplified expressions for  $\rho_{xx}$  and  $\rho_{xy}$ :

$$\rho_{xx} = \frac{1}{e} \cdot \frac{1}{n_1 \mu_1 + n_2 \mu_2} = \frac{1}{e} \cdot \frac{1}{n_{Hall} \cdot \mu_{Hall}} \quad (2.14)$$

$$\rho_{xy} = \frac{B}{e} \cdot \frac{n_1 \mu_1^2 + n_2 \mu_2^2}{(n_1 \mu_1 + n_2 \mu_2)^2} = \frac{B}{e} \cdot \frac{1}{n_{Hall}} . \quad (2.15)$$

It is reasonable to assume, that the mobility  $\mu_2$  of a newly populated, higher subband is much lower than the mobility  $\mu_1$  of the ground (first) subband, i.e.  $\mu_2 \ll \mu_1$  [46]. In this case, the above expression (2.15) for  $\rho_{xy}$  can be further simplified to

$$n_{Hall} = \frac{(n_1 \mu_1 + n_2 \mu_2)^2}{n_1 \mu_1^2 + n_2 \mu_2^2} \approx \frac{(n_1 \mu_1 + n_2 \mu_2)^2}{n_1 \mu_1^2} . \quad (2.16)$$

This expression shows that the measured Hall density contains the individual charge densities of the contributing channels, whose density values are further weighted by the mobility of the respective channel.

### 2.1.2 The quantum Hall effect

For sufficiently high magnetic fields, i.e.  $\omega_c \tau_{tr} \gg 1$ , the description of the magneto-transport in a 2DEG within the semiclassical Drude model breaks down. As was first addressed by Landau [47], the corresponding Hamiltonian for electrons in a 2DEG, which are subjected to an external magnetic field, reads as

$$\mathcal{H} = \frac{(\mathbf{p} + |e|\mathbf{A})^2}{2m^*} + V(z) , \quad (2.17)$$

where  $V(z)$  is the confinement potential and  $\mathbf{A}$  is the vector potential. In Landau gauge,  $\mathbf{A}$  can be written as  $\mathbf{A} = (0, Bx, 0)$  with  $\mathbf{B} = (0, 0, B)$ . With the ansatz  $\Psi(x, y, z) = u(x)e^{iky}\chi(z)$  for the electron wave function, the problem can be reduced to the form of a

1D quantum mechanical harmonic oscillator. The quantized energy states  $E_{n_{xy}}$  are given by

$$E_{n_{xy}} = \hbar\omega_c \left( n_{xy} + \frac{1}{2} \right), \quad (2.18)$$

with  $n_{xy}$  being the Landau quantum number. All states with different  $k_y$  inside a Landau level  $n_{xy}$  are energetically degenerate. By means of periodic boundary conditions for  $k_y$ , the number of states in a Landau level per unit area are determined as

$$n_L = \frac{|e|B}{h}. \quad (2.19)$$

For a given electron density  $n_s$ , the Landau level filling factor  $\nu$ , which is the amount of populated Landau levels at a given magnetic field  $\mathbf{B}$ , is calculated with

$$\nu = \frac{n_s}{n_L}. \quad (2.20)$$

### Oscillatory magnetoresistance

In the case of a constant 2D charge density  $n_s$ , the magnetic field dependence of the DOS of a Landau level manifests itself in an oscillatory behavior of  $E_F$ . Correspondingly, this results in a sinusoidal oscillation of the magnetoresistivity  $\rho_{xx}$  in  $1/B$ , the so-called *Shubnikov-de Haas oscillations*. A semi-classical description of  $\rho_{xx}(B)$  was first given by Coleridge et al. [48]:

$$\Delta\rho_{xx} = \rho_0 + 4 \cdot \frac{2\pi k_B T m^*}{\hbar e B} \cdot \frac{1}{\sinh \frac{2\pi k_B T m^*}{\hbar e B}} \cdot \exp\left(-\frac{\pi m^*}{e\tau_q} \cdot \frac{1}{B}\right) \cdot \cos\left(\frac{2\pi \mathcal{E} m^*}{\hbar e} \cdot \frac{1}{B} - \pi\right), \quad (2.21)$$

with  $\mathcal{E} = E_F - E_n$ , where  $E_n$  is the energy of the  $n$ th subband and  $k_B$  is the Boltzmann constant.  $\tau_q$  is the quantum lifetime, which is also often referred to as single particle lifetime. It specifies the lifetime of the quantum state, i.e. the time, in which one is able to define an electronic momentum eigenstate in the system in the presence of scattering. We can identify the second term in equation (2.21) as a description of the temperature-dependent DOS of the Landau levels with a Lorentzian energy broadening, introduced by scattering. Therein, the exponential term  $\exp\left(-\frac{\pi m^*}{e\tau_q} \cdot \frac{1}{B}\right)$ , which is commonly referred to as the *Dingle factor*, determines the magnitude of the Shubnikov-de Haas oscillations [43, 49–51].

In high-mobility samples  $\tau_q$  can be more than ten times smaller than the transport lifetime  $\tau_{tr}$ . This is due to the fact that the single particle lifetime  $\tau_q$  takes every scattering event into account, irrespective of the scattering angle  $\phi$ . It is described by

$$\frac{1}{\tau_q} = \frac{m^*}{\hbar^2} \int_0^{2\pi} W(\phi) \frac{d\phi}{2\pi},$$

## 2 Fundamental concepts of 2D and 1D electric transport

wherein  $W(\phi)$  is the scattering cross section into a particular direction. For high-mobility systems, however, small-angle scattering predominates. In the description of the transport lifetime  $\tau_{tr}$ , which determines the mobility in a system, large-angle back-scattering is more strongly weighted since it leads to a significant change of the momentum direction [43, 50–52]:

$$\frac{1}{\tau_{tr}} = \frac{m^*}{\hbar^2} \int_0^{2\pi} W(\phi)(1 - \cos(\phi)) \frac{d\phi}{2\pi}.$$

When the Fermi level lies in between two subsequent Landau levels and negligible scattering of charge carriers into neighboring, extended energy states takes place, we find a minima in the longitudinal resistivity of the system. A maximum in  $\rho_{xx}(B)$  arises when the Fermi level passes the center of the DOS of the topmost Landau level. Consequently, by means of the above expression (2.21), the sheet density  $n_s$  of the 2DEG can be determined by evaluating the neighboring minima of the Shubnikov-de Haas oscillations in  $1/B$  via following relation:

$$\Delta\left(\frac{1}{B}\right) = \frac{1}{B_{i+1}} + \frac{1}{B_i} = \frac{2|e|}{\hbar n_s}. \quad (2.22)$$

Within this thesis, values of  $n_s$ , which are determined via this formula from the Shubnikov-de Haas oscillations, are labeled as  $n_{sdH}$ .

### The integer quantum Hall effect

Simultaneously to the appearance of the Shubnikov-de Haas oscillations in the longitudinal magnetoresistivity  $\rho_{xx}(B)$ , well-pronounced plateaus in the transversal resistivity  $\rho_{xy}$  emerge. This presents the so-called *quantized Hall effect* [53, 54]. Therein, steps in  $\rho_{xy}(B)$  arise at specific resistivity values, which are given by

$$\rho_{xy}^{plateau} = \frac{1}{p} \frac{h}{e^2} = \frac{1}{p} R_K, \quad (2.23)$$

with  $p \in \mathbb{N} \setminus \{0\}$ .  $R_K = 25812.807\Omega$  is the well-known *von Klitzing constant*. Consequently, plateaus in  $\rho_{xy}$  occur when the Landau level filling factor is close to an integer value of  $\nu$ . Utilising the relations (2.7) and (2.8) in order to calculate the corresponding components of the conductivity tensor at the Hall plateau values, we find:

$$\sigma_{xx}^{plateau} = 0 \quad (2.24)$$

$$\sigma_{xy}^{plateau} = i \frac{e^2}{h}. \quad (2.25)$$

This means that in the case of an integer value of  $\nu$ , the transversal Hall conductance is quantized in units of  $e^2/h$ , which is the so-called *conductance quantum*.

In the Landauer-Büttiker picture [4], the conductance quantization can be well described as the perfect transmission of one-dimensional edge channels between the source and

the drain contact. Due to the spatial separation of the edge channels at the opposing Hall bar interfaces, these counterpropagating channels do not interact since energy states inside the Hall bar region are localized. Each (spin-degenerate) edge channel contributes a conductance of  $2e^2/h$  to the total conductance of the system.

### Zeeman effect

An external magnetic field  $\mathbf{B}$ , which breaks the time reversal symmetry, lifts the spin degeneracy. The corresponding Hamiltonian can be written as

$$\mathcal{H}_Z = \frac{1}{2}g^*\mu_B\boldsymbol{\sigma} \cdot \mathbf{B}, \quad (2.26)$$

with the Pauli matrices  $\boldsymbol{\sigma}$  and  $\mu_B$  being the Bohr magneton. For bulk semiconductors, in first order, the energetical Zeeman splitting  $\Delta E_Z$  is isotropic in space and can be described with

$$\Delta E_Z = g^*\mu_B B, \quad (2.27)$$

where  $g^*$  is the effective Landé g-factor. Thus, the spin-splitting strength is not only proportional to the applied magnetic field  $B$ , but also to the prefactor  $g^*$ . Deviations from the free-electron g-factor arise due to a coupling of the electron's spin to the angular lattice-periodic part of the Bloch wave functions. For a system with reduced symmetry, for example due to spatial confinement, and which additionally lacks bulk inversion asymmetry,  $g^*$  has to be described by a tensor. The in- and out-of plane anisotropy arises from the  $\mathbf{k} \cdot \mathbf{p}$ -coupling between different subbands. The in-plane anisotropy is predicted to be proportional to built-in electric fields in the system and scales with the strength of the Dresselhaus contribution to spin-orbit interaction [55].

As we find later in chapter 3, the Dresselhaus contribution to spin-orbit coupling can be neglected in our analysed heterostructures. Furthermore, solely magnetic fields perpendicular to the sample surface are applied in the course of this work. We can therefore treat  $g^*$  as a scalar in order to give an estimate of the Zeeman spin-splitting in our MT measurements.

Including the Zeeman spin-splitting from equation (2.27) into the description of the Landau level eigenstates in equation (2.18) yields the following expression:

$$E_{n_{xy}} = \hbar\omega_c \left( n_{xy} + \frac{1}{2} \right) \pm \frac{1}{2}g^*\mu_B B. \quad (2.28)$$

Correspondingly, the energy spin-splitting of the Landau levels enters the description of the Landau level DOS, which thus provokes a modification of the periodicity of the Shubnikov-de Haas oscillations for sufficiently high magnetic fields. Since in the spin-split case the factor of two in equation (2.22) does not have to be included anymore, a transition of the  $1/B$ -periodicity of the magnetooscillations from a frequency  $f$  to a frequency  $2f$  can be observed (as long as the description by means of equation (2.21) still holds).

### Magneto-intersubband scattering

In the case that an additional 2D electron system contributes to magnetotransport, the Fermi level crosses a second size-quantized subband. Thus, the description of the Shubnikov-de Haas oscillations by means of equation (2.21) has to be extended. According to equation (2.18), this second 2DEG contributes an additional set of Landau level eigenenergies to the B-field-dependent energy spectrum of the system. In first approximation, the respective resistivities  $\rho_{xx,i}$ , where  $i = 1, 2$  accounts for the two contributing 2D systems, can be described by means of equation (2.21), with the corresponding quantum lifetime  $\tau_{q,i}$  and electron density  $n_{s,i}$ . In addition, a further effect in  $\rho_{xx}(B)$  can arise, which is generally referred to as the *magneto-intersubband scattering effect (MIS)*. This term has been coined by the work of Raikh and Shabazyan [56]. In the case of two spatially non-separated 2DEGs, i.e. two size-quantized subbands of a QW for instance, this interaction effect has to be taken into account. As the name implies, MIS accounts for the increased intersubband scattering processes when the Landau levels of the two size-quantized subbands cross. This level crossing can be described by following energy-dependent relation:

$$E_1 + E_{LL,1} = E_2 + E_{LL,2} = E_1 + E_{1,2} + E_{LL,2} . \quad (2.29)$$

$E_1$  and  $E_2$  describe the onset of the first and second size-quantized subbands of the QW and  $E_{1,2} = |E_1 - E_2|$  represents the energy difference between the two subbands.  $E_{LL,1}$  and  $E_{LL,2}$  constitute the Landau level energies of the first and second subband, respectively. Inserting the (spin-degenerate) expression for the Landau level eigenstates of equation (2.18) into the above equation (2.29) yields

$$E_1 + \hbar\omega_c \left( n + \frac{1}{2} \right) = E_1 + E_{1,2} + \hbar\omega_c \left( m + \frac{1}{2} \right) \quad (2.30)$$

$$\Rightarrow (n - m) = \frac{m^*}{\hbar e} \cdot E_{1,2} \cdot \frac{1}{B} , \quad (2.31)$$

with  $n, m$  being the Landau level indices of the two size-quantized subbands, respectively. Note that  $n > m$  is always true, so that  $(n - m) > 0$ . The latter equation can be viewed as a magnetic field-dependent condition for Landau level-crossing in a 2D system. The modulation of  $\rho_{xx}(B)$  due to MIS was first correctly described by Coleridge [57] and was later refined by Leadley et al. [58] to

$$\frac{\Delta\rho_{xx}}{\rho_0} = A_1 \frac{\langle \Delta g_1 \rangle}{g_0} + A_2 \frac{\langle \Delta g_2 \rangle}{g_0} + B_{12} \frac{\langle \Delta g_1 \Delta g_2 \rangle}{g_0^2} , \quad (2.32)$$

with

$$\frac{\Delta g_i}{g_0} = 2\phi(T_{D_i}) \cos \left( 2\pi \frac{E_F - E_i}{\hbar\omega_c} + \pi \right) \quad (2.33)$$



and

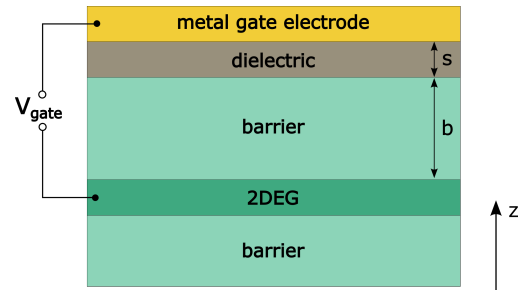
$$\frac{\langle \Delta g_1 \Delta g_2 \rangle}{g_0} = 2\phi(T_{D_1} + T_{D_2}) \left( D(2X) \cos \left( 2\pi \frac{f_1 + f_2}{B} \right) + \cos \left( 2\pi \frac{f_1 - f_2}{B} \right) \right). \quad (2.34)$$

The thermal damping factor  $X/\sinh X$ , with  $X = \frac{2\pi_2 k_B T}{\hbar \omega_c}$ , from equation (2.21) is labeled here as  $D(X)$ .  $f_i = \frac{ne}{2h}$ , with  $i = 1, 2$ , present the density-related magnetooscillation frequencies of the first and second subbands of the 2DEG. The thermal broadening of the Fermi distribution in formula (2.32) is expressed by means of the angular brackets in  $\langle \Delta g_i \rangle$ .  $\phi(T_D) = \exp \left( \frac{-2\pi^2 k_B T_D}{\hbar \omega_c} \right)$  represents the Dingle factor. The prefactors  $A_i$  and  $B_{12}$  incorporate intra- and intersubband scattering, respectively.

Thus, by means of the above formula (2.32), the resulting magnetoresistivity of the system can be described in form of two contributing Shubnikov-de Haas-terms, i.e. the first and second term in equation (2.32), plus a third term, which accounts for the subband-interaction. This third term introduces two additional frequencies, the sum- and the difference-frequencies  $f_1 + f_2$  and  $f_1 - f_2$  (see equation (2.34)), to the density-related frequencies  $f_1$  and  $f_2$  of  $\rho_{xx}(B)$  over  $1/B$  of the two 2D systems.

### 2.1.3 The field-effect

**Figure 2.1:** Sketch of a gate stacking at which a voltage  $V_{gate}$  is applied between the metal gate electrode and the semiconductor 2DEG. The metal gate electrode and the 2DEG form the two plates of a capacitor, which are separated by a dielectric layer (grey) and a semiconducting spacer material (bright green) of thickness  $s$  and  $b$ , respectively.



By exploiting the field-effect, we are able to manipulate the electron sheet density  $n_s$  of the 2D electron system. In good approximation, the 2DEG in our heterostructure and an attached metal gate electrode on top of our layer system serve as two plates of a capacitor. This situation is schematically illustrated in figure 2.1. The gate electrode and the 2DEG are separated by an insulating dielectric layer and the semiconducting barrier material. The capacitance  $C$  of a plate capacitor is given by

$$C = \frac{Q}{V_{gate}} \quad \text{with} \quad C = \epsilon_0 \epsilon_r \frac{A}{d},$$

where  $A$  is the area of a capacitor plate and  $d$  is the distance between the two plates.  $\epsilon_0$  presents the vacuum permittivity and  $\epsilon_r$  is the permittivity of the spacer material between the two capacitor plates.  $V_{gate}$  is the applied gate voltage between the metal gate

## 2 Fundamental concepts of 2D and 1D electric transport

---

electrode and the 2DEG layer.

A key parameter which describes the electric response of the 2D system to a variation of the applied  $V_{gate}$  presents the capacitive coupling  $c$ . Accordingly,  $c$  is defined as

$$c = \frac{\partial n_s}{\partial V_{gate}} = \frac{C}{eA} = \frac{\epsilon_0 \epsilon_r}{ed}. \quad (2.35)$$

Our layer configuration, which is displayed in figure 2.1, corresponds to a number of individual capacitors connected in series. Thus, we describe the capacitive coupling  $c$  of the gate stackings, which we will analyse in the course of this work, as follows:

$$c = \frac{\epsilon_0}{e} \left( \sum_i \frac{d_i}{\epsilon_i} \right)^{-1} \Rightarrow c = \frac{\epsilon_0}{e} \left( \frac{s}{\epsilon_{dielectric}} + \frac{b}{\epsilon_{barrier}} \right)^{-1}. \quad (2.36)$$

In the above formula for  $c$ , we have omitted two band structure related terms, which incorporate the quantum capacitance, accounting for the finite DOS of the 2DEG, and the influence of the quantization energy in a size-quantized system. Due to their little influence on  $c$ , these quantum correction terms will be neglected in the course of this work and we will thus treat the field-effect response of our systems classically by means of the above equation (2.36). A more detailed description of the complete formula for  $c$  is given in [43].

## 2.2 Ballistic electron transport in a 1D channel

If the motion of the conduction electrons in the 2DEG (free motion in  $x$ - $y$ -plane) is further reduced in one dimension, for example in the  $y$ -direction, additional size quantization effects in the dispersion of the system become visible as soon as the Fermi wavelength is of the order of the additional confining potential. The kinetic energy of the system is then discretized in two directions: We obtain energy quantization for the motion in growth ( $z$ -) direction, as well as energy quantization for the motion along the  $y$ -direction. In this situation, free motion in  $x$ -direction is preserved. The energy eigenstates of this 1D system are then described by the dispersion relation

$$E_{n,m}(k_x) = E_n(k_z) + E_m(k_y) + \frac{\hbar^2 k_x^2}{2m^*}, \quad (2.37)$$

with  $n, m$  being the quantum numbers for the respective subbands in  $z$ - and  $y$ -direction. The resulting 1D DOS (with  $g_s = 2$  and  $g_y = 1$ ) is described by

$$\mathcal{D}_{1D}(E) = \frac{1}{\pi} \left( \frac{dE_m}{dk_x} \right)^{-1} = \frac{1}{\pi \hbar} \left( \frac{m^*}{2E} \right)^{1/2}. \quad (2.38)$$

To obtain the exact solution for the 1D eigenstates and eigenenergies of the system, the confinement can be treated in the envelope function and effective mass approximation. Assuming an infinite barrier height in the  $z$ - and  $y$ -direction yields

$$E_{n,m}(k_x) = \frac{\hbar^2 \pi^2}{2m^*} \left( \left( \frac{n}{L_z} \right)^2 + \left( \frac{m}{L_y} \right)^2 \right) + \frac{\hbar^2 k_x^2}{2m^*}, \quad (2.39)$$

with  $n, m \in \mathbb{N}$  and  $L_z$  and  $L_y$  being the potential well width in the corresponding directions.

In the following, we consider a 2DEG, which is - by definition - only populated in the lowest subband. Furthermore, we superimpose a confining potential in  $y$ -direction, whereby we create a 1D wire structure, in which electrons can freely move in  $x$ -direction. The electron transport in such a system is equivalent to transversal modes, travelling in a waveguide. If the dimensions  $L_x$  and  $L_y$  of the probed 1D wire are smaller than the mean free path  $l_{mfp}$ , i.e. the electrons travel ballistically inside the 1D wire, remarkable quantum effects arise in the transport properties of the system. The conductance  $G$ , being the inverse of the resistance, exhibits well-pronounced quantization steps, which are given by

$$G = \frac{2e^2}{h} N = 2N \cdot G_0, \quad (2.40)$$

with  $N \in \mathbb{N}$  being an integer number.  $G_0 \equiv e^2/h = R_K^{-1}$  is the conductance quantum, which already appeared in equation (2.23) in the description of the quantum Hall conductance plateaus in  $\rho_{xy}$ .

In the following, we briefly present the key steps towards the derivation of this relation for  $G$ , whereby we follow the deduction in [43].

### 2.2.1 Conductance quantization in an ideal 1D wire structure

Let us consider the above described 1D wire structure, formed by an additional confining potential in  $y$ -direction in the  $x$ - $y$ -plane of a 2DEG. For simplicity, we assume the 1D channel to be long, by which we exhibit translational invariance in  $x$ -direction. The wave function inside the 1D wire can then be written as

$$\psi_{n\mathbf{k}}(\mathbf{r}) = \chi_n(y, z) \cdot \frac{1}{\sqrt{L}} e^{ik_x x}, \quad (2.41)$$

with  $n$  being the quantum number of the transversal modes  $\chi_n(y, z)$ . The quantum mechanical current density  $d\mathbf{j}_{nk_x}(\mathbf{r})$  reads as

$$d\mathbf{j}_{nk_x}(\mathbf{r}) = -\frac{|e|\hbar}{2im^*} \left( \psi_{nk_x}^*(\mathbf{r}) \nabla \psi_{nk_x}(\mathbf{r}) - \psi_{nk_x}(\mathbf{r}) \nabla \psi_{nk_x}^*(\mathbf{r}) \right). \quad (2.42)$$

Inserting the wave function (2.41) into equation (2.42) yields

$$d\mathbf{j}_{nk_x}(\mathbf{r}) = -\mathbf{e}_x \frac{|e|}{2\pi} |\chi_n(y, z)|^2 \frac{\hbar k_x}{m^*} dk_x. \quad (2.43)$$

## 2 Fundamental concepts of 2D and 1D electric transport

This relation can be identified with the current density from the Drude picture  $\mathbf{j} = en_s \mathbf{v}_D$ , whereby the sheet density  $n_s$  is expressed as the 1D charge density  $\mathcal{D}_{1D}$ . Thus, we find  $j = e\mathcal{D}_{1D}Ev_D$ . The drift velocity  $v_D$  in equation (2.43) is presented by the quantum mechanical expectation value of the velocity in  $x$ -direction as

$$\mathbf{v}_n(k_x) = \mathbf{e}_x \frac{\hbar k_x}{m^*} = \mathbf{e}_x \frac{1}{\hbar} \frac{\partial E_n(k_x)}{\partial k_x} .$$

Converting the small interval  $dk_x$  in equation (2.43) into the corresponding energy interval by means of  $dk_x = dE \frac{\partial k_x}{\partial E_n k_x}$  yields an expression, which is identical to the 1D DOS from equation (2.38) up to a factor of  $\pi$ . Consequently, the quantum mechanical current density reads as

$$d\mathbf{j}_{nE}(\mathbf{r}) = \pm \mathbf{e}_x \frac{2|e|}{h} |\chi_n(y, z)|^2 dE . \quad (2.44)$$

We obtain a minus (plus) sign for states with  $k_x > 0$  ( $k_x < 0$ ). Thus, we find that the energy dependence of the group velocity and the energy dependence of the 1D DOS exactly cancel each other.

Since  $dE/|e|$  has the units of a voltage and by exploiting the fact that the transverse modes  $\chi_n(y, z)$  are normalized, we can write for the total current  $I_{tot}$  in the case of a small applied bias  $V_{SD}$  between the ends of the 1D wire:

$$I_{tot} = \frac{2e^2}{h} \cdot N \cdot V_{SD} . \quad (2.45)$$

$N$  presents the number of participating modes, described by the quantum number  $n$ , in the 1D channel. Thus, the conductance  $G$  of an ideal 1D wire in the limit of  $T = 0$  reads

$$G = \frac{I_{tot}}{V_{SD}} = \frac{2e^2}{h} \cdot N . \quad (2.46)$$

### 2.2.2 Electron transmission in the adiabatic approximation

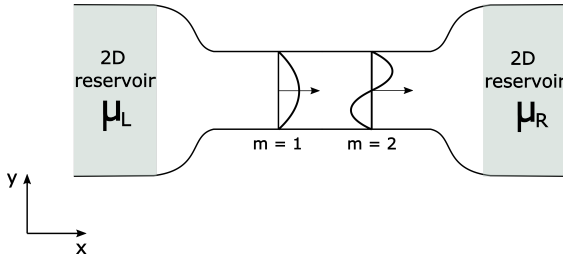


**Figure 2.2:** Sketch of a 1D wire structure in  $x$ -direction, which connects the left 2D reservoir, exhibiting a chemical potential  $\mu_L$ , to the right 2D reservoir with  $\mu_R$ . Two transversal modes  $m = 1, 2$  inside the constriction are indicated.

In a real device, the above assumed translational invariance of the 1D channel in  $x$ -direction is not fulfilled since the 1D wire in the plane of the 2DEG is connected to larger 2D reservoirs. This situation is illustrated in figure 2.2. Thus, for a realistic description of

the conductance through the 1D constriction, the transition from the large 2D reservoir into the 1D wire structure (and vice versa) has to be taken into account.

A commonly applied method is the description of the conductance quantization in the adiabatic approximation, i.e. the wave function changes smoothly in  $x$ -direction. Thereby, the transition from the 2D reservoir into the 1D wire is assumed to be smooth on the length scale of the Fermi wavelength  $\lambda_F$  [59, 60]. The corresponding single particle Hamiltonian

$$\mathcal{H} = -\frac{\hbar^2}{2m^*} \nabla^2 + V(x, y, z)$$

can be separated into two parts

$$\begin{aligned} \mathcal{H}_x &= -\frac{\hbar^2}{2m^*} \frac{\partial^2}{\partial x^2} \\ \mathcal{H}_{y,z}(x) &= -\frac{\hbar^2}{2m^*} \left( \frac{\partial^2}{\partial y^2} + \frac{\partial^2}{\partial z^2} \right) + V(x, y, z) , \end{aligned}$$

in which  $x$  in the expression of  $\mathcal{H}_{y,z}(x)$  parameterizes the wire-induced potential height in  $x$ -direction. Based on the assumed adiabatic approximation, it can be shown that the quantum mechanical wire problem reduces to a simplified 1D potential problem:

$$-\frac{\hbar^2}{2m^*} \frac{\partial^2 \zeta_m(x)}{\partial x^2} + V_m^{eff}(x) \zeta_m(x) = E \zeta_m(x) . \quad (2.47)$$

$V_m^{eff}(x)$  is the effective potential which a conduction electron in the transversal mode  $m$  experiences when traversing the 1D constriction.  $\zeta_m(x)$  are the expansion coefficients of the orthonormalized eigenfunctions of  $\mathcal{H}_{y,z}(x)$ . We now follow the deduction in the preceding subsection 2.2.1, where we employed the quantum mechanical expression for the current density in order to obtain the equation for the total conductance  $G$  (see equation (2.46)). This way, we find in the limit of a small applied source-drain bias between the 2D reservoirs with chemical potentials  $\mu_L$  and  $\mu_R$  the following expression for  $G$  in a 1D wire structure in adiabatic approximation:

$$G = \frac{2e^2}{h} \sum_m \int_{-\infty}^{+\infty} dE \mathcal{T}_m(E) \left( -\frac{\partial f_L(E)}{\partial E} \right) . \quad (2.48)$$

$\mathcal{T}_m(E)$  is the energy-dependent transmission probability of a transversal mode  $m$  through the constriction. At low temperatures, the derivative of the Fermi-Dirac distribution at the Fermi energy is sharply peaked and equation (2.48) simplifies to

$$G = \frac{2e^2}{h} \sum_m \mathcal{T}_m(E_F) . \quad (2.49)$$

In order to obtain values for the transmission probabilities of a mode  $m$ , the constriction-

## 2 Fundamental concepts of 2D and 1D electric transport

---

defining potential  $V(x, y, z)$  has to be further specified. The 1D wire structures, that we analyse in the course of this work, are well-described by a saddle potential, which create a short and narrow constriction. This structure is commonly referred to as *quantum point contact (QPC)*.

In the saddle point model,  $V(x, y, z)$  takes the form

$$V(x, y, z) = -\frac{1}{2}m^*\omega_x^2x^2 + \frac{1}{2}m^*\omega_y^2y^2 + V(z), \quad (2.50)$$

where  $\omega_x$  and  $\omega_y$  parameterize the curvature of the confining parabolic potentials in  $x$ - and  $y$ -direction. A sketch of the potential landscape in the  $x$ - $y$ -plane is shown in figure 6.2 in chapter 6. The quantum mechanical problem of the saddle-point-defined QPC can be again separated into the corresponding spatial contributions. For the confinement in  $y$ -direction, we gain harmonic oscillator solutions of the form  $E_y = \hbar\omega_y(m + 1/2)$ . For the motion in  $x$ -direction, we obtain the simplified expression

$$\left(-\frac{\hbar^2}{2m^*}\partial_x^2 - \frac{1}{2}\omega_x^2x^2\right)\zeta(x) = E_x\zeta(x). \quad (2.51)$$

As shown in [6], the transmission of a transversal mode  $m$  through the parabolic potential barrier in  $x$ -direction can be described as

$$\mathcal{T}_m(E) = \frac{1}{1 + e^{-2\pi\epsilon_m}}, \quad (2.52)$$

with the energy parameter

$$\epsilon_m = \frac{E - \hbar\omega_y(m + 1/2) - E_z}{\hbar\omega_x}. \quad (2.53)$$

Thus, from equations (2.52) and (2.53), it follows that a transversal mode  $m$  in a QPC exhibits a high transmission probability when the condition  $\omega_y/\omega_x \gg 1$  is fulfilled.

### 2.2.3 Non-ideal 1D transport

In a realistic QPC, non-idealities in the 1D transport through the constriction have to be taken into account. A non-adiabatic transition from the 2D reservoirs into and out of the QPC generally leads to transversal mode mixing in the QPC, whereby the transmission coefficients, given in equation (2.52), can be altered. Furthermore, a deviation from the above assumed smooth saddle potential may lead to the formation of local potential minima in the channel. This introduces a particular energy-dependence of the transmission probabilities in the 1D wire. For example, Coulombic impurities, which are located in the direct vicinity of the QPC, are likely to impose a disorder potential on the QPC-defining potential. This may lead to fluctuations of the conductance through the 1D constriction.

Non-ideal 1D transport related phenomena in conductance measurements will be further discussed in chapter 6 and 8.

### 2.2.4 1D transport in a perpendicular magnetic field

Applying an external magnetic field  $\mathbf{B}$  perpendicular to the plane of the 2DEG in which the QPC is created further modifies the energy dispersion inside the 1D constriction [61–63]. In the above considered QPC, we assumed a harmonic confinement potential in  $y$ -direction, i.e.  $V(y) = \frac{1}{2}m^*\omega_y y^2$ , where  $\omega_y$  describes the strength of the confinement in  $y$ , whereas we have free motion in the  $x$ -direction. The single-particle Hamiltonian of the QPC when an additional external magnetic field is applied can be expressed in the Landau gauge  $\mathbf{A} = (By, 0, 0)$  as

$$\mathcal{H}_{xy} = -\frac{\hbar^2}{2m^*} \frac{\partial^2}{\partial y^2} + \frac{(-i\hbar \frac{\partial}{\partial x} + eBy)^2}{2m^*} + \frac{1}{2}m^*\omega_y y^2. \quad (2.54)$$

The dispersion relation  $E(n, k_x)$  of the resulting *hybrid magnetoelectronic* 1D subbands can be written as

$$E(n, k_x) = (n + \frac{1}{2})\hbar\omega + \frac{\hbar^2 k_x^2}{2m^*(B)} = E_n(B) + \frac{\hbar^2 k_x^2}{2m^*(B)}, \quad (2.55)$$

with

$$\omega^2 = \omega_y^2 + \omega_c^2 \quad (2.56)$$

$$\omega_c = \frac{eB}{m^*} \quad (2.57)$$

$$m^*(B) = \left(\frac{\omega}{\omega_y}\right)^2. \quad (2.58)$$

Thus, the external magnetic field results in an increased 1D subband separation  $\Delta E_n(B)$  due to an increase of the oscillator frequency  $\omega$ . With an increasing external magnetic field  $\mathbf{B}$ , the 1D subbands become successively depopulated. Additionally, the effective mass of the electrons  $m^*(B)$  is increased, which leads to a flattening of the subband dispersion curve. In the limit of a strong perpendicular magnetic field, the hybrid magnetoelectronic subbands evolve into magneto subbands, i.e. the Landau levels, described by equation (2.18). The evolution of the 1D subband dispersion with increasing magnetic field is schematically depicted in figure 2.3.

Owing to the increased 1D subband spacing, the application of a perpendicular B-field in 1D transport measurements generally leads to an improvement of the ballisticity inside the 1D channel since backscattering is reduced.

The 1D DOS (see equation (2.38)) in an external magnetic field is concomitantly modified and we obtain

$$\mathcal{D}_{1D}^B(E, \omega) = \frac{\omega}{\pi \hbar \omega_c} \left( \frac{2m^*}{E - E_n} \right)^{1/2}. \quad (2.59)$$

## 2 Fundamental concepts of 2D and 1D electric transport

---

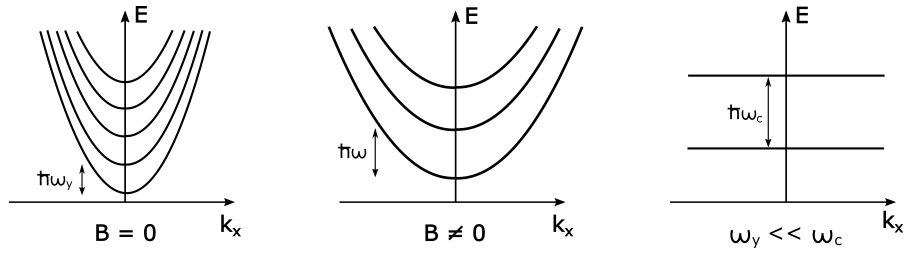


**Figure 2.3:** 1D subband dispersion with an increasing perpendicular magnetic field from left to right.

Accordingly, the 1D DOS peak is narrower as compared to the case when no external magnetic field is applied to the system (see equation (2.38)).



# 3

## Fundamental concepts of spin-orbit interaction

An electron, moving in an electric field  $\mathbf{E} = -\nabla V(\mathbf{r})$  experiences in its restframe an effective magnetic field  $\mathbf{B}_{\text{eff}}$  via Lorentz transformation. This effective field, acting on the electron's spin, reads as  $\mathbf{B}_{\text{eff}} = -\frac{1}{c^2}\mathbf{v} \times \mathbf{E}$ , where  $c$  is the velocity of light [55, 64]. Hence, the spin of the electron is affected by its orbital motion in the electric field which is commonly referred to as spin-orbit coupling (SOC) or spin-orbit interaction (SOI). In the case of an electron moving in a crystal,  $V_0$  is the Coulomb potential of the atomic cores of the crystal. The so-called Pauli SOI-term, which enters the Hamiltonian of the moving electron, can be expressed as

$$\mathcal{H}_{SO} = -\frac{\hbar}{4m_0^2c^2}\boldsymbol{\sigma} \cdot \mathbf{p} \times (\nabla V_0) , \quad (3.1)$$

where  $\mathbf{p}$  is the momentum operator and  $\boldsymbol{\sigma}$  is the vector of Pauli spin matrices. Calculating the band structure of a semiconductor crystal by means of the  $\mathbf{k} \cdot \mathbf{p}$ -perturbation theory near band extrema, whereby the atomic SOI via  $\mathcal{H}_{SO}$  is taken into account, reveals the effect of atomic SOC on the electronic band structure in first approximation. Therein, SOC is parameterized by matrix elements, which incorporate band edge parameters of the system. By employing this method, one obtains a splitting of the topmost valence bands with  $j = \frac{3}{2}$  and  $j = \frac{1}{2}$ , where  $j$  is the total angular momentum. The  $j = \frac{3}{2}$  and  $j = \frac{1}{2}$  states are separated by the so-called spin-orbit (SO) gap  $\Delta_0$ . Incorporating the effect of the valence bands on the conduction band perturbatively via higher order terms unveils the effect of SOC on the spin-state of the conduction electrons. This yields a further modification of the band structure of the crystalline solid.

In the following chapter, we briefly introduce the effect of band-related SOI on 2D and 1D systems, together with thereby arising effects in (magneto)transport.

## 3.1 SOI in 2D systems

Spin degeneracy of electrons and hole states in a semiconductor system is a consequence of the combination of inversion symmetry in space and time [64]. By breaking the space inversion symmetry, we find the Kramers degeneracy

$$E_+(k) = E_-(-k)$$

to still be valid, yet the spin degeneracy of the system is lifted.

In the semiconductor material systems, analysed in this thesis, spatial inversion asymmetry is generated by the asymmetry of the crystal potential, as well as by structure-related confinement potentials.

### 3.1.1 Bulk inversion asymmetry (BIA)

The first contribution to band-related spin-splitting in our system is the so-called Dresselhaus term or the *bulk inversion asymmetry* (BIA). BIA arises due to a microscopic electric field that is generated by a lack of inversion symmetry in the zinc blende lattice. For a 3D crystal structure, the corresponding Hamiltonian takes the form

$$\mathcal{H}_D^{bulk} = \gamma[\sigma_x k_x(k_y^2 - k_z^2) + \sigma_y k_y(k_z^2 - k_x^2) + \sigma_z k_z(k_x^2 - k_y^2)] , \quad (3.2)$$

where  $\sigma_x$ ,  $\sigma_y$  and  $\sigma_z$  are the Pauli spin matrices.  $\gamma$  is a material-dependent parameter, describing the strength of the bulk inversion asymmetry.  $\mathbf{x}$ ,  $\mathbf{y}$ , and  $\mathbf{z}$  point into the direction of the cubic axes. The Dresselhaus term can also be expressed in the form of an effective momentum-dependent magnetic field  $\Omega_D^{bulk}(\mathbf{k})$ , which acts on the spin  $\boldsymbol{\sigma}$ . In the case of a bulk semiconductor the corresponding energy splitting is cubic in  $\mathbf{k}$  [65, 66].

Owing to energy quantization in 2D systems, where we take  $\mathbf{z}$  as the quantization (growth) axis, the Dresselhaus contribution  $\mathcal{H}_D$  to SOI is reduced to a linear term in  $k$  [67]. The exact form of  $\mathcal{H}_D$  depends on the choice of the describing coordinate system. For  $x \parallel [1\bar{1}0]$ ,  $y \parallel [110]$  and  $z \parallel [001]$  the Dresselhaus contribution can be written as

$$\mathcal{H}_D = \beta(k_y \sigma_x + k_x \sigma_y) = \Omega_D(\mathbf{k}) \cdot \boldsymbol{\sigma} , \quad (3.3)$$

with

$$\Omega_D = \beta \cdot \begin{pmatrix} k_y \\ k_x \\ 0 \end{pmatrix} .$$

The prefactor  $\beta$ , which describes the strength of the linear Dresselhaus contribution to SOI, can be expressed as:  $\beta = \gamma \langle k_z^2 \rangle \propto 1/L_W^2$  [66, 68].  $\langle k_z^2 \rangle$  describes the expectation value of the electron momentum in the size-quantized  $z$ -direction. Since  $\gamma$  stems from the crystal fields, the only way to modify the Dresselhaus contribution is thus by changing the quantum well (QW) thickness  $L_W$ , whereby the expectation value of  $k_z$  is altered.

### 3.1.2 Structure inversion asymmetry (SIA)

In semiconductor heterostructures another effect can give rise to SOI. This additional contribution to SOI, often referred to as *structure inversion asymmetry* (SIA), was first formulated by Bychkov and Rashba [69, 70] and is generated by rather macroscopic electric fields, which act on the conduction electrons. It originates from built-in or external electric fields, as well as from band edge discontinuities in the heterosystem. The asymmetry of the confining potential results in an effective magnetic field  $\Omega_R(\mathbf{k})$  [55]. In first approximation, the corresponding energy spin-split term is linear in  $k$  and can be expressed with the single-particle Hamiltonian

$$\mathcal{H}_R = \alpha(k_y\sigma_x - k_x\sigma_y) = \Omega_R(\mathbf{k}) \cdot \boldsymbol{\sigma} , \quad (3.4)$$

with

$$\Omega_R = \alpha \cdot \begin{pmatrix} -k_y \\ k_x \\ 0 \end{pmatrix} .$$

This Rashba Hamiltonian  $\mathcal{H}_R$  can be reformulated in a way, which underlines the experimental access to tune the corresponding spin-splitting in the system:

$$\mathcal{H}_R^{6c6c} = r_{41}^{6c6c} \boldsymbol{\sigma} \cdot \mathbf{k} \times \boldsymbol{\mathcal{E}} = r_{41}^{6c6c} \mathcal{E}_z \cdot (k_y\sigma_x - k_x\sigma_y) . \quad (3.5)$$

Hereby,  $r_{41}^{6c6c}$  is a material-specific prefactor [55] and the electric field  $\boldsymbol{\mathcal{E}}$ , corresponding to the confining potential, points into the  $z$ -direction.

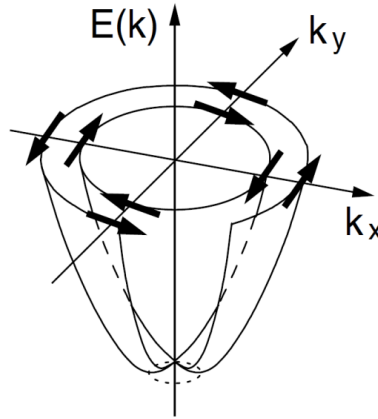


**Figure 3.1:** Spin-split dispersion  $E(\mathbf{k})$  of electrons in a 2D system with Rashba-type SOI. The arrows indicate the spin orientation of the eigenstates. [55]

The resulting dispersion relation  $E(\mathbf{k}) \equiv E_{\pm}(\mathbf{k}_{\parallel})$  of the conduction electrons inside the 2D system is displayed in figure 3.1. The SO-induced effective magnetic field  $B_{eff}$  is oriented perpendicular to the growth direction and to the corresponding electron momentum. This results in a vortex-like structure of  $B_{eff}$  in  $k$ -space. The spin-resolved eigenstates can be described with

### 3 Fundamental concepts of spin-orbit interaction

$$E_{\pm}(k_{||}) = \langle \mu_c \rangle \mathbf{k}_{||}^2 \pm \langle r_{41}^{6c6c} \mathcal{E}_z \rangle |\mathbf{k}_{||}|, \quad (3.6)$$

where  $\mu_c/2\hbar^2$  is the reciprocal effective mass and  $k_{||}^2 = k_x^2 + k_y^2$  is the quasi-crystal momentum of conduction electrons in the QW plane.

Thus, the strength of Rashba-type SOI, i.e.  $\alpha = \langle r_{41}^{6c6c} \mathcal{E}_z \rangle$ , is controlled by the total electric field  $\mathcal{E}_z$  in  $z$ -direction, multiplied by a material-dependent prefactor  $r_{41}^{6c6c}$ . For GaAs  $r_{41}^{6c6c}$  takes the value  $5.206e\text{\AA}^2$ , for InAs we find  $r_{41}^{6c6c} = 117.1e\text{\AA}^2$  [55].

Nitta et al. [71] were the first to demonstrate the ability to experimentally modulate the strength of Rashba-type SOI via the application of an external electric field in a top-gated  $\text{In}_{0.53}\text{Ga}_{0.47}/\text{In}_{0.52}\text{Al}_{0.48}\text{As}$  2D electron system.

#### 3.1.3 Combination of SIA and BIA

In a 2DEG, both contributions to SOI, i.e. SIA and BIA, generally influence the energy eigenstates of the conduction electrons. In the most general form, the resulting 2D SOI-Hamiltonian can be expressed as a sum of  $\mathcal{H}_R$  from equation (3.4) and  $\mathcal{H}_D$  from equation (3.3) as

$$\mathcal{H}_{SOI} = \mathcal{H}_R + \mathcal{H}_D = \alpha(k_y\sigma_x - k_x\sigma_y) + \beta(k_y\sigma_x + k_x\sigma_y). \quad (3.7)$$

De Andrada e Silva et al. [72] showed that the total electric field, entering the description of SOI, can lead to a highly anisotropic spin-splitting in  $k$  since both effects interfere, particularly when they become equal in strength, i.e.  $\beta = \pm\alpha \equiv \lambda/2$ . For these two special cases, the resulting effective magnetic field  $\Omega_{PST}$  can be expressed as

$$\Omega_{PST} = \lambda \cdot \begin{pmatrix} k_y \\ 0 \\ 0 \end{pmatrix} \quad \text{and} \quad \Omega_{PST} = \lambda \cdot \begin{pmatrix} 0 \\ k_x \\ 0 \end{pmatrix},$$

with the index PST being the abbreviation of the term *persistent spin-texture* [66]. For this special form of  $\Omega_{PST}$ , we see that the spin-splitting vanishes in certain directions in  $k$ -space [73, 74]. Furthermore, it results in a spatially periodic mode of the spin-state, being independent of the momentum direction. This effect is called the *persistent spin-helix* (PSH) [75].

To evaluate the resulting spin-splitting in our 2D electron system, being hosted in an (InAs/)  $\text{In}_{0.75}\text{Ga}_{0.25}\text{As}/\text{In}_{0.75}\text{Al}_{0.25}\text{As}$  heterostructure in the form of a QW with a thickness of  $20\text{nm}$  (see chapter 5), it is important to consider the relative strengths of Rashba- and Dresselhaus-contributions to SOI. A first estimate is given by literature:

Lommer et al. [76] showed that in general SIA dominates over BIA for small band-gap semiconductors, such as InAs and InSb, whereas for large band-gap materials like GaAs the trend is often opposite. While Winkler [55] pointed out that  $\text{In}_{0.53}\text{Ga}_{0.47}\text{As}$ -based material systems are in an intermediate regime where both contributions from BIA and SIA have to be considered, Luo et al. [77] showed that for InAs heterostructures the SIA

contribution clearly dominates over BIA. Furthermore, studying the magnetotransport in a symmetrically doped, 10nm In<sub>0.53</sub>Ga<sub>0.47</sub>As QW, Faniel et al. [78] were able to experimentally demonstrate that the BIA contribution to SOI is much smaller than the contribution from SIA. The MT measurements of Schäpers et al. [79] found that the BIA-term in their In<sub>0.77</sub>Ga<sub>0.23</sub>As/InP heterostructure can be neglected as compared to the SIA contribution.

Based on these literature reports, we can summarize that for structures having a higher In content and a larger QW thickness, the Rashba-mechanism is expected to clearly dominate over the Dresselhaus contribution. Considering the comparably large thickness of our 20nm In<sub>0.75</sub>Ga<sub>0.25</sub>As QWs, we consequently infer that the PSH-state, as well as BIA spin splitting can be neglected in the analysis of SOI-related effects in our heterostructure.

## 3.2 Evaluation of SOI strength

An experimental method to estimate the strength of Rashba-type SOI in a 2D system is given by the evaluation of the magnetooscillations, arising in the longitudinal resistivity in a MT measurement. In the following, we briefly summarize the two commonly employed evaluation methods of the Shubnikov-de Haas oscillations to obtain the Rashba coefficient  $\alpha$  of the system.

### 3.2.1 FFT analysis of the magnetooscillations

The most commonly utilised approach to determine the SOI strength is by a fast Fourier transformation (FFT) of the longitudinal resistivity  $\rho_{xx}(B)$ , acquired in a MT measurement. Therein, the coefficient  $\alpha$  is calculated on the basis of the determined 2D electron densities in the FFT of  $\rho_{xx}$ . Here, we shortly recapitulate the main steps towards the description of Rashba-type SOI based on the electron densities of the 2DEG, wherein we follow an envelope function approach as presented in [80] and [79]. Considering the  $\mathbf{k} \cdot \mathbf{p}$ -interaction of the  $\Gamma_6$  conduction band with the remote valence bands to which the coupling is strongest, i.e. the  $\Gamma_7$  and  $\Gamma_8$  valence bands, the corresponding Hamiltonian for a 2D electron system can be written as

$$\mathcal{H}_{2D} = \left( E_z^{sub} - \frac{\hbar^2}{2m^*} \Delta_{\parallel}^2 + \varphi(r_{\parallel}) \right) \cdot \mathbf{1} + \frac{1}{\hbar} \alpha \cdot \left( \sigma \times \frac{\hbar}{i} \nabla \right). \quad (3.8)$$

$E_z^{sub}$  is the energy of the first size-quantized subband of the QW and  $z$  points along the (001) growth direction. The effective mass  $m^*$  in the above equation takes the form

$$m^{*-1} = \langle \Psi_z | m^{*-1}(z) | \Psi_z \rangle ,$$

with  $|\Psi_z\rangle$  being the wave function of the unperturbed electrons of the first subband. By expressing  $m^*$  in this form, the leakage of the wave function into the barrier material is included in the calculations. It can be shown that the corresponding Rashba coefficient  $\alpha$

### 3 Fundamental concepts of spin-orbit interaction

of the above equation (3.8) can be written as

$$\alpha = \frac{\hbar^2 E_p}{6m_0} \{a' \langle \mathcal{E}_A \rangle + b' (\langle \mathcal{E}_{B_u} \rangle + \langle \mathcal{E}_{B_l} \rangle) - \frac{1}{2} b (|\Psi_{z_u}|^2 - |\Psi_{z_l}|^2)\} . \quad (3.9)$$

$E_p$  is a so-called  $\mathbf{k} \cdot \mathbf{p}$ -interaction parameter, which describes the coupling strength of the  $\Gamma_6$  conduction band to the coupled valence bands  $\Gamma_7$  and  $\Gamma_8$ .  $\langle \mathcal{E}_A \rangle$  represents the expectation value of the electric field inside the QW, i.e. material A,  $\langle \mathcal{E}_{B_u} \rangle$  and  $\langle \mathcal{E}_{B_l} \rangle$  describe the expectation values of the electric field in the upper and lower barriers of the QW, i.e. material B.  $|\Psi_{z_u}|^2$  and  $|\Psi_{z_l}|^2$  are the wave function probabilities at the upper and lower QW barriers. The prefactor  $a'$ ,  $b'$  and  $b$  contain material-dependent band structure parameters, as well as the energy level  $E$  of the electronic state inside the QW. These prefactors can be expressed as

$$a' = \left( \frac{1}{(E - E_{\Gamma_7}^A)^2} - \frac{1}{(E - E_{\Gamma_8}^A)^2} \right) \quad (3.10)$$

$$b' = \left( \frac{1}{(E - E_{\Gamma_7}^A - \Delta E_{\Gamma_7})^2} - \frac{1}{(E - E_{\Gamma_8}^A - \Delta E_{\Gamma_8})^2} \right) \quad (3.11)$$

$$b = \left( \frac{\Delta E_{\Gamma_7}}{(E - E_{\Gamma_7}^A - \Delta E_{\Gamma_7})^2} + \frac{\Delta E_{\Gamma_7}}{(E - E_{\Gamma_7}^A)^2} - \frac{\Delta E_{\Gamma_8}}{(E - E_{\Gamma_8}^A - \Delta E_{\Gamma_8})^2} - \frac{\Delta E_{\Gamma_8}}{(E - E_{\Gamma_8}^A)^2} \right) . \quad (3.12)$$

The terms  $\Delta E_{\Gamma_7}$  and  $\Delta E_{\Gamma_8}$  present the valence band offsets of materials A and B.

By means of equation (3.9) with the prefactors as described by the above relations (3.10) to (3.12), we deduce that the Rashba SOI is based on the coupling of the conduction band with the valence bands. By partitioning the Rashba term as in expression (3.9), it becomes clearly visible that the resulting Rashba-coupling coefficient  $\alpha$  is comprised of three contributing terms:

- (1) The first term containing the prefactor  $a'$  parameterizes the SOI strength due to an electric field inside the QW, i.e. material A, acting on the conduction electrons. It can be simply written as the expectation value of the field inside the well, i.e.  $\langle \mathcal{E}_A \rangle$ , multiplied by a material- and energy-dependent prefactor,  $a'$ . For an infinitely deep QW, this would be the only contribution to the Rashba spin-splitting.
- (2) The second term takes the extension of the wave function  $|\Psi_z\rangle$  into the barrier material B into account. Thus, this contribution is proportional to the expectation value of the electric field inside the barrier layers, i.e.  $\langle \mathcal{E}_{B_u} \rangle$  and  $\langle \mathcal{E}_{B_l} \rangle$ .
- (3) The third contribution to  $\alpha$  arises from the abrupt change of material the wave function experiences at the interfaces between materials A and B. This contribution can be described as the difference of the probability densities of the conduction electrons at the upper and lower QW interfaces, multiplied by a band structure-dependent parameter  $b$ , which contains the corresponding band offsets [81, 82]. For a correct calculation of the Rashba parameter the last term in equation (3.9) is of vital importance as was explicitly shown in various publications in literature [79–85].

Thus, we find that an external electric field, which is for example generated by a gate electrode, enters into all of the three terms contributing to the expression (3.9) of  $\alpha$ , since it modulates the band profile, as well as the wave function probability distribution.

As already introduced in the preceding section, the resulting energy dispersion  $E(k_{\parallel})$  of the conduction electrons inside the QW splits into two spin-resolved parabolas, which are shifted horizontally in  $k$ -space according to

$$E(k_{\parallel}) = E_z^{sub} + \frac{\hbar k_{\parallel}^2}{2m^*} \pm \alpha |k_{\parallel}| . \quad (3.13)$$

The horizontal shift of the two spin-split parabolas is determined by the above described Rashba-coefficient  $\alpha$ . The energy eigenstates for a specific value of  $k_x$  are separated in energy by  $\Delta E_k = 2\alpha k$ . Commonly, one refers to this energy difference as the spin-splitting energy  $\Delta E_{ss}$  for a specific  $k$ .

Furthermore, the effective mass of an electron in a spin-resolved eigenstate depends on the particular energy branch: Electrons on the outer branch exhibit a larger effective mass than electrons on the inner branch. Consequently, the energy spin-splitting manifests itself in the 2D DOS, which is given by

$$\mathcal{D}_{\pm}(E) = \frac{1}{2} \frac{m^*}{\pi \hbar^2} \left( 1 \mp \frac{1}{\sqrt{1 + [2(E - E_z^{sub})\hbar^2]/(\alpha m^*)}} \right) . \quad (3.14)$$

The individual DOS of each branch is found to resemble half the one of the spin-degenerate 2D system, i.e.  $\mathcal{D}_{2D} = 2m^*/(\pi \hbar^2)$ , which is now further modified by an energy-dependent correction factor. This factor takes the altered effective electron masses on the inner and outer parabolas into account. Looking at a particular Fermi energy  $E_F$ , we see by means of equation (3.14) that an imbalance of the charge carrier densities in the two spin-split energy branches is present. By integrating over the DOS  $\mathcal{D}_+(E)$  and  $\mathcal{D}_-(E)$  up to  $E_F$  yields the corresponding spin-degenerate electron densities, which are now labeled as  $n_+$  and  $n_-$ .

In a MT measurement, these two spin-split branches in the 2DEG with the densities  $n_+$  and  $n_-$  both contribute to the Shubnikov-de Haas oscillations, described by equation (2.21). If the SOI lifts the spin degeneracy in this manner, a FFT of the longitudinal resistivity  $\rho_{xx}(B)$  over  $1/B$ , which spectrally decomposes the signal, yields a prominent double-peak structure, which thus serves as an experimental signature of the spin-split dispersion. The two frequencies obtained in the FFT spectrum correspond to the densities  $n_+$  and  $n_-$ . The FFT process is described in detail in subsection 9.2.4.

As was first pointed out by Luo et al. [86], measuring  $n_+$  and  $n_-$  in a MT measurement therefore yields access to the SOC coefficient  $\alpha$  via the relation

$$\alpha = \frac{\Delta n \hbar^2}{m^*} \sqrt{\frac{\pi}{2(n - \Delta n)}} . \quad (3.15)$$

Here,  $\Delta n$  is the difference of the electron concentrations of the two spin-split branches, i.e.

### 3 Fundamental concepts of spin-orbit interaction

$\Delta n = n_+ - n_-$ , whereas  $n$  is the average value of the charge carrier densities  $n = n_+ + n_-$ . If no further conducting channel contributes to the transport in the system,  $n$  can be substituted by the measured Hall density  $n_{Hall}$ .

We want to point out that for the derivation of formula (3.15) Zeeman spin-splitting, as well as contributions from BIA are neglected. Since we expect the Dresselhaus contribution to spin-splitting to be small as compared to the SIA contribution in our system, the effect of Zeeman spin-splitting will dominate potential deviations of the calculated  $\alpha$  from reality in our case.

#### 3.2.2 Beating-node analysis of the magnetooscillations

Based on the analysis of the magnetooscillations in the longitudinal resistivity, there is a second evaluation method to determine the SOI strength, which we will present in the following. In contrast to the above presented method, however, Zeeman spin-splitting is not incorporated in the estimation of the Rashba coefficient.

The total Hamiltonian describing a Rashba spin-orbit coupled system in an external magnetic field can be expressed as

$$\mathcal{H} = \mathcal{H}_O + \mathcal{H}_Z + \mathcal{H}_R .$$

Therein,  $\mathcal{H}_O$  is the Hamiltonian of a quasi-free electron in a magnetic field,  $\mathcal{H}_Z$  is the contributing Zeeman term and  $\mathcal{H}_R$  takes the structure-induced inversion asymmetry into account. The corresponding eigenenergy spectrum is given by [70, 87]:

$$E_{n_{\pm}} = \hbar\omega_c \left(n + \frac{1}{2} \pm \frac{1}{2}\right) \mp \sqrt{(\hbar\omega_c - g^* \mu_B B)^2 + \frac{8\alpha^2 e B}{\hbar} \left(n + \frac{1}{2} \pm \frac{1}{2}\right)} \quad (3.16)$$

(+) and (−) denote the two spin-resolved eigenstates. Whereas the DOS of the Landau levels and the Zeeman spin-splitting go linearly with the applied external magnetic field  $B$  - if  $\mathbf{B}$  is orthogonal to the 2DEG - the Rashba SOI causes a B-field-dependent enhancement of the spin-splitting in the system. Hence, the ratio of the total spin-splitting energy  $\delta_{ss}$  and the Landau level separation  $\Delta E_{LL} = \hbar\omega_c$ , i.e.  $\delta_{ss}/\Delta E_{LL}$ , is not constant anymore as it would be for an inversion-symmetric system subjected to a perpendicular magnetic field. In this case, the ratio  $\delta_{ss}/\Delta E_{LL} = g^* \mu_B B / \hbar\omega_c$  is constant. Owing to the presence of Rashba SOI, the ratio becomes  $B$ -field-dependent.

The modification of  $\delta_{ss}$  due to SOI becomes more dominant in the limit of small magnetic field values. Here, Landau levels, described by equation (3.16), cross when the ratio  $\delta_{ss}/\Delta E_{LL}$  takes an integer value. The alteration of the energy separation of the eigenstates by sweeping the external magnetic field manifests itself in an amplitude modulation of the Shubnikov-de Haas oscillations: a beating in  $\rho_{xx}(B)$  arises. A node in  $\rho_{xx}(B)$  corresponds to the situation where the energy separations of the neighboring eigenstates from equation (3.16) exhibit equivalent distances, whereas a peak in the amplitude of the envelope of  $\rho_{xx}(B)$  is observed when the eigenstates are not equally spaced in energy.



This can be translated into a mathematical relation: A node in  $\rho_{xx}(B)$  appears when the ratio  $\delta_{ss}/\hbar\omega_c$  becomes half-integer.

Via the amplitude modulation of the Shubnikov-de Haas oscillation, the Rashba SOI-strength  $\alpha$  can be determined. As was shown by Das et al. [83], to obtain a good estimate for the SOI strength  $\alpha$ , the total spin-splitting of the eigenstates (3.16) can be approximated as

$$\delta_{ss} \approx \Delta E_{so} + sg^* \mu_B B .$$

The modulation of the amplitude  $A$  of the Shubnikov-de Haas oscillation in a MT measurement of  $\rho_{xx}$  is given by

$$A \propto \cos\left(\pi \frac{\delta}{\hbar\omega_c}\right) .$$

Hence, the condition for a node-position reads as

$$\frac{\delta_{ss}}{\hbar\omega_c} = i - \frac{1}{2} ,$$

with  $i \in \mathbb{R}^+$  being the node index of the beating in  $\rho_{xx}$ . Inserting  $\mu_B = \frac{e\hbar}{2m_0}$  into the upper equation yields

$$i = \frac{2m^* \alpha k_F}{\hbar e} \left(\frac{1}{B}\right) + \left(\frac{g^* m^*}{2m_0} + \frac{1}{2}\right) . \quad (3.17)$$

Thus, from the slope of the linear dependence of the node-index  $i$  on  $1/B$  the Zeeman spin-splitting-independent estimation of the Rashba spin-orbit parameter  $\alpha$  can be obtained [79].

Yet, to give a meaningful estimation of  $\alpha$  by means of this beating-node analysis at least three clear nodes in  $\rho_{xx}(B)$  have to be present. This often impedes the implementation of this experimental evaluation method in reality.

Furthermore, from the intersection of the linear fit with the y-axis, the effective g-factor,  $g^*$ , can be determined.

### 3.3 SOI in 1D systems

Additionally to the above described SOI terms in 2D, arising from the periodic microscopic crystal potential (BIA term), as well as from electric fields, generated by the symmetry breaking along the growth-direction ( $z$ -axis) due to heterointerfaces, doping and/or the application of an external electric field (SIA term), a further contribution to SOI can be identified in gate-defined 1D narrow constrictions. The electronic confinement potential of a QPC introduces a lateral inversion asymmetry in the transversal direction (here  $y$ -direction), generating electric fields at the opposing potential walls of the narrow constrictions [63, 88, 89]. This may lead to a spin accumulation at the opposing sidewalls

### 3 Fundamental concepts of spin-orbit interaction

of the QPC in a spin-orbit coupled system. For a symmetric confinement potential, the spin polarizations inside the 1D channel cancel each other. Yet, for an asymmetric confinement one particular spin polarization predominates. This effect was already implemented in a proof-of-concept all-electric spin-polarizer device by Debray et al. [19].

In asymmetric QW systems the contribution of this lateral SOI (LSOI) is generally up to three orders of magnitude smaller than SIA-type SOI for symmetric biasing of the QPC [79, 88]. However, introducing a pronounced asymmetry in the confinement potential of the 1D channel by means of a gate electric field between the QPC-defining finger-gate electrodes leads to an enlarged LSOI, which is likely to dominate the SOI-terms of the system [13]. Such an experimental situation is shown in figure 3.2(a), in which a split-gate (SG) defined QPC is introduced in a 2DEG with high intrinsic SOI.

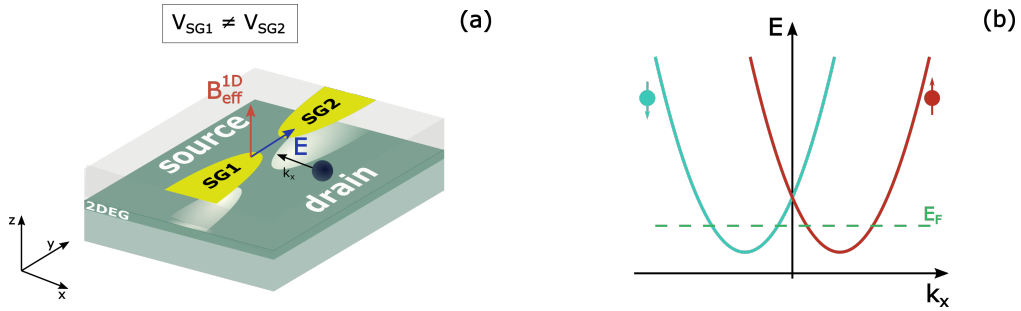


**Figure 3.2:** (a) Sketch of a SG-defined QPC, asymmetrically biased with  $V_{SG1} \neq V_{SG2}$ . An electron moving with  $k_x$  through the 1D constriction experiences the electric field  $E$  between SG1 and SG2 as an effective magnetic field  $B_{eff}^{1D}$ , pointing in  $z$ -direction in their restframe. (b) Dispersion relation of electrons inside a QPC, in which the 1D subbands are laterally shifted due to LSOC. The green dashed line indicates the Fermi energy  $E_F$ .

Biasing the SG-electrodes SG1 and SG2 asymmetrically with  $V_{SG1} \neq V_{SG2} < 0V$  introduces an electric field  $E = -\nabla V(\mathbf{r})$  in the channel. For simplicity, we assume a linear potential gradient between SG1 and SG2 with  $V(\mathbf{r}) = c \cdot \mathbf{e}_y$ . By means of relation (3.5), the corresponding SOI Hamiltonian for electrons moving with momentum  $k_x$  in the 1D channel can be expressed as

$$\mathcal{H}_R^{1D} = \alpha \nabla V(\mathbf{r}) \cdot \mathbf{k} \times \boldsymbol{\sigma} = \alpha c \sigma_z k_x. \quad (3.18)$$

The corresponding effective magnetic field  $B_{eff}^{1D} \equiv \Omega_{LSOC}$  reads as

$$\Omega_{LSOC} = \alpha \begin{pmatrix} 0 \\ 0 \\ ck_x \end{pmatrix}.$$

Accordingly, the conduction electrons inside the QPC experience an effective magnetic field  $B_{eff}^{1D}$ , directed along the  $z$ -axis, perpendicular to their direction of motion  $k_x$  and to the electric field  $E$  between the SG-electrodes.

The LSOI results in a lateral shift of the 1D subbands for spin-up and spin-down electrons against each other as displayed in figure 3.2(b). The strength of the LSOI, and thus of the shift of the two spin-branches can be tuned by the applied offset-voltage  $\Delta V_{SG} = |V_{SG1} - V_{SG2}|$  between the SG-electrodes. Tuning the Fermi energy  $E_F$  under the crossing point of the two branches and by applying a current between the source and drain 2D electron reservoirs leads to a spin-polarized current in  $x$ -direction. Thus, the QPC acts as an all-electrical spin filter with a theoretical spin-polarization efficiency of 100%. This concept of spin polarization can be employed in an all-electric spin-transistor device [13], which is schematically depicted in figure 3.3.

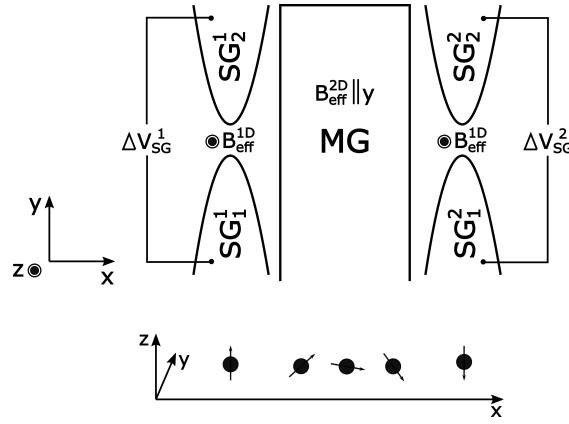


**Figure 3.3:** Sketch of an all-electric spin-transistor concept, composed of two serial QPCs, QPC1 with  $SG_1^1$  and  $SG_2^1$  and QPC2 with  $SG_2^1$  and  $SG_2^2$ , having a distance  $d < l_{mfp}$  in  $x$ -direction. Via Rashba-type SOI, the middle gate-electrode  $MG$  controls the spin precession of the conduction electrons moving in  $k$  by modifying the strength of Rashba-type SOI in the 2DEG underneath.

Therein, two serial SG-defined QPCs are formed in a 2DEG with large intrinsic SOI. The SG-electrodes of QPC1 and QPC2 are biased asymmetrically with the corresponding offset voltages being defined as  $\Delta V_{SG}^1 = |V_{SG1}^1 - V_{SG2}^1|$  at QPC1 and  $\Delta V_{SG}^2 = |V_{SG1}^2 - V_{SG2}^2|$  at QPC2. The distance  $d$  between the QPCs in  $x$ -direction has to be smaller than the elastic mean free path of the conduction electrons travelling inside the device. Thereby, the spin-polarized electrons flow ballistically from QPC1 to QPC2 and thus spin relaxation can be neglected. In this device, QPC1 acts as a spin polarizer, whereas QPC2 serves as a spin analyser. When  $B_{eff}^{1D}$  in QPC1 and in QPC2 point into the same direction, the conduction electrons can pass through both constrictions. For the opposite sign of  $B_{eff}^{1D}$  in QPC1 and QPC2, the resistance of the device is increased.

The current flow through the constrictions can be further modified by an additional middle-gate (MG) situated in between the two QPCs. Applying an external electric field along the  $z$ -direction via the MG yields an effective magnetic field  $B_{eff}^{2D}$ , pointing along the  $y$ -direction for electrons with momentum  $k_x$ . By tuning the voltage  $V_{MG}$  at the MG-electrode, the resulting spin precession angle of the conduction electrons impinging on QPC2 can be adjusted, which eventually controls the current through the device.

### 3 Fundamental concepts of spin-orbit interaction

---



# Epitaxy and methods

<b>4</b>	<b>Experimental methods .....</b>	<b>37</b>
4.1	Molecular-beam epitaxy .....	37
4.2	Postgrowth crystal characterisation methods .	39
4.3	Electric transport measurements.....	40
<b>5</b>	<b>Design and characterisation of In- GaAs/InAlAs systems.....</b>	<b>45</b>
5.1	Buffer layer growth .....	45
5.2	Design of InGaAs/InAlAs active layer systems .	49
5.3	Discussion and conclusion.....	55
5.4	Comment on other material systems .....	57



# 4

## Experimental methods

This chapter shortly presents the applied structural and electrical characterisation methods of the heterostructure devices, which we employ during the course of this thesis. We further give technical details to the used molecular-beam epitaxy system, as well as to our low-temperature setups.

### 4.1 Molecular-beam epitaxy

High-quality and monocrystalline semiconductor layer systems can be fabricated with molecular-beam epitaxy (MBE), operating in an ultra-high vacuum (UHV) chamber. The ability to fabricate heterostructures with atomic precision, the low density of incorporated and growth-related background impurities and the wide variety of materials, which can be deposited by this technique, present the advantages of this processing method of heterostructures.

#### 4.1.1 The MBE system

In this work, a modified Veeco GEN II solid source MBE system is used for the epitaxial growth of the studied III-V heterostructures. The high-purity group III source materials In, Al and Ga are stored in Knudsen-type effusion cells in the MBE system. The group V materials As and Sb are provided by valved cracker cells. Furthermore, as doping material Si, C and Mn are available in our system in form of filament cells and a sublimating effusion cell, respectively. Via a beam flux ionization gauge we are able to determine the beam equivalent pressure (BEP), as well as the beam flux ratio, which is a characteristic parameter for MBE growth conditions. The background pressure in our UHV main chamber is  $< 10^{-11} \text{ mbar}$ . The growth rate is regulated by the temperature-controlled flux of the group III material while As is in abundance. Typically, we apply As<sub>4</sub>-rich growth conditions by employing an As<sub>4</sub>-BEP of  $6 - 8 \cdot 10^{-6} \text{ Torr}$ . The MBE chamber is

## 4 Experimental methods

further equipped with a reflection high energy electron diffraction (RHEED) gun, enabling in-situ crystal growth analysis. In addition, RHEED is used for the calibration of the cell temperature-controlled growth rates of the different materials. Further technical details on the MBE system are given in [90–92].

### 4.1.2 Calibration of the In cell

In order to fabricate ternary  $\text{In}_x\text{Al}_{1-x}\text{As}$  and  $\text{In}_x\text{Ga}_{1-x}\text{As}$  heterostructures of varying composition (therefore see section 5.1), we need to precisely calibrate the flux of the In effusion cell. The generally applied calibration method is based on the comparison of the AlAs growth rate to the growth rate of  $\text{In}_x\text{Al}_{1-x}\text{As}$  for different temperatures of the In effusion cell via evaluating the corresponding RHEED oscillations. Commonly, we use a GaAs (001) substrate for the RHEED calibration of the In cell since the costs of an InAs wafer are several times higher. Furthermore, a GaAs substrate, dedicated for growth rate calibrations, is readily available owing to the therewith conducted RHEED calibration of the Ga and Al growth rates prior to each growth process with these materials. An exemplary InAlAs/AlAs-RHEED calibration curve is shown in figure 4.1(a). The temperature dependence of the In growth rate is determined to be logarithmic over a wide temperature range. A difficulty in this calibration method is that  $\text{In}_x\text{Al}_{1-x}\text{As}$  is not lattice matched to the utilised GaAs substrate. Thus, the amplitude of the RHEED oscillations, which reflect the smoothness of the wafer surface, is efficiently damped for higher In cell temperatures, i.e. for a higher In flux. For lower In cell temperatures, however, inaccuracies in the manual determination of the RHEED oscillation period present the main source of error.

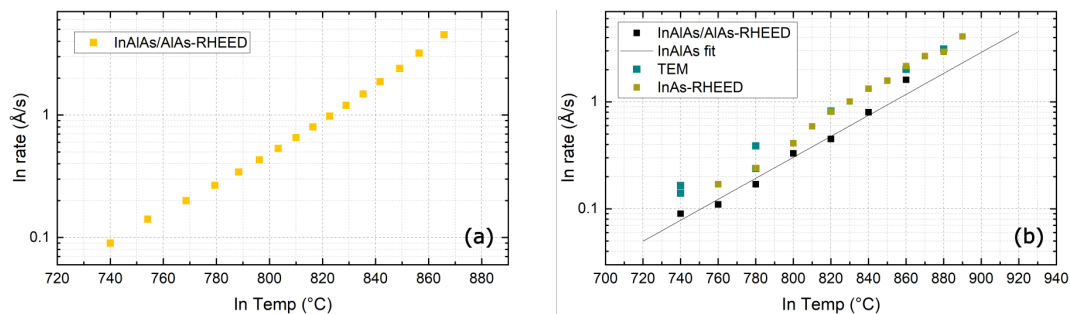


**Figure 4.1:** In calibration curves displaying the In growth rate as a function of the In cell temperature in °C (a) prior to the chamber opening (b) after chamber opening in November 2017.

During the course of this work, the III-V MBE chamber has been opened several times for maintenance, as well as to restock source material. After a chamber opening it is standard to re-calibrate the flux characteristics of the In effusion cell. To account for initial changes of the emission characteristics of the cell, the InAlAs/AlAs-RHEED calibration is repeated several times. In the course of this work further calibration methods are applied



in order to test the validity and accuracy of the above described calibration method. To this end, we calibrate the In growth rate via the evaluation of InAs-RHEED oscillations on an InAs substrate. In addition, transmission electron microscopy images of cross-sectional specimens of In-containing heterostructures are employed to determine the In growth rate at a particular cell temperature. The corresponding calibration curves after a chamber opening in November 2017 are shown in figure 4.1(b).

Moreover, secondary ion mass spectroscopy measurements (described in subsection 4.2.1) from our heterostructures provide a precise experimental method to determine the In, Ga and Al concentrations in the individual layers. In this way, we are able to further evaluate the applied cell calibrations and analyse the composition of the individual  $\text{In}_x\text{Al}_{1-x}\text{As}$  buffer steps.

## 4.2 Postgrowth crystal characterisation methods

To analyse the epitaxial crystal structure of our ternary alloy systems, as well as the fabricated metal gate electrodes and working elements in our studied devices, we apply several characterisation methods. These will be presented in the following.

### 4.2.1 Secondary ion mass spectroscopy

By means of secondary ion mass spectroscopy (SIMS) measurements, performed by Probion Analysis, we gain information on the elemental composition of the individual heterostructure layers and on the MBE-grown layer thicknesses. In a SIMS measurement, the wafer surface is sputtered with a focused primary ion beam. A fraction of the ejected atoms is ionized and presents the secondary ion beam. This second beam passes several focus and filter elements (spatial, energy- and mass-filter), after which it is collected and measured via a photo multiplier or a Faraday cup. Depending on the analysed elements, different ion beams and acceleration voltages, ranging from  $500\text{eV}$  to  $15\text{keV}$ , are applied. To quantify the major elements in our MBE-grown heterostructures, i.e. In, Al and Ga, the process is run in the so-called MCs+ mode. To quantify residual impurity elements, such as for example C and Si, a higher impact energy is needed, which leads to a degraded depth resolution.

### 4.2.2 Transmission electron microscopy

In transmission electron microscopy (TEM) imaging of our heterostructure, electrons are transmitted through a thinned cross-sectional specimen of the wafer material. The image contrast is generated by the interaction - and thus transmission - of the accelerated electrons with the specimen. Owing to the small de-Broglie wavelength of the imaging electrons, the resolution lies in the sub-Å range. Further information on the imaging

## 4 Experimental methods

process, as well as on technical details are given in [93].

The TEM images shown in this work are provided by Felix Schwarzhuber from the group of Prof. Dr. Zweck at the university of Regensburg with a FEI Tecnai F30 operating at  $300kV$ .

### 4.2.3 Atomic force microscopy

In order to study the surface texture of our ternary alloy system, as well as the structure of fabricated gate electrodes, a Veeco Dimension Icon Atomic Force Microscope (AFM) is employed, operating in tapping mode. Thereby, the force between the sample surface and the oscillating Si-tip is measured from which the mutual spatial separation can be calculated.

## 4.3 Electric transport measurements

The utilised measurement setups, as well as the applied measurement concepts for the experiments conducted in this work are presented in the following.

### 4.3.1 Device design

We use three different sample geometries of our heterostructures in the course of this thesis: MT measurements are performed on samples in van der Pauw geometry, as well as on lithographically defined Hall bar structures. The 1D transport characteristics are analysed on a Hall bar mesa, being equipped with additional finger-gate electrodes.

#### Measurement concepts

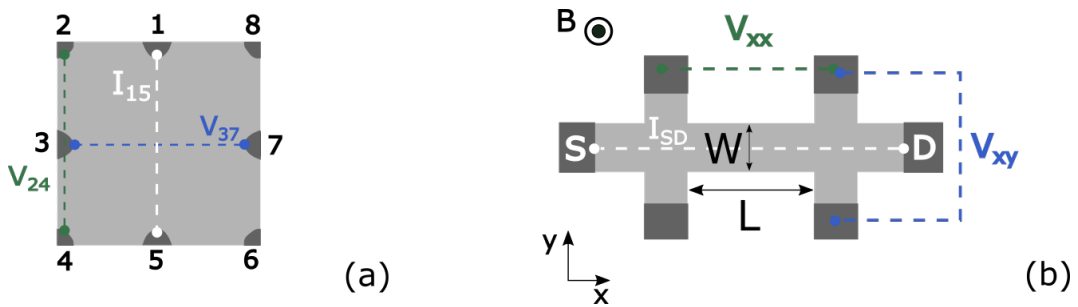


**Figure 4.2:** (a) Sketch of the vdP sample geometry with an exemplary Hall measurement configuration. The numbered, dark grey points at the sample border present alloyed In contacts, deposited with a soldering iron. (b) Standard Hall bar geometry of width  $W$  and length  $L$ . The dark grey squares present lithographically defined ohmic contacts. The configuration of a Hall measurement is schematically sketched.

**Van der Pauw measurements** A convenient method for initial rapid sample characterisation is provided by MT measurements in van der Pauw (vdP) geometry, with which the charge density and the corresponding mobility can be determined [43, 94]. Figure 4.2(a) shows the measurement scheme of an exemplary vdP Hall measurement in which the longitudinal voltage  $V_{24}$  and the transversal voltage  $V_{37}$  (with respect to the applied current  $I_{15}$ ) are recorded as a function of the perpendicularly applied magnetic field.

The transport properties  $n_s$  and  $\mu$  are determined by permutatively switching the employed contacts in a four-terminal measurement. Thereby, the sheet resistivity  $\rho_{xx}$  together with the Hall resistivity  $\rho_{xy}$  can be calculated. Therefore, we have to determine

$$R_{24,68} = \frac{V_{68}}{I_{24}} \quad \text{and} \quad R_{46,82} = \frac{V_{82}}{I_{46}}.$$

It can be shown that the sheet resistivity can be expressed as

$$\rho_{xx} = \frac{\pi}{\ln 2} \cdot \frac{R_{24,68} + R_{46,82}}{2} \cdot f\left(\frac{R_{24,68}}{R_{46,82}}\right), \quad (4.1)$$

with  $f$  being a function of only the ratio  $\frac{R_{24,68}}{R_{46,82}}$ .

The Hall resistivity is determined as

$$\rho_{xy} = \frac{R_{62,48}(B) - R_{62,48}(0) + R_{48,62}(B) - R_{48,62}(0)}{2}. \quad (4.2)$$

The charge density  $n_s$  and the mobility  $\mu$  are then calculated with

$$n_s = \left( e \cdot \frac{\partial \rho_{xy}}{\partial B} \Big|_{B=0} \right)^{-1} \quad (4.3)$$

$$\mu = \left( e \cdot n_s \rho_{xx}(B=0) \right)^{-1}. \quad (4.4)$$

Generally, we find that the determined values of the charge densities and mobilities with a vdP sample are less accurate than when determined via MT measurements on a lithographically defined Hall bar structure. We identified two main and generic error sources in vdP measurements: Firstly, a possible misalignment of the manually soldered contacts leads to an intermixing of the determined values of  $\rho_{xx}$  and  $\rho_{xy}$ . Furthermore, the finite size of the soldered contacts distorts the applicability of the made assumptions in the derivation of the formula (4.1) of the vdP evaluation method.

**Hall bar measurements** A more accurate electric characterisation of a 2D electron system can be achieved via MT measurements on a lithographically defined Hall bar structure, schematically sketched in figure 4.2(b). Fabrication details are summarized in the appendix A. The dimensions of our employed Hall bar structure, the Hall bar channel

## 4 Experimental methods

width  $W$  and the Hall bar channel length  $L$ , are  $20\mu\text{m}$  and  $300\mu\text{m}$ , respectively. As introduced in chapter 2,  $n_s$  and  $\mu$  are determined by measuring the B-field dependence of  $V_{xx}$  and  $V_{xy}$ , with  $\mathbf{B} \parallel \mathbf{z}$ , when a source-drain (SD) current  $I_{SD}$  is applied along the Hall bar. With

$$\rho_{xx} = \frac{V_{xx}}{I_{SD}} \frac{W}{L} \quad \text{and} \quad \rho_{xy} = \frac{V_{xy}}{I_{SD}}, \quad (4.5)$$

where the ratio  $W/L$  accounts for the geometry of the sample,  $n_s$  and  $\mu$  can be calculated via the equations (4.3) and (4.4).

Most of our Hall bar samples are equipped with a global Ti/Au top-gate (TG) above the Hall bar mesa. The gate electrode is separated by an insulating layer of  $\text{Al}_2\text{O}_3$  from the semiconducting heterostructure. By varying the applied TG-voltage  $V_{TG}$ , the charge density  $n_s$  can be controlled via the field-effect (see subsection 2.1.3).

MT measurements are performed with a standard low-frequency lock-in technique at  $f = 17\text{Hz}$  or  $f = 37\text{Hz}$ . The source-drain current  $I_{SD}$  is generated via the internal oscillator of the lock-in amplifier. We control the sinusoidal current  $I_{SD}$  with a pre-resistor at the lock-in output.

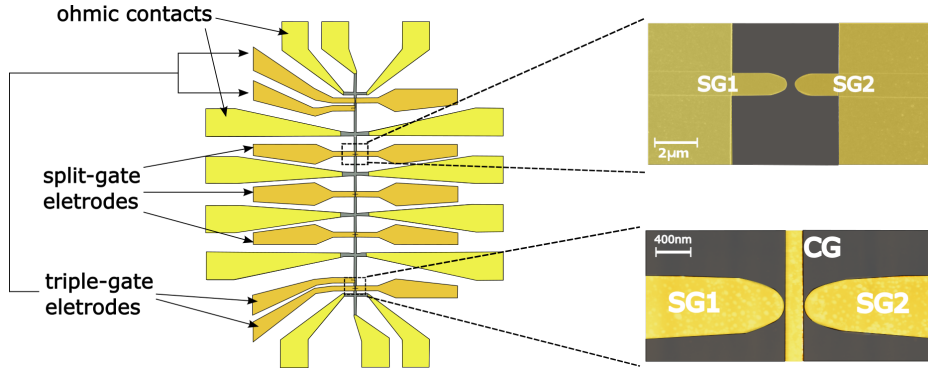


**Figure 4.3:** Schematic sketch of the utilised Hall bar geometry. Gate-defined QPCs are located on top of the mesa in between two consecutive Hall crosses. The inner three segments of the Hall bar mesa are equipped with SG-electrodes as is shown in the zoom (SEM image). For the outer two segments a TrG-electrode gate layout is chosen, shown in the corresponding zoom (AFM image) on the right side. The SEM and AFM images are false color coded.

**1D transport measurements** In this work, we investigate the conductance  $G$  through electrostatically defined QPCs in epitaxially grown  $\text{In}_{0.75}\text{Ga}_{0.25}\text{As}/\text{In}_{0.75}\text{Al}_{0.25}\text{As}$  heterostructures. Our applied sample geometry is shown in figure 4.3. On top of a Hall bar mesa, we lithographically define finger-gate electrodes, with which the 1D constrictions in the underlying 2DEG are formed by employing the field-effect. This enables the determination of the 1D and 2D transport characteristics of the very same device. The

three inner Hall bar segments are equipped with so-called *split-gate* (SG) electrodes. The zoom into the inner section of the Hall bar segment (right side of figure 4.3) shows a scanning electrode microscopy (SEM) image of our generally utilised SG-electrodes. During the course of this work several SG-layouts are tested. This topic is further addressed in chapter 6. The two outer Hall bar segments are supplied with a triple-gate (TrG) electrode, shown in the AFM image on the right side of figure 4.3. Therein, an additional gate electrode, the *center-gate* (CG) is inserted in between the SG-electrodes SG1 and SG2. The concept of a TrG-defined QPC is addressed in detail in subsection 6.3.2.

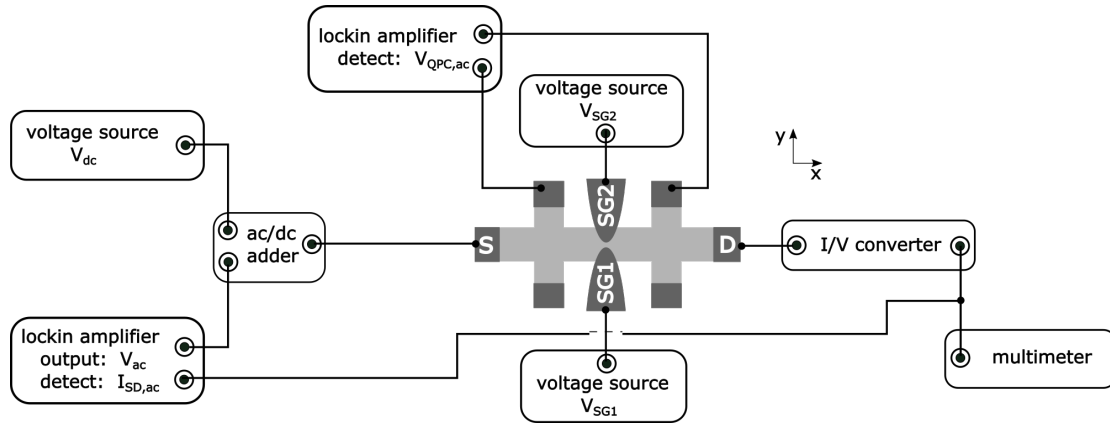


**Figure 4.4:** Sketch of the utilised measurement scheme of the differential conductance of a QPC. A dc voltage  $V_{dc}$  with a superimposed ac voltage  $V_{ac}$  is applied between the source and the drain contact of the sample. The voltage drop over the QPC  $V_{QPC,ac}$  is determined with a lock-in amplifier in a four-terminal configuration. After amplification,  $I_{SD,ac}$  is measured with a lock-in. A dc voltage  $V_{SG1}$  and  $V_{SG2}$  is applied at the corresponding finger-gate electrodes SG1 and SG2, whereby the 1D channel width can be electrically tuned via the field-effect.

The conductance  $G$  through the constriction is detected differentially in order to reduce residual noise in our setup. Moreover, this also extends the validity range of the calculation of  $G$  via the applied source-drain current  $I_{SD}$  and the measured voltage drop to non-ohmic systems. The scheme of our measurement technique is displayed in figure 4.4. A dc source-drain voltage  $V_{dc}$  is superimposed with a small ac voltage  $V_{ac}$  of  $50\mu V$  with a frequency of  $f = 37Hz$  or  $f = 137Hz$  in a specially designed ac/dc voltage adder<sup>1</sup>. The ac/dc adder signal is then applied between the source and the drain contact of the Hall bar device.  $V_{dc}$  is chosen small enough such that an adverse population of energetically higher 1D subbands is prohibited. The voltage across the 1D constriction  $V_{QPC,ac}$ , as well as  $I_{SD,ac}$  is recorded via lock-in measurements. By taking the serial channel resistance

<sup>1</sup>The development of a convenient ac/dc adder, as well as our applied 1D measurement technique was part of this work and is summarized in form of a master thesis in [95].

## 4 Experimental methods

---

$R_{ch}$  of the 2DEG into account, the conductance of the constriction is calculated with

$$G_{QPC} = \frac{I_{SD,ac}}{V_{QPC,ac} - I_{SD,ac} \cdot R_{ch}}.$$

In a typical conductance measurement, we analyse the conductance  $G$  of a QPC as a function of the 1D channel width, which is controlled by the applied SG-voltages  $V_{SG1}$  and  $V_{SG2}$ . Further measurement details can be found in [95].

### 4.3.2 Measurement setups

#### <sup>4</sup>He dewar

Most of our samples are characterised in a <sup>4</sup>He dewar at a temperature of  $T = 4.2K$  or  $T = 1.5K$ . With our setup, magnetic fields in the range of  $\pm 5T$  and  $\pm 6T$  perpendicular to the sample plane can be applied. The sample rod is equipped with a red light emitting diode (LED) with  $E_{photon} \approx 1.6 - 2eV$ , which is positioned in direct proximity to the sample holder. We refer to a sample as being *in the illuminated state* after illuminating the sample for 60s with the LED at  $T = 4.2K$  or  $T = 1.5K$ .

Star-point grounding at the top of our sample rod prevents the formation of ground loops. At the star-point, all shields of the coaxial lines are connected to each other. Our measurements are recorded with either a Labview or a Matlab based program.

The <sup>4</sup>He setup is used for rapid sample characterisation via vdP measurements, as well as for gated Hall bar measurements to analyse the transport behavior of our heterostructures under the application of an external electric field. Furthermore, the majority of our 1D transport measurements is conducted in this setup, since the initial electric characterisation of the MBE-grown wafer material requires repeated thermal recycling, as well as frequent sample exchange. Further technical details on the setup are given in [95–98].

#### <sup>3</sup>He cryostat

Selected samples are characterised in a <sup>3</sup>He cryostat at temperatures between  $T = 350mK$  and  $T = 4.2K$ . For this setup, two sample rods are available, allowing transport measurements with an in-plane magnetic field as well as with a magnetic field perpendicular to the sample surface. The sample chamber of the cryostat is a closed inner circuit, which is filled with <sup>3</sup>He. The surrounding and separated outer circuit is filled with <sup>4</sup>He and serves to cool the <sup>3</sup>He. Via pumping on the sample chamber, the temperatures in the inner sample space can be lowered to 350mK. The earthing is similar to the <sup>4</sup>He dewar. Further technical details are given in [98, 99].

# 5

## Design and characterisation of InGaAs/InAlAs systems

The implementation of the all-electric spin-transistor concept is based on two pillars: the realization of robust ballistic 1D transport in a gate-defined QPC, which is implemented in a 2D system, exhibiting a large zero-field spin splitting due to structural inversion asymmetry. Owing to the large intrinsic SOI, InAs-based heterostructures present themselves as promising materials for the implementation of spinorbitronic device applications [55]. MBE growth engineering of these heterostructures gives us the ability to actively influence the structural inversion asymmetry in the 2D system, with which the strength of the Rashba-type SOI can be tuned. The application of an external gate electric field provides a further possibility to tailor SOI in the 2DEG [13, 71, 79, 84, 100].

Along with research, targeting SOI effects in InAs-based heterostructures, there has been put much effort into the achievement of high mobile 2D charge carrier systems as one generally lacks a lattice matched substrate for these material systems [35–38].

This chapter provides a brief introduction into the applied buffer layer concepts in the epitaxial growth process of InAs-based ternary alloy systems, which have been established in preceding works in our group [90, 97]. For the realization of high-mobility 2D electron gases we design our active layer structure by means of epitaxial growth-engineering. In this context, we discuss modulation doped and undoped (InAs/InGaAs/InAlAs heterostructures in the view of spinorbitronic device applications.

### 5.1 Buffer layer growth

The lattice mismatch of  $\Delta a = 6.7\%$ , with  $a$  being the lattice constant, between the zinc blende InAs and GaAs crystal structures [101] prevents the epitaxial growth of InAs-based compound systems on the commonly employed GaAs substrate. Thus, except for the ternary compound  $\text{In}_{0.53}\text{Ga}_{0.47}\text{As}$ , which is lattice matched to available - yet expensive - InP substrates, we lack a lattice matched substrate for In-containing ternary alloy systems. To overcome this limitation in the choice of material system, sophisticated buffer layer

## 5 Design and characterisation of InGaAs/InAlAs systems

concepts have to be applied to accommodate for the lattice mismatch between the active layer and the employed substrate material whilst ensuring strain relaxation during the buffer layer growth in order to achieve defect-free active layer structures [35, 36, 38, 102–108]. In this work, we use semi-insulating GaAs (001) as substrate material for the MBE growth process. In order to achieve high zero-field spin-splitting, we choose an (InAs/) $\text{In}_{0.75}\text{Ga}_{0.25}\text{As}$  QW as host material for the 2D electron system. As the high band gap material, we employ  $\text{In}_{0.75}\text{Al}_{0.25}\text{As}$  since it is lattice matched to  $\text{In}_{0.75}\text{Ga}_{0.25}\text{As}$  at this particular In concentration.

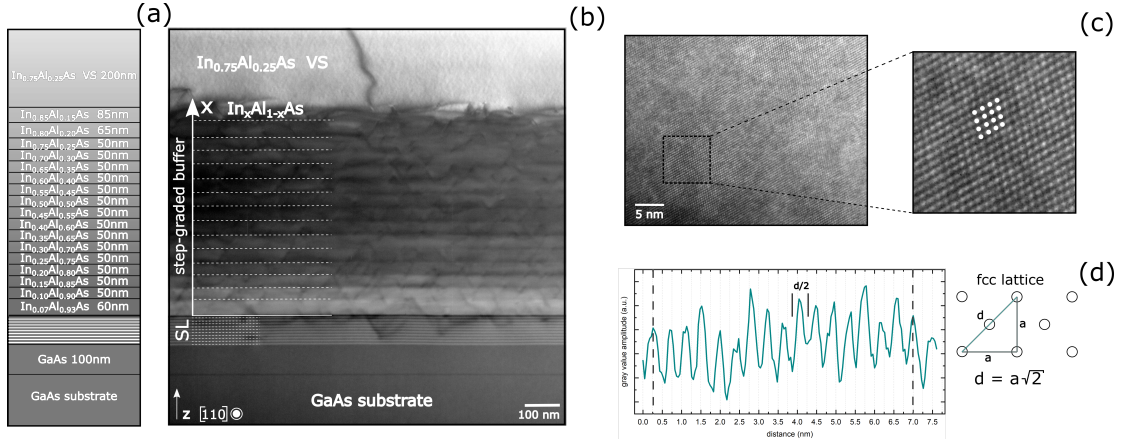


**Figure 5.1:** (a) Schematic layer sketch of the applied step-graded  $\text{In}_x\text{Al}_{1-x}\text{As}$  buffer layer to accommodate for the lattice mismatch between the used GaAs (001) substrate and the active  $\text{In}_{0.75}\text{Ga}_{0.25}\text{As}/\text{In}_{0.75}\text{Al}_{0.25}\text{As}$  layers, which exhibit a significantly larger lattice constant than GaAs. (b) The aligned cross-sectional TEM image along the  $[110]$  crystallographic direction illustrates the formation of in-plane misfit dislocations due to plastic strain relaxation inside the buffer layer. The constant composition layer, i.e. the  $\text{In}_{0.75}\text{Al}_{0.25}\text{As}$  VS, is almost free of threading dislocations, implying a well-functioning buffer layer system. (c) The HRTEM image of the VS shows the lattice planes of the  $\text{In}_{0.75}\text{Al}_{0.25}\text{As}$  zinc blende lattice. (d) Evaluating the grey-scale oscillations of a line-cut along the  $[110]$  direction yields the lattice constant of the corresponding  $\text{In}_{0.75}\text{Al}_{0.25}\text{As}$  layer.

A key to defect-free strain relaxation is the minimization of the amount of threading dislocations which reach the sample surface, whereby they penetrate the active layers and hence the 2DEG. To this end, the interaction of misfit dislocations parallel to the sample surface has to be reduced, which can be tailored by the applied buffer layer. Following the epitaxial growth study of Capotondi et al. [103], we employ an  $\text{In}_x\text{Al}_{1-x}\text{As}$  step-graded buffer layer concept in the epitaxial growth process of our heterostructures. Therein, the In concentration of the ternary compound material  $\text{In}_x\text{Al}_{1-x}\text{As}$  is stepwise increased during the growth process. A compositional overshoot to an In concentration of 85% is commonly employed as it has been proven to be beneficial for the strain-free adaption



of the lattice constant for the 75% In-containing  $\text{In}_{0.75}\text{Ga}_{0.25}\text{As}/\text{In}_{0.75}\text{Al}_{0.25}\text{As}$  active layers. Figure 5.1(a) displays a sketch of the employed buffer system. The epitaxial growth process is initiated with a deoxidation of the GaAs substrate wafer, followed by the growth of a 100nm GaAs seed layer. The subsequent incorporation of short-period alternating  $\text{Al}_{0.50}\text{Ga}_{0.50}\text{As}/\text{GaAs}$  layers, i.e. the superlattice (SL), with each layer having a thickness of 5nm, has been proven to be crucial for the screening of the following  $\text{In}_x\text{Al}_{1-x}\text{As}$  buffer layers from impurities, which reside at the GaAs substrate interface. Our  $\text{In}_x\text{Al}_{1-x}\text{As}$  step-graded buffer system starts with an In concentration of  $x \approx 0.07$  and is increased in 5%-steps to  $x = 0.75$  by keeping the Al flux constant and ramping the In cell temperature. Each  $\text{In}_x\text{Al}_{1-x}\text{As}$  buffer step has a thickness of 50nm. The step-graded buffer is terminated by two broader, auxiliary  $\text{In}_x\text{Al}_{1-x}\text{As}$  steps with  $x = 0.80$  and  $x = 0.85$ , presenting the compositional overshoot, whereby residual compressive strain is reduced. Subsequently, the In concentration is reduced to 75% and several hundred nanometers of  $\text{In}_{0.75}\text{Al}_{0.25}\text{As}$ , the so-called virtual substrate (VS), are grown. The VS provides the strain-relaxed substrate for the following active layer system.

During the growth process, the BEP of  $\text{As}_4$  is commonly kept at  $8 \cdot 10^{-6}\text{Torr}$ . For the growth of the GaAs seed layer and the SL, the temperature of the substrate holder of the MBE system is set to  $T = 620^\circ\text{C}$ . For the  $\text{In}_x\text{Al}_{1-x}\text{As}$  buffer layer the substrate temperature is reduced to  $T_{\text{buf}} \approx 360^\circ\text{C}$  to prevent the formation of 3-dimensional crystal islands during growth [37, 109]. Based on the work of Loher [97], who determined that an increase of the substrate temperature during the growth of the VS and the active layer system to  $T_{\text{act}} \approx 460^\circ\text{C}$  proves to be beneficial to achieve a highly mobile 2D charge carrier system, we employ a similar substrate temperature for the growth of our active  $\text{In}_{0.75}\text{Ga}_{0.25}\text{As}/\text{In}_{0.75}\text{Al}_{0.25}\text{As}$  layers.

To investigate the functionality of the applied buffer layer system, detailed TEM-based studies of the step-graded  $\text{In}_x\text{Al}_{1-x}\text{As}$  buffer are conducted. Thereby, we are able to analyse the crystalline quality of the semiconducting layers, the strain relaxation, as well as the incorporation of structural defects in the system. Figure 5.1(b) shows an exemplary cross-sectional TEM image of the  $\text{In}_x\text{Al}_{1-x}\text{As}$  buffer system along the [110] crystallographic direction, aligned to the schematic sketch of the buffer layer sequence in figure 5.1(a). We find that misfit dislocations efficiently annihilate each other inside the buffer layers since the VS is almost free of threading dislocations. This demonstrates effective strain relaxation by means of the employed buffer concept. A single piercing threading dislocation can be seen as dark line in the centre of the TEM image in figure 5.1(b). Figure 5.1(c) depicts a high-resolution TEM (HRTEM) image of the  $\text{In}_{0.75}\text{Al}_{0.25}\text{As}$  VS layer from figure 5.1(b). The zoom into the image reveals the individual crystal lattice planes as small grains. Since we know the crystal orientation of the HRTEM image, we are able to determine the effective lattice constant  $a(\text{In}_x\text{Al}_{1-x}\text{As})$  of the VS layer from the oscillation of the grey-value in a line-cut through this image. From the thereby obtained value of  $a(\text{In}_x\text{Al}_{1-x}\text{As})$ , we are able to deduce the material composition of the layer. This presents an experimental opportunity to cross-check the applied In calibration in the epitaxy of our heterostructure. The applied calculation method is illustrated in the sketch in figure 5.1(d). With  $a(\text{InAs}) = 6.0583\text{\AA}$  and  $a(\text{GaAs}) = 5.65325\text{\AA}$  at  $T = 300^\circ\text{C}$

## 5 Design and characterisation of InGaAs/InAlAs systems

[101], we can write in first approximation  $a(\text{In}_x\text{Al}_{1-x}\text{As}) = 5.65325\text{\AA} + 0.40505\text{\AA} \cdot x$ . Evaluating the grey-value oscillation period yields an In composition of  $x = 0.745$ . This value is in excellent agreement with the targeted In concentration of 75% for the VS and thus confirms our employed In-cell calibration. Further in-depth investigations of the applied  $\text{In}_x\text{Al}_{1-x}\text{As}$  step-graded buffer concept via TEM can be found in [93, 97]. Figure 5.2(a) displays an exemplary plan view AFM image of the wafer surface of an  $\text{In}_{0.75}\text{Ga}_{0.25}\text{As}/\text{In}_{0.75}\text{Al}_{0.25}\text{As}$  heterostructure, for which the above described step-graded buffer layer concept has been utilised.

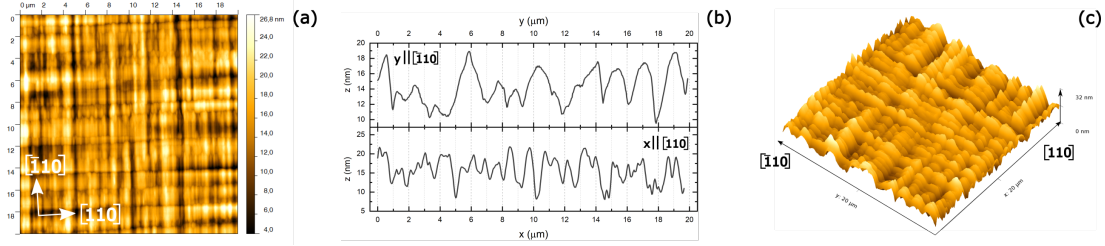


**Figure 5.2:** Wafer C160428A: **(a)**  $20 \times 20\mu\text{m}$  plan view AFM image of the wafer surface, revealing 5 – 15nm deep trenches along the  $\langle 110 \rangle$  crystallographic directions. **(b)** Profile sections along the  $y \parallel [\bar{1}10]$  and  $x \parallel [110]$  direction. **(c)** Three dimensional plot of the profile of the wafer surface shown in (a).

We see clear undulations in the surface structure of the wafer in form of a cross hatching pattern, which is perfectly aligned along the  $[\bar{1}10]$  and  $[110]$  crystallographic directions with a pronounced anisotropy in the corresponding oscillation periods. Such a cross hatched pattern is generally considered as characteristic for MBE-grown buffer layer systems [103, 110–114]. The trenches in our samples generally exhibit a depth of 5 – 15nm in both directions. As shown in figure 5.2(b), displaying two profile sections along the two marked crystallographic directions, we find for the undulations along the  $[\bar{1}10]$  direction a periodicity of 1.0 – 1.6 $\mu\text{m}$ , for the  $[110]$  direction the undulation period takes values of 0.4 – 1.0 $\mu\text{m}$ . The surface texturing is clearly visualized in the three dimensional plot of the wafer surface in 5.2(c). It has been experimentally shown that locally varying strain fields inside the heterostructure lead to anisotropic growth rates along the  $[\bar{1}10]$  and  $[110]$  directions, as well as to In segregation, which causes a modulation of the underlying band structure. Such processes are likely to contribute to the generation of the surface structuring in buffer systems. Yet, there is no unified explanation for the cross hatching phenomenon, however, it is also widely suggested that the surface modulations can be associated with the formation of an orthogonal network of the misfit dislocations along the  $[\bar{1}10]$  and  $[110]$  crystallographic directions during the epitaxial growth process. Thus, the development of a cross-hatched surface texture is generally regarded as an indicator of a well-functioning buffer system [103, 106, 111, 113, 115].

In a next step, building on the obtained strain-relaxed and defect-free  $\text{In}_{0.75}\text{Al}_{0.25}\text{As}$  VS, we growth-engineer the active  $\text{In}_{0.75}\text{Ga}_{0.25}\text{As}/\text{In}_{0.75}\text{Al}_{0.25}\text{As}$  layer design under the perspective of spinorbitronic device applications.

## 5.2 Design of InGaAs/InAlAs active layer systems

A peculiar material property of the  $\text{In}_{0.75}\text{Ga}_{0.25}\text{As}/\text{In}_{0.75}\text{Al}_{0.25}\text{As}$ -based material system presents the inherent n-type doping mechanism: Arsenic-related antisite defects inside the  $\text{In}_{0.75}\text{Al}_{0.25}\text{As}$  semiconducting layers incorporate deep level donor states [37, 39]. With an activation energy of  $0.12\text{eV}$  and  $0.17\text{eV}$ , these deep level donor states lie energetically inside the conduction band offset of  $\text{In}_{0.75}\text{Ga}_{0.25}\text{As}$  and  $\text{In}_{0.75}\text{Al}_{0.25}\text{As}$ . Consequently, they provide electrons for an  $\text{In}_{0.75}\text{Ga}_{0.25}\text{As}$  QW that is embedded in  $\text{In}_{0.75}\text{Al}_{0.25}\text{As}$ . Under commonly applied MBE growth conditions, the density of the deep level donor states is found to be as high as  $N_D \approx 1 - 3 \cdot 10^{16}\text{cm}^{-3}$  [37, 38, 116, 117]. Except for their doping properties [14, 37–39, 116–118], these InAlAs defect states have been scarcely addressed in literature so far.

### Inverted modulation doped InGaAs/InAlAs heterostructures

In order to realize highly mobile  $\text{In}_{0.75}\text{Ga}_{0.25}\text{As}/\text{In}_{0.75}\text{Al}_{0.25}\text{As}$  2DEGs, we systematically vary the active layer design of our heterostructures. Firstly, we analyse a modulation doped near-surface  $\text{In}_{0.75}\text{Ga}_{0.25}\text{As}/\text{In}_{0.75}\text{Al}_{0.25}\text{As}$  QW structure, wafer C160229A, which is schematically depicted in figure 5.3(a). The 2DEG is hosted in a  $20\text{nm}$   $\text{In}_{0.75}\text{Ga}_{0.25}\text{As}$  QW, embedded in  $\text{In}_{0.75}\text{Al}_{0.25}\text{As}$ . To prevent the system from oxidation, a  $5\text{nm}$   $\text{In}_{0.75}\text{Ga}_{0.25}\text{As}$  capping layer is grown on top of the heterostructure. In the course of this work, metal gate electrodes are employed to control the transport properties of the 2DEG. Thus, the Si  $\delta$ -doping layer is placed underneath the  $\text{In}_{0.75}\text{Ga}_{0.25}\text{As}$  QW, whereby we circumvent a potential screening of the gate electric field at the QW. Additionally, by means of the employed inversion doping, we avoid potential charge transfer between the QW and the Si-doping layer when the band structure is tilted in an external electric field. Furthermore, the doping layer gives rise to a structural inversion asymmetry in the system, which contributes to Rashba-type SOI due to the induced internal electric field in growth direction. For rapid sample characterisation, we perform vdP measurements in the illuminated and non-illuminated state, with which we determine the 2D transport properties  $n_{\text{vdP}}^{\text{dark}}$ ,  $\mu_{\text{vdP}}^{\text{dark}}$  and  $n_{\text{vdP}}^{\text{ill}}$ ,  $\mu_{\text{vdP}}^{\text{ill}}$ , respectively. The transport characteristics are summarized in table 5.1. For the vdP sample C160229A, we determine an electron mobility of only  $\mu_{\text{vdP}}^{\text{dark}} = 21000\text{cm}^2/\text{Vs}$  at a charge density of  $n_{\text{vdP}}^{\text{dark}} = 8.8 \cdot 10^{11}\text{cm}^{-2}$  in the non-illuminated state. Illuminating the sample increases the measured sheet density by almost a factor of two to  $n_{\text{vdP}}^{\text{ill}} = 15.8 \cdot 10^{11}\text{cm}^{-2}$ . The mobility increases along with the charge density to a value of  $\mu_{\text{vdP}}^{\text{ill}} = 31000\text{cm}^2/\text{Vs}$ . The elastic mean free path is calculated as  $l_{\text{mfp}}^{\text{dark}} = 0.33\mu\text{m}$  in the non-illuminated state and  $l_{\text{mfp}}^{\text{ill}} = 0.64\mu\text{m}$  after illumination. Generally, higher values of  $l_{\text{mfp}}$  facilitate the realization of ballistic transport. Here, we assume that segregation of the Si-doping atoms reduces the mobility in the sample. This interpretation is in line with experimental findings of Loher [97], who determined a significant diminishing of the mobility in Mn inversion-doped InAs/InGaAs/InAlAs

## 5 Design and characterisation of InGaAs/InAlAs systems

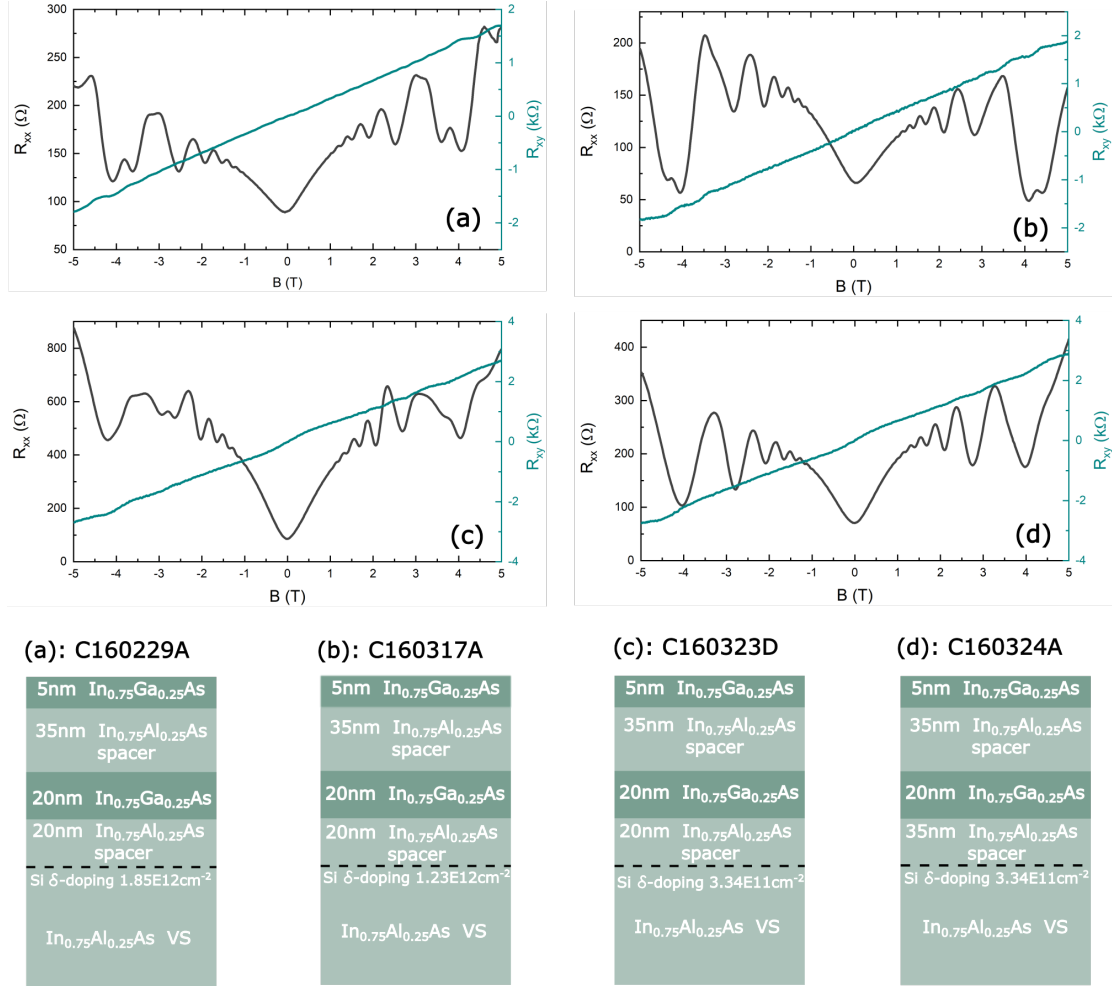


**Figure 5.3:** Layer structure and vdP Hall measurements in the illuminated state at  $T = 1.5K$  of wafer (a) C160229A (b) C160317A (c) C160323D (d) C160324A.

systems. A Hall measurement of the vdP sample C160229A in the illuminated state at a temperature of  $T = 1.5K$  is shown in figure 5.3(a). The MT measurement shows clear indications of parallel conductance: a superimposed parabolic background in the sheet resistance  $R_{xx}$ , together with distinct undulations of the magnetooscillations, as well as a slightly s-shaped Hall resistance  $R_{xy}$  (therefore see chapter 2). This suggests that the employed doping density of  $n_{dop} = 1.85 \cdot 10^{12}cm^{-2}$  is chosen too high.

Thus, in order to minimize the effects of Si segregation and to simultaneously impede parallel transport in the system, we stepwise decrease the applied doping density  $n_{dop}$  in our heterostructures in a set of newly grown wafers. Hall measurements of two exemplary vdP samples of this growth series are displayed in figures 5.3(b) and (c), for which a doping density of  $n_{dop} = 1.2 \cdot 10^{12}cm^{-2}$  (wafer C160317A) and  $n_{dop} = 3.3 \cdot 10^{11}cm^{-2}$  (wafer C160323D) is chosen. The determined transport properties of the vdP samples C160317A and C160323D are listed in table 5.1. As expected, a reduction of  $n_{dop}$  leads to

## 5.2 Design of InGaAs/InAlAs active layer systems

wafer	$n_{vdP}^{dark} (\cdot 10^{11} \text{cm}^{-2})$	$\mu_{vdP}^{dark} (\text{cm}^2/\text{Vs})$	$n_{vdP}^{ill} (\cdot 10^{11} \text{cm}^{-2})$	$\mu_{vdP}^{ill} (\text{cm}^2/\text{Vs})$
C160229A	8.8	21000	15.8	31000
C160317A	7.3	21000	12.2	50000
C160323D	3.8	4900	7.1	70000
C160324A	3.1	3100	6.9	67000

**Table 5.1:** Transport properties determined via vdP measurements at  $T = 4.2K$ .

a decreased sheet carrier density before and after illumination of the samples. However, the decrease in electron density in the non-illuminated state has a rather adverse effect on the electron mobility as can be seen for sample C160323D. In this device,  $\mu_{vdP}^{dark}$  is reduced to  $4900 \text{cm}^2/\text{Vs}$ . Illuminating the samples markedly increases the mobility of the conduction electrons in contrast to the highly doped sample C160229A. Nevertheless, both samples still exhibit substantial parallel conductance in the vdP Hall measurements as can be seen in figures 5.3(b) and (c). We assign this overdoping even at low  $n_{dop}$  to an apparently significant contribution of the deep level donor states inside the InAlAs spacer layers to the epitaxially introduced modulation doping in the heterostructures. This can be nicely seen by means of the determined value of  $n_{vdP}^{ill} = 7.1 \cdot 10^{11} \text{cm}^{-2}$  of sample C160323D, which is twice as high as the employed Si-doping density  $n_{dop} = 3.3 \cdot 10^{11} \text{cm}^{-2}$ . In an attempt to reduce the adverse effects of Si segregation in the 2DEG, we increase the InAlAs spacer layer thickness between the  $\delta$ -doping layer and the QW to  $35 \text{nm}$ . The corresponding heterostructure, wafer C160324A, is shown in figure 5.3(d). We find similar 2D transport properties, listed in table 5.1, as for the equivalent sample C160323D with an InAlAs spacer thickness of  $20 \text{nm}$ . We thus conclude that a mere increase of the InAlAs spacer thickness is insufficient to achieve an enhancement of the mobility in the 2D system.

Due to the impaired electron mobility and the parallel conduction, which is present even at low doping densities, we grow a new set of undoped heterostructures. By this, we also gain insight into the inherent doping mechanism in the material system.

### Undoped InGaAs/InAlAs heterostructures

Figure 5.4(a) shows the active layer structure of wafer C160331B, which is identical to the active layer design of the above studied samples, yet without the incorporation of a Si  $\delta$ -doping layer. The corresponding vdP transport properties are summarized in table 5.2. Even without the incorporation of an intentional doping layer, we find a conducting 2DEG to be developed. In the illuminated state, we determine a greatly enhanced electron mobility of  $\mu_{vdP}^{ill} = 130000 \text{cm}^2/\text{Vs}$  at a charge density of  $n_{vdP}^{ill} = 4.7 \cdot 10^{11} \text{cm}^{-2}$  compared to the modulation doped samples. This finding conformably points out that Si segregation in the inverted modulation doped heterostructures strongly reduces the electron mobility inside the 2DEG.

## 5 Design and characterisation of InGaAs/InAlAs systems

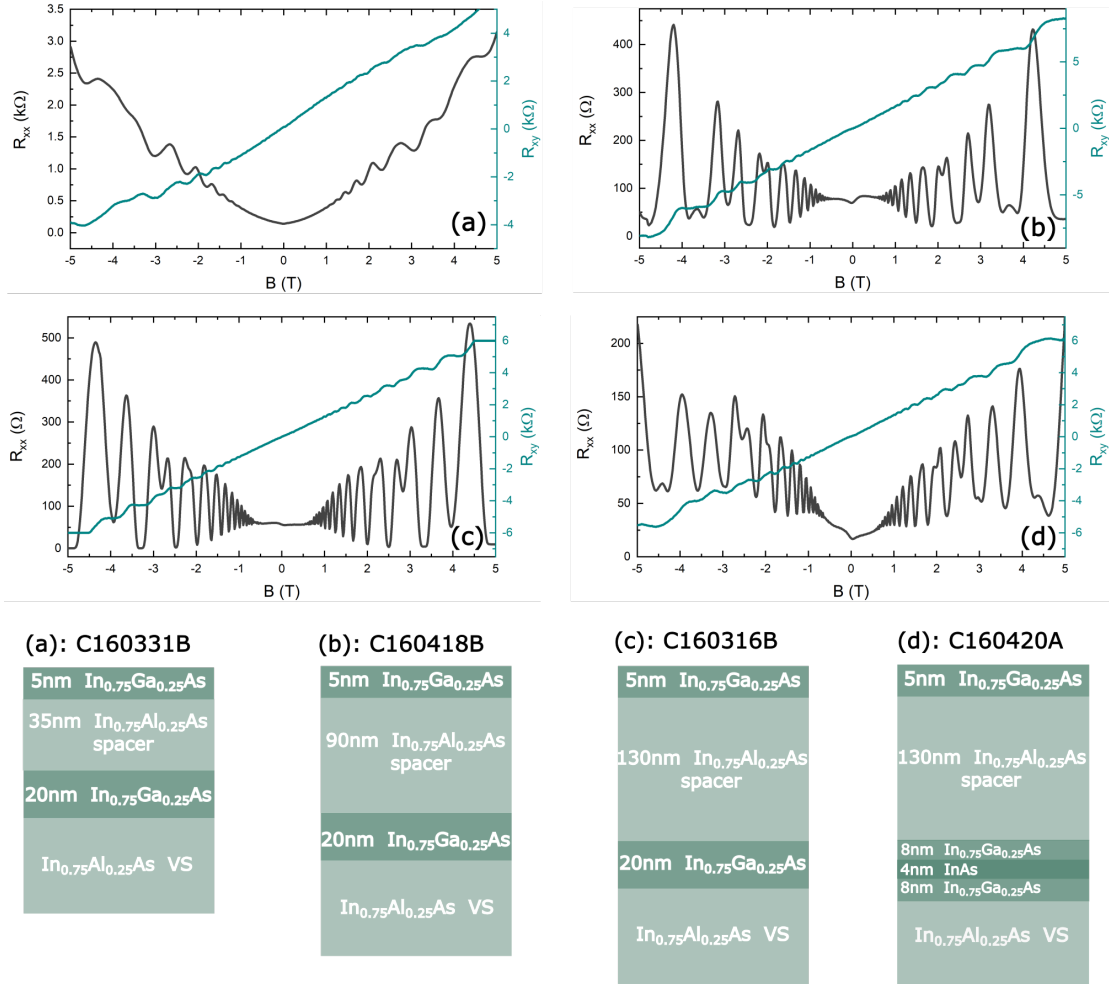


**Figure 5.4:** Layer structure and vdP Hall measurements in the illuminated state at  $T = 1.5K$  of wafer (a) C160331B (b) C160418B (c) C160316B (d) C160420A.

In order to further enlarge the mean free path in the 2D electron systems, we aim to reduce interface-related scattering by increasing the thickness of the upper InAlAs barrier layer in the undoped layer design. Two exemplary heterostructures, wafer C160418B and C160316B, for which we choose a spacer thickness of  $90nm$  and  $130nm$ , respectively, are shown in figures 5.4(b) and (c). The vdP transport properties are summarized in table 5.2. Whereas we find very similar transport properties for both devices in the illuminated state as for the near-surface heterostructure C160331B, the transport properties in the non-illuminated state follow a clear trend: The larger the InAlAs spacer thickness is chosen, the higher the achieved mobility  $\mu_{vdP}^{dark}$  at a similar  $n_{vdP}^{dark}$ . For sample C160316B the mobility is even increased up to a value of  $\mu_{vdP}^{dark} = 70000 cm^2/Vs$  at an electron density of only  $n_{vdP}^{dark} = 2.2 \cdot 10^{11} cm^{-2}$ . This presents a distinct enlargement of  $\mu_{vdP}^{dark}$  compared to all previously achieved values in our heterostructures. To test the reproducibility of the intrinsic doping mechanism in the InAlAs/InGaAs layer system when the same MBE

## 5.2 Design of InGaAs/InAlAs active layer systems

wafer	$n_{vdP}^{dark} (\cdot 10^{11} \text{cm}^{-2})$	$\mu_{vdP}^{dark} (\text{cm}^2/\text{Vs})$	$n_{vdP}^{ill} (\cdot 10^{11} \text{cm}^{-2})$	$\mu_{vdP}^{ill} (\text{cm}^2/\text{Vs})$
C160331B	3.6	2000	4.7	130000
C160418B	2.3	19000	5.3	166000
C160316B	2.2	70000	4.9	135000
C160420A	4.1	70000	6.2	145000

**Table 5.2:** Transport properties determined via vdP measurements at  $T = 4.2K$ .

growth conditions are employed, we regrow the heterostructure of wafer C160316B for several times, i.e. wafers C160428A, C160428B and C160429A. The corresponding vdP transport properties are summarized in table 5.3, the Hall measurements of the vdP samples are displayed in figure B.1 in the appendix. Within the limits of accuracy of a vdP measurement (see section 4.3), we find very similar transport properties, in both, the non-illuminated and the illuminated state. This demonstrates that a fixed amount of intrinsic dopants is generated in the InAlAs spacer layers, being reproducible in epitaxy.

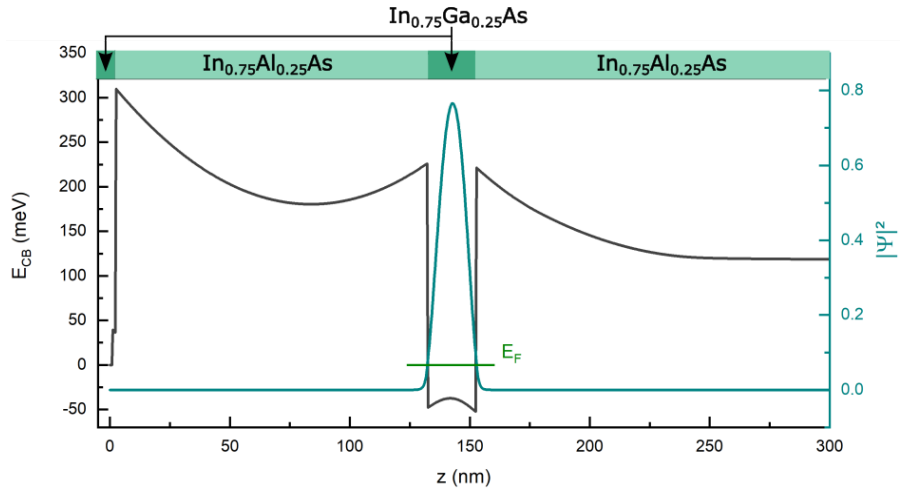


**Figure 5.5:** Self-consistent Schrödinger-Poisson simulation of the conduction band profile  $E_{CB}$  (black curve) of the active layer structure of wafer C160316B. The cyan curve displays the wave function probability  $|\Psi|^2$ , the green line indicates the Fermi energy  $E_F$  in the QW.

We self-consistently simulate the band profile of the above analysed undoped heterostructure C160316B with a Schrödinger-Poisson solver [119–122]. For the calculation, we assume a Fermi level pinning of  $40 \text{ meV}$  under the conduction band edge [14, 37]. Furthermore, we introduce an InAlAs deep level donor density of  $N_D^{total} = 3 \cdot 10^{16} \text{ cm}^{-3}$  in the InAlAs barrier layers of the InGaAs QW. The gained conduction band profile  $E_{cb}$  of the simulation, together with the Fermi energy  $E_F$  and the electron wave function probability

## 5 Design and characterisation of InGaAs/InAlAs systems

$|\Psi|^2$  are shown in figure 5.5. With the above listed input parameters for the band structure simulations, we are able to reproduce the experimentally determined transport properties of our system. This confirms that the applied doping-providing InAlAs defect state density of  $N_D^{total} = 3 \cdot 10^{16} \text{cm}^{-3}$  in the calculation presents a correct value for our heterostructures. Furthermore, the band structure calculations show that only the first subband of the  $20\text{nm}$   $\text{In}_{0.75}\text{Ga}_{0.25}\text{As}$  QW is populated and no electron population of the energy states inside the  $5\text{nm}$   $\text{In}_{0.75}\text{Ga}_{0.25}\text{As}$  capping layer is present. These results agree with our experiments since we find no signs of parallel transport in the undoped heterostructures.

wafer	$n_{vdP}^{dark} (\cdot 10^{11} \text{cm}^{-2})$	$\mu_{vdP}^{dark} (\text{cm}^2/\text{Vs})$	$n_{vdP}^{ill} (\cdot 10^{11} \text{cm}^{-2})$	$\mu_{vdP}^{ill} (\text{cm}^2/\text{Vs})$
C160316B	2.2	70000	4.9	135000
C160428A	1.9	110000	4.0	200000
C160428B	1.9	110000	3.9	200000
C160429A	1.7	130000	3.8	220000

**Table 5.3:** Transport properties determined via vdP measurements at  $T = 4.2\text{K}$ .

As a next step, we analyse the 2D transport properties of a more intricate QW design: We insert a thin layer of InAs into the  $\text{In}_{0.75}\text{Ga}_{0.25}\text{As}$  QW. This presents itself as an interesting QW system since InAs offers a larger Rashba SOC parameter than  $\text{In}_{0.75}\text{Ga}_{0.25}\text{As}$  [55]. Additionally, experimental findings in literature suggest that the insertion of an InAs layer into the QW generally leads to an increase of the electron mobility inside the 2DEG owing to reduced alloy disorder the wave function is subjected to [104, 106, 108, 123, 124]. Since InAs exhibits a lattice mismatch of 1.7% to  $\text{In}_{0.75}\text{Ga}_{0.25}\text{As}$ , the pseudomorphic growth of an InAs channel is limited to a thickness of around  $4\text{nm}$  before plastic strain relaxation sets in, which would decrease the mobility in the 2D system [108]. Accordingly, we choose an InAs channel thickness of  $4\text{nm}$ , which we symmetrically insert in the  $\text{In}_{0.75}\text{Ga}_{0.25}\text{As}$  QW so that a total QW thickness of  $20\text{nm}$  is attained. The corresponding active layer sequence of this wafer, i.e. C160420A, is shown in figure 5.4(d) together with a vdP Hall measurement in the illuminated state. The transport properties are summarized in table 5.2. Contrary to our expectations, we find the mobility to be markedly reduced at an equivalent electron density as compared to samples with an  $\text{In}_{0.75}\text{Ga}_{0.25}\text{As}$  QW. This observation is yet not fully understood, however, we suspect partial plastic strain relaxation to be responsible for the impaired transport properties.

We want to note that we find no indications of SOI effects in the MT measurements of our samples. We attribute this observation to a rather symmetric conduction band profile, reducing the effect of Rashba-type SOI. The tuning of the SOI strength with an external gate electric field will be addressed at a later point in this thesis.



**Determination of the effective mass  $m^*$**  Cyclotron resonance measurements<sup>1</sup> provide an experimental access to determine the effective mass  $m^*$  of the conduction electrons in our system. Thereby, the transmission of a THz pulse is probed as a function of the applied magnetic field perpendicular to the sample plane. Varying the employed THz frequency yields a 2D THz-transmission plot as shown in the false color-coded figures 5.6(a) and (b). Therein,  $m^*$  can be determined with a linear fit of the reduced transmission line, at which the resonance condition  $\omega_{pulse} = \omega_c$  is fulfilled, with  $\omega_{pulse} = 2\pi f$  being the THz frequency, and  $\omega_c = \frac{|e|B}{m}$  is the cyclotron frequency.

**Figure 5.6:** Cyclotron resonance measurements of wafer (a) C160420B with a 20nm In<sub>0.75</sub>Ga<sub>0.25</sub>As QW (b) C160420A with an In<sub>0.75</sub>Ga<sub>0.25</sub>As QW and a 4nm InAs inset. The steps in the linear fitting curves are measurement related.

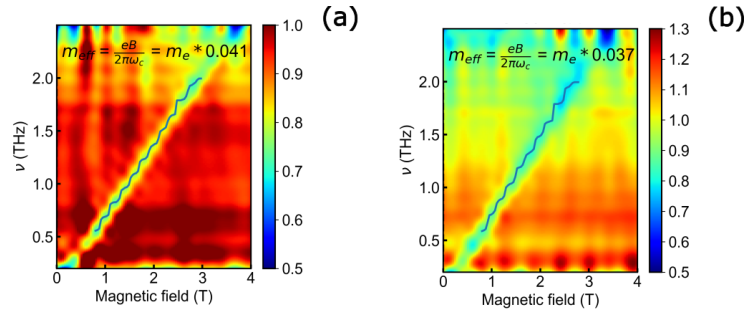


Figure 5.6(a) displays a cyclotron resonance measurement of a 20nm In<sub>0.75</sub>Ga<sub>0.25</sub>As QW (wafer C160420B), whose active layer structure together with the vdP Hall measurement are displayed in figure B.1 in the appendix. Figure 5.6(b) shows a cyclotron measurement of the above analysed sample C160420A with the 4nm InAs inset inside the In<sub>0.75</sub>Ga<sub>0.25</sub>As QW. For sample C160420B, we determine an effective mass of  $m^* = m_e \cdot 0.041$ , where  $m_e$  is the free electron mass, in the case off sample C160420A, we find the effective mass to be reduced to  $m^* = m_e \cdot 0.037$ . Our determined values for the effective masses are in excellent agreement with experimental and theoretical findings in literature [13, 101, 125]. The lower effective mass of the conduction electrons in sample C160420A nicely displays the effect of the InAs inset inside the In<sub>0.75</sub>Ga<sub>0.25</sub>As QW since InAs exhibits a lower effective mass of  $m^*(InAs) = m_e \cdot 0.026$  as compared to GaAs with  $m^*(GaAs) = m_e \cdot 0.067$  [101].

## 5.3 Discussion and conclusion

In our MBE growth study of In<sub>0.75</sub>Ga<sub>0.25</sub>As/In<sub>0.75</sub>Al<sub>0.25</sub>As QW systems, we find the mobility of inverted modulation doped heterostructures strongly impaired as compared to non-intentionally doped layer systems. Furthermore, we find that doped heterostructures show clear indications of a contributing parallel transport channel, which is also present in samples with a low doping density. We assign this finding to the natural doping mechanism, present in InGaAs/InAlAs-based systems, which arises from As-related deep level donor states inside the InAlAs spacer layers providing free electrons for the InGaAs

<sup>1</sup>The measurements are conducted by Maike Halbhuber from the group of Prof. Dr. Dominique Bougeard.

## 5 Design and characterisation of InGaAs/InAlAs systems

QW. For non-intentionally doped heterostructures, we reproducibly find an electron density of  $n_{vdP}^{dark} \approx 2 \cdot 10^{11} \text{ cm}^{-2}$  in the non-illuminated state with a corresponding mobility of approximately  $\mu_{vdP}^{dark} \approx 110000 \text{ cm}^2/\text{Vs}$ . Illuminating the sample increases the electron density by around a factor of two with a similar increase in mobility. This yields a mean free path of several micrometers for the conduction electrons inside the 2DEG, providing a suitable basis for the analysis of ballistic conductance in gate-defined 1D constrictions in this material system.

By means of self-consistent Schrödinger-Poisson simulations, we are able to effectively describe the transport characteristics in our heterostructures. From these calculations, we determine a density of InAlAs deep level donor states of  $N_D^{total} = 3 \cdot 10^{16} \text{ cm}^{-3}$ . This is in line with values reported in literature [37–39].

For all analysed samples, we find no clear signs of SOI effects in the MT measurements. We hypothesize that for modulation doped heterostructures, in which structural inversion asymmetry is certainly present due to the nearby doping layer, the absence of measurable SOI is caused by the impaired electron mobility we determined in these systems. This leads to strongly obscured Shubnikov-de Haas oscillations, whereby a meaningful evaluation of SOI-related effects on the magnetooscillations is impaired, especially in the presence of parallel conductance, which further alters the magnetooscillations. For undoped heterostructures, we assume the structural inversion asymmetry to be too small to induce a significant zero-field spin-splitting. However, since we are able to control Rashba-type SOI via the application of an external gate electric field [55, 71] and owing to the achieved high electron mobility in these systems, we choose an undoped  $\text{In}_{0.75}\text{Ga}_{0.25}\text{As}/\text{In}_{0.75}\text{Al}_{0.25}\text{As}$  QW system as depicted in figure 5.4(c) as initial testing platform for the realization of ballistic 1D conductance. This will be addressed in the following chapter.

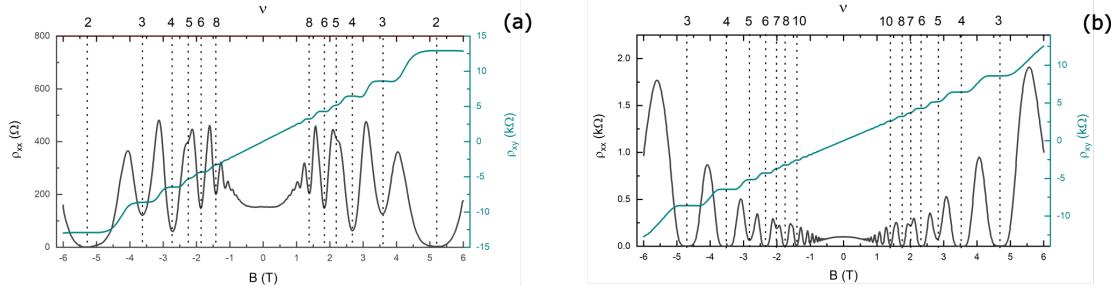


**Figure 5.7:** MT measurement of a Hall bar at  $T = 4.2 \text{ K}$  (a) in the non-illuminated state (b) in the illuminated state.

On these grounds, we fabricate Hall bar devices, which are further equipped with SG-electrodes on top of the Hall bar mesa (described in the appendix in A). By this, we are able to analyse the 1D and 2D transport properties of the very same device. We choose  $20 \text{ nm}$  of ALD-deposited  $\text{Al}_2\text{O}_3$  as dielectric material, which insulates the finger-gate electrodes from the underlying semiconducting materials. Figures 5.7(a) and (b) display exemplary MT measurements of a Hall bar from wafer C160429A in the non-illuminated and in the illuminated state. During a MT measurement, the SG-voltages  $V_{SG1}$  and

$V_{SG2}$  are set to 0V. In the non-illuminated state, we determine a sheet carrier density of  $n_s^{dark} = 2.5 \cdot 10^{11} cm^{-2}$  and a mobility of  $\mu^{dark} = 150000 cm^2/Vs$ . Illuminating the sample increases the sheet carrier density to  $n_s^{ill} = 3.3 \cdot 10^{11} cm^{-2}$  with  $\mu^{ill} = 195000 cm^2/Vs$ . For both measurements, we find the Hall plateaus in  $\rho_{xy}$  to perfectly match integer values of the Landau level filling factor  $\nu$ . Furthermore, the minima of the magnetooscillations reach zero resistivity and we find a single frequency in  $\rho_{xx}$  in  $1/B$ , with the corresponding Shubnikov-de Haas density  $n_{SDH}$  being exactly equal to the determined Hall density, i.e.  $n_{SDH} = n_{Hall} \equiv n_s$ . Thus, we expect a single highly mobile 2DEG without parallel conductance to be present.

In addition, we further test Hall bar samples of identically grown wafers, i.e. wafer C160316B, C160428A, C160428B and C160429A. The determined transport properties, together with the corresponding fabrication details, are listed in table B.2 in the appendix. We generally find a perceptible dependence of  $n_s^{dark}$  and  $\mu^{dark}$  on the fabrication details: Hall bar samples, which are equipped with  $Al_2O_3$  as dielectric, exhibit a higher electron density in the non-illuminated state as compared to samples without dielectric. This effect seems to be further enhanced the closer the QW is located at the surface, i.e. the smaller the InAlAs spacer thickness. This was tested with a supplementary Hall bar test series, in which the InAlAs spacer thickness has been stepwise reduced. The transport properties of the corresponding Hall bars are given in table B.1 in the appendix. Hall bar samples, being equipped with a global TG-electrode above the mesa, exhibit a further increased electron density  $n_s^{dark}$ , even when a TG-voltage of  $V_{TG} = 0V$  is applied.

In conclusion, for samples with an InAlAs spacer thickness of 130nm and a 20nm InGaAs QW, we determine  $n_s^{dark}$  to vary in the range of  $2.0 - 4.2 \cdot 10^{11} cm^{-2}$  with an electron mobility  $\mu^{dark} \approx 70000 - 200000 cm^2/Vs$ . After illumination, however, all samples exhibit similar transport properties with  $n_s^{ill} \approx 3.6 - 4.6 \cdot 10^{11} cm^{-2}$  and  $\mu^{ill} \approx 130000 - 200000 cm^2/Vs$ . This photoconductivity is proven to be stable at least on the timescale of approximately 24 hours at a temperature of  $T = 4.2K$ .

We want to note that at a later point of this thesis, we were faced with temporal obstacles in the MBE growth process of the  $In_xAl_{1-x}As$  buffer system, which prevented further growth optimizations of our heterostructure. At the present time, the  $In_xAl_{1-x}As$  buffer concept is working again. The underlying mechanisms of the deteriorated buffer layer growth are still under debate. Within the scope of a doctoral thesis, the buffer concept is currently optimized and refined [126].

## 5.4 Comment on other material systems

During the course of this work, other material systems were tested in regard to their applicability as substrate material for the implementation of mesoscopic and spintronic device concepts. InAs/AlSb heterostructures present themselves as attractive candidates since they exhibit high intrinsic SOC [55] and generally large elastic mean free paths can be achieved in these material systems [127, 128]. Our transport study of InAs/AlSb

heterostructures is presented in detail in [129]. In contrast to other III-V and group IV materials, we determined that the fabrication process of AlSb-containing devices is rather complex: AlSb exhibits a pronounced hygroscopic behavior when exposed to wet-chemical etchants, water or air. Furthermore, the oxidation of exposed AlSb surfaces during device fabrication leads to the formation of a thin layer of elementary Sb. This metal layer can cause a shorting of neighboring working elements on a device. Furthermore, due to the high interface roughness of etched surfaces, we find that the devices are prone to leakage current between the semiconducting layers and the metal gate electrodes. Moreover, exposed InAs surfaces at the etched mesa sidewalls introduce parasitic conducting edge channels, that cannot be fully electrically depleted by means of gating [18, 130]. A possible solution to the error-prone fabrication process of InAs/AlSb devices is presented in the application of a purely gate-defined device layout as was recently realized in [20, 131]. Hence, further experiments on edgeless devices provide an attractive approach for the realization of mesoscopic devices in this material system since the above listed fabrication obstacles can be nicely circumvented.



# Study of 1D and 2D transport features

<b>6</b>	<b>Realization of conductance quantization in InGaAs/InAlAs .....</b>	<b>61</b>
6.1	Finger-gate layout.....	61
6.2	2D and 1D transport in the model system GaAs/AlGaAs.....	64
6.3	1D transport in InGaAs/InAlAs systems .....	73
6.4	Conclusion and discussion .....	87
<b>7</b>	<b>Gating response of various III-V heterostructures.....</b>	<b>89</b>
7.1	Sample fabrication and MT measurement sequence.....	90
7.2	Chemical treatment and different surface terminations .....	91
7.3	Post-deposition thermal annealing.....	117
7.4	Variation of the dielectric material.....	121
7.5	Charge carrier mobility and scattering sources.....	124
7.6	Towards the reduction of InAlAs deep level donor states .....	130
7.7	Conclusion.....	131
<b>8</b>	<b>Ballistic conductance in InGaAs/InAlAs-based systems.....</b>	<b>135</b>
8.1	Realization of robust ballistic 1D conductance .....	136
8.2	Tuning the ballistic conductance .....	139
8.3	1D conductance in alternative heterostructures .....	143
8.4	Conclusion.....	146
<b>9</b>	<b>Signatures of Rashba-type spin-orbit interaction.....</b>	<b>147</b>
9.1	Gating response of undoped InGaAs/InAlAs heterostructure.....	147
9.2	FFT of magnetooscillations.....	148
9.3	Double-peak generation in FFT .....	156
9.4	SOI in undoped InGaAs/InAlAs systems .....	159
9.5	Conclusion.....	168
<b>10</b>	<b>Conclusion and outlook.....</b>	<b>169</b>



# 6

## Realization of conductance quantization in InGaAs/InAlAs

This chapter serves to present the experimental process in the course of this work towards the realization of conductance quantization in  $\text{In}_{0.75}\text{Ga}_{0.25}\text{As}/\text{In}_{0.75}\text{Al}_{0.25}\text{As}$  heterostructures, which we discussed and characterised in the previous chapter 5. Using highly mobile  $\text{GaAs}/\text{Al}_{0.31}\text{Ga}_{0.69}\text{As}$  heterostructures as a model system, we develop a finger-gate electrode layout, suitable for the realization of an adiabatic 1D confining potential for deeply buried 2DEGs ( $d_{\text{spacer}} \approx 130\text{nm}$ ), which are predominantly discussed in this work. This finger-gate layout is then further modified to account for the lower electron mobility in the  $\text{In}_{0.75}\text{Ga}_{0.25}\text{As}/\text{In}_{0.75}\text{Al}_{0.25}\text{As}$  system as compared to  $\text{GaAs}/\text{Al}_{0.31}\text{Ga}_{0.69}\text{As}$  heterostructures. We provide a holistic study of the transport through the electrostatically defined QPCs, with focus on the electric stability of the transport characteristics. For clarity, the experiments presented here are mainly based on measurements of three devices, being identical in structure. All the conclusions made are supported by multiple other devices.

### 6.1 Finger-gate layout

In our 1D transport experiments, we define a QPC electrostatically by a pair of parabolic finger-gate electrodes, placed on top of the heterostructures. This so-called *split-gate* (SG) technique was pioneered by Thornton et al. [132] and Zheng et al. [133]. Biasing the SG-electrodes negatively leads to a depletion of the underlying 2DEG via the field-effect. This is illustrated in figure 6.1(a), showing a sketch of a semiconductor heterostructure, hosting the 2DEG (dark green layer), together with the mounted SG-electrodes SG1 and SG2. The depletion of the 2D system is displayed in form of the white shaded areas underneath the SG-electrodes. Further increasing the gate voltage squeezes the transport channel laterally in width (figure 6.1(b)), until the channel is totally pinched off. When the channel width  $w$  becomes comparable to the Fermi wavelength  $\lambda_F$ , the conductance  $G$  of the channel becomes quantized and conductance steps at multiples of

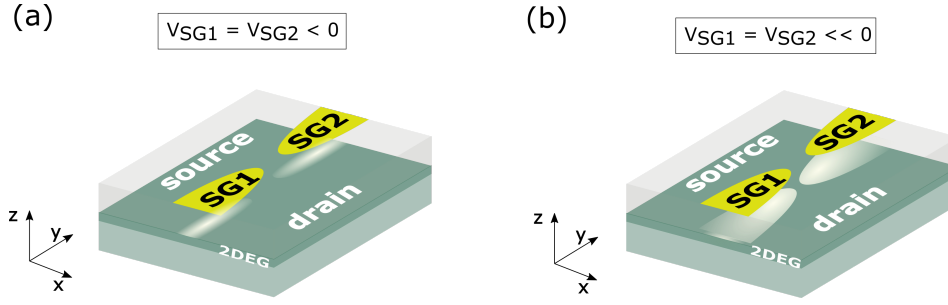


**Figure 6.1:** Illustration of a layer structure, hosting a 2DEG (dark green) with SG-electrodes SG1 and SG2 (yellow) attached on top of the heterostructure. Negatively biasing the gate electrodes creates a narrow constriction between the 2D electron reservoirs, labeled as *source* and *drain*. **(a)** For a small negative symmetrically applied bias  $V_{SG1} = V_{SG2}$ , the 2DEG is depleted underneath the gate electrodes, visualized as white shaded areas in the 2DEG plane. **(b)** For sufficiently large negative SG-voltages, the channel becomes laterally depleted and a QPC is formed when the 1D channel width  $w$  is in the order of the Fermi wavelength  $\lambda_F$ .

$2 \cdot G_0 = 2e^2/h$ , with  $G_0$  being the conductance quantum, arise. A necessary ingredient for the observation of clear quantization steps in  $G$  is that both, the channel width  $w$  and length  $L$  are smaller than the mean free path  $l_{mfp}$  of the conduction electrons, whereby the ballistic transport regime is entered. Non-ideal conductance quantization arises for a non-adiabatic coupling of the electron wave functions in and out of the QPC. For realistic devices an energy-dependent transmission coefficient  $\mathcal{T}_m(E)$ , with  $m$  being the transversal mode index of the channel, enters the description of conductance quantization. Modelling the gate-defined constriction in the form of a saddle potential, we find for the transmission through the QPC (see section 2.2 and [6]):

$$\mathcal{T}_m(E) = \frac{1}{1 + e^{-2\pi\epsilon_m}} , \quad (6.1)$$

with

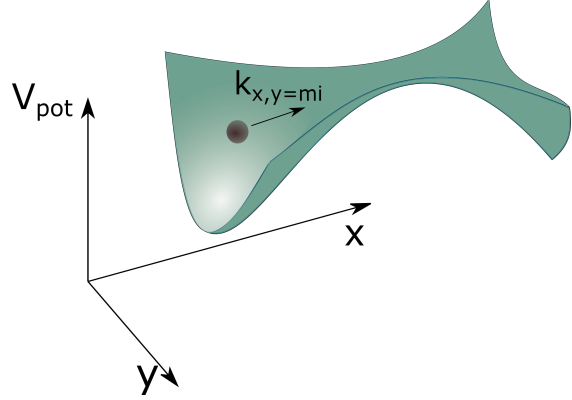
$$\epsilon_m = \frac{E - \hbar\omega_y(m + 1/2) - E_z}{\hbar\omega_x} .$$

Here,  $E_z$  denotes the energy eigenstates due to quantization in  $z$ -direction (growth direction).  $\omega_y$  indicates the strength of the lateral confinement potential and  $\omega_x$  of the longitudinal confinement potential in transport direction.

A saddle potential is schematically sketched in figure 6.2. By means of equation (6.1), we find the transmission coefficient  $\mathcal{T}_m(E)$  to be maximum if the ratio  $\omega_y/\omega_x > 1$ . We therefore have to meet the following requirements with our SG-layout for the generation of pronounced conductance steps: The tips of the finger-gate electrodes have to exhibit a weak curvature, i.e. a small  $\omega_x$ , and the tip-to-tip distance has to be small in order to guarantee for a steep confinement potential in  $y$ -direction, i.e. a large  $\omega_y$ .



**Figure 6.2:** Illustration of a harmonic confinement potential  $V_{pot}$  in  $x$ - and  $y$ -direction, forming a QPC. The width of the constriction in  $y$ -direction, as well as the strength of the confinement is a function of the position  $x$ . The dark sphere represents a conduction electron with the wavenumber  $k_{x,y}$ , evolving adiabatically into an eigenstate of the QPC.  $m$  indicates a mode of the QPC due to the confinement in  $y$ -direction.



In the course of this work several layouts of SG-electrodes were tested, including line-shaped electrodes, which are shown in the scanning electron microscopy (SEM) image in figure 6.3(a). However, transport measurements through 1D constrictions defined with such line-shaped finger-gate electrodes often exhibited unwanted features in the conductance characteristics. We attribute these properties to the presence of local potential minima in the vicinity of the SG-electrodes, whereby bound states inside the channel are created. Such Coulomb blockade-like transport features can be seen in figure 6.3(b), displaying an exemplary 2D-plot of a conductance measurement through a QPC with line-shaped gate electrodes. The current  $I$  through the constriction is plotted as a function of the symmetrically applied SG-voltage  $V_{SG1} = V_{SG2} \equiv V_{SG}$  and the applied source-drain voltage  $V_{SD}$  at the 2D electron reservoirs. In this measurement,  $V_{SG}$  is stepwise decreased into the negative direction; for each value of  $V_{SG}$ , the source-drain voltage is then swept within the adjusted bias interval  $[-|V_{SD}|, +|V_{SD}|]$ . The maximum applied  $|V_{SD}|$  is chosen such that the energy bias window is smaller than the estimated energy-level separation due to the confining potential in  $y$ -direction<sup>1</sup>. The plot corresponds to the situation of a 1D channel in the vicinity of pinch-off. We see clear undulations in the current  $I$ , for example when comparing the line-cut into the  $V_{SD}$ -direction at  $V_{SG} \approx -2.2V$  to the line-cut at  $V_{SG} \approx -2.15V$ , which evidences a modulation of the transmission probability, dissenting from ideal quantized conductance of a QPC.

To prevent the formation of such localized bound states and to improve the adiabatic coupling of the electron wave functions in and out of the QPC, we test a parabolic SG-design, emulating the aspired saddle potential in the 1D constriction. We initially test the parabolic SG-layout on a GaAs/Al<sub>0.31</sub>Ga<sub>0.69</sub>As heterostructure, as it presents itself as a high-mobility 2D model system, exhibiting a comparable permittivity as the In<sub>0.75</sub>Ga<sub>0.25</sub>As/In<sub>0.75</sub>Al<sub>0.25</sub>As layer system (see subsection 7.2.2). Thereby, we are able to analyse and evaluate the SG-induced potential without the need to account for intricacies such as for example disorder potentials, which are present in InGaAs/InAlAs

<sup>1</sup>This estimation is based on the assumption of a Fermi wavelength of  $\lambda_F \leq 50nm$  and  $N \approx 2w/\lambda_F$ ,  $N$  being the number of occupied channel modes. Near pinch-off, an almost rectangular 1D potential well can be assumed, whereby the 1D subband spacing is calculated as  $\geq 10meV$ .

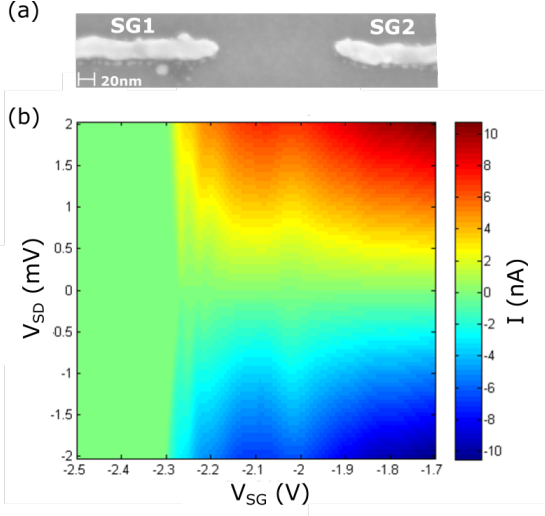


**Figure 6.3:** (a) SEM image of line-shaped SG-electrodes SG1 and SG2 on top of an  $\text{In}_{0.75}\text{Ga}_{0.25}\text{As}/\text{In}_{0.75}\text{Al}_{0.25}\text{As}/\text{Al}_2\text{O}_3$  heterostructure; linebar for scale. (b) 2D-scan of the dc source-drain current  $I$  through the finger-gate defined 1D constriction as function of the applied source-drain voltage  $V_{SD}$  and the symmetrically applied SG-voltage  $V_{SG}$  at a temperature of  $T = 370\text{mK}$ . The undulations in  $I$  evidence local potential minima (bound states), leading to Coulomb blockade-like features in the transport measurement.

heterostructures due to the ionized deep level donor states inside the InAlAs spacer layers.

## 6.2 2D and 1D transport in the model system GaAs/AlGaAs

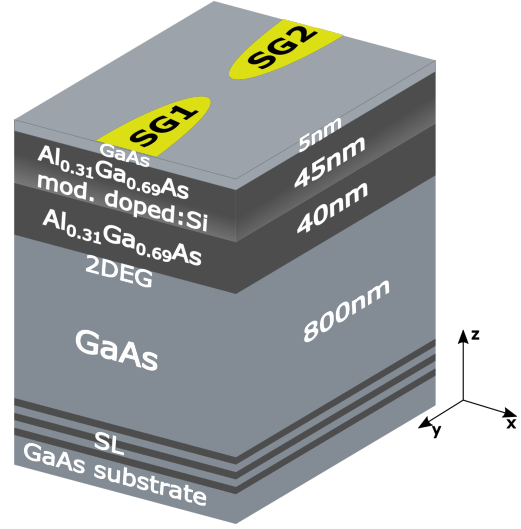
In this section, we study the 1D transport in high-mobility GaAs/ $\text{Al}_{0.31}\text{Ga}_{0.69}\text{As}$  heterostructures to test the electric confining potential which is created with our parabolic SG-electrode design. To yield significant results in this comparative analysis, we choose a GaAs/ $\text{Al}_{0.31}\text{Ga}_{0.69}\text{As}$  modulation doped heterostructure with a similar 2DEG depth as our  $\text{In}_{0.75}\text{Ga}_{0.25}\text{As}/\text{In}_{0.75}\text{Al}_{0.25}\text{As}$  layer structures<sup>2</sup>.

### 6.2.1 2D magnetotransport properties

Figure 6.4 shows the layer structure of the employed GaAs/ $\text{Al}_{0.31}\text{Ga}_{0.69}\text{As}$  system. The 2DEG is formed in the triangular potential well, which is created at the GaAs/ $\text{Al}_{0.31}\text{Ga}_{0.69}\text{As}$  interface. A  $40\text{nm}$   $\text{Al}_{0.31}\text{Ga}_{0.69}\text{As}$  spacer layer separates the 2DEG from the Si-doped  $\text{Al}_{0.31}\text{Ga}_{0.69}\text{As}$  film. The sample is terminated with a  $5\text{nm}$  GaAs capping layer that prevents the heterostructure from oxidation and effectively pins the Fermi level near midgap due to As-As dimer formation, creating a high density of energy states at the interface [134–136]. As described in chapter 4, we fabricate Hall bar samples on top of which SG-electrodes are deposited. Thereby, we yield access to the 2D transport properties of the very same device of which we also study ballistic 1D transport. Figure 6.5 displays the corresponding MT measurements, recorded in the non-illuminated

<sup>2</sup>Here, we focus on the highly mobile samples with  $d_{\text{spacer}} = 135\text{nm}$ . Samples with varying spacer thicknesses are analysed in chapter 8.

**Figure 6.4:** Schematic sketch of the layer structure of the analysed GaAs/Al<sub>0.31</sub>Ga<sub>0.69</sub>As heterostructure, grown on GaAs (001). At the GaAs/Al<sub>0.31</sub>Ga<sub>0.69</sub>As interface a triangular potential well is formed, hosting the 2DEG. The Si modulation doping starts 50nm below the surface and fades in the growth direction, indicated by the white shading. Due to the formation of a sufficiently high Schottky barrier, the SG-electrodes (yellow) are deposited right on top of the GaAs cap.



and illuminated state. Without illumination, we determine a sheet carrier density of  $n_s^{dark} = 2.3 \cdot 10^{11} \text{ cm}^{-2}$  with a mobility of  $\mu^{dark} = 9.53 \cdot 10^5 \text{ cm}^2/\text{Vs}$ . By means of

$$l_{mfp} = \frac{\hbar}{e} \sqrt{2\pi n_s \mu} ,$$

we determine a mean free path of  $l_{mfp}^{dark} = 7.6 \mu\text{m}$ . Illuminating the sample for 60s with a red LED ionizes the DX-centers<sup>3</sup> inside the modulation doped region of the sample, whereby the electron density in the 2D channel is increased. Figure 6.5(b) shows a MT measurement of the sample after illumination. The charge carrier density is increased to  $n_s^{ill} = 4.4 \cdot 10^{11} \text{ cm}^{-2}$ , while the mobility remains approximately the same with  $\mu^{ill} = 9.54 \cdot 10^5 \text{ cm}^2/\text{Vs}$ , yielding a mean free path of  $l_{mfp}^{ill} = 10.4 \mu\text{m}$ . Whereas the MT measurements in the illuminated state are reproducible for various cool-downs, we find variations in the 2D transport characteristics of the sample in the non-illuminated state. Even though, the SG-electrodes are consistently set to the laboratory ground potential at room temperature (RT) prior to each cool-down, whereby we aim to generate a pre-defined and reproducible electrostatic situation underneath the gate electrodes, the conductivity perceptibly differs when the sample is thermally recycled and then cooled down again. Although no negative voltage is applied at the SG-electrodes, the band structure is apparently altered by the sole presence of the gate electrodes attached on top of the heterostructure, leading to a reduced electron density in the 2D channel underneath. We find that after some cool-downs the 2D channel is even completely pinched off so that we are not able to draw a current through the Hall bar. Illuminating the samples leads to a much more reproducible situation for which we consistently determine  $n_s^{ill} = 4.4 \cdot 10^{11} \text{ cm}^{-2}$ . We interpret the deviations of the 2D transport behavior in the

<sup>3</sup>A DX-center is a deep electronic state, located 0.12meV under the conduction band edge of Al<sub>0.31</sub>Ga<sub>0.69</sub>As, which is negatively charged at cryogenic temperatures but can be discharged after illumination with light of sufficiently high energy.

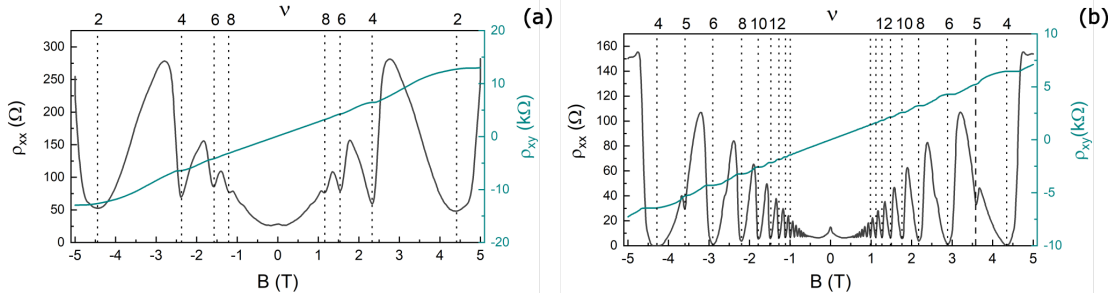


**Figure 6.5:** MT measurements of a Hall bar sample, fabricated from wafer C120522B **(a)** at  $T = 4.2K$  in the non-illuminated state, **(b)** at  $T = 1.5K$  in the illuminated state. The vertical dashed lines indicate the minima of the Shubnikov-de Haas oscillations with the corresponding Landau level filling factor  $\nu$ . For both measurements we find distinct Hall plateaus at integer values of  $\nu$ . In the illuminated situation in (b), the B-field-induced Zeeman splitting occurs for  $|B| > 3.7T$ .

non-illuminated state as a variation of the occupation of DX-centers with electrons at RT. This fluctuating electron population of energy states is then brought to cryogenic temperatures. On the microscopic scale of the SG-electrodes of only a few hundreds of nanometers, these fluctuations do not average out as they do on the scale of a Hall bar channel but distinctly influence the electrostatic potential in the 1D constriction. Furthermore, due to a SG-induced band bending, more DX-centers underneath the SG-electrodes seem to be populated with electrons, leading to an effectively applied negative voltage at the externally unbiased SG-electrodes. This bottle-neck situation leads to a decreased conductivity through the 2D channel when charge carriers have to pass the SG-defined constriction.

In the following, we study the 1D ballistic transport through the SG-defined constrictions in the GaAs/Al<sub>0.31</sub>Ga<sub>0.69</sub>As samples.

### 6.2.2 1D transport in SG-defined QPCs

As discussed in section 6.1, we model the targeted harmonic confinement potential forming the QPC with parabolic SG-electrodes. This shape should guarantee an adiabatic transition from the 2D reservoirs, i.e. source and drain, to the 1D channel without the generation of localized states, that would increase backscattering and thereby hamper ballistic transport. Figure 6.6 shows a SEM image of the tested SG-layout. The left picture is false color coded: In blue, the underlying heterostructure is displayed, whereas in yellow the deposited SG-electrodes with their much larger contacts are depicted. The right image presents a zoom into the tip region of the SG-electrode pair SG1 and SG2. At the foremost part, the finger-gates are shaped parabolically with a channel length  $L$  of about  $480nm$ . The tip-to-tip distance of the SG-electrodes is approximately  $350nm$ .

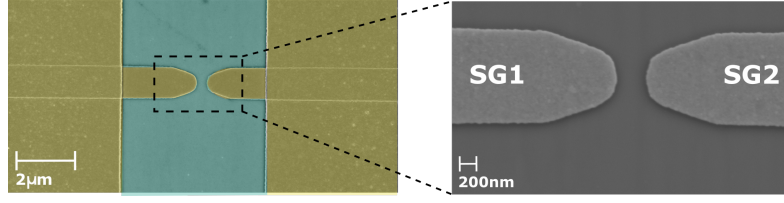


**Figure 6.6:** SEM images of the SG-defined constrictions with linebars for scale: The left image (false color coded) displays the finger-gate electrodes with their much larger contacts (both in yellow), with which the QPCs are formed in the semiconducting layer (blue area) underneath. The right figure shows a zoom into the parabolic-shaped tip area of the SG-electrodes. The tip-to-tip distance is about  $w \approx 350\text{nm}$ .

### Conductance quantization in the non-illuminated state

As already described above, during the process of cooling down the sample to cryogenic temperatures, the SG-electrodes are set to the laboratory ground potential. In a conductance measurement, we record the conductance  $G$  through the QPC as a function of the symmetrically applied SG-voltage  $V_{SG1} = V_{SG2} \equiv V_{SG}$ . Commonly, a sweep-rate of  $2 - 5\text{mV/s}$  is chosen. Since we determine that  $G$  does not depend on the SG-bias history, we do not distinguish between up- and downwards-swept curves, i.e. the depletion and the opening of the 1D channel with  $V_{SG}$ , respectively. The applied source-drain voltage at the 2D electron reservoirs consists of a small dc contribution ( $V_{sd}^{dc} < 200\mu\text{V}$ ), superimposed to an ac voltage of  $V_{sd}^{ac}$  of  $50\mu\text{V}$  (as described in chapter 4). We find that neither the source-drain voltage nor the sweep rate influence the conductance characteristics of the analysed QPCs when held under these values.

Figure 6.7(a) displays five subsequent conductance measurements at  $T = 1.5\text{K}$  in the non-illuminated state, for which  $G$  is plotted in multiples of twice the conductance quantum, i.e.  $2 \cdot G_0 = 2e^2/h$ , as a function of  $V_{SG}$ . A serial channel resistance of  $R_{ch} = 300\Omega$  is subtracted to fit the conductance steps to integer multiples of  $2e^2/h$ . The SG-voltage is swept into the negative direction, thus depleting the 2D channel underneath until total pinch-off, i.e.  $G = 0$ . The individual conductance curves are vertically offset for clarity. Even at  $V_{SG} = 0\text{V}$ , we find that the conductance through the constriction is as low as approximately  $5 \cdot G_0$ , which indicates that the channel is already laterally confined in size. With decreasing SG-voltage, the conductance  $G$  drops almost linearly with distinct conductance steps developing before the channel is totally pinched off at  $V_{SG} \approx -0.275\text{V}$ . The small conductance step at  $0.7 \cdot 2e^2/h$  can be assigned to the 0.7-anomaly, a result of electron-electron interactions, with its exact origin being still under debate [7, 137–143]. All measured curves in figure 6.7(a) show the same transport behavior, thus confirming the reproducibility of the transport characteristics over time.

Figure 6.7(b) shows a single 1D conductance measurement (cyan curve), together with the corresponding conductance derivative  $dG/dV_{SG}$  (dotted curve). By evaluating the quantization value  $G_m$ , with  $m \in \mathbb{N}$  being the channel mode index, at the mathematical

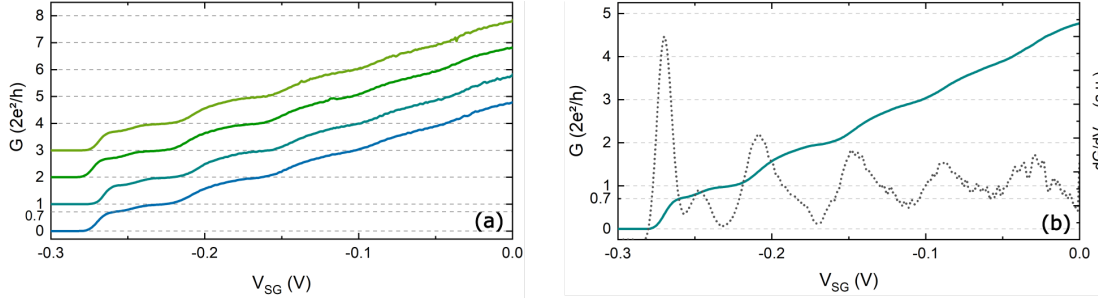


**Figure 6.7:** Sample C120522B2 at  $T = 1.5\text{K}$  in the non-illuminated state: **(a)** Five subsequent conductance curves, displaying  $G$  as a function of  $V_{SG}$ . The curves are vertically offset for clarity. A serial channel resistance of  $R_{ch} = 300\Omega$  is taken into account to match the conductance steps to  $n \cdot 2e^2/h$ , with  $n \in \mathbb{N}$ . **(b)** Single conductance curve (cyan line) of the same QPC as in (a), with the corresponding conductance derivative  $dG/dV_{SG}$  (dotted curve).

minimum of the derivative-curve provides an easy access to the transmission probabilities  $\mathcal{T}_m(E)$  of the individual 1D modes in the channel. The quantity  $Q_m$ , defined as  $Q_m = \frac{G_m h}{2me^2}$ , specifies the conductance of the  $m$ -th channel. The average quantization  $Q_{av}$  can then be calculated as  $Q_{av} = \frac{1}{N} \sum Q_m$ , with  $N$  being the number of contributing transversal channel modes  $m$ . By means of  $Q_{av}$ , the 1D conductance quantization of different samples and their congruency with ideality can be quantitatively compared [18]. All determined conductance curves of the GaAs/ $\text{Al}_{0.31}\text{Ga}_{0.69}\text{As}$  samples in the non-illuminated state show three distinct quantization steps with  $Q_{av} = 0.97 - 0.99$ , indicating pronounced ballistic conductance for each fully developed mode. Nevertheless, the steps in figure 6.7(a) are blurred. This can be ascribed to enhanced backscattering when a mode is newly populated and electron momentum transfer for a scattering event is sufficiently small, making momentum transfer more likely than for the case when the Fermi level lies in between two subsequent levels. In the non-illuminated state, backscattering is likely to be enhanced because of the poor screening in the channel due to the small electron density  $n_s^{dark}$ . Furthermore, scattering from potential fluctuations generated by remote dopants, which are partially ionized, enhances the scattering probability inside the 1D channel and creates quasi-localized states [144, 145]. We find that the ratio  $\omega_y/\omega_x$  is likely to be reduced since solely a small SG-voltage  $V_{SG}$  has to be applied to change the number of participating modes, thus indicating a weak curvature of the confining potential in  $y$ -direction. For the sake of completeness, temperature blurring can be listed here, which smears out the mode-transitions.

In a next step, the sample is illuminated, whereby doping-providing DX-centers in the spacer layer are ionized. This results in an enhanced sheet carrier density  $n_s^{ill}$  with better screening ability. Consequently, we expect the potential fluctuations in the remote doping layer above to be minimized, leading to a sharpened conductance-step transition.



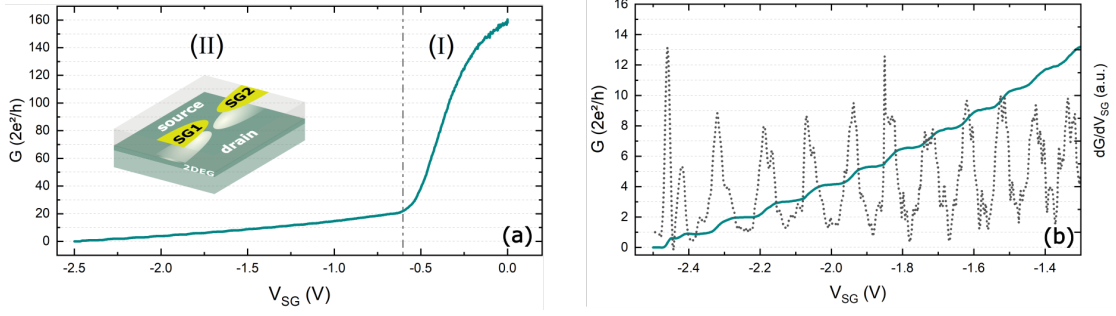


**Figure 6.8:** Sample C120522B2 at  $T = 1.5K$  in the illuminated state: **(a)** Conductance  $G$  as a function of  $V_{SG}$ . The Roman numerals (I) and (II) indicate the two characteristic pinch-off areas of the QPC. The inset shows a sketch of the QPC in area (II), where the channel is laterally depleted. **(b)** Zoom into gating area (II) of the measurement in (a), displaying the conductance  $G$  (cyan line) together with the corresponding derivative  $dG/dV_{SG}$  (dotted curve). A serial resistance of  $R_{ch} = 100\Omega$  is subtracted.

### Conductance quantization in the illuminated state

Figure 6.8(a) displays the conductance curve of the same sample as in subsection 6.2.2 after illumination. The curve can be divided into two gating areas (I) and (II), characteristic for a SG-defined QPC [146]: Decreasing the SG-voltage from 0V into negative direction steeply decreases the conductance through the constriction. Hereby, labeled as area (I) in the plot, the 2DEG underneath the SG-electrodes is depleted. By further sweeping  $V_{SG}$  into the negative voltage direction, i.e. area (II), the channel starts to be depleted laterally. This situation is illustrated by the QPC sketch in the inset of figure 6.8(a). In this SG-voltage range well-defined conductance steps develop due to lateral size-quantization effects. To match the conductance steps of our measurement to integer multiples of  $2e^2/h$  a channel resistance of  $R_{ch} = 100\Omega$  is subtracted. We find more than 13 well-developed conductance steps, which perfectly match integer values of  $2 \cdot G_0$ . Analogously to the non-illuminated case, the 0.7-anomaly is clearly developed. To analyse the transmission probability of the individual modes of the 1D channel,  $dG/dV_{SG}$  is calculated, which is shown in figure 6.8(b) as dotted curve. Taking the first distinct eight steps into account, we find  $Q_{av} = 0.99$ . This implies ideal conductance in the 1D channel when  $E_F$  lies in between two subsequent 1D subband levels. The sharpened conductance step-transition when a new mode starts to contribute to the 1D transport indicates small-angle scattering to be distinctly reduced compared to the non-illuminated case, which was shown in the preceding subsection 6.2.2 in figure 6.7.

**Time stability of photoconductance** In Hall bar measurements of GaAs/AlGaAs heterostructures (not shown here), we determined the photoconductance to be persistent at least on the timescale of hours at  $T = 4.2K$ . Figure 6.9(a) shows four conductance curves of the QPC analysed above, recorded over 40 minutes, whereby the numbers (1) to (4)

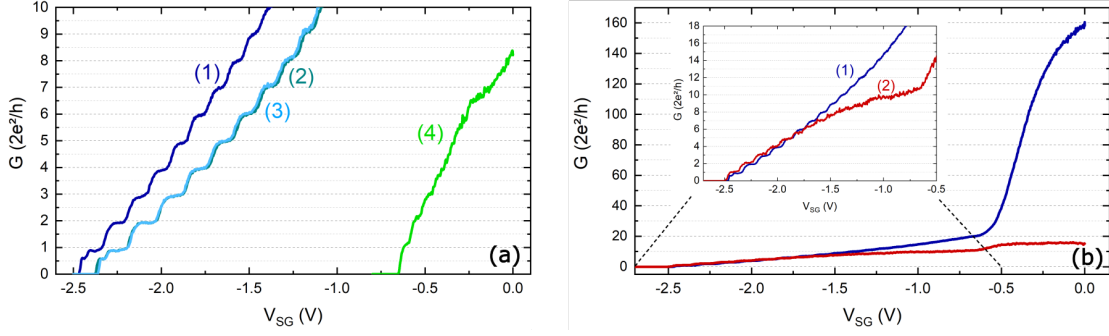


**Figure 6.9:** Sample C120522B2 at  $T = 1.5K$  in the illuminated state: **(a)** Four conductance curves, which are recorded over 40 minutes. Numbers (1) to (4) give the chronological order of the measurements. **(b)** Two conductance measurements between which the sample is re-illuminated. The conductance curve (1) (blue curve) presents the same measurement as curve (1) in (a).

indicate the chronological order. We find the pinch-off point to vary distinctly between the measurements, abruptly shifting towards less negative SG-voltages in subsequent sweeps. With the relocation of the conductance curves, a degradation of the quantization steps occurs: The steps are less pronounced, i.e. they have a smaller width in  $V_{SG}$ -direction, indicating a reduced 1D subband spacing, and exhibit increased conductance fluctuations in form of small spikes superimposed on the signal. For  $Q_{av}$  of measurements (1) to (4), we find values between 0.98 and 0.99, implying again ideal conductance when  $E_F$  lies in between two subsequent 1D-mode subbands. This implies that small-angle scattering is effectively reduced in the 1D transport.

Re-illuminating the sample does not succeed to restore the initial situation as is shown in figure 6.9(b). Here, the blue curve, labeled as (1), displays the initial  $V_{SG}$ -down sweep after the first illumination of the sample (also curve (1) in figure 6.9(a)), whereas the red curve, marked as (2), depicts the first recorded 1D conductance measurement after re-illumination. Especially for SG-voltages close to 0V, we find the conductance  $G$  to vary distinctly in the different measurement sweeps, whereas for  $V_{SG} < -1.5V$  the conductance characteristics converge. Additionally, the noise of curve (2) is enhanced as compared to (1). Solely a thermal recycling fully recovers the initial electrostatic situation, i.e. curve (1). A shift of the whole pinch-off curve into positive  $V_{SG}$ -direction corresponds to an intrinsic upwards band bending, induced by a newly formed negative space charge region above the 2D channel. We assign this behavior to a reoccupation of the photoionized DX-centers, which results in the observed shifting of the pinch-off point. Indeed, the repeated strong band bending the sample encounters during the up- and down-sweeps of the SG-voltage triggers charge transfer from the 2DEG towards the remote doping region. This spatially varying electron migration apparently varies in space, leading to an inhomogeneous charge distribution inside the doping layer. This negative charge acts as an additional confinement potential to the QPC, causing an earlier pinch-off of the channel at more positive  $V_{SG}$ , and furthermore introduces potential fluctuations, visibly



impeding ballistic transport. As we find that re-illumination of the sample does not restore the initial charge configuration of measurement (1), we conclude that charge carriers apparently relax into deeper lying energy states, that are not addressed by the photons of the red LED.

**Figure 6.10:** Time stability measurement of sample C120522B2 at  $T = 1.5K$ : **(a)**  $G$  as a function of  $V_{SG}$ . The colored dots on the curve mark the measuring points of  $G$ , for which a dwell time of several minutes is applied. **(b)**  $V_{SG}$  as a function of time  $t$ . **(c)**  $G$  as a function of  $t$ . For (a) and (c) a serial resistance of  $R_{ch} = 100\Omega$  is subtracted.

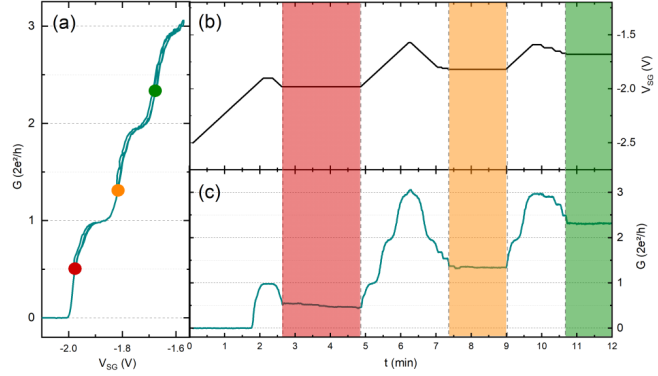
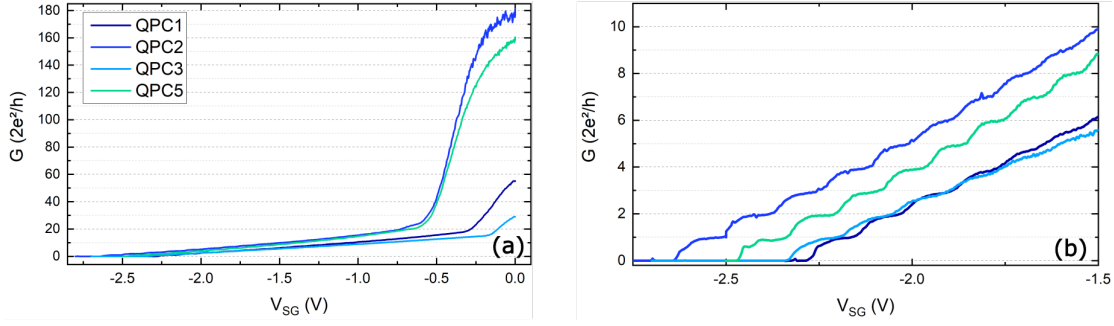


Figure 6.10 displays a time stability measurement of the conductance  $G$ , when  $V_{SG}$  is adjusted such that the measurement point is positioned in a transition area between two subsequent conductance steps. Tested points on the conductance curve are indicated as colored dots in figure 6.10(a). These measuring points offer the most sensitive control of the time stability and robustness of the 1D conductance in the system. At these points, a dwell time of several minutes is applied during which we test the electric stability of the conductance  $G$ . Figure 6.10(b) displays  $V_{SG}$  as a function of time  $t$ , applied to tune  $G$  to a particular operating point. The SG-voltage areas are color-coded as in (a). Figure 6.10(c) shows the resulting conductance  $G$  as a function of time  $t$ . We find the conductance at the measuring points to be reasonably stable at least on a timescale of minutes at a base temperature of  $T = 1.5K$ . Whereas a slight decrease of the conductance takes place at the first operating point (red area),  $G$  is stable at the second and third measurement points (yellow and green area). We thus conclude that the conductance through the 1D constriction is reasonably stable, yet with the uncertainty of sudden charge transfer processes, that modify the electrostatic 1D confinement potential.

In addition to the time stability of the 1D conductance properties, it is crucial to achieve a high reproducibility of the transport characteristics in the 1D channels, defined with a SG-layout. To this end, we test the conductance of different split-gated 1D constrictions, formed in the same heterostructure.

**Variance of the transport behavior of identical QPCs** As described in chapter 4, our Hall bar mesas are equipped with several, nominally identical QPCs. In sample C120522B2, five SG-defined QPCs are positioned in between the Hall crosses. Thereby, we can study the transport behavior of these constrictions, fabricated in the same processing run on the same device.

Figure 6.11(a) shows the depletion curves of four different QPCs on one sample in



**Figure 6.11:** (a) Conductance  $G$  of four identical QPCs on the same sample (C120522B2) at  $T = 1.5K$ . (b) Zoom into the pinch-off area in (a). Each curve presents the initial depletion measurement after the cool-down and illumination. For the right plot a serial resistance is subtracted to match the conductance steps to integer values of  $2e^2/h$ .

the whole bias range from  $V_{SG} = 0V$  to  $-2.75V$  (no channel resistance is considered here). Figure 6.11(b) presents a zoom into the area near pinch-off. QPC 5, which we already analysed in the previous section, exhibits the most pronounced conductance quantization. More than 12 distinct steps are clearly visible. QPC 2 shows a comparable conductance curve, however, with a smaller number of quantization steps being clearly developed. In contrast, we find markedly smoothed quantization steps for QPCs 1 and 3, pointing towards an increased scattering rate between mode transitions. We attribute the discrepancies in the transport properties to variations in the confinement potential for the different QPCs due to variations in the lift-off process of the SG-electrodes, as well as to intrinsic crystalline imperfections, such as for example impurities in the vicinity of the 1D channel. Furthermore, a non-uniform photoionization of the remote doping layer can cause such deviations between the transport properties in different QPC devices on the same sample. For  $Q_{av}$ , we determine the values to range from 0.93 to 0.99, indicating for all QPCs that backscattering is strongly suppressed.

Our experimental results are in line with findings in literature [7, 147]. In a statistical study of 256 nominally identical GaAs/AlGaAs QPCs, Smith et al. [7] demonstrated the impact of potential fluctuations on the 1D transport characteristics. In more than 59% of the tested QPCs they found disorder-induced conductance variations in the form of a smoothing of the conductance steps as we observe in our measurements.

### 6.2.3 Conclusion

In our analysis of 1D transport in SG-defined QPCs in the model system GaAs/AlGaAs, we determine well-defined quantization steps in  $G$ , which ideally match integer multiples of  $2e^2/h$  in the non-illuminated, as well as in the illuminated state.

In non-illuminated measurements, the QPCs are already near pinch-off, exhibiting a total conductance of around  $5 \cdot G_0$  at  $V_{SG} = 0V$ , with a smoothed transition of the

conductance in between two subsequent steps when a new mode is (de-)populated. Due to the low electron density of the 2DEG, the screening ability of remote impurities is reduced, which leads to increased potential fluctuations acting on the 1D confinement potential, thus obscuring a steep mode transition.

After illumination, our devices show more than ten well-defined conductance steps, with the 1D transport properties reasonably reproducible for different, nominally identical QPCs. However, after illumination, the samples are prone to abrupt recharging processes inside the heterostructure, leading to a global shift of the conductance curve as a function of  $V_{SG}$  as well as to a deterioration of the conductance steps. Both effects are attributed to additional negative charge, being transferred from the 2DEG towards the ionized remote doping layer, thereby effectively increasing and modifying the SG-induced confining potential.

To summarize, we find the here tested parabolic SG-layout suitable for studying 1D transport in deeply buried 2DEGs. At the same time, this analysis provides first signs for upcoming challenging aspects which we are likely to face with the InGaAs/InAlAs heterosystem, being a ternary alloy with certainly present InAlAs defect states inside the spacer layers.

## 6.3 1D transport in InGaAs/InAlAs systems

This section presents our approach towards the realization of 1D conductance quantization in the ternary alloy system  $\text{In}_{0.75}\text{Ga}_{0.25}\text{As}/\text{In}_{0.75}\text{Al}_{0.25}\text{As}$ , characterised in chapter 5. By means of exemplary devices, the 1D transport characteristics in the non-illuminated and in the illuminated state are analysed. The measurements shown in this section are representative for multiple devices, which have been tested in the course of this work. As long as not stated otherwise, the samples are cooled down with all ohmic contacts set to the laboratory ground potential and the SG-electrodes set to a voltage of  $V_{SG} \equiv V_{CD} = 0\text{V}$  to predefine a reproducible initial electrostatic situation. Most of the measurements are conducted at a base temperature of  $T = 1.5\text{K}$  in a He dewar.

### 6.3.1 1D transport in SG-defined QPCs

The split-gated Hall bar sample layout is identical to the one, which we tested and approved with the GaAs/AlGaAs devices as presented in the previous section 6.2.

#### Conductance quantization in the non-illuminated state (SG)

Figure 6.12 displays a sketch of the InGaAs/InAlAs heterostructure we choose for the first 1D conductance measurements in this material system. The 2D transport properties are discussed in chapter 5. We find that for ungated Hall bar samples in the non-illuminated state the charge carrier density values are in the range of  $n_s^{\text{dark}} = (2.5 - 3.3) \cdot 10^{11} \text{cm}^{-2}$  with a mobility of  $\mu^{\text{dark}} \approx (1.0 - 1.7) \cdot 10^5 \text{cm}^2/\text{Vs}$ . These transport values yield a mean

## 6 Realization of conductance quantization in InGaAs/InAlAs

free path of  $l_{mfp} \approx (1.0 - 1.6)\mu m$ , being considerably smaller than the mean free path we achieved in the GaAs/AlGaAs samples. As we described at the end of chapter 5, some of the split-gated Hall bar samples exhibit an insulating transport behavior with a markedly reduced sheet carrier density and mobility after the cool-down. This high resistance state could solely be lifted by thermal recycling. These experimental findings constitute first indications of the affect of (re)chargeable defect states inside our gate stacking, influencing the 2D transport properties in this ternary alloy system.

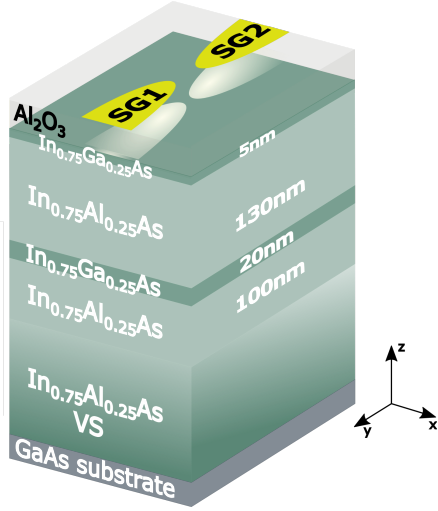


**Figure 6.12:** Layer sketch of the analysed  $\text{In}_{0.75}\text{Ga}_{0.25}\text{As}/\text{In}_{0.75}\text{Al}_{0.25}\text{As}$  heterostructure. The charge carriers are provided by the deep level antisite defect states inside the  $\text{In}_{0.75}\text{Al}_{0.25}\text{As}$  spacer layers, surrounding the  $\text{In}_{0.75}\text{Ga}_{0.25}\text{As}$  QW. The heterostructure is terminated with a  $5\text{nm}$   $\text{In}_{0.75}\text{Ga}_{0.25}\text{As}$  capping layer. As dielectric  $\text{Al}_2\text{O}_3$  is chosen with a layer thickness of  $20\text{nm}$  to separate the SG-electrodes (yellow) from the semiconducting layers.

Figure 6.13(a) shows an exemplary conductance curve of an  $\text{In}_{0.75}\text{Ga}_{0.25}\text{As}/\text{In}_{0.75}\text{Al}_{0.25}\text{As}$  QPC device in the non-illuminated state. The conductance  $G$  through the constriction is plotted in multiples of  $2e^2/h$  as a function of the symmetrically applied SG-voltage  $V_{SG1} = V_{SG2} \equiv V_{SG}$ . As for the GaAs/AlGaAs samples in the previous section 6.2, we obtain the characteristic pinch-off areas in the conductance curve of a SG-defined QPC: In area (I), the channel underneath the SG-electrodes is depleted, in area (II), we start to pinch-off the channel laterally, thus forming a 1D size-quantized conducting channel until the total pinch-off of the channel is reached at approximately  $V_{SG} = -1.15\text{V}$ . The inset in figure 6.13(a) presents a zoom into the conductance curve near depletion after subtracting a channel resistance of  $R_{ch} = 10k\Omega$ . We find no clear steps in  $G$  to be developed. Solely a weak modulation of the otherwise monotonous conductance indicates characteristic 1D transport features.

Figure 6.13(b) shows four subsequent conductance measurements of the same SG-structure as in (a). The odd-numbered curves depict the down-sweeps towards pinch-off, even-numbered curves present the corresponding up-sweep measurements back to  $V_{SG} = 0\text{V}$ . We find the individual up- and down-sweep curves to be perfectly congruent, with only a small shift of less than  $0.02\text{V}$  between the developed up- and down-sweep branches. In comparison to the studied GaAs/AlGaAs heterostructures, ballistic 1D conductance is severely hampered, which infers that the SG-induced electrostatic confinement potential is distinctly altered in the 2DEG. We assign this modification of the conductance to originate from charged impurities in the vicinity of the 1D channel, which act on the

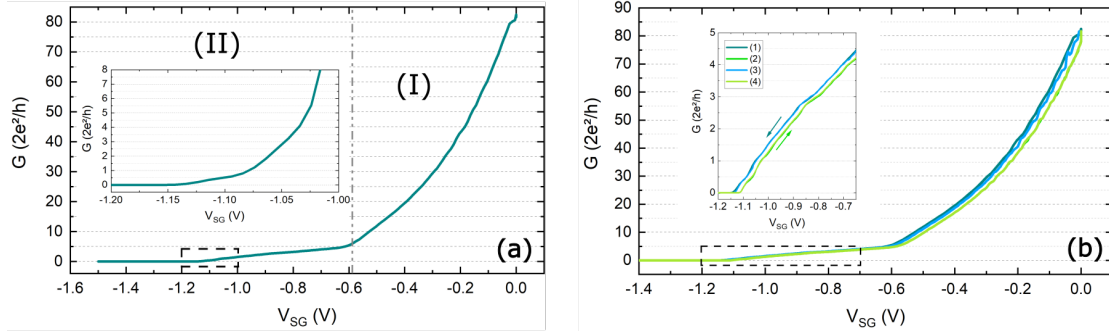


**Figure 6.13:** Conductance curves of sample C160428A1 (QPC4) in the non-illuminated state at  $T = 1.5K$ : (a)  $G$  as a function of  $V_{SG}$ , with (I) and (II) indicating the characteristic gating areas of the depletion curve of a QPC. The inset displays a zoom into the section, marked by the dashed rectangle, with  $R_{ch} = 10k\Omega$  being subtracted. (b) Four consecutive conductance curves of QPC4: odd numbers depict down-sweeps towards depletion of the QPC, even numbers show the corresponding up-sweeps. The inset presents a zoom into the marked area with  $R_{ch} = 2k\Omega$  taken into account.

confining potential of the constriction. Potential candidates are the doping providing InAlAs defect states since they are located in the direct proximity of the QW, as well as defect states at the  $\text{In}_{0.75}\text{Ga}_{0.25}\text{As}/\text{Al}_2\text{O}_3$  interface and inside the dielectric layer. We interpret the dependence of the conductance through the QPC on the SG-bias history, i.e. the small shift between up- and down-sweep branch, as a further indication of the influence of chargeable defect states in the system.

Figure 6.14 shows three conductance curves, which differ in the chosen final SG-voltage  $V_{SG}^{final}$  which we apply for pinch-off. Furthermore, two different dwell times at  $V_{SG}^{final}$  are employed. For the conductance measurement, where we choose  $V_{SG}^{final} = -1.3V$  (royal blue curve), we find the up- and down-sweep curves to be reasonably congruent. By choosing  $V_{SG}^{final} = -5V$ , which is far in the pinch-off of the QPC, we test the influence of the bias history on the conductance characteristics. For the cyan curve we apply no waiting time at  $V_{SG}^{final}$  before the up-sweep of  $V_{SG}$  is conducted. For the measurement presented by the yellow curve, we introduce a dwell time of  $10min$  in pinch-off at  $V_{SG}^{final}$ . We find the up- and down-sweep curves in both measurements with  $V_{SG}^{final} = -5V$  to exhibit a pronounced hysteric behavior, i.e. the pinch-off point  $V_p$  of the QPC shifts towards more negative  $V_{SG}$ -values for the up-swept curve. Furthermore, we find the hysteresis to scale with the dwell time in pinch-off at  $V_{SG}^{final} = -5V$ . A more negative  $V_p$  indicates an effectively more positive  $V_{SG}$  as compared to the down-swept curve. We understand this behavior as a migration of electrons, which were initially fixed in trap states underneath the SG-electrodes. When a sufficiently negative  $V_{SG}$  is applied these electrons are laterally transferred towards energetically more favourable states. Consequently, the confining potential of the 1D channel is altered.

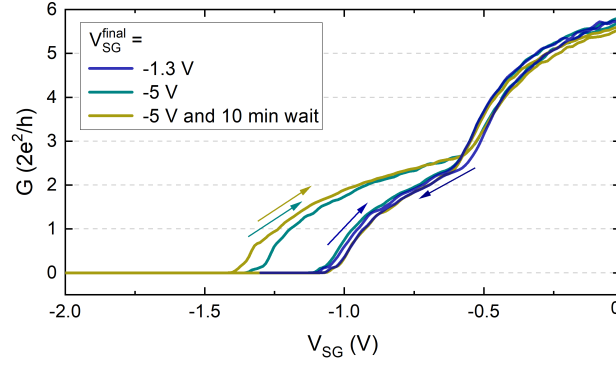


**Figure 6.14:** Three conductance curves (up- and down-sweep) of sample C160429A1 (QPC4) in the non-illuminated state at  $T = 1.5K$ : two different  $V_{SG}^{final}$  of  $-1.3V$  and  $-5V$  are applied with no dwell time in pinch-off. The yellow curve displays a conductance measurement with  $V_{SG}^{final} = -5V$  and an additionally applied dwell time of  $10min$  in pinch-off. The arrows indicate the sweep-direction.

In a next step, we study the 1D transport properties in the samples after illumination. The 1D transport study of GaAs/AlGaAs QPC structures showed that illumination generally increases the ballisticity in the electron system due to ameliorated screening properties of the 2DEG.

### Conductance quantization in the illuminated state (SG)

Figure 6.15(a) shows the conductance through the same QPC as studied above after illumination. As in the non-illuminated case, the conductance curve can be again divided into the two characteristic depletion regimes (I) and (II). The inset of figure 6.15(a) presents a zoom into the marked area near depletion, revealing at least three narrow but quite clear conductance steps near integer multiples of  $2e^2/h$  when we take a serial resistance of  $R_{ch} = 6.5k\Omega$  near pinch-off into account. Repeating the measurement for several times displays the reproducibility of the conductance characteristics. Figure 6.15(b) shows eight subsequent conductance measurements of the same sample as in (a): Odd numbers depict down-sweeps of  $V_{SG}$  towards the pinch-off of the QPC, even numbers show the corresponding up-swept curves. As can be seen more clearly in the inset of figure 6.15(b), which presents a zoom into the area near depletion, solely the first two conductance curves (1) and (2) slightly deviate from the following sweeps, for which the measured curves coalesce into a bundle. The difference in the gating responses of measurements (1) and (2) in comparison to all following measurements can be considered as an initialization process of the QPC, during which charge reconfigurations inside the 1D constriction take place. Apart from this, the depletion curves in figure 6.15(b) demonstrate a good reproducibility of the 1D transport characteristics in the QPCs. However, as in the non-illuminated state, we find a hysteresis between up- and down-sweeps to develop when

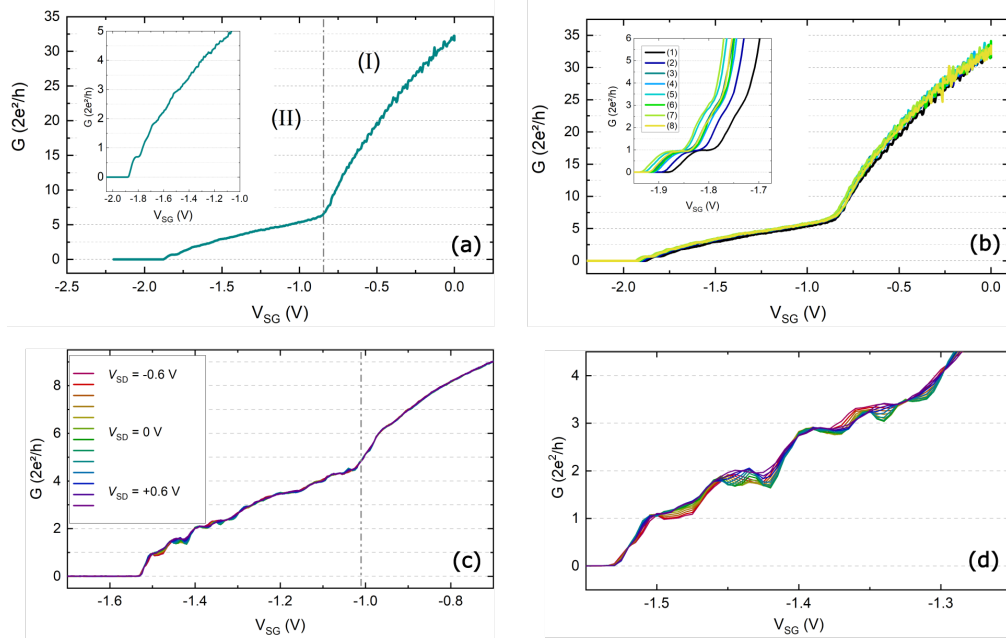


**Figure 6.15:** (a) and (b): Conductance of sample C160428A1 QPC4 in the illuminated state at  $T = 1.5K$ . For the insets, displaying a zoom into the area near depletion,  $R_{ch} = 6.5k\Omega$  is subtracted. Plot (a) shows the initial depletion curve after illumination with the characteristic depletion regimes (I) and (II). Plot (b) displays eight subsequent conductance curves: Odd numbers depict the down-sweeps, even numbers show the corresponding up-sweeps. (c) and (d): Conductance of sample C160316B4 QPC1 in the illuminated state at  $T = 370mK$  with  $R_{ch} = 1.7k\Omega$  subtracted. Plot (c) shows the conductance curves for several source-drain voltages  $V_{SD}$ , plot (d) presents a zoom into the area near pinch-off in (c).

a sufficiently negative  $V_{SG}^{final}$  and/or a longer dwell time in pinch-off are applied. By cooling the device down to  $T = 370mK$ , we gain further insight into the electric potential landscape in the QPC. Figure 6.15(c) shows several conductance measurements of a SG-defined QPC, whereby each curve is recorded for a different applied dc source-drain voltage  $V_{SD}$ <sup>4</sup>. Figure 6.15(d) presents a zoom into the conductance area near pinch-off. We find that the width and steepness of the conductance steps is increased as compared to the measurements at  $T = 1.5K$ . This indicates that the 1D subbands are more clearly separated, whereby mode-intermixing is efficiently reduced by the decreased temperature. Yet, the first steps exhibit a pronounced discontinuity in  $G$ , which is reproduced when the measurement is repeated. Oscillatory features arise on  $G$  when we sweep  $V_{SG}$ .

Conductance oscillations in the ballistic transport characteristics have been reported to

<sup>4</sup> $V_{SD}^{total} = V_{SD}^{dc} + V_{SD}^{ac}$  with  $V_{SD}^{ac} = 50\mu V$  and variable  $V_{SD}^{dc} \equiv V_{SD}$



arise as a quantum interference pattern due to random potential disorder [144, 145, 148–150]. As a second effect, the electric field of charged impurities, located in the SG-defined channel area, may alter the saddle potential in such a way that local potential minima are created, through which tunneling at a certain energy takes place. This resonant tunneling process introduces a particular energy-dependence in the reflection and transmission coefficients as is visualized by the  $V_{SD}$ -dependence of the measured conductance in the analysed QPC. These features, i.e. quantum interference and resonant tunneling, are most pronounced at very low temperatures, since higher temperatures blur the fine structures of  $G$  due to energy averaging. Moreover, at elevated temperatures, e.g. at  $T = 1.5K$  in our transport study, a reduction of the phase coherence length can lead to an annihilation of these quantum interference patterns [144, 145]. Yakimenko et al. [145] studied the effect of randomly distributed impurities in a modulation doped GaAs/AlGaAs heterostructure on the conductance through a QPC on the basis of numerical calculations. They found the conductance modulation to be most pronounced when the separation between the 2DEG and the ionized impurities is less than  $50nm$ . Additionally, the fine structure in the simulated conductance was washed out with increasing 2DEG depth. We can relate our experimental results to the findings of Yakimenko et al.: In our heterostructures, we lack the presence of a deliberately introduced modulation doping layer. The intrinsic InAlAs defect states, being - most likely - evenly distributed inside the InAlAs spacer layers, provide the charge carriers in our system. Due to the direct proximity of the InAlAs defect states to the QPCs, we hypothesize that the electrostatic influence on 1D transport is quite strong, thus creating conductance modulations. Furthermore, remote surface charge, interface roughness, fabrication imperfections of the SG-layout, as well as ternary alloy disorder additionally introduces a texturing of the SG-defined potential in the 2DEG. Applying an offset voltage to the arms of the SG-electrodes shifts the QPC laterally in space. We find the oscillatory conductance modulations to depend perceivably on the offset bias. We assign this behavior to a spatial shift of the QPC in the 2DEG plane whereby the electrostatic environment of the 1D constriction - and thus the ballisticity of the channel - is consequently altered. Illustrative measurements of asymmetric biasing are shown in chapter 8.

**Conclusion** Recapitulating, we find first clear characteristics of conductance quantization near integer values of  $2e^2/h$  in the InGaAs/InAlAs heterostructures after illumination. However, the conductance steps are much less pronounced as compared to GaAs/AlGaAs samples, which are equipped with the same pair of parabolic finger-gate electrodes. Measurements conducted at  $T = 370mK$  reveal the influence of an inherent disorder potential on the conductance quantization in form of oscillations in  $G$ , which are smeared out at higher temperature. Besides, intrinsic defect states affect the 1D transport properties, manifesting itself in form of a hysteresis between the depletion and opening of the channel. The strength of the hysteresis further depends on the applied  $V_{SG}^{final}$ , as well as on the dwell time in pinch-off.

In a next step, we attempt to improve the ballisticity in the 1D channel by a modification



of the finger-gate layout, which is supposed to suppress adverse electrostatic effects of impurities on the 1D confinement potential.

#### 6.3.2 1D transport in TrG-defined QPCs

In order to facilitate ballistic transport in the QPC devices, we introduce an additional gate electrode, the *center-gate* (CG), in our finger-gate layout. The CG-electrode is inserted in-between the two SG-electrodes SG1 and SG2 as is shown in figure 6.16. Such a gate arrangement has been used in the literature under the aspect of analysing Fabry-Pérot interferences, which can be generated in a QPC that is tuned to act as a resonator [151]. In our 1D transport study, the CG constitutes a further tuning knob for the modification of the electrostatic confining potential [8].

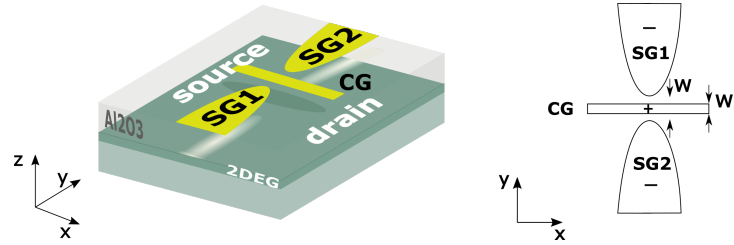


**Figure 6.16:** Sketch of the triple-gate layout for improving the electrostatic potential, defining the QPC. The width of the additionally introduced CG is  $w_c = 200nm$ , the SG tip-to-tip distance  $w$  is determined as  $\approx 350nm$ .

The right sketch in figure 6.16 displays the characteristic lengths of the individual building blocks of the device, i.e. the CG-electrode and the SG-electrodes, which we will term as triple-gated (TrG) QPC in the remainder of this thesis. The tip-to-tip distance  $w$  between the two SG-electrodes SG1 and SG2 is approximately  $350nm$ . The CG-electrode, having a width  $w_c = 200nm$ , is inserted symmetrically in the SG-electrode slit. The CG and the SG-electrodes are fabricated in the same ESL step to circumvent adverse effects due to misalignment in the lithographic process.

To improve ballisticity, we apply a positive voltage at the CG-electrode, which leads to a narrowing and deepening of the confinement potential in  $y$ -direction. Thereby, the 1D subband spacing is increased and detrimental influence of background disorder potentials should be reduced [8, 144, 152, 153]. Zagoskin et al. [153] showed that by increasing the 1D subband spacing, the density of quasi-bound states inside the constriction can be exponentially decreased.

#### Conductance quantization in the illuminated state (TrG)

Figure 6.17(a) shows the conductance  $G$  through a TrG-defined QPC as function of  $V_{SG}$  in the illuminated state. A constant CG-voltage of  $V_{CG} = 0V$  is chosen, whereby  $V_{SG1}$  and  $V_{SG2}$  are symmetrically swept. Even for  $V_{CG} = 0V$ , we find that the additional

## 6 Realization of conductance quantization in InGaAs/InAlAs

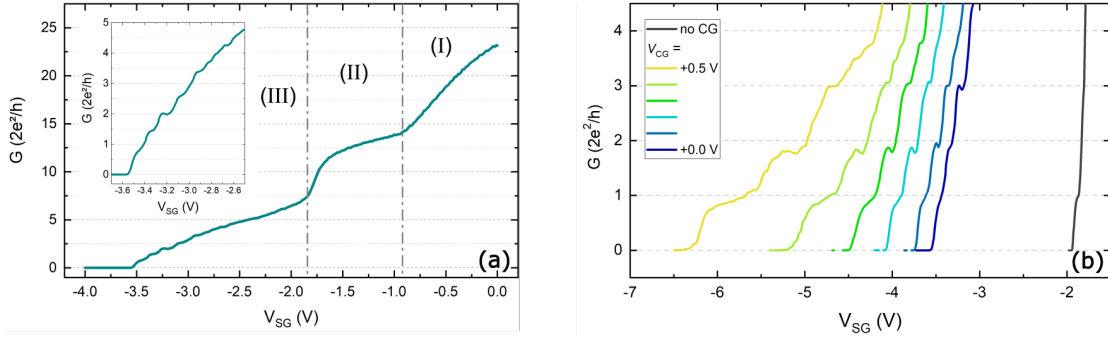


**Figure 6.17:** Conductance through a TrG-defined constriction (sample C160428A1 TrG1) at  $T = 1.5K$  in the illuminated state: **(a)**  $G$  as a function of  $V_{SG}$  for  $V_{CG} = 0V$ , exhibiting three distinct gating areas (I), (II) and (III). The inset presents a zoom into the depletion area with  $R_{ch} = 1k\Omega$  being subtracted. **(b)** Depletion curves for several  $V_{CG}$ , increasing from  $0V$  to  $+0.5V$  in  $0.1V$ -steps with a suitable  $R_{ch}$  subtracted. For comparison the conductance of a split-gated QPC (no CG) of the same sample is plotted (grey curve).

CG-electrode clearly modifies the conductance through the constriction as compared to SG-defined QPCs. As depicted in the graph, the depletion curve of the TrG-defined QPC exhibits three distinguishable gating areas (I), (II) and (III). Whereas the areas (I) and (III) resemble the determined characteristic SG-induced depletion regimes, area (II) is newly developed in this triple-gated device. In area (II), a further decrease of  $V_{SG}$  hardly changes the conductance through the constriction. Whereas in (I), the 2DEG area underneath the SG-electrodes gets depleted, we relate the response of  $G$  in this second  $V_{SG}$ -area to the energetical lifting of the semiconductor band structure underneath the positively biased CG. This requires a more negative SG-voltage in contrast to the purely SG-defined QPCs. Yet, the reduced slope of the conductance curve in area (II) compared to area (I) indicates a difference in the electrostatic situation in the area underneath the SG-electrodes and the CG-electrode. In area (III), the channel is then laterally depleted. The inset of figure 6.17(a) displays a zoom into the conductance curve near depletion. Several clear conductance steps near integer multiples of  $2e^2/h$  arise. This clearly demonstrates the improvement of ballistic 1D conductance in triple-gated samples - even in the zero-biased case - compared to SG-defined QPCs. In a next step,  $V_{CG}$  is stepwise increased, whereby we enhance the curvature  $\omega_y$  of the confining potential in  $y$ -direction. Figure 6.17(b) shows  $G$  as a function of  $V_{SG}$  for various CG-voltages.  $V_{CG}$  increases from the right from  $V_{CG} = 0V$  (dark blue curve) to  $V_{CG} = +0.5V$  (yellow curve) in  $0.1V$ -steps. For each SG-sweep,  $V_{CG}$  is held constant and a suitable serial resistance  $R_{ch}$  is subtracted to fit the first plateau to  $2e^2/h$ . We find that  $R_{ch}$  decreases with increasing  $V_{CG}$ . The rightmost grey curve displays the conductance of a SG-defined constriction on the same sample. For better comparison, this curve is horizontally shifted by  $-1.5V$ . For small values of  $V_{CG}$ , i.e.  $V_{CG} < +0.2V$ , the CG does not significantly improve the conductance quantization as compared to the SG-defined QPC. Further increasing

$V_{CG}$  leads to well-defined and more widened conductance plateaus, demonstrating the beneficial effect of the positively biased CG for realizing ballistic transport. As intended with this gate layout, an increased 1D subband spacing is created by the steepened channel potential with  $V_{CG} > 0V$ . Furthermore, we observe the pinch-off voltage  $V_p$  to shift into the negative  $V_{SG}$ -direction the higher  $V_{CG}$  is chosen. This is a consequence of the positive applied CG-voltage, which has to be compensated by a more negative SG-voltage in order to deplete the channel [8].

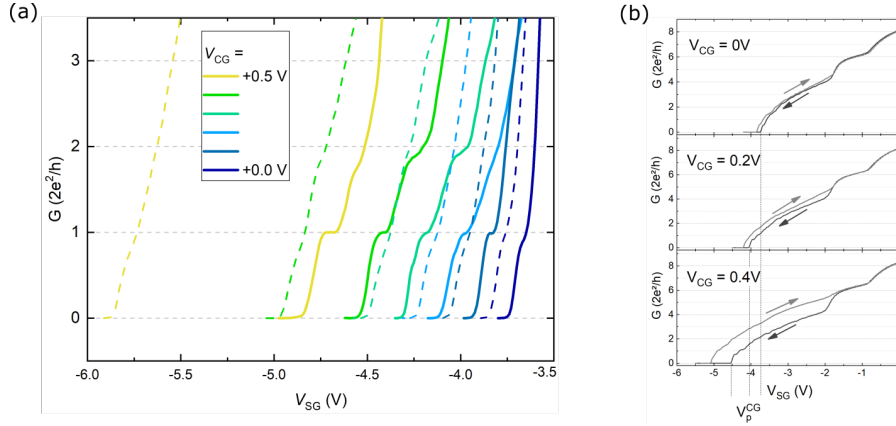


**Figure 6.18:** Sample C160429A1 TrG1 at  $T = 1.5K$  in the illuminated state: **(a)**  $G$  as function of  $V_{SG}$  of several down-sweeps (solid line) with the subsequent up-sweeps (dashed line) for different  $V_{CG}$ , increasing from  $0V$  to  $+0.5V$  in  $0.1V$ -steps with  $R_{ch} = 1.5k\Omega$  subtracted. **(b)** Evolution of hysteresis with  $V_{CG}$ .

So far, we have only discussed depletion curves, i.e. the down-sweeps of  $V_{SG}$  towards the pinch-off of the TrG devices. Figure 6.18(a) depicts several depletion curves (solid lines) together with the subsequent up-sweep conductance curves (dashed lines) for various  $V_{CG}$ . We find that the pinch-off points  $V_p$  of all up-sweep conductance curves are shifted towards more negative values of  $V_{SG}$ , denoting that the channel conductance is recovered at a more negative SG-voltages than for the preceding down-sweep. The shift of  $V_p$  scales with the applied  $V_{CG}$ : The more positive  $V_{CG}$  is chosen, the larger the shift of  $V_p$  into the negative  $V_{SG}$ -direction. This is illustrated in figure 6.18(b), where the total conductance curves (up- and down-sweep) for three different  $V_{CG}$ , i.e.  $V_{CG} = 0V$ ,  $+0.2V$  and  $+0.4V$ , of the measurements in (a) are depicted. The arrows indicate the sweep direction of  $V_{SG}$ . The hysteresis is enlarged the more positive the applied CG-voltage is chosen. Most significantly, the ballistic conductance is severely deteriorated when the channel is reopened again. Quantized conductance steps, which are developed in the down-sweep, have vanished in the subsequent up-sweep. This is most prominently illustrated by the opening curve of the QPC with  $V_{CG} = +0.5V$  in figure 6.18(a), where the up-sweep exhibits a rather linear response of  $G$  to an increase in  $V_{SG}$ .

This hysteretic behavior of the 1D conductance in triple-gated devices will be discussed in detail in the following, where we analyse the transport in our TrG devices in the non-illuminated state.

### Conductance quantization in the non-illuminated state (TrG)

In this subsection, we investigate the transport characteristics of triple-gated QPCs in the non-illuminated state. The experimental analysis of the electrostatic stability of the devices is further extended.

For all measurements shown in the following subsection a sweep rate of  $20\text{mV/s}$  and a small dc contribution of  $V_{SD} = 0.5\text{mV}$  to the source-drain voltage is chosen unless otherwise noted.

**Initialization of the QPC** Figure 6.19 shows several conductance curves in the non-illuminated state of the same sample (C160429A1 TrG1), which we analysed in the preceding subsection.  $V_{CG}$  is kept constant at  $+1\text{V}$  during the measurements. The sample is cooled down from RT to  $T = 1.5\text{K}$  with all ohmic contacts set to the laboratory ground potential and the TrG-electrodes held constant at a voltage of  $0\text{V}$ .

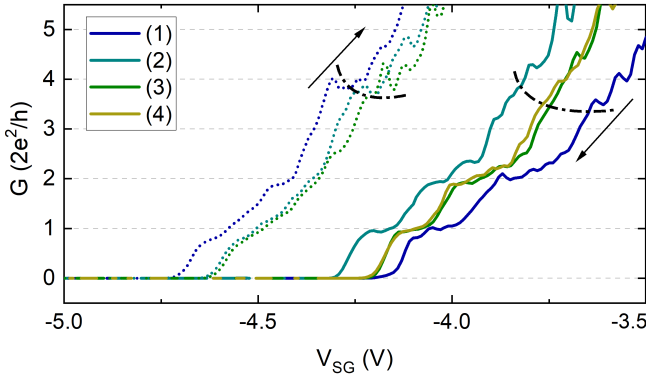


**Figure 6.19:** Conductance curves of sample C160429A1 TrG1 at  $T = 1.5\text{K}$  with  $V_{CG} = +1\text{V}$  after a zero-biased cool-down ( $V_{CD} = 0\text{V}$ ) in the non-illuminated state: Four consecutive down-sweeps (solid curves) with the corresponding up-sweeps (dotted lines), enumerated chronologically. A serial resistance of  $R_{ch} = 5\text{k}\Omega$  is taken into account.

The down-sweep measurements (solid lines) and the corresponding up-sweep curves (dotted lines) are color-coded and numbered chronologically. As for the illuminated case, we find the first two measurements (1) and (2) to deviate from all subsequent conductance curves. For clarity, solely two consecutive measurements, i.e. (3) and (4), are displayed. Subtracting a serial resistance of  $R_{ch} = 5\text{k}\Omega$  matches the first two conductance steps very well to  $2e^2/h$  and  $4e^2/h$ . For the up-swept curves, however, the plateaus are less pronounced and narrowed in width as compared to the preceding depletion curves. This hints towards a decreased subband spacing, which we assign to a less sharp confining potential in  $y$ -direction due to a blurring of the electric potential by partially deionized InAlAs defect states. As we also observed in the illuminated measurements, a hysteresis develops between the depletion and the opening conductance curves of the QPC.

This hysteretic behavior is now investigated in the following.

**Electronic stability in the non-illuminated state** For the measurements shown in this paragraph a CG-voltage of  $V_{CG} = +1\text{V}$  is chosen. Since we focus here on the full-range conductance of the devices, no channel resistance  $R_{ch}$  is subtracted in

the calculation of the conductance  $G^5$ . All measurements shown in the following are conducted after an initialization of the QPC, i.e. a repeated depletion and opening of the QPC until the curves of the up- and down-sweep branches are congruent.

We first examine the dependence of the hysteresis on the employed  $V_{SG}^{final}$ . Figure 6.20(a) displays three conductance curves for different applied  $V_{SG}^{final}$ . The depletion of the channel by sweeping  $V_{SG}$  into negative direction is immediately followed by an up-sweep of  $V_{SG}$ . The arrows indicate the corresponding sweep directions.

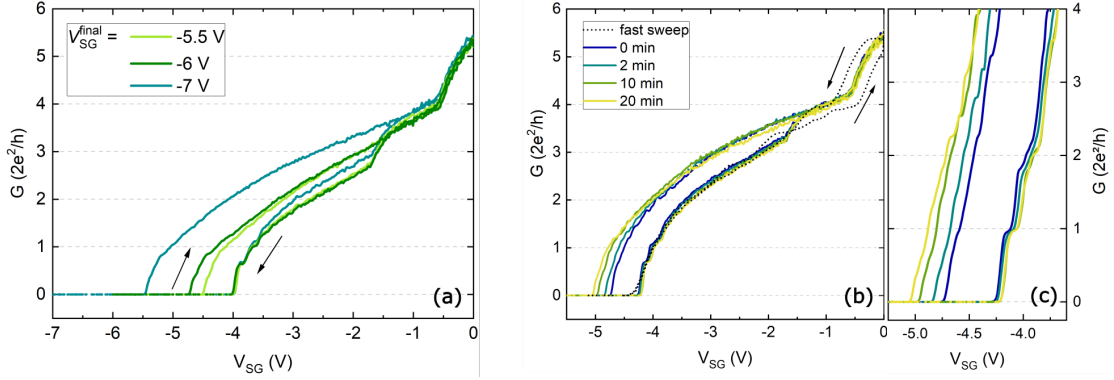


**Figure 6.20:** Conductance curves of sample C160429A1 TrG1 at  $T = 1.5K$  in the non-illuminated state for  $V_{CG} = +1V$  with no  $R_{ch}$  subtracted: (a)  $G$  as function  $V_{SG}$  for different  $V_{SG}^{final}$  of  $-5.5V$ ,  $-6V$  and  $-7V$ , color-coded. (b)  $G$  as function  $V_{SG}$  for different dwell times at  $V_{SG}^{final} = -5.5V$ . The dotted curve shows a measurement with a sweep-rate of  $200mV/s$  for which no dwell time is applied at  $V_{SG}^{final}$ . (c) Zoom into the pinch-off area of the conductance measurements in (b).

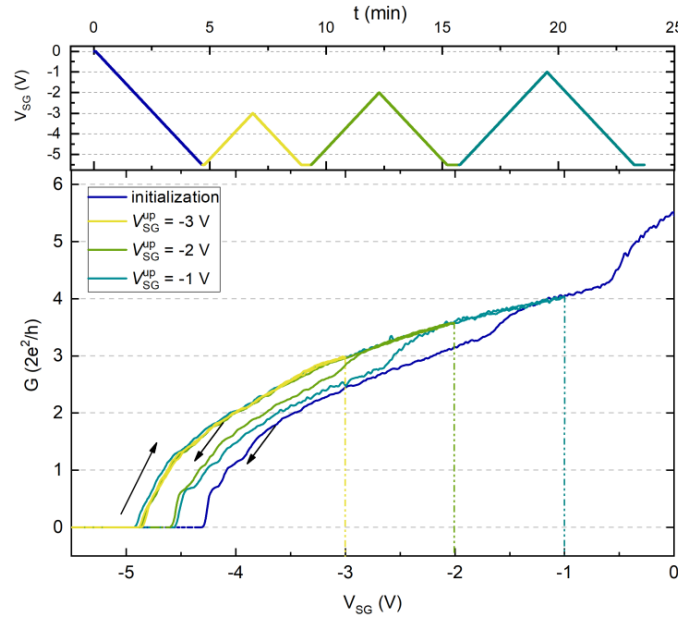
As we observed in the measurements with the split-gated samples, the hysteresis in the triple-gated devices increases the more negative we choose  $V_{SG}^{final}$ . The shift of  $V_p$  into negative  $V_{SG}$ -direction is accompanied by an obscuring of the conductance steps. This indicates enhanced charge reconfiguration between the depletion and the opening process of the QPC, which is clearly linked to the strength of the gate-induced band bending.

Figure 6.20(b) depicts five pairs of down- and upwards sweeps for which we choose  $V_{SG}^{final} = -5.5V$ . We vary the dwell time, whereby we unveil a distinct time-dependence of the band bending-induced charge transfer processes inside the heterostructure. This yields further information on the energy states towards which the electrons inside the heterostructure are transferred to. The dwell time increases from  $0min$  (blue curve) up to  $20min$  (yellow curve). Additionally, the dotted curve displays a measurement, for which we increase the sweep rate to  $200mV/s$  and apply no dwell time at the chosen  $V_{SG}^{final}$ . Figure 6.20(c) presents a zoom into the area near pinch-off. We determine the magnitude

<sup>5</sup>We generally find that the 2D channel resistance  $R_{ch}$  strongly depends on  $V_{SG}$  and thus on the width of the QPC constriction.

of the hysteresis to be clearly linked to the time the band profile is held in a tilted state: Whereas there is almost no deviation between up- and down-sweep in the case of the high sweep-rate of  $200\text{mV/s}$ , we find the pinch-off point  $V_p$  to be continuously shifted towards more negative voltages the longer the dwell time is chosen. Even after a waiting time of  $20\text{min}$ ,  $V_p$  still shifts continuously with a rather long time constant into negative direction. This reveals that the charge migration processes towards an energetically equilibrated situation exhibits a rather small transfer rate.

For all preceding measurements, the QPC channels are pinched off and we subsequently sweep  $V_{SG}$  back to  $0\text{V}$ . This constitutes a reset of the charge transfer in the vicinity of the QPC in depletion mode.  $V_{SG} = 0\text{V}$  has proven to be sufficiently high enough to completely restore the charge reconfiguration of the QPC after the first initialization sweeps.



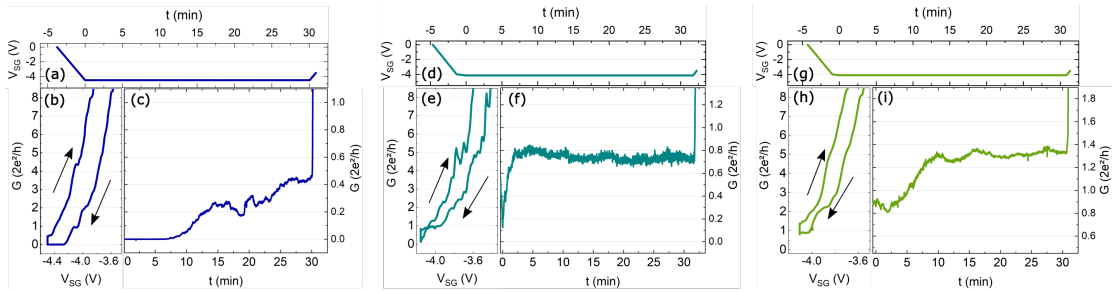
**Figure 6.21:** Sample C160429A1 TrG1 at  $T = 1.5\text{K}$  in the non-illuminated state for  $V_{CG} = +1\text{V}$  with no  $R_{ch}$  subtracted,  $V_{CD} = 0\text{V}$ : Upper panel shows  $V_{SG}$  as function of time  $t$ , lower panel displays the conductance  $G$  as function of  $V_{SG}$  for different  $V_{SG}^{up}$ . The arrows indicate the sweep direction of  $V_{SG}$ .

In a next experiment, we aim to determine the SG-voltage, which we have to apply in the opening process of the QPC in order to restore the electrostatic situation of the preceding down-sweep, which presents a reset of the device. Thus, after depleting the QPC channel,  $V_{SG}^{up}$  is subsequently increased until the following down-sweep is congruent to the initial depletion curve. The upper panel in figure 6.21 is a plot of  $V_{SG}$  over time, while  $V_{CG}$  is held constant at  $+1\text{V}$ . Firstly, the 1D channel is fully depleted, whereby a  $V_{SG}^{final}$  of  $-5.5\text{V}$  is chosen (dark blue curve). The channel is then partially re-opened up to a SG-voltage of  $V_{SG}^{up}$ , followed by an immediate down-sweep back to  $V_{SG} = -5.5\text{V}$ .  $V_{SG}^{up}$  is stepwise



increased from  $-3V$  (yellow curve), to  $-2V$  (green curve) and finally to  $-1V$  (cyan curve). The resulting conductance through the QPC with respect to  $V_{SG}$  is shown in the panel below. The arrows indicate the corresponding sweep direction of  $V_{SG}$ , the vertical dashed lines mark the turning points of the up-sweep back to  $V_{SG} = -5.5V$ . The measurements demonstrate that the wider the QPC constriction is re-opened, i.e. the more positive  $V_{SG}^{up}$  is chosen, the more the subsequent down-sweep approaches the initial conductance curve (dark blue line). We find that for a complete restoration of the initial depletion curve, the QPC has to be driven into the characteristic gating area (I) (see figure 6.17(a)). This behavior evidences a constant redistribution of charge carriers underneath the finger-gate electrodes as long as the applied SG-voltage is changed. Thus, for a triple-gated QPC with  $V_{CG} > 0V$  a total reset requires an increase of  $V_{SG}$  of several volts. Such a 1D transport property is adverse and impractical for the implementation of the QPC in more complex device applications.

In addition, the time stability of  $G$  in the gating area before pinch-off presents an important property for later QPC applications. In a next experiment, we thus test the time stability of the conductance in a triple-gated QPC. Therefore, three strategic measuring points on the conductance curve are chosen.



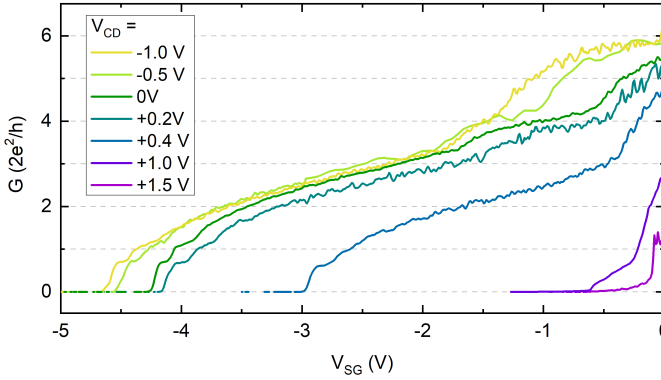
**Figure 6.22:** Time stability of sample C160429A1 TrG1 at  $T = 1.5K$  in the non-illuminated state for  $V_{CG} = +1V$  with  $R_{ch} = 6k\Omega$  subtracted,  $V_{CD} = 0V$ : The measuring points are chosen at (a) - (c):  $V_{SG} = -4.5V$  in pinch-off, (d) - (f):  $V_{SG} \approx -4.16V$  on the slope to the first conductance step, (g) - (i):  $V_{SG} \approx -4.1V$  in the first conductance step. A dwell time of  $30min$  is applied at each measuring point. Figure (a), (d) and (g) display  $V_{SG}$  as function of time  $t$ ; (b), (e) and (h) show  $G$  as a function of  $V_{SG}$ ; (c), (f) and (i) show  $G$  as a function of  $t$ . Between the individual measurement sets,  $V_{SG}$  is swept back to  $0V$ .

Figure 6.22 shows three sets of measurements, each displaying an experiment, in which the 1D channel is depleted up to a specifically chosen conductance value of  $G$ , where a dwell time of about  $30min$  is applied before the subsequent up-sweep is conducted. The first measurement set (figures 6.22(a) to (c)) presents the situation, in which the QPC is completely pinched off. A  $V_{SG}^{final}$  of  $-4.5V$  is chosen, which is only slightly smaller than the determined  $V_p \approx -4.27V$ . During the dwell time in pinch-off, we find that the channel becomes conducting again, whereby  $G$  increases continuously with time.

Thereby, a distinct hysteresis develops. Figures 6.22(d) to (f) display the situation in which the measuring point is positioned on the slope of the first conductance step at about  $0.13 \cdot 2e^2/h$ . For the set shown in (g) to (i) the measuring point is positioned at the first conductance plateau at  $2e^2/h$ . In both measurements,  $G$  increases steeply during the first period of the applied dwell time and then starts to saturate. Correspondingly, a hysteresis between up- and down-sweep is recorded. Hence, we conclude that the equilibrated situation to which the system evolves when it is subjected to band tilting clearly depends on the applied finger-gate voltage.

Our investigation of a single conductance curve over time demonstrates a severe conductance instability of the QPC transport properties. For the chosen measuring points, we find adverse charge transfer inside the heterostructure to take place as a function of dwell time. This leads to a degraded formation of the formerly well-defined conductance steps. Thus, to attain constant conductance near channel depletion, the system requires a gate-dependent relaxation time towards a  $V_{SG}$ -dependent energy equilibrium.

**Biased cool-down** We further visualize the presence of chargeable defect sites inside the heterostructure by a series of biased cool-down measurements. Therein, we systematically vary the cool-down voltage  $V_{CD}$  which we apply at the finger-gate electrodes during the cool-down of the sample from RT to cryogenic temperatures<sup>6</sup>. After the cool-down to  $T = 1.5K$ ,  $V_{SG}$  is then set to 0V and  $V_{CG}$  to +1V. Figure 6.23 displays a series of conductance measurements, each curve recorded for a different  $V_{CD}$  in the bias-range of  $-1.0V$  to  $+1.5V$  after the QPC has been initialized. For all applied  $V_{CD}$  the depletion curves are reproduced in several cool-downs (not shown here). No channel resistance is subtracted, as the full depletion curves are analysed.



**Figure 6.23:** Conductance of sample C160429A1 TrG1 at  $T = 1.5K$  in the non-illuminated state for  $V_{CG} = +1V$  with no  $R_{ch}$  subtracted. Various cool-down voltages  $V_{CD}$  in the range between  $-1.0V$  and  $+1.5V$  are applied at the CG and SG-electrodes during the cool-down from RT to  $T = 1.5K$ .

We find  $V_p$  as well as the number and texture of the conductance steps to substantially differ from each other. The higher  $V_{CD}$  is chosen, the lower the conductance at  $V_{SG} = 0V$  at the beginning of each measurement. Furthermore, the conductance steps become less well-defined at higher  $V_{CD}$ . For large positive  $V_{CD}$  as, e.g.  $V_{CD} > +1.0V$ , we determine a complete extinction of the 1D transport features. Thus, we conclude that a positive

<sup>6</sup>For samples, being illuminated after the cool-down, the bias status during the cool-down has no influence on subsequent transport measurements.



cool-down activates detrimental charge transfer inside the heterostructure at RT. This charge configuration is then frozen out at  $T = 1.5K$ . Consequently, we determine an effectively more negative bias situation of the SG-electrodes, which shifts the pinch-off point towards less negative SG-voltages.  $V_{CD} < 0V$  does not present itself to be evidently beneficial as compared to a zero-biased cool-down. However, no detrimental charge transfer at RT is thereby triggered.

We deduce that the application of a positive  $V_{CD}$  leads to significant adverse effects on the ballisticity in the 1D channel due to the transfer of electrons towards the heterostructure interface.

## 6.4 Conclusion and discussion

In the study of 1D transport in InGaAs/InAlAs-based heterostructures, we systematically analysed the electric transport characteristics of SG- and TrG-defined QPCs in the illuminated and non-illuminated state.

For split-gated devices we solely observe conductance quantization near  $2e^2/h$  at  $T = 1.5K$  after illumination of the sample. The number of well-resolved plateaus increases when the sample is cooled down to  $T = 370mK$ . Measurements at such low temperatures reveal reproducible and energy-dependent conductance oscillations. This clearly demonstrates the influence of adverse electric disorder potentials, acting on the confining potential of the QPC. We attribute this disorder potential to the presence of remote ionized impurities in the vicinity of the 1D constriction.

In order to facilitate ballistic transport in the QPC, we introduce an additional CG in-between the two SG-electrodes as a further tuning knob of the electrostatic potential in the 1D channel. Thereby, we are able to demonstrate improved ballisticity as we observe well-defined conductance plateaus at integer multiples of  $2e^2/h$  in the illuminated, as well as in the non-illuminated state.

Furthermore, we fabricated several QPC samples with an additional global TG, attached above the finger-gate electrodes to tune the electron density and thus the screening ability of the 2D system, whereby the conductance should be altered. However, we found that increasing the 2DEG electron density by applying a positive TG-voltage had no positive effect on the 1D transport characteristics in our devices. Furthermore, for a fixed  $V_{CG}$  and  $V_{SG}$ , no 1D conductance features developed when we recorded  $G$  as a function of  $V_{TG}$  (not shown here). Applying a small perpendicular magnetic field to the samples during a conductance measurement did not prove to be beneficial for conductance quantization in the system. This is in contrast to several experimental findings in literature [2, 5, 144, 145, 150] for which a small B-field normal to the sample plane generally leads to reduced backscattering, thereby facilitating ballistic conductance.

In a systematic series of measurements, we test the electric stability and reproducibility of the performance of the QPC devices. We find the conductance characteristics of our studied QPCs to significantly depend upon the bias history: Clear 1D conductance features that we observe when the QPC is pinched off are blurred or completely vanish in

a subsequent up-sweep of  $V_{SG}$ . Additionally, a hysteresis develops between the depletion and opening conductance curves of the QPC. This shift of the pinch-off point  $V_p$  is then further analysed. We find a distinct time- and voltage-dependence of the magnitude of the hysteresis: To summarize,  $V_p$  is a function of  $V_{CG}$ ,  $V_{CD}$ ,  $V_{SG}^{final}$ , as well as of the dwell time in pinch-off and of the chosen sweep-rate of  $V_{SG}$ .

We conclude that by sweeping  $V_{SG}$  into negative direction, whereby we tilt the band structure of the system, we drive the heterostructure out of an energetically equilibrated situation. This introduces a  $V_{SG}$ -dependent transfer rate of parasitic, trapped charge carriers inside the layer system, constantly modifying the electrostatic confinement potential in the QPC devices. This conclusion is further supported by probing the time stability of the conductance at different strategic measuring points on the depletion curve, where we find  $G$  to distinctly vary over time when the measuring points are chosen near or in pinch-off. Owing to the dependence on the bias history and the instability of the conductance over time, we were not able to record the transconductance of our 1D channel as a function of  $V_{SD}$  and  $V_{SG}$ , by means of which a meaningful evaluation of the 1D subband spacing could be conducted and further information on the confining potential could be gained. Our experimental findings resemble the results of a study by Koester et al. [18] on the 1D transport behavior of SG-defined QPCs in an InAs/AlSb QW. Therein, impurities inside the MBE-grown heterostructure, as well as surface states at the GaSb capping layer, which provide the charge carriers in this material system [154], are identified to give rise to similar 1D conductance instabilities as we observe in our devices. We want to point out that our non-intentionally doped InGaAs/InAlAs heterostructures with  $\text{Al}_2\text{O}_3$  as dielectric offers several defect states as source for the observed instabilities: Defect states inside the InAlAs spacer layers [37, 39], as well as a variety of surface states at the InGaAs interface [14, 136, 155–158], together with energy states inside the dielectric [159–162] are likely to play a major role in the gating ability of this material system. Furthermore, other parameters, such as for example the finite curvature of the tip of the SG-electrodes and fabrication-related gate-edge roughness, are likely to affect the transport behavior in our devices besides the non-uniform impurity potential.

We thus dedicate the next chapter to a comprehensive understanding of the gating response of the analysed heterostructures. On the basis of top-gated Hall bar samples, we study the role of the above-mentioned defect states under gate operation. A holistic charge transfer picture is then established, which is able to elucidate the experimental findings of this chapter. On the basis of the newly gained understanding of the material system, we identify an active layer design with which robust 1D conductance is then realized (therefore see chapter 8).

## Gating response of various III-V heterostructures

In the last chapter, we studied the 1D transport in SG- and TrG-defined QPCs in  $\text{In}_{0.75}\text{Ga}_{0.25}\text{As}/\text{In}_{0.75}\text{Al}_{0.25}\text{As}$  systems. In a series of measurements, we investigated the electric stability and quality of the ballistic 1D conductance in our devices. Therein, we determined that the conductance in split-gated QPC devices was severely affected by impurity-related Coulombic disorder potentials, acting on the confining potential. This led to obscured conductance quantization at a measurement temperature of  $T = 1.5\text{K}$ . Decreasing the temperature to  $T = 370\text{mK}$  gave rise to the generation of localized energy states inside the 1D channel, provoking energy-dependent conductance oscillations. By introducing an additional CG in between the SG-electrodes which provides the possibility of tuning the confining potential in the QPC, we were able to realize clear conductance quantization steps even at a temperature of  $T = 1.5\text{K}$ . Yet, all TrG devices exhibited a markedly hysteretic behavior under the application of a positive CG-voltage in order to facilitate ballistic conductance in the channel. Building on the experimental results of the 1D transport study, we assigned the hysteresis to charge migration processes in the heterostructures, provoked by the large voltage difference applied between the CG-electrode and the SG-electrodes. We inferred that the ballisticity in the QPC devices is substantially deteriorated owing to the reallocated charge carriers and the thereby modified confining potential in the 1D channel.

The following chapter serves to gain deeper insight into the materials-related origins of the electrostatic response of the InGaAs/InAlAs-based systems. To this end, we systematically evaluate the field-effect tunability of the 2D transport properties in these heterostructures.

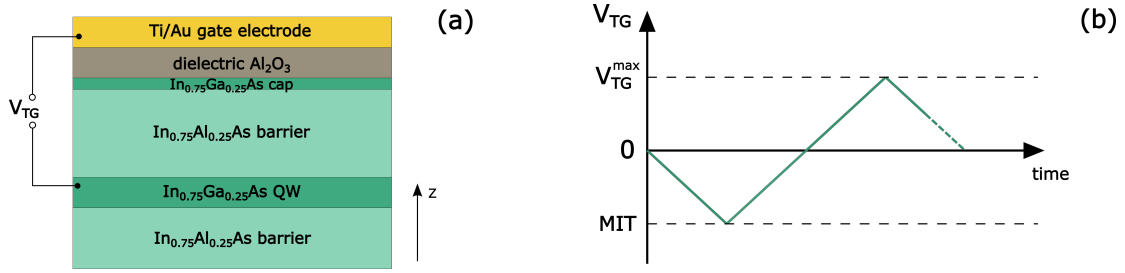


**Figure 7.1:** (a) Schematic sketch of the analysed gate stacking. (b) Applied TG-voltage  $V_{TG}$  as a function of time during a MT measurement sequence.  $V_{TG}^{max}$  marks the maximum applied TG-voltage,  $MIT$  indicates the minimum applied TG-voltage before the resistivity of the sample is significantly increased owing to the onset of an apparent metal-to-insulator transition, impeding a meaningful MT measurement in this  $V_{TG}$ -range.

### 7.1 Sample fabrication and MT measurement sequence

In order to analyse the observed charge migration processes in our heterostructures, we employ a more controllable system than an electrostatically defined QPC: a top-gated Hall bar. From the gate dependency of the 2D transport characteristics, i.e. the 2D electron density and mobility, of the Hall bar device, we aim to deduce information on the participating defect states in the system under gate operation. As described in subsection 2.1.3, we classically expect the electron density of the QW to scale linearly with the applied TG-voltage  $V_{TG}$ . From deviations of the textbook-like behavior, we gain access to the spatial location and dynamics of participating defect states.

We start the 2D transport analysis with the same heterostructure that we used in the preceding 1D transport study of our QPC devices. The corresponding gate stacking is depicted in figure 7.1(a). To insulate the metal gate electrode from the semiconducting layers and to passivate the In<sub>0.75</sub>Ga<sub>0.25</sub>As cap surface layer, we deposit Al<sub>2</sub>O<sub>3</sub> as dielectric material via atomic layer deposition (ALD) on top of the MBE-grown heterostructure. This deposition process is often referred to as *self-cleaning* since during the first cycles of ALD the native III-V oxides are largely eliminated, in particular, the Fermi level pinning-dominating oxides As<sub>2</sub>O<sub>3</sub> and As<sub>2</sub>O<sub>5</sub>. This has been the subject of various experimental studies in literature, mostly employing CV, XPS and TEM measurements as evaluation methods [163–167]. In MT measurements on near-surface InAs/ In<sub>0.75</sub>Ga<sub>0.25</sub>As/ In<sub>0.75</sub>Al<sub>0.25</sub>As QWs, Prager [168] found clear evidence of an efficient unpinning of the Fermi level after depositing Al<sub>2</sub>O<sub>3</sub> via ALD, which points towards an effective reduction of the Fermi level-pinning oxides.

The MT measurements for the sample characterisation are conducted at a base temperature of  $T = 4.2K$  in a liquid He dewar. The sample is brought to cryogenic temperatures with the TG-electrode set to  $V_{CD} = V_{TG} = 0V$  and the ohmic contacts set to the laboratory

ground potential.  $V_{TG}$  is then varied while we monitor the electric response of the 2DEG. For each adjusted value of  $V_{TG}$ , we carry out a MT measurement in which the longitudinal and transversal resistivities are recorded. Figure 7.1(b) displays the applied TG-voltage as a function of time during our employed MT measurement sequence: After the cool-down of the sample, we start at  $V_{TG} = 0V$ . The TG-voltage is then swept into the negative TG-bias direction. This initial down-sweep is stopped when the metal-to-insulator transition (MIT) of the system sets in. Subsequently,  $V_{TG}$  is increased into positive TG-voltage direction towards a maximum applied voltage  $V_{TG}^{max}$ . The sequence is then terminated with a final down-sweep back to  $V_{TG} = 0V$ , or respectively to the onset of the MIT transition as is indicated by the dashed line in figure 7.1(b). This MT measurement sequence will be used for several representative samples in the following.

## 7.2 Chemical treatment and different surface terminations

### 7.2.1 5nm $\text{In}_{0.75}\text{Ga}_{0.25}\text{As}$ cap

#### Gating response of sample A

We start the analysis with a newly fabricated Hall bar device, labeled as sample A. Figure 7.2 shows the gating response of sample A, i.e. the sheet carrier density  $n_s$  of the probed QW as a function of applied  $V_{TG}$ . Here, the Hall density  $n_{Hall}$  (dots) together with the calculated charge carrier density  $n_{SDH}$  from the Shubnikov-de Haas oscillations (triangles) are displayed. For all measurement points, we find  $n_{Hall} \approx n_{SDH}$ , which is commonly regarded as a proof for the absence of parallel conduction inside the probed heterostructure. Via the field-effect, we are able to vary  $n_s$  in the range between channel depletion, i.e.  $n_s < 1.5 \cdot 10^{11} \text{cm}^{-2}$ , and a maximum achievable electron density  $n_s^{peak} \approx 3.75 \cdot 10^{11} \text{cm}^{-2}$ . The gating curve can be clearly divided into two areas, I and II: In area I, the electron density increases linearly with  $V_{TG}$  as it is classically expected from the field-effect. The corresponding capacitive coupling is calculated as  $c = \partial n_s / \partial V = 1.27 \cdot 10^{11} \text{cm}^{-2} \text{V}^{-1}$ . In regime II, i.e. for  $V_{TG} > -0.5V$ , the gating response deviates from the linear behavior, whereby the measured charge carrier density starts to saturate at  $n_s^{sat} = n_s^{peak} = 3.75 \cdot 10^{11} \text{cm}^{-2}$  and cannot be further increased even for an applied  $V_{TG}^{max}$  as high as  $+4.0V$ . This saturation presents a loss of capacitive coupling of the metal gate to the 2DEG. Indeed, to recover a variation of  $n_s$  with  $V_{TG}$ , we have to reduce the TG-voltage to  $V_{TG} \leq +3V$ . In the final down-sweep,  $n_s$  is found to be smaller than for the up-sweep at a given  $V_{TG}$ . This hysteretic behavior has been observed in various other material systems [95–99, 129]. Most of these literature references ascribe it to an asymmetric charge transfer process between doping sites and/or interface trap states and the probed transport channel. This topic will be addressed in detail in section 7.2.3. The inset of figure 7.2 displays the electron mobility  $\mu$  as a function of  $V_{TG}$ . Throughout this chapter we use the value of  $n_{Hall}$  for the calculation of  $\mu$ . We find that  $\mu$

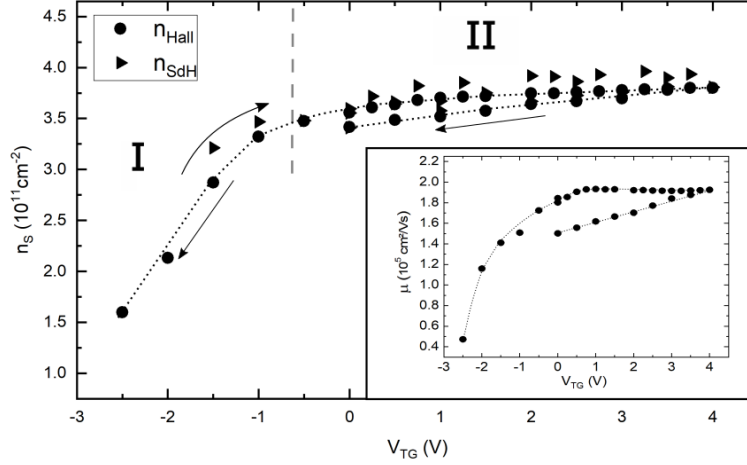


**Figure 7.2:** MT measurement sequence of sample A (wafer C160429A) in the non-illuminated state for a cool-down voltage  $V_{CD} = 0V$  at  $T = 4.2K$ , displaying  $n_s$  as a function of  $V_{TG}$ . The Roman numerals I and II divide the measured curve into two characteristic gating intervals. The inset shows the corresponding electron mobility  $\mu$  as a function of  $V_{TG}$ .

shows a similar gating response as  $n_s$ : Along with the increase in  $n_s$  with rising  $V_{TG}$ ,  $\mu$  increases as well. The simultaneous increase of  $\mu$  with  $n_s$  is attributed to an improved screening of the wave function inside the QW from surrounding scattering centers at a higher charge carrier density. Furthermore, smaller wave vectors of the conduction electrons, corresponding to a small  $n_s$ , are more prone to the interaction with surrounding Coulomb disorder, generated by charged background impurities inside the heterostructure as well as by remote surface charge [46]. Then, at the same  $V_{TG}$  where  $n_s$  reaches  $n_s^{peak}$ , we find the electron mobility to saturate in gating area II as well.

The loss of capacitive coupling to the 2DEG in area II for  $V_{TG} > +3V$  is a clear demonstration of the presence of a parasitic conductive layer above the QW, which effectively shields the 2DEG from the TG-electrode. Given that we found clear evidence for charge migration inside the gate stacking in 1D transport measurements as well as here in 2D MT measurements, we test this hypothesis via biased cool-down measurements.

### Biased cool-down

In the process of a biased cool-down, we apply a non-zero voltage  $V_{TG} \equiv V_{CD}$  at the metal gate electrode at room temperature (RT). Due to the thereby induced band bending, free electrons, provided by the InAlAs deep level donor states, are transferred to available, more favourable energy sites. This electrostatic situation is then brought to cryogenic temperatures, whereby the transferred electrons are frozen at these energy sites. In our transport analysis of sample A, we choose positive TG-voltages ( $V_{CD} > 0V$ ) for the different cool-down processes. Accordingly, the band profile is tilted downwards in positive  $z$ -direction, facilitating electron transfer towards potential trap states which are

located above the QW. To initialize our measurement sequence, we sweep  $V_{TG}$  from the chosen value of  $V_{CD}$  to 0V. Subsequently, the MT measurement sequence as described in section 7.1 is conducted.

**Figure 7.3:** MT measurement sequences of sample A (wafer C160429A) in the non-illuminated state at  $T = 4.2K$  for  $V_{CD} = 0V$ ,  $+1.0V$  and  $+2.0V$ , displaying  $n_{Hall}$  as a function of  $V_{TG}$ . The final down-sweep from  $V_{TG}^{max}$  to 0V is not shown here. The inset displays the initial down-sweep measurements of the measurement sequences.

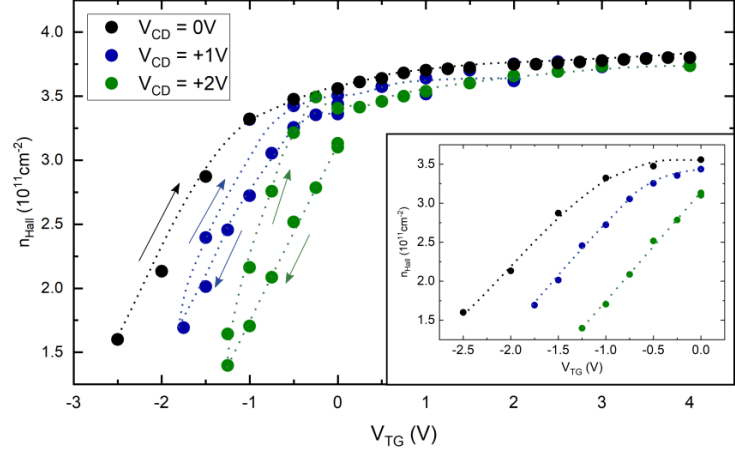


Figure 7.3 shows three MT measurement sequences from different cool-downs with  $V_{CD} = 0V$  (black),  $+1V$  (blue) and  $+2V$  (green). For all three cool-down sequences, we obtain similar gating responses with coinciding values of  $n_s^{sat}$ . However, the curves are horizontally shifted with respect to each other. The higher  $V_{CD}$  is chosen, the larger the overall shift of the curve into the positive  $V_{TG}$ -direction. Consequently, a  $V_{CD} > 0V$  decreases the charge carrier density obtained at a particular  $V_{TG}$  as compared to the zero-bias cool-down case. As a second observation, we find that after a non-zero biased cool-down a hysteresis between the first down-sweep to the MIT transition and the subsequent up-sweep of  $V_{TG}$  develop:  $n_s$  is increased in the up-sweep at a given  $V_{TG}$ . Yet, this increased value of  $n_s$  during the up-sweep is still smaller at a given  $V_{TG}$  as compared to the determined value of  $n_s$  in the MT measurement sequence with  $V_{CD} = 0V$ . We attribute this gating behavior to an interplay of several defect states inside the heterostructure: An overall horizontal shift of the measured gating curve into positive direction as we observe for  $V_{CD} > 0V$  requires a negative and fixed charge density between the metal gate electrode and the QW. The superposition of the applied TG electric field and the electric field due to this additional negative charge results in an effective decrease of  $V_{TG}$  acting on the QW. Based on several studies in literature [159, 169], we hypothesize that trap states inside the  $Al_2O_3$  dielectric layer, which are created by oxygen and aluminum vacancies and interstitials, to be involved in the charge migration processes during the biased cool-down. Electrons, transferred to these energy states at RT, are then efficiently frozen out at  $T = 4.2K$ . This assumption is further supported by our finding that after a cool-down with  $V_{CD} > 0V$ , we are not able to restore the electrostatic situation equivalent to a zero-bias cool-down by applying a large negative  $V_{TG}$  to the heterostructure. According to the direction of band tilting, this would trigger free electron transfer towards the QW. To reset the charge configuration after a biased cool-down, the sample has to be thermally recycled, i.e. warmed up to RT.

A partial back-transfer of electrons towards the QW after a positively biased cool-down manifests itself in the additionally created hysteretic response of the heterostructure between the initial down-sweep of  $V_{TG}$  to the MIT transition and the subsequent up-sweep. We mainly attribute this observation to electron transfer from InAlAs deep level donor states, which were not ionized during the cool-down with  $V_{CD} > 0V$  as compared to the case of  $V_{CD} = 0V$ , to the QW.

As a third observation, we find the loss of capacitive coupling for all three measurements in figure 7.3 at the same electron density  $n_s^{sat} = 3.75 \cdot 10^{11} cm^{-2}$ . For a complete loss of capacitive coupling to the probed 2DEG as in gating area II, however, a sufficiently conductive layer has to be present. A mere distribution of single acceptor states inside an otherwise insulating dielectric would not be sufficient to cause such a behavior. Furthermore, on the basis of supplementary transport measurements on an  $In_{0.75}Al_{0.25}As$  layer at  $T = 4.2K$ , we can exclude parasitic bulk conductance to be present in our system. This result is supported by experimental findings from Capotondi et al. [37]: Even at RT, they report the absence of free charge carriers in their nominally undoped  $In_{0.75}Al_{0.25}As$  layers, exhibiting a similar deep level donor state density as our heterostructures.

We hypothesize that the observed parasitic conductive layer is formed at the InGaAs/ $Al_2O_3$  interface. This finding is indeed not evident inasmuch the parasitic layer does not manifest itself in any other way in our MT measurements such as for example in  $n_{Hall}$ . Furthermore, the Schrödinger-Poisson simulations (see section 5.2) suggest a significant occupation of the InGaAs cap-QW only for much higher electron densities.

The exact nature of the shielding layer cannot exactly be derived from our transport measurements. We suspect a combination of 2D subband states, provided by the InGaAs capping, together with energy states at the  $Al_2O_3$ /InGaAs interface (see [156]) to host the screening electron accumulation. To test our assumption, we reduce the InGaAs cap thickness in an attempt to prevent the formation of the shielding charge layer inside the capping at such low charge density values. To this end, we grow a new wafer (C160420B), which only differs in its cap thickness of  $d_{cap} = 2.5nm$  to the previously analysed heterostructures. The gating response of this new heterostructure is analysed in the following.

### 7.2.2 2.5nm $In_{0.75}Ga_{0.25}As$ cap

#### Gating response of samples *B*, *C* and *D*

**Fabrication details** From wafer C160420B, we fabricate three top-gated Hall bars, labeled as samples *B*, *C* and *D*, in the same processing-run. For these samples, we choose three different  $Al_2O_3$  thicknesses  $d_{Al_2O_3}$  as enlisted in table 7.1. In order not to interrupt the deposition processes, we apply a separate ALD-run for each sample, yet on the same day to ensure similar fabrication conditions. As in the processing of sample *A*, the only chemical treatment prior to the ALD process is a degreasing of the wet-etched Hall bar mesas in the solvents acetone and propanol.



## 7.2 Chemical treatment and different surface terminations

sample	$d_{\text{cap}}$ (nm)	HCl-treatment	$d_{\text{Al}_2\text{O}_3}$ (nm)	$c_i$ ( $\cdot 10^{11} \text{cm}^{-2} \text{V}^{-1}$ )
A	5	/	60	1.27
B	2.5	/	20	4.36
C	2.5	/	30	4.13
D	2.5	/	100	2.60
E	2.5	✓	20	4.52
F	2.5	✓	30	4.07
G	2.5	✓	50	3.45

**Table 7.1:** List of specifications of samples A to G. The check mark (slash) indicates that a HCl-dip is (not) applied prior to the dielectric deposition. The capacitive coupling constants  $c_i$  are determined in the first linear gating area I.

**Measurement sequence** Figures 7.4(a) to (c) show the measurement sequences of samples B, C and D after a cool-down with  $V_{CD} = 0V$ . We can distinguish between two differing types of gating responses. On the one hand, the transport behavior of sample B is equivalent to the gating response of sample A, which we previously discussed in subsection 7.2.1: After a linear increase of  $n_s$  with  $V_{TG}$ , we find the charge density of sample B to saturate at  $n_s^{\text{peak}} \approx 4.3 \cdot 10^{11} \text{cm}^{-2}$  for  $V_{TG} \geq 0V$ . For samples C and D, we find the gating response to be altered as compared to samples A and B: After reaching a peak electron density of  $n_s^{\text{peak}} = 5.2 \cdot 10^{11} \text{cm}^{-2}$  with sample C and  $n_s^{\text{peak}} = 5.4 \cdot 10^{11} \text{cm}^{-2}$  with sample D,  $n_s$  starts to decrease when we further increase  $V_{TG}$ . Furthermore, a settling time of several minutes is required before  $\rho_{xx}$  and  $\rho_{xy}$  stabilize so that a meaningful MT measurement can be conducted. After this stabilization, we find the MT measurements to be perfectly reproducible on the timescale of hours at a temperature of  $T = 4.2K$ , meaning that the equilibrium, that has been reached, is persistent. Moreover, in contrast to samples A and B, we find for samples C and D that the measured Hall density  $n_{\text{Hall}}$  and the calculated Shubnikov-de Haas density  $n_{\text{SDH}}$  do not coincide anymore in the density interval  $n_s^{\text{peak}} > n_s > n_s^{\text{sat}}$ . In this density interval, the calculation of  $n_{\text{SDH}}$  by evaluating the inverse of the magnetooscillation minima in  $\rho_{xx}$  seems no longer applicable since the thereby determined curve cannot be described by a single linear fit, i.e. a single charge density  $n_{\text{SDH}}$ . For a sufficient increase of  $V_{TG}$ , the charge density starts to saturate. The determined value of  $n_s^{\text{sat}} \approx 4 \cdot 10^{11} \text{cm}^{-2}$  with the samples B, C and D is approximately equal to the value of  $n_s^{\text{sat}} = 3.75 \cdot 10^{11} \text{cm}^{-2}$  of sample A. In the saturation regime, we find  $n_{\text{Hall}}$  and  $n_{\text{SDH}}$  to coincide again. As in the case of sample A, in order to restore the capacitive coupling for samples B, C and D the bias voltage has to be decreased underneath a threshold value of  $V_{TG}$ . We thus conclude that in samples B, C and D a parasitic conductive layer at the interface is still generated for positive enough  $V_{TG}$ .

## 7 Gating response of various III-V heterostructures

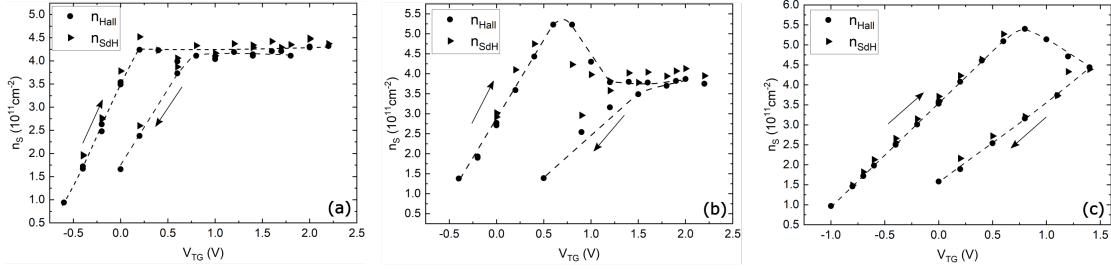


**Figure 7.4:** MT measurement sequences in the non-illuminated state at  $T = 4.2K$ ,  $V_{CD} = 0V$ , displaying  $n_{Hall}$  (dots) and  $n_{SdH}$  (triangles) as a function of  $V_{TG}$  of (a) sample *B* with  $d_{Al_2O_3} = 20nm$ , (b) sample *C* with  $d_{Al_2O_3} = 30nm$ , (c) sample *D* with  $d_{Al_2O_3} = 100nm$ .

**Estimation of  $\epsilon_{Al_2O_3}$**  From the evaluation of the linear dependence of  $n_s$  on  $V_{TG}$  in gating area I, we are able to determine the permittivity  $\epsilon_{Al_2O_3}$  of the dielectric material  $Al_2O_3$ , based upon the differing dielectric thickness values  $d_{Al_2O_3}$  of samples *B*, *C* and *D*. The capacitive coupling  $c$  of the metal gate electrode to the InGaAs 2DEG can be classically described as

$$c = \frac{\partial n}{\partial V} = \frac{\epsilon_0}{e} \cdot \left( \frac{d_{Al_2O_3}}{\epsilon_{Al_2O_3}} + \frac{d_{cap}}{\epsilon_{cap}} + \frac{d_{spacer}}{\epsilon_{spacer}} \right)^{-1}, \quad (7.1)$$

where  $d_{cap} = 2.5nm$  presents the InGaAs cap thickness and  $d_{spacer} = 130nm$  is the InAlAs spacer width.  $\epsilon_{cap}$  and  $\epsilon_{spacer}$  are the corresponding permittivities. Combining the dielectric contributions of the thin InGaAs cap and the much thicker InAlAs spacer layer into a single expression by setting  $\epsilon_{cap} \stackrel{!}{=} \epsilon_{spacer}$  in equation (7.1) and using  $d_{cap} + d_{spacer} \equiv d_{c+s} = 132.5nm$ , we yield a simplified formula for  $c$ :

$$c = \frac{\epsilon_0}{e} \cdot \left( \frac{d_{Al_2O_3}}{\epsilon_{Al_2O_3}} + \frac{d_{c+s}}{\epsilon_{c+s}} \right)^{-1}. \quad (7.2)$$

$c$  is determined from the slope of the individual MT measurement sequences of samples *B*, *C* and *D* via  $c = \frac{\partial n}{\partial V}$ . The determined values of  $c_i$ , with  $i = B, C, D$ , are listed in table 7.1. Since  $d_{Al_2O_3}$  and  $d_{c+s}$  are known quantities, we can formulate three equations on the basis of equation (7.2), which then solely contain two unknown quantities, i.e.  $\epsilon_{Al_2O_3}$  and  $\epsilon_{c+s} \hat{=} \epsilon_{InAlAs}$ . In order to calculate one of them, for example  $\epsilon_{Al_2O_3}$ , we take two of the calculated  $c_i$  values as input. By combining the values for  $c_i$  pairwise, we thus receive three separate values for  $\epsilon_{Al_2O_3}$  from the different possible combination choices of  $c_i$ :

$$\begin{aligned} c_B \ \& \ c_C &\rightarrow \ \varepsilon_{Al_2O_3}^{BC} = 14.17 \\ c_B \ \& \ c_D &\rightarrow \ \varepsilon_{Al_2O_3}^{BD} = 9.36 \\ c_C \ \& \ c_D &\rightarrow \ \varepsilon_{Al_2O_3}^{CD} = 8.93 \end{aligned}$$

Whereas  $\varepsilon_{Al_2O_3}^{BC} = 14.17$  deviates substantially from the other two determined values,  $\varepsilon_{Al_2O_3}^{BD}$  and  $\varepsilon_{Al_2O_3}^{CD}$  are similar in magnitude and also in good agreement with reported values in literature [170]. Owing to the discrepancies of the determined values of  $\varepsilon_{Al_2O_3}$ , we omit an evaluation of  $\varepsilon_{InAlAs}$  here.

**Discussion and conclusion** The gating responses of samples *B*, *C* and *D* differ significantly from each other: Whereas the transport behavior of sample *B* is similar to sample *A* with a cap thickness of  $5nm$ , for samples *C* and *D* an additional peculiar gating interval develops, in which the charge density decreases with increasing  $V_{TG}$  before saturation at an equivalent density as for samples *A* and *B* sets in. Thus, we infer that by solely reducing the InGaAs cap thickness, we are not able to suppress the formation of the parasitic conductive layer at the InGaAs/ $Al_2O_3$  interface, at least in the regime of high  $V_{TG}$ . This experimental observation cannot be explained by means of our band structure simulation, in which we assumed a Fermi level pinning of  $40meV$  under the conduction band edge as it is suggested in literature [14, 37, 117]. Neither an unpinning of the Fermi level is able to reproduce our experimental results. The differing gating responses of samples *B*, *C* and *D*, together with the deviations in the estimated values for the permittivity  $\varepsilon_{Al_2O_3}$  reflect the unsystematic gating behavior of this Hall bar series. Generally, we can identify several typical mechanisms for III-V materials, which are responsible for the creation of midgap states at the surface: As-O bond formation, interface intermixing, as well as dangling bonds can be named as root causes [156]. In practice, X-ray photoelectron spectroscopy (XPS) measurements are applied to gain experimental insight to the defect state formation and density [155, 163, 166, 167, 171–173]. Via XPS measurements on our samples before and after the deposition of  $Al_2O_3$  (not shown here), we were able to confirm a substantial reduction of the Fermi level pinning native oxides  $As_2O_3$  and  $As_2O_5$ , which we deduce from an almost complete disappearance of the corresponding peaks in the XPS spectra for samples with  $Al_2O_3$ . Yet, we observe further peaks in the XPS spectra of our samples. There is a vast range of publications, dealing with the identification of the native III-V oxides, at the head, photoemission experiments. Many of these studies focus on the analysis of the modifications of arsenic and gallium native oxides, whereas less studies concentrate on alternative oxidation states and other In-containing oxide compounds [155, 171, 174–176]. In their XPS measurements, Brennen et. al [155] were able to identify at least eight different oxide peaks in the  $As3d$ -spectrum, amongst them  $As_2O_3$ ,  $As_2O_5$  and  $GaAsO_4$ .  $As_2O_3$  and  $As_2O_5$  are found to be responsible to effectively pin the Fermi level at InGaAs interfaces. Relevant oxides in the  $In4d$  and  $Ga3d$  spectra are stated to be  $In_2O$ ,  $In_2O_3$ ,

## 7 Gating response of various III-V heterostructures

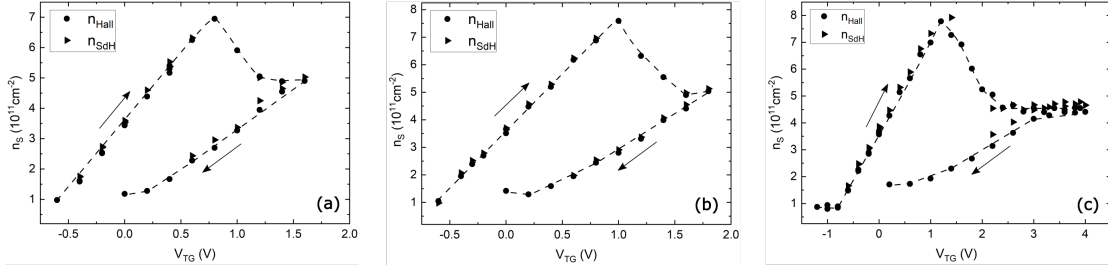


**Figure 7.5:** MT measurement sequences in the non-illuminated state at  $T = 4.2K$  at  $V_{CD} = 0V$ , displaying  $n_{Hall}$  (dots) and  $n_{SdH}$  (triangles) as a function of  $V_{TG}$  of (a) sample *E* with  $d_{Al_2O_3} = 20nm$ , (b) sample *F* with  $d_{Al_2O_3} = 30nm$ , (c) sample *G* with  $d_{Al_2O_3} = 50nm$ .

$In_xGa_yO_z$  (with  $x > y$ ), as well as  $Ga_2O$  and  $Ga_2O_3$ .

In order to test the effect of residual native oxides on the gating response of the analysed heterostructure, we fabricate top-gated Hall bar devices, for which an additional cleaning step prior to the ALD process is introduced.

### Gating response of samples *E*, *F* and *G*

**Fabrication details** Three additional top-gated Hall bar devices, labeled as samples *E*, *F* and *G*, from wafer C160420B are processed. Prior to the  $Al_2O_3$  deposition with ALD, the samples are dipped in aqueous hydrochloric acid (HCl) for one minute, followed by a rinsing in deionized water. In an experimental study, Kobayashi et al. [177] confirmatively found that the native oxides  $GaO_x$ ,  $InO_x$  and  $AsO_x$  are efficiently removed by HCl. As for samples *B*, *C* and *D* in the preceding subsection, we choose three different dielectric thicknesses  $d_{Al_2O_3}$  for the samples *E*, *F* and *G*, summarized in table 7.1, to determine the corresponding permittivities  $\epsilon_{Al_2O_3}$  and  $\epsilon_{In_{0.75}Al_{0.25}As}$ .

**Measurement sequence** Figures 7.5(a) to (c) display the gating responses of samples *E*, *F* and *G* in the MT measurement sequence for  $V_{CD} = 0V$ . All three samples exhibit the same characteristic transport features in their gating response: After a linear increase of the sheet density with  $V_{TG}$ ,  $n_s$  starts to decrease after reaching  $n_s^{peak}$ , until a saturation at  $n_s^{sat} \approx 5 \cdot 10^{11} cm^{-2}$  sets in. For the density interval  $n_s^{peak} > n_s > n_s^{sat}$ , we find  $n_{Hall} \neq n_{SdH}$ . This gating behavior is equivalent to samples *C* and *D*. However, we find  $n_s^{peak}$  of samples *E*, *F* and *G* to be significantly larger with values for  $n_s$  of up to  $7 - 7.8 \cdot 10^{11} cm^{-2}$ . We want to emphasize, that this presents almost a doubling of the maximum achievable electron density in the 2DEG in comparison to the previously studied samples *A* to *D*.

Yet, as can be clearly seen in the measurement sequence of sample *G*, we again loose capacitive coupling to the 2DEG after a distinct drop of the charge density from  $n_s^{peak}$  to  $n_s^{sat}$ . In addition, removing the residual native oxides at the InGaAs surface with

HCl clearly increases the reproducibility of the gating response of the heterostructure. However, it does not lead to an annihilation of the parasitic conductive layer at sufficiently positive  $V_{TG}$ .

**Estimation of  $\varepsilon_{In_{0.75}Al_{0.25}As}$  and  $\varepsilon_{Al_2O_3}$**  From the linear dependence of  $n_s$  on  $V_{TG}$  in the density range  $n_s < n_s^{peak}$ , we determine the capacitive coupling constants  $c_i$  of samples  $E$ ,  $F$  and  $G$ . The corresponding values are summarized in table 7.1. As classically expected, the capacitive coupling decreases with increasing  $d_{Al_2O_3}$  in a linear fashion, since  $d_{cap}$  and  $d_{spacer}$  are similar for all three samples.

As described in paragraph 7.2.2, the permittivity  $\varepsilon_{Al_2O_3}$  of the deposited  $Al_2O_3$  is calculated by pairs of  $c_i$ :

$$\begin{aligned} c_E \ \& \ c_F &\rightarrow \ \varepsilon_{Al_2O_3}^{EF} = 7.37 \\ c_E \ \& \ c_G &\rightarrow \ \varepsilon_{Al_2O_3}^{EG} = 7.89 \\ c_F \ \& \ c_G &\rightarrow \ \varepsilon_{Al_2O_3}^{FG} = 8.18 \end{aligned}$$

The calculated values of  $\varepsilon_{Al_2O_3}$  are all in good agreement and furthermore coincide with reported values in literature [170]. On this basis, we are able to determine a meaningful value of the permittivity  $\varepsilon_{In_{0.75}Al_{0.25}As}$  of the  $In_{0.75}Al_{0.25}As$  spacer material. For this purpose, we take the average value  $\bar{\varepsilon}_{Al_2O_3}^{i,j}$  from the calculated permittivities above, which yields  $\bar{\varepsilon}_{Al_2O_3} = 7.81$ . With equation (7.2), we can write for  $\varepsilon_{c+s}$ , which is approximately  $\varepsilon_{In_{0.75}Al_{0.25}As}$ :

$$\varepsilon_{In_{0.75}Al_{0.25}As} \hat{=} \varepsilon_{c+s} = d_{c+s} \cdot \left( \frac{d_{Al_2O_3}}{\bar{\varepsilon}_{Al_2O_3}} - \frac{\varepsilon_0}{e \cdot c} \right)^{-1}. \quad (7.3)$$

Independent of the chosen value of  $c_i$ ,  $i = E, F, G$  (with the corresponding  $d_{Al_2O_3,i}$ ) we utilise for the above calculation, we consistently find:  $\varepsilon_{In_{0.75}Al_{0.25}As} = 13.7$ . This value for  $\varepsilon_{In_{0.75}Al_{0.25}As}$  is in very good agreement with values reported in literature [178].

### Comparison of samples $B$ to $G$

To illustrate the severe influence of the residual native oxides on the gating response of the heterostructure, we plot the MT measurement sequences of samples  $B$ ,  $C$  and  $D$ , for which the additional cleaning step in the fabrication process is omitted, in one graph (figure 7.6(a)), and the gating curves of samples  $E$ ,  $F$  to  $G$ , having experienced the auxiliary HCl dip, in one graph (figure 7.6(c)). The corresponding mobility responses are shown in figure 7.6(b) and (d) and will be discussed in more detail later in the course of this chapter (see subsection 7.5.1). This graphical comparison further underlines the lack of predictability of the gating responses of samples  $B$ ,  $C$  and  $D$ . The remnant oxides at the  $InGaAs/Al_2O_3$  interface lead to an arbitrary surface potential and consequently to an uncontrolled gating response of the heterostructure with a reduced linear gating

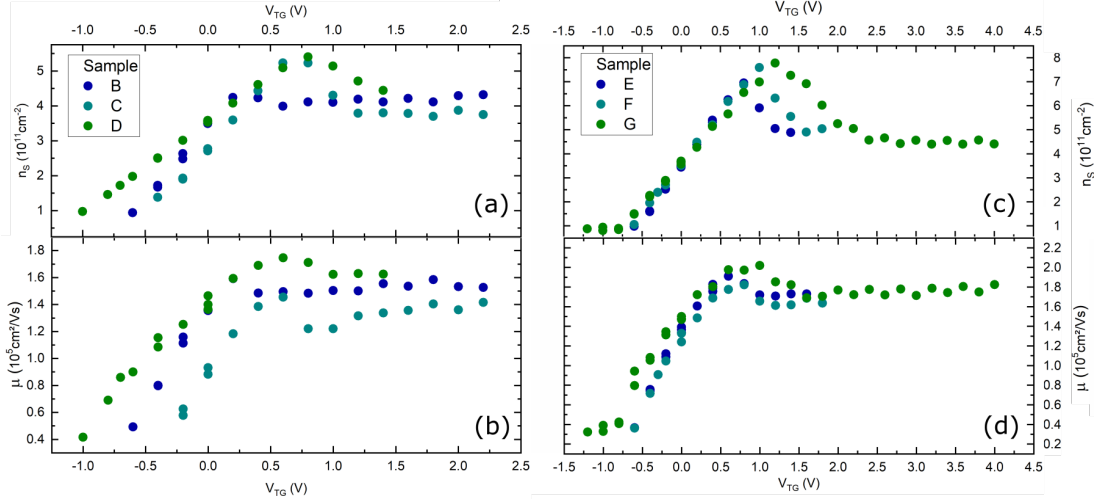


**Figure 7.6:** MT measurement sequences of (a)-(b): samples *B*, *C* and *D*, for which no chemical removal of residual native oxides is conducted in the fabrication process. Figure (a) displays the electron density  $n_{Hall}$  as a function of  $V_{TG}$ , figure (b) the electron mobility  $\mu$  as a function of  $V_{TG}$ . (c)-(d): samples *E*, *F* and *G*, for which a wet-chemical removal of residual native oxides is introduced in the fabrication process. Figure (c) displays the electron density  $n_{Hall}$  as a function of  $V_{TG}$ , figure (d) the electron mobility  $\mu$  as a function of  $V_{TG}$ .

area I and differing values for  $n_s^{peak}$ . From these experimental findings, we infer that the onset of the charge migration towards the interface is clearly linked to the density of parasitic interface states. The gating responses of samples *E*, *F* and *G*, in particular their mobility response, is much more congruent, which demonstrates the efficiency of the HCl treatment in removing residual oxides at the semiconductor surface. Building on the experimental finding that a reduction of  $d_{cap}$  from  $5 \text{ nm}$  to  $2.5 \text{ nm}$  results in an increase of  $n_s^{peak}$  to  $5 \cdot 10^{11} \text{ cm}^{-2}$  for at least two out of three samples in our study even without the removal of the surface oxides with HCl, we infer that energy states inside the InGaAs cap also affect the interface density of states, and thus the onset of the charge migration from the QW.

Recapitulating, by means of our experimental analysis of the gating response of samples *A* to *G*, we are able to identify several types of defect states, which affect the transport characteristics in the heterostructure. Charge migration towards the surface is clearly linked to energy states at the semiconductor/dielectric interface, yet we find for all analysed samples that a parasitic conductive layer develops at the interface for sufficiently positive  $V_{TG}$ . Before a saturation of the charge density sets in at an electron density  $n_s^{sat}$ , we find a distinct decrease of  $n_s$  after reaching  $n_s^{peak}$  with further increasing  $V_{TG}$ . In the following, we develop a microscopic model description of this rather peculiar gating behavior of the system. This is done on the basis of the measurement sequence of sample *G*.

### 7.2.3 Charge transfer model

On the basis of the MT measurement sequence of sample *G*, we discuss the physical origin of the different regimes in the gating response of the heterostructure. Based on our observations, we create a model description of the charge transfer processes in the gate stack, which is then further validated with a quantitative evaluation of the density response under gate operation.

**Figure 7.7:** MT measurement sequences of sample *G* (wafer C160420B) in the non-illuminated state for  $V_{CD} = 0V$  at  $T = 4.2K$ : No. 1 (black) for  $V_{TG}^{max} = +4.0V$  and No. 2 (cyan) for  $V_{TG}^{max} = +1.6V$ . The Roman numerals I to VI label the constituent gating areas.

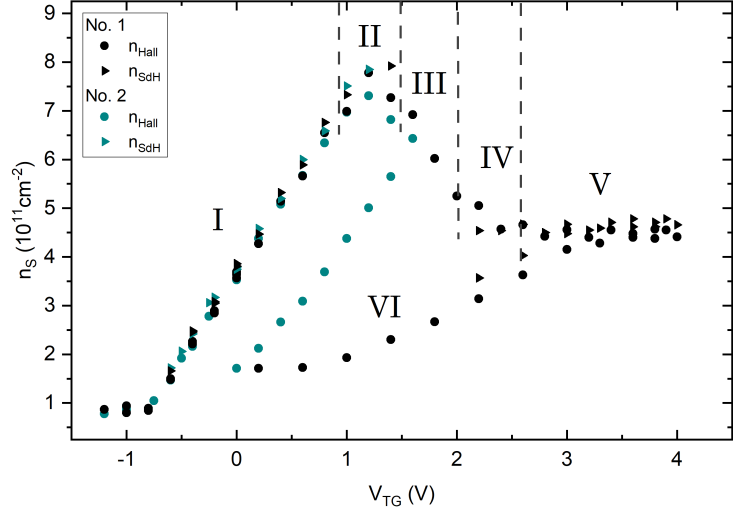


Figure 7.7 displays the gating curve of sample *G* with  $n_{Hall}$  and  $n_{SdH}$  as a function of  $V_{TG}$ . Two separate measurement sequences are shown, for which two different maximum applied voltages  $V_{TG}^{max}$  are chosen. To initialize each measurement sequence, we thermally reset the sample in between the two gating sequences. For the first measurement sequence (black curve), a  $V_{TG}^{max}$  of  $+4.0V$  is chosen, whereas for sequence 2 (cyan curve), we commence the final down-sweep after reaching a  $V_{TG}^{max}$  of  $+1.6V$ . For measurement sequence no. 1, we identify six different gating areas, labeled with Roman numerals I to VI in the plot.  $V_{TG}^{max} = +1.6V$  of the second gating sequence is chosen such that we do not enter regime V before the final down-sweep back to  $V_{TG} = 0V$  is conducted. For the following discussion, we also submit representative MT measurement curves of the longitudinal resistivity  $\rho_{xx}(B)$  of each gating regime I to VI, shown in figure 7.8.

#### Description of the gating response of sample *G*

The physics in region I, i.e.  $-1V \leq V_{TG} \leq +1V$ , are well described by the classical field-effect so that we can consider the active layer system as a plate capacitor. Thereby, the QW and the TG-electrode serve as the two plates of the capacitor with area  $A$  and distance  $d$  and a dielectric, i.e. the InAlAs spacer, in between:

$$C = Q/V_{TG} \quad \text{with} \quad C = \epsilon_0 \epsilon_r \frac{A}{d},$$

## 7 Gating response of various III-V heterostructures

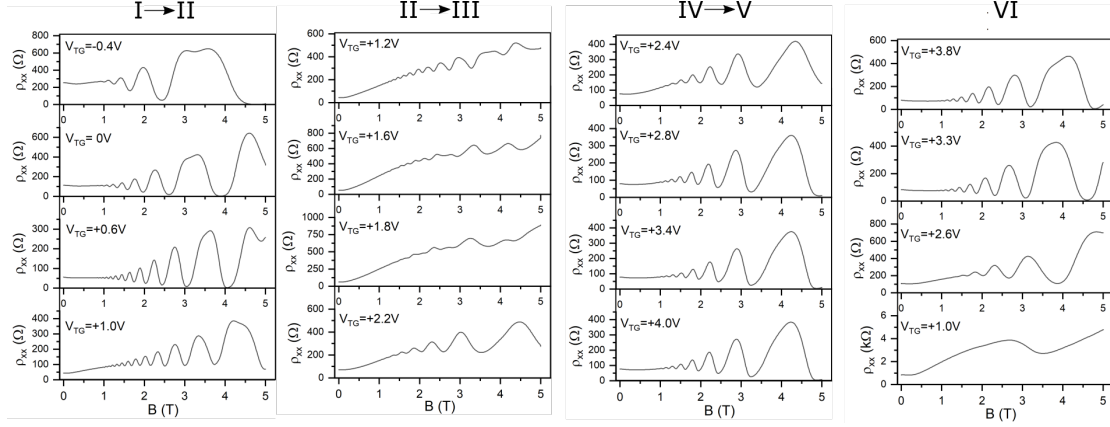


**Figure 7.8:** Exemplary MT measurements of sample *G* (wafer C160420B) in the non-illuminated state for  $V_{CD} = 0V$  at  $T = 4.2K$ : longitudinal resistivity  $\rho_{xx}(B)$  of the constituent gating areas I to VI.

with  $C$  being the capacitance of the system. The sheet density  $n_s$  increases as a function of  $V_{TG}$  in gating regime I. Thus, we can write for gating area I:

$$n_s = \epsilon_0 \epsilon_r \frac{d}{e} V_{TG} . \quad (7.4)$$

Furthermore, we find that  $n_s$  responds instantaneously to a change in  $V_{TG}$  and is stable over time. For  $+1V < V_{TG} < +1.5V$ , however, the gating response of the system diverges significantly from this linear behavior since we determine that the slope of the density curve smoothly decreases and even changes its sign: The charge density peaks at  $n_s^{peak} = 7.8 \cdot 10^{11} cm^{-2}$  and then starts to decrease with increasing  $V_{TG}$ . In gating area III, i.e.  $+1.5V < V_{TG} < +2.2V$ , the charge density drops rapidly. In the experiment, when a more positive  $V_{TG}$  is adjusted in gating area II and III,  $\rho_{xx}$  and  $\rho_{xy}$  are unstable on the timescale of minutes. They only sufficiently stabilize after a settling time of tens of minutes so that a conclusive MT measurement can be conducted after each change of  $V_{TG}$  in this TG-range. Furthermore, it is characteristic for this second and third gating area that  $n_{Hall}$  and  $n_{SDH}$  do not coincide anymore. This can be clearly seen in figure 7.8, where an undulation in  $\rho_{xx}(B)$  arises in these gating areas. A FFT of  $\rho_{xx}$  over  $1/B$  reveals two closely-spaced frequencies in the spectrum. This observation will be discussed in detail in chapter 9. The arising texture in the Shubnikov-de Haas oscillations is accompanied by a parabolic magnetic field dependency of  $\rho_{xx}$ , that sets in at the end of gating regime I when we reach  $n_s^{peak}$ .

In measurement sequence 2, we conduct the final down-sweep after  $V_{TG}^{max} = +1.6V$  in gating regime III. During the down-sweep from  $V_{TG}^{max}$  back to  $0V$ , no additional settling time is needed for  $\rho_{xx}$  and  $\rho_{xy}$  to stabilize.

For sequence 1, in which the TG-voltage is increased up to  $V_{TG}^{max} = +4.0V$ , the decrease of  $n_{Hall}$  starts to flatten smoothly in the gating interval  $+2.2V < V_{TG} < +3.1V$ , i.e. regime IV, until a saturation of the measured sheet density at about  $4.5 \cdot 10^{11} cm^{-2}$  sets in for



$V_{TG} > +3.1V$ . This gating area is labeled as regime V. In regime IV and V, we find that  $n_{Hall}$  and  $n_{SdH}$  coincide again. The MT measurements of  $\rho_{xx}(B)$  in these gating areas display an absence of the parabolic background in contrast to regimes II and III. Furthermore, we determine a single frequency for the magnetooscillations in  $\rho_{xx}(B)$ . Further increasing  $V_{TG}$  in regime V has no measurable effect on  $\rho_{xx}(B)$ , as well as on  $n_{Hall}$  and  $n_{SdH}$ . Thus, the capacitive coupling is lost - the probed QW is efficiently screened from the applied TG-voltage. In the final down-sweep of  $V_{TG}$  back to 0V, i.e. gating regime V and VI,  $n_s$  stays at the saturation value of  $4.5 \cdot 10^{11} cm^{-2}$  at first, before the capacitive coupling between the gate electrode and the 2DEG is restored for  $V_{TG} < +3V$  in regime VI, revealing a pronounced hysteresis. As compared to the linear gating area I, the capacitive coupling in regime VI is reduced and depends on the applied  $V_{TG}^{max}$  (see measurement sequences 1 and 2): The higher  $V_{TG}^{max}$  is chosen, the smaller the capacitive coupling during the down-sweep and the larger the hysteresis.

In the following section, we will discuss this experimental analysis and interpret the underlying microscopic mechanisms in terms of a phenomenological charge transfer model, which is consistent with all our experimental observations.

For the sake of completeness, we want to note that a deviation of the linear field-effect in the gating response of a 2DEG can be caused by the population of the second size-quantized subband at sufficiently high TG-voltages. Here, we refer to section 9.3.1, where this mechanism is excluded as possible origin.

### Model description of the gating response

**Figure 7.9:** Cross sectional schematic sketch of sample G: the metal gate electrode (dark grey) is separated by a 50nm  $Al_2O_3$  layer from the semiconducting layers. The annealed ohmic contacts to the QW are depicted in light grey as  $n^+$ -contact regions. The current path from source (S) to drain (D) is depicted with the orange dots.

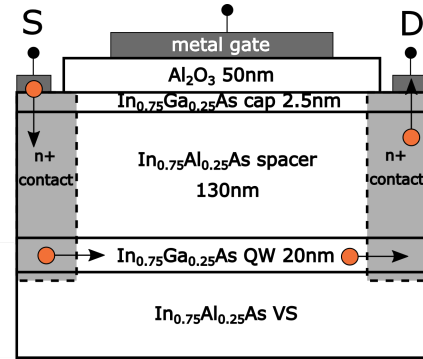


Figure 7.9 sketches the schematic cross section of the analysed gated Hall bar sample G. In light grey, the annealed ohmic contacts of the heterostructure are depicted. They penetrate through the whole heterostructure into the probed InGaAs QW. As already pointed out earlier, we experimentally verified that no measurable charge transport across the InAlAs spacer layer takes place, even though deep level donor states inside the ternary alloy films are known to exist. These energy states, which provide the doping in our system, are generated by arsenic antisite defects induced during the MBE growth process of the system [37–39]. We therefore expect the current from the source to the drain contact to flow through the InGaAs QW, as indicated in the sketch.

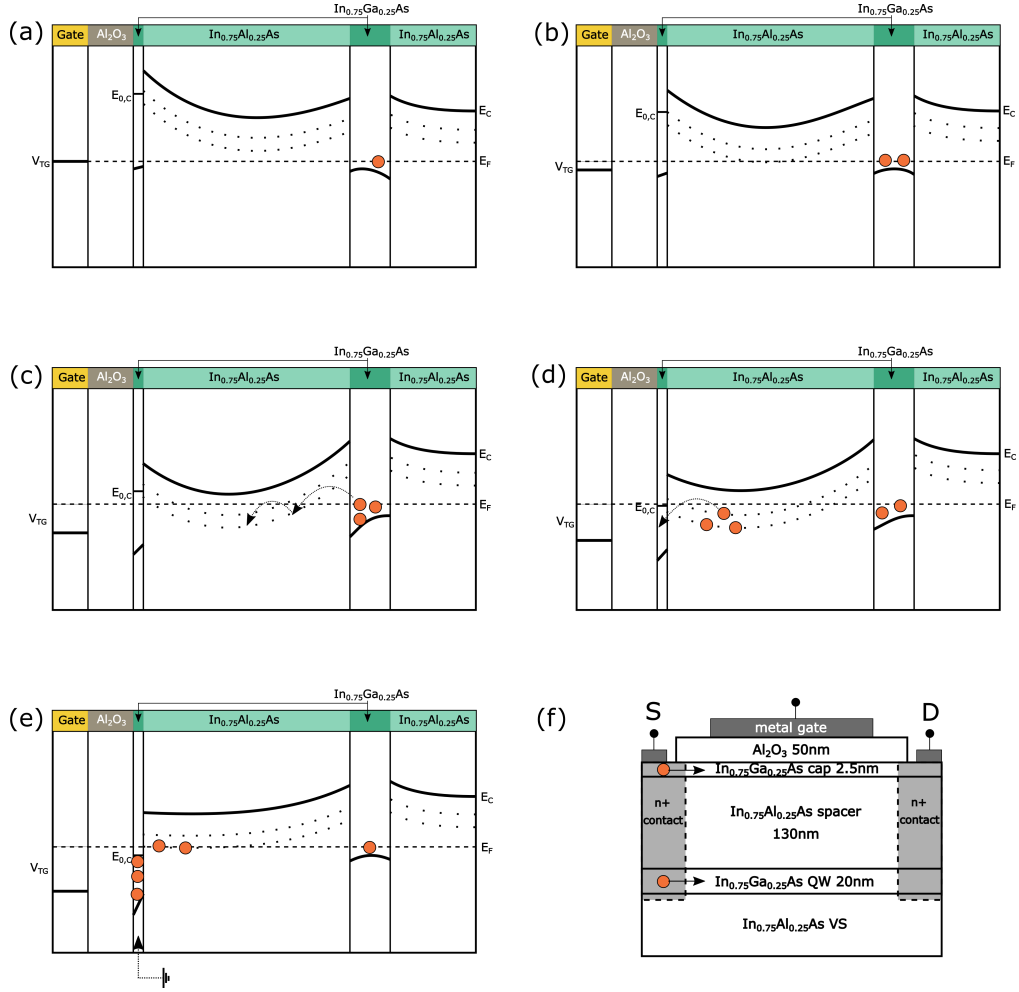
## 7 Gating response of various III-V heterostructures

Figure 7.10(a) illustrates a sketch of the band profile of the heterostructure gate stack for the case of  $V_{TG} = 0V$ . The deep level donor states inside the InAlAs layers are drawn as dotted curves under the conduction band edge. A second surface QW is present in the  $2.5nm$  InGaAs cap, however, with the lowest subband energy  $E_{c,0}$  lying well above the ground state of the deeply buried InGaAs QW, which has a much larger width of  $20nm$ . Furthermore, we expect the cap-QW to be of much lower crystal quality due to surface roughness and the presence of spatially varying trap states, since it is in direct contact with the dielectric material. Even for zero applied gate voltage, the band profile is tilted due to the ionization of the InAlAs defect sites. Electrons from the InAlAs spacer and the VS are transferred into InGaAs/ $Al_2O_3$  interface states, as well as into the QW. From self-consistent calculations of the band structure with a Schrödinger-Poisson solver<sup>1</sup>, we find the InAlAs donor sites in the spacer layer to be fully ionized, generating a trough-shaped band profile in the InAlAs as shown in figure 7.10(a). Though the donor sites of the InAlAs VS are fully ionized in the first tens of nanometers, the simulation only predicts a partial ionization of these defect states as the distance to the QW increases. Due to this asymmetric electron distribution inside the active region of the heterostructure for  $V_{TG} = 0V$ , we find the QW to be even tilted downwards at the deeper lying QW interface.

Increasing the applied voltage at the gate electrode in the linear gating area I tilts the band profile downwards with respect to the QW and increases the charge density of the 2DEG according to equation (7.4). This situation is shown in figure 7.10(b). The system is still in equilibrium, since the most favourable energy state presents the first subband of the InGaAs QW. Further increasing  $V_{TG}$  leads to a non-equilibrium situation of the system as is illustrated in figure 7.10(c): Deep level donor sites of the InAlAs spacer are pulled under the Fermi level. Although the ohmic contacts are in contact with this layer, according to our experimental observations no lateral charge transfer inside the InAlAs spacer across the whole mesa length can take place to remedy this created system-imbalance. Thereby, the TG-induced electric field creates a triangular-shaped potential barrier at the upper interface of the QW between the lowest QW-subband and the InAlAs defect states under the Fermi level. For a sufficiently large gate electric field, electrons start to tunnel from the QW into the more favourable defect states as is illustrated by the dotted arrows in the sketch. Spatial fluctuations in the band profile - and thus also of the tunnel processes - lead to a smooth truncation of the linear density response in gating area II as we would expect from the classical field-effect. We assume the deep level donor state concentration  $N_D^{total} \approx 3 - 4 \cdot 10^{16} cm^{-3}$  to be divided approximately equal into the two defect state densities  $N_D^{total}/2 = N_{D,1} = N_{D,2}$ . Thus, the distance between two doping sites of the same type is calculated as  $\approx 32nm$ . The effective Bohr radius  $a_0^* = \frac{\epsilon_{sc}}{m^*} \cdot \frac{4\pi\epsilon_0\hbar^2}{e^2}$ , which is a measure of the spatial latitude of an electron bound to a doping site in a semiconductor with a permittivity of  $\epsilon_{sc}$ , yields  $a_0^* = 18nm$  when using the previously determined value  $\epsilon_{sc} = \epsilon_{In_{0.75}Al_{0.25}As} = 13.7$  and an effective mass of  $m^* = 0.041 \cdot m_0$  (see chapter 5). Comparing  $a_0^*$  of a defect-bound electron to the deep-level-donor distance,

<sup>1</sup>We assume the total density of the InAlAs defect sites to be  $N_D^{total} = 3 - 4 \cdot 10^{16} cm^{-3}$  [37, 38].

## 7.2 Chemical treatment and different surface terminations

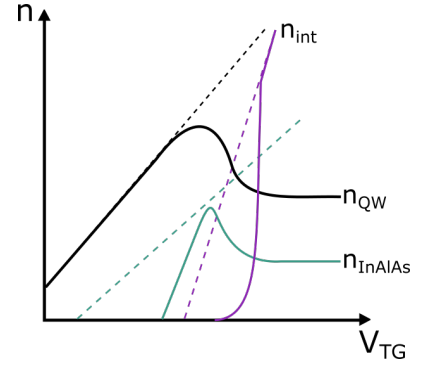


**Figure 7.10:** Schematic description of the evolution of the band profile of the system during our MT measurement sequence: **(a)** displays the conduction band edge  $E_c$  (thick solid line) for  $V_{TG} = 0V$ . Electrons from the InAlAs deep level donor states (dotted lines) are transferred into the QW and into interface states. The lowest cap-QW energy state  $E_{c,0}$  is well above the Fermi level  $E_F$  (dashed line). **(b)**  $V_{TG} > 0V$  (gating area I) increases the charge carrier density inside the QW. Step-by-step, the system is driven into a non-equilibrated state, since InAlAs defect states are pulled under  $E_F$ . **(c)** Gating regime II and III: electrons tunnel from the QW into InAlAs defect states as indicated by the dotted arrows. The trough-shaped InAlAs band profile is flattened and the system is stuck in a metastable state. **(d)** Gating regime IV and V: a second imbalance is created as soon as  $E_{c,0}$  is pulled under  $E_F$ . For sufficiently high  $V_{TG}$  charge transfer into these interface states sets in. **(e)** For  $n_{int} > n_c$ , the interface region is conducting, whereby electrons flow laterally from the ohmic source contact (S) into the drain contact (D) as shown in **(f)**.

we find electron transfer between two adjacent defect sites in an external electric field to be feasible. We assume Fowler-Nordheim tunneling to be the dominant charge transfer process between the QW and the InAlAs defect sites. In the literature [179, 180], this mechanism is suggested to be responsible of charge transfer from a 2D system into the cap through a spacer layer with the thickness in the range of  $14 - 40\text{nm}$  in the case of a sufficiently strong band tilting. In our case, multi-step tunnelling or hopping processes manifest themselves in the experiment in the form of a long settling time on the timescale of tens of minutes after a sweep of  $V_{TG}$ . Increasing  $V_{TG}$  further makes the triangular potential barrier sufficiently transparent so that efficient tunnelling from the QW into InAlAs deep level donor sites sets in. This process corresponds to the charge density drop in gating regime III. Following the potential gradient induced by the applied electric field, transferred electrons will populate the InAlAs defect states, which are located on the base of the trough-shaped band profile. This additional negative charge in the spacer material partially compensates the applied TG-field and leads to a flattening of the band profile. This situation is schematically sketched in figure 7.10(d). Consequently, the tunnel process is stopped before the system can reach its total equilibrium, meaning it is stuck in a metastable state. The transferred electrons are localized and do not contribute to transport according to our experimental observations. A further increase of  $V_{TG}$  in gating area III thus still leads to a tilting of the band profile with respect to the QW and switches the triangular potential barrier again into a transparent state. With increasing TG-voltage, however, we create a second imbalance in the system: Energy states  $E_{c,0}$  at the InGaAs/Al<sub>2</sub>O<sub>3</sub> interface [136, 156–158] are pulled under the Fermi level, as it is shown in figure 7.10(e). For sufficiently high  $V_{TG}$ , i.e. gating area IV, electrons start to tunnel locally from the InAlAs defect sites into  $E_{c,0}$ . Interface roughness and the non-uniform texture of the semiconductor/dielectric bonds create a strongly fluctuating potential profile at the surface [181], which leads to the formation of so-called charge puddles. A critical charge carrier density  $n_c$  has to be accumulated at the interface so that the screening ability of the respective 2D system is reached and electrons start to flow laterally from the ohmic contacts into the interface layer. This is further visualized by the ground-symbol newly inserted at the InGaAs cap layer in figure 7.10(e). The system relaxes into an equilibrated state, whereby the band tilting of the spacer and the QW is reduced. This situation is visualized in figure 7.10(e) and (f). Owing to the poor conductive quality of the interface layer, the 2D system inside the  $20\text{nm}$  InGaAs QW will dominate the density and mobility output of our MT measurements (see subsection 2.1.1). A further increase of  $V_{TG}$  now solely accumulates electrons at the interface region since the QW is effectively short-circuited, leaving the charge density of the QW unchanged. This situation corresponds to gating area V, in which no capacitive coupling to the QW is present.

The  $V_{TG}$ -dependencies of the three main contributing charge carrier densities of the system are schematically illustrated in figure 7.11. The dashed curves represent the  $V_{TG}$ -dependence of the individual charge densities in equilibrium. We assume a linear increase of  $n_{int}$  and  $n_{QW}$  with  $V_{TG}$  according to the classical field-effect, described by equation (7.4). The deep level donor sites inside the InAlAs layer of the system are

**Figure 7.11:** Sketch of electron densities of the QW  $n_{QW}$  (black), the InAlAs deep level donor density  $n_{InAlAs}$  (cyan) and the surface density  $n_{int}$  (purple) as a function of applied  $V_{TG}$ . The thermally equilibrated situation of the system is sketched with the dashed curve. The black solid curve of  $n_{QW}$  also presents the charge carrier density we determine in our MT measurement sequence.



expected to be evenly distributed in space. In contrast to energy states of the QW and the interface, these defect sites do not constitute a fully conducting band, whereby we cannot describe the voltage dependence of their charge density, i.e. the ionization state of the defect level, in the picture of the plate capacitor. However, as a simple approximation for this illustration, we also assume a linear field dependence since with rising  $V_{TG}$  continuously more InAlAs defect states are pulled under the Fermi level whereby the  $n_{InAlAs}$ -value in thermal equilibrium increases steadily. The solid lines represent the situation in our experiment, which deviates from the dashed curves when the system is driven out of equilibrium due to the band tilting imposed by the gate voltage and the low temperature, preventing an equilibration of the system. While the charge carrier density of the 2D system  $n_s \equiv n_{QW}$  increases with  $V_{TG}$ , the deep level donor states  $n_{InAlAs}$  are pulled under  $E_F$ , indicated by the cyan-colored dashed curve. As soon as the transfer-path towards these states is sufficiently transparent,  $n_{QW}$  drops and  $n_{InAlAs}$  increases. A change of  $n_{InAlAs}$  is linked to the gating regimes II and III. The second imbalance arises when the TG-voltage is further increased and energy states at the interface, parameterized by the density  $n_{int}$ , are pulled under the Fermi energy (purple dashed curve). A population of these states leads to a decrease of  $n_{InAlAs}$ , as well as to a saturation of  $n_{QW}$  and  $n_{InAlAs}$ . The equilibrium value of  $n_{int}$ , i.e. when the solid and dashed purple curves match, represents the beginning of gating area V.

Decreasing  $V_{TG}$  into gating regime VI of our measurement sequence firstly leads to a depopulation of the interface states  $n_{int}$ . As soon as  $n_{int} < n_c$ , the screening of the gate field-effect is lifted and capacitive coupling to the 2DEG sets in again by which we are able to deplete the QW. The capacitive coupling in VI is decreased as compared to the up-sweep in I. We assign this observation to a partial regain of electrons, which have been previously transferred towards the interface in gating areas II to IV: While the band profile is tilted upwards again in regime VI (corresponding to the sweep direction of  $V_{TG}$  back to 0V), the QW becomes energetically more favourable, triggering a repopulation of the QW and thus decreasing the experimentally observed capacitive coupling  $c = \frac{\partial n}{\partial V_{TG}}$ . The hysteresis between up- and down-sweep of  $V_{TG}$ , i.e. a loss of charge carriers in the QW, can be traced back to electrons that relaxed into energetically deep trap states, in which they are robustly localized and do not contribute to the transport anymore. Potential trap states in the amorphous  $Al_2O_3$  layer can be found in literature [159–162].

## 7 Gating response of various III-V heterostructures

---

As shown by Choi et al. [159], inside the  $\text{Al}_2\text{O}_3$  layer aluminum and oxygen vacancies introduce acceptor levels, whereas aluminum interstitials generate deep donor states. Oxygen interstitials, on the other hand, form deep electron trap states. Furthermore, the antibonding state of an As-As dimer at the InGaAs interface generates energy states, situated right under the conduction band edge. Since the As-As dimer state is not removed by the self-cleaning ALD-process (see [136]), it forms a further acceptor state at the interface. In total, this robust trapping of electrons leads to an asymmetric charge transfer between up- and down-sweep of  $V_{TG}$ . The electric field, caused by the electrons inside the trap states, partially compensates the applied electric field from the TG during the down-sweep. This results in a smaller electron density inside the QW for regime VI than in regime I at the same  $V_{TG}$  value. We want to note that the charge transfer rate back to the QW is also influenced by the DOS of the initial and final states. According to Fermi's golden rule, the final-state DOS directly enters the transition probability, i.e. the charge transfer rate from one state to another, creating an asymmetry for the charge transfer process between energy states of different dimensions, i.e. from the 2DEG towards a localized (zero dimensional) state and vice versa.

Further measurements on a top-gated Hall bar sample C160406B1 (shown in the appendix B), in which the InAlAs spacer thickness is reduced from  $130\text{nm}$  to  $35\text{nm}$ , gives further weight to our model: For small positive TG-voltages, i.e.  $V_{TG} = +0.4\text{V}$ , the charge density inside the QW already starts to saturate at  $n_s = 4 \cdot 10^{11}\text{cm}^{-2}$  after the linear gating regime I. Gating regimes II and III, which are based on the presence of a metastable state inside the InAlAs spacer layer, are not developed in the gating response of this heterostructure. We conclude that electrons tunnel directly from the QW into interface states, whereby the charge density curve smoothly flattens and starts to evolve to the saturation density, corresponding to the initial density situation of  $V_{TG} = 0\text{V}$ . This clear dependence of the saturation mechanism on the spacer thickness is a further indication for the validity of our charge transfer model, which, as we want to emphasize here, is based on step-by-step tunnel processes via InAlAs defect states rather than lateral charge transfer from the ohmic contacts into the interface states.

Furthermore, we want to note that to the best of our knowledge, there is no equivalent undoped material system, which shows such a peculiar gating response as our heterostructures, i.e. a robust decrease in charge density with increasing  $V_{TG}$ . Studies on undoped Si/SiGe 2DEGs revealed a saturation of  $n_s$  for sufficiently positive  $V_{TG}$ , followed by a total breakdown of the current at high TG-voltages [98, 179, 180]. This behavior can be well understood in the framework of our charge transfer model. The general absence of gating areas II and III in other undoped material systems point out the importance of the InAlAs deep level donor sites for the electric stability of our system.

In the following, our qualitative model will be substantiated with quantitative considerations.

**Quantitative verification of charge transfer model** To verify the developed model above, we consider the first measurement sequence of sample *G* in figure 7.7:

## 7.2 Chemical treatment and different surface terminations

For the first linear gating regime I, ranging from  $-1V \leq V_{TG} \leq +1V$ , we determine the capacitive coupling  $c_I$  between the TG-electrode and the 2DEG as

$$c_I = \frac{\partial n}{\partial V} = 3.45 \cdot 10^{11} \text{ cm}^{-2} \text{ V}^{-1} .$$

Extrapolating this linear dependence with  $c_I$  in gating area II to IV, i.e.  $+1.2V \leq V_{TG} \leq +2.4V$ , yields  $n_s^{\text{target}}(V_{TG} = +2.4V) = 11.7 \cdot 10^{11} \text{ cm}^{-2}$  at the end of regime IV. Yet, in the experiment we find  $n_s(V_{TG} = +2.4V) \equiv n_s^{\text{exp}}(V_{TG} = +2.4V) = 4.6 \cdot 10^{11} \text{ cm}^{-2}$ . This corresponds to a charge deficiency  $\Delta n_{II \rightarrow IV}$  of

$$\Delta n_{II \rightarrow IV} = n_s^{\text{target}}(V_{TG} = +2.4V) - n_s^{\text{exp}}(V_{TG} = +2.4V) = 7.1 \cdot 10^{11} \text{ cm}^{-2} .$$

In the saturation regime V, the electron accumulation at the InGaAs/Al<sub>2</sub>O<sub>3</sub> interface leads to a shorting of the QW and to the onset of screening. As a result, increasing  $V_{TG}$  in regime V solely leads to an increase of the interface charge density. Even though, we do not measure any change of the electron density inside the QW in this gating area, we are able to calculate the particular capacitive coupling  $c_V$  from the gate electrode to the interface conductive layer, since we know the values of the permittivity of the participating layer. With  $\varepsilon_{\text{Al}_2\text{O}_3} = 7.81$ , experimentally deduced in subsection 7.2.2, we find

$$c_V = \frac{\varepsilon_0 \cdot \varepsilon_{\text{Al}_2\text{O}_3}}{e \cdot d_{\text{Al}_2\text{O}_3}} = 8.62 \cdot 10^{11} \text{ cm}^{-2} \text{ V}^{-1} .$$

By means of  $c_V$ , we can estimate the charge density  $\Delta n_V$ , which is accumulated in the conductive layer at the interface in the bias interval V, which is  $\Delta V_{TG} = 4V - 2.4V = 1.6V$ :

$$\Delta n_V = c_V \cdot \Delta V_{TG} = 1.38 \cdot 10^{12} \text{ cm}^{-2} .$$

During the downsweep in regime VI, we experimentally determine the capacitive coupling constant  $c_{VI}$  as

$$c_{VI} = \frac{\partial n}{\partial V} = 1.16 \cdot 10^{11} \text{ cm}^{-2} \text{ V}^{-1} .$$

As described in our charge transfer model in the preceding subsection, we assign the reduced capacitive coupling in VI as compared to I to the partial back transfer of electrons from the interface and the dielectric to the probed QW.

In the following, we test our determined values for the density loss  $\Delta n_i$  and the capacitive coupling constants  $c_i$  by comparing the calculated size of the hysteresis with the experimentally determined one. We exemplarily choose the measurement point  $V_{TG} = +1V$  (see figure 7.7). The experimentally determined size of the hysteresis, i.e.  $\Delta n_s^{\text{exp}}(V_{TG} = +1V)$ , short labeled as  $\Delta n_s^{\text{exp}}$ , is

$$\Delta n_s^{\text{exp}}(V_{TG} = +1V) = n_I(V_{TG} = +1V) - n_{VI}(V_{TG} = +1V) = 5.1 \cdot 10^{11} \text{ cm}^{-2} .$$

## 7 Gating response of various III-V heterostructures

From our charge transfer model,  $\Delta n_S^{theo}(V_{TG} = +1V)$ , short labeled as  $\Delta n_S^{theo}$ , should be composed as

$$\Delta n_S^{theo} = \underbrace{\left[ \Delta n_{II \rightarrow IV} + \Delta n_V \right]}_{(i)} - \underbrace{\left[ c_V \cdot (4V - 3V) \right]}_{(ii)} + \underbrace{\Delta c \cdot (3V - 1V)}_{(iii)} + \underbrace{c_{VI} \cdot (3V - 1V)}_{(iv)},$$

with  $\Delta c = c_I - c_{VI}$ . Here, the term (i) denotes the sum of the total density deviation of the experiment from the theoretical estimation in the regimes II to IV, (ii) accommodates for the removed charge from the interface bypass via the field-effect during the down-sweep from  $V_{TG} = +4V$  until capacitive coupling to the QW is restored at  $+3V$ , (iii) specifies the parallel charge transfer back to the QW from the interface, expressed as the difference in capacitive coupling for up- and down-sweep and (iv) describes the field-effect from the TG downsweep. Correspondingly, we obtain

$$\begin{aligned} \Delta n_S^{theo} &= \underbrace{\left[ 7.1 \cdot 10^{11} cm^{-2} + 1.38 \cdot 10^{12} cm^{-2} \right]}_{(i)} - \\ &\quad - \underbrace{\left[ 8.62 \cdot 10^{11} cm^{-2} \right]}_{(ii)} + \underbrace{4.6 \cdot 10^{11} cm^{-2}}_{(iii)} + \underbrace{2.32 \cdot 10^{11} cm^{-2}}_{(iv)} \\ &\approx 5.3 \cdot 10^{11} cm^{-2}. \end{aligned}$$

By comparing  $\Delta n_S^{theo}$  with  $\Delta n_S^{exp}$ , we find

$$\Delta n_S^{exp} = 5.1 \cdot 10^{11} cm^{-2} \approx 5.3 \cdot 10^{11} cm^{-2} = \Delta n_S^{theo}.$$

This shows a quantitative excellent agreement between experiment and calculation and gives further weight to our developed charge transfer model as it proves our assignments of the loss of capacitive coupling to the QW and the corresponding physical processes, to be correct.

## Conclusion

In this subsection, we studied the gating response of a newly grown  $In_{0.75}Ga_{0.25}As/In_{0.75}Al_{0.25}As$  heterostructure with a reduced cap thickness (from  $d_{cap} = 5nm$  to  $2.5nm$ ) in order to eradicate the parasitic conductive layer at the semiconductor/dielectric interface at small positive  $V_{TG}$ . However, we find that a mere reduction of  $d_{cap}$  does not substantially improve the gating response of the system. To expand the density interval, in which we are able to tune the charge density of the QW before charge migration sets in, we have to apply an additional wet-chemical cleaning step prior to the ALD process, to remove residual native oxides at the semiconductor interface. We find this additional cleaning step



to be crucial in order to ensure a high reproducibility of the 2D transport characteristics between different fabricated gated Hall bar devices. For these surface-treated samples, we can generally identify six characteristic gating areas in our measurement sequence: In gating area I, the charge density of the QW increases linearly with rising  $V_{TG}$ . After reaching a peak electron density, the density curve smoothly flattens into gating regime II, followed by a significant drop of the charge density in regime III. Here, when we adjust a new  $V_{TG}$ , the system requires a settling time of several minutes before  $n_s$  is stabilized. In regime IV, the system smoothly transits into the saturation area V, which is characterised by a total loss of capacitive coupling to the QW. Reducing  $V_{TG}$  in the down-sweep requires a sufficient decrease of  $V_{TG}$  before coupling to the 2DEG is restored in gating area VI. The final down-sweep reveals a pronounced hysteresis. By means of our experimental results in the gating studies of samples A to G, we are able to describe the underlying physical processes of the individual gating areas I to VI in terms of a charge transfer model. This phenomenological model description is further validated by a quantitative estimation: The linear gating area I is well described via the field-effect, where the metal gate electrode and the QW can be viewed as two plates of a capacitor. Increasing  $V_{TG}$  leads to an increase of  $n_s$ . In gating regime II, however, the system is no longer in equilibrium as the deep level donor states inside the InAlAs spacer are pulled under the Fermi level of the QW. A steep triangular potential barrier is created at the upper QW interface due to the trough-shaped InAlAs band profile in the external electric field of the TG. A sufficient increase of  $V_{TG}$  enables tunneling of the electrons into the deep level donor states. Initially, this process occurs only locally due to a non-uniform band profile, and then starts to spread evenly over the whole length of the channel, which leads to a drop in electron density in regime III. The additional electric field of the migrated electrons flattens the InAlAs band profile of the spacer. This causes an enlargement of the triangular InAlAs tunnel barrier, which thereby evolves towards opacity, i.e. a diminishing of electron migration. After a sufficient settling time, the system is then found to be in a metastable state, in which electron migration is effectively stopped. The transferred electrons are localized at InAlAs defect sites of the spacer layer. Since these defect states are laterally not conducting, capacitive coupling to the QW is still maintained until the band profile is sufficiently tilted when  $V_{TG}$  is further increased. Electron transfer from the InAlAs deep level donor states into energy states at the InGaAs/Al<sub>2</sub>O<sub>3</sub> interface sets in (regime IV). As soon as the charge density at the interface exceeds a critical charge density  $n_c$ , the charge accumulation at the interface becomes fully conducting. This leads to a shorting of the underlying QW, marked as gating area V in our measurement sequence. Since the electron mobility at the interface is substantially lower than the mobility inside the QW, we continue to predominantly measure the charge density of the QW in a MT measurement. To restore capacitive coupling to the QW in the down-sweep in regime VI, the parasitic interface channel has to be depleted again. This is achieved by a sufficient reduction of  $V_{TG}$ . The hysteresis between up- and down-sweep is caused by residual electrons, which are effectively trapped in interface and acceptor states inside the dielectric.

We conclude that the linear and non-hysteretic gating area I in the heterostructure is limited

by charge migration from the QW into intrinsic deep level donor states for sufficiently high TG-voltages. In comparison to other undoped material systems, such as for example Si/SiGe heterostructures [98, 179, 180], charge migration from the QW towards the interface at high values of  $V_{TG}$  leads to a saturation of  $n_s$  of the QW. In these studies, a total breakdown of the current is expected for a sufficiently conductive charge accumulation at the interface. This behavior differs from our experimental results in that it lacks the creation of a metastable state of the system, i.e. gating areas II and III. A key distinction of our studied system is the presence of the doping providing deep level donor states inside the InAlAs layer, which lead to an intrinsic distortion of the band profile of the InAlAs spacer layer in a trough-shaped manner. This important distinguishing feature further confirms the crucial role of the InAlAs deep level donor states for our experimentally observed gating behavior.

From the comparison of samples *B*, *C* and *D*, for which residual native oxides are still present at the semiconductor/dielectric interface, to the surface-treated samples *E*, *F* and *G*, we find the interface termination and thus the corresponding interface density of states to significantly determine the onset of gating area II. By reducing the interface density of states for samples *E*, *F* and *G*, we were able to gain full electrostatic control of the system for charge densities as high as  $n_s > 7 \cdot 10^{11} \text{ cm}^{-2}$ . This presents a doubling of the maximum achievable electron density as compared to the samples studied in chapter 6. In a next step, we test the gating response of the heterostructure, for which the low-band gap cap material InGaAs is completely removed by wet-chemical etching since it introduces additional interface states.

### 7.2.4 In<sub>0.75</sub>Al<sub>0.25</sub>As surface termination

In the last subsection, we found charge migration into deep level donor states inside the InAlAs spacer layer, as well as towards the semiconductor/dielectric interface to be efficiently suppressed when the interface density of states is sufficiently reduced by the chemical removal of residual native oxides on the semiconductor surface. However, due to the lower band gap of InGaAs as compared to the spacer material InAlAs, the thin InGaAs capping provides additional energy states at the interface. In an attempt to further extend and stabilize the linear gating response of the 2DEG before charge migration sets in, we completely remove the InGaAs cap layer by wet-chemical etching<sup>2</sup>, whereby we create a surface termination with the high-band gap material InAlAs. As for the samples with an InGaAs surface termination, we apply a HCl-dip to the etched InAlAs surface prior to the ALD process in order to remove large parts of the residual oxides, which would introduce additional parasitic energy states at the surface.

For InAlAs in contact to air, Chou et al. [182] found a weak and composition-dependent Fermi level pinning. Their experiments clearly show that the pinning is related to the thickness of the (undoped) InAlAs spacer layer that separates the surface from a highly n-type doped conducting InAlAs channel, which is experimentally studied in

---

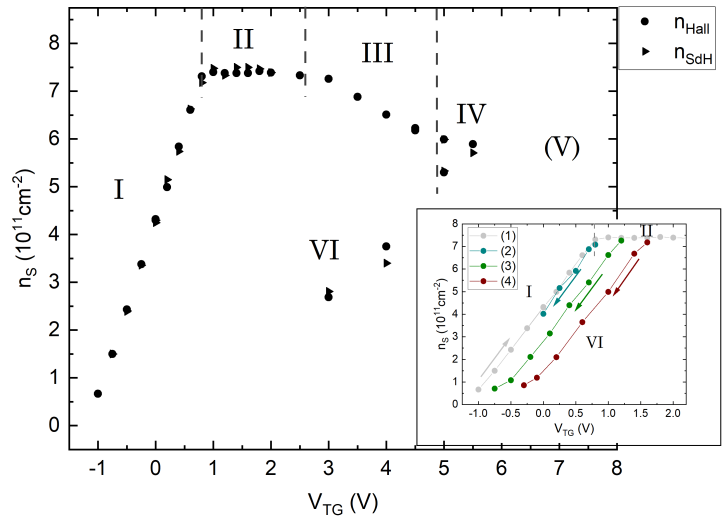
<sup>2</sup>etching-solution of  $\text{C}_6\text{H}_8\text{O}_7 : \text{H}_2\text{O}_2 : \text{H}_3\text{PO}_4 : \text{H}_2\text{O} = 22 : 2 : 1.5 : 88$

that publication. Shabani et al. [14] postulate a Fermi level pinning near midgap for undoped  $\text{In}_{0.75}\text{Al}_{0.25}\text{As}$ , however, without further reference. Similar to InGaAs, reports in literature imply that the self-cleaning effect of the TMA-pulse in the ALD process leads to a decrease of the density of states at the InAlAs/ $\text{Al}_2\text{O}_3$  interface, thus reducing the Fermi level pinning at the interface [156, 183, 184].

In the following, we present the gating response of our newly fabricated top-gated Hall bar device, sample *H*, with an InAlAs surface termination. Particularly, we focus on the extension of the linear gating area I before charge migration sets in.

### Description of the gating response of sample H

**Figure 7.12:** MT measurement sequences of sample *H* (wafer C160429A) in the non-illuminated state for  $V_{CD} = 0\text{V}$  at  $T = 4.2\text{K}$ . The Roman numerals I to VI label the constituent gating areas. The inset shows three additional measurement sequences (2) to (4) for different  $V_{TG}^{max}$  in gating area II. Sequence (1) presents the measurement shown in the main plot.



The main plot of figure 7.12 displays a MT measurement sequence of sample *H* with a  $V_{TG}^{max} = +5.5\text{V}$  before the subsequent down-sweep of  $V_{TG}$  is conducted. Again, we clearly identify six different gating areas in the measurement sequence, accordingly labeled with the Roman numerals I to VI in the plot. Furthermore, the inset of the figure displays three additional MT measurement sequences, marked as (2), (3) and (4), for which  $V_{TG}^{max}$  is chosen such that we do not exceed gating regime II before the final down-sweep back to  $V_{TG} = 0\text{V}$  is conducted. Sequence (1) is the measurement shown in the main plot.

Complementary, we analyse the longitudinal resistivity  $\rho_{xx}(B)$  of exemplary MT measurements of the gating regimes I to VI as shown in figure 7.13. As for the InGaAs surface-terminated samples *E*, *F* and *G*<sup>3</sup>, we find an extended linear gating interval I, in which we can robustly adjust the charge carrier density. The maximum achievable electron density is as high as  $n_s^{peak} = 7.5 \cdot 10^{11} \text{cm}^{-2}$ . A further increase in  $V_{TG}$  leads to a deviation from the linear gating response. However, in this second gating area II, unlike for InGaAs surface-terminated samples, we find  $n_s$  to saturate at  $n_s^{peak}$  and  $n_{Hall} = n_{SdH}$

<sup>3</sup>From now on, if we refer to *InGaAs surface-terminated* we assume surface-treated devices, i.e. samples *E*, *F* and *G*.

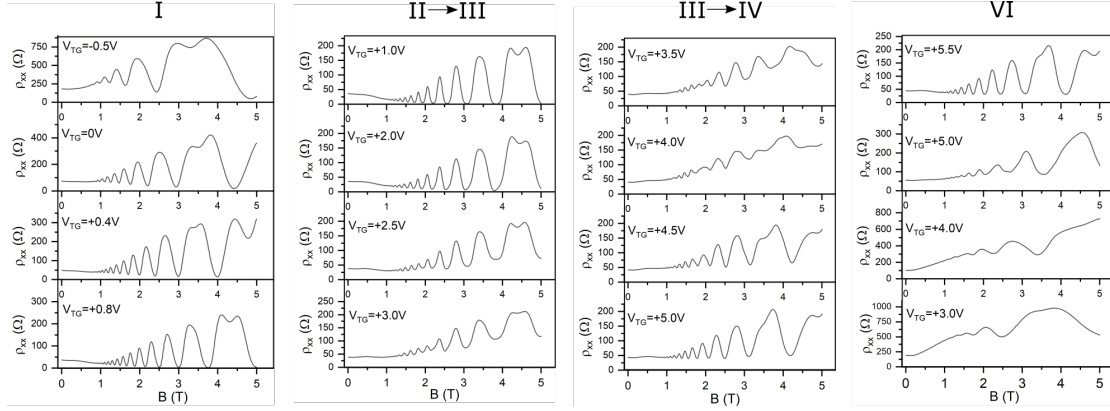


**Figure 7.13:** Exemplary MT measurements of sample *H* (wafer C160429A) in the non-illuminated state for  $V_{CD} = 0V$  at  $T = 4.2K$ : longitudinal resistivity  $\rho_{xx}(B)$  of the constituent gating areas I to VI as introduced in figure 7.12.

to be still valid. Yet, a settling time of several minutes is required for  $\rho_{xx}$  and  $\rho_{xy}$  to stabilize after a preceding sweep of  $V_{TG}$ . Decreasing  $V_{TG}$  in this second gating area, as it is shown in the inset of figure 7.12 for measurement sequences (2) to (4), reveals a hysteresis, which is a clear indication for charge migration from the QW towards defect states above. We find the magnitude of the hysteresis to scale with the applied  $V_{TG}^{max}$ . The longitudinal resistivity  $\rho_{xx}$  in gating areas I and II (see figure 7.13) shows no signs of parallel conduction. For  $V_{TG} > +2.5V$ , i.e. gating area III, however, a parabolic background in  $\rho_{xx}$  develops, together with a clear beating in the amplitude of the Shubnikov-de Haas oscillations. Furthermore, we find  $n_{Hall} \neq n_{SDH}$  in this gating regime. A FFT of  $\rho_{xx}$  over  $1/B$  reveals two closely-spaced frequencies in this newly entered gating area III. The origin of this second frequency in  $\rho_{xx}$  will be addressed in detail in chapter 9. Along with the arising background in  $\rho_{xx}$ , the charge density of the QW decreases with increasing  $V_{TG}$ , resembling the gating response of the previously analysed sample *G*. For a sufficiently high TG-voltage, i.e. regime IV with  $V_{TG} > +5V$ , a smooth saturation of the measured sheet density at  $n_s^{sat} \approx 5 \cdot 10^{11} cm^{-2}$  sets in where we find  $n_{Hall} = n_{SDH}$  again. The MT measurements of  $\rho_{xx}(B)$  in figure 7.13 display the absence of the parabolic background and also of the second frequency in the Shubnikov-de Haas oscillations. Decreasing  $V_{TG}$  in the down-sweep back to 0V (regime VI) displays a pronounced hysteresis.

As supplementary information, biased cool-down measurements of sample *H* are shown in the appendix in figure B.5(a). As for sample *A* (figure 7.3), we determine that a positive  $V_{CD}$  leads to an overall shift of the gating curve horizontally into positive  $V_{TG}$ -direction.

## Discussion

The gating response of the InAlAs-terminated sample *H* is equivalent to the gating behavior of InGaAs-capped samples: We find a similar  $n_s^{peak}$ , which terminates the

linear gating area I before charge migration sets in (regime II). In contrast to the charge migration in regime II of sample *G*, we find  $n_s$  of sample *H* to saturate at  $n_s^{peak}$  in this second gating area. Decreasing  $V_{TG}$  in II reveals a  $V_{TG}^{max}$ -dependent hysteresis. From this experimental observation, we infer that an increase of  $V_{TG}$ , and thus of  $n_s$ , in area II is compensated by a charge migration towards the interface. The electric field of the additional negative charge above the QW balances any increase of  $V_{TG}$ , which leads to the observed saturating behavior in  $n_s$ . Only after a charge density  $n_{loss} \approx 6.4 \cdot 10^{11} \text{ cm}^{-2}$  is transferred from the QW towards the interface<sup>4</sup>, a distinct decrease of  $n_s$  in the QW sets in at  $V_{TG} > 2.5 \text{ V}$ , i.e. the onset of gating regime III. Compared to sample *G*, the decrease of  $n_s$  with increasing  $V_{TG}$  is less steep. Hence, we conclude that the charge transfer from the QW into the InAlAs deep level donor states is hampered for the InAlAs-terminated sample *H*, indicating a modified intrinsic potential profile of the InAlAs spacer layer. We assume that the triangular potential barrier at the upper QW interface is less transparent as a result of a less pronounced trough-shaped InAlAs band profile. A reduced density of interface states for InAlAs surface-terminated samples results in less charge transfer from the deep level donor sites into the interface region, thereby leading to a flattening of the conduction band profile of the InAlAs spacer layer. A sufficient amount of negative charge has to be transferred into the interface region in regime II, generating a trough-shaped potential profile in the spacer. Only then, electrons can efficiently migrate into the deep donor states, creating a metastable state of the system in regime III. The pronounced hysteresis in gating area VI indicates that a larger portion of interface electrons remains fixed at deep trap states when the TG-voltage is reduced in sample *H* as compared to the InGaAs-capped case. For  $V_{TG} < +3 \text{ V}$ , i.e.  $n_s < 2.8 \cdot 10^{11} \text{ cm}^{-2}$ , no evaluable Hall measurement can be conducted anymore due to an apparent MIT. As compared to the gating regime I, this enlarged critical density, which is required for the system to become sufficiently conducting, is attributed to increased scattering at remote charged impurity sites, generated by the transferred electrons into deep trap states. This observation, combined with the longer settling time needed to guarantee a stable charge configuration inside the heterostructure after a change of TG-voltage, implies that there are less defect states available to which electrons are transferred from the QW. A smaller density of final transition states would cause smaller transition rates. This is also the case for regime II where any increase of electron density in the 2DEG is compensated by a loss of charge density of equal amount so that the measured electron density inside the QW stays the same.

### 7.2.5 Conclusion

In an attempt to expand the linear gating response of the InGaAs/InAlAs-based heterostructures and to gain a comprehensive understanding of the charge migration processes under the application of external gate electric fields, we studied the gating response of several

<sup>4</sup>With a capacitive coupling of  $c_H = 3.75 \cdot 10^{11} \text{ cm}^{-2}/\text{V}$ , increasing  $V_{TG}$  in II from  $+0.8 \text{ V}$  to  $+2.5 \text{ V}$  corresponds to the charge density  $n_{loss} = c_H \cdot \Delta V_{TG}^{II} \approx 6.4 \cdot 10^{11} \text{ cm}^{-2}$ .

## 7 Gating response of various III-V heterostructures

---

heterostructures, being equipped with differing surface terminations. For top-gated Hall bar samples with an InGaAs cap thickness of  $5\text{nm}$  (sample *A*), a parasitic conductive layer at the InGaAs/ $\text{Al}_2\text{O}_3$  interface is present already at  $V_{TG} = 0\text{V}$ . On the basis of a phenomenological charge transfer model we developed to describe the physical processes in our measurement sequences (see subsection 7.2.3), we explain this saturation behavior of sample *A* via the presence of a high density of interface states, which are energetically available even for  $V_{TG} = 0\text{V}$ . Electrons from the doping-providing InAlAs deep level donor states are efficiently transferred into these interface states at RT. For samples with a  $5\text{nm}$  InGaAs cap, the interface charge accumulation exceeds a critical density  $n_c$ , above which the interface layer becomes sufficiently conducting, whereby the underlying QW is shorted.

To annihilate this parasitic conductive layer, a new wafer is grown for which the InGaAs cap thickness is reduced to  $2.5\text{nm}$ . Only in combination with a chemical removal of residual native oxides, which create detrimental energy states at the semiconductor/dielectric interface, we achieve to substantially expand the linear gating area I, in which a robust and non-hysteretic gating response of the 2D system is present (samples *E*, *F* and *G*). For electron densities  $n_s > 7 \cdot 10^{11}\text{cm}^{-2}$ , the gating responses deviate from the linear behavior since charge migration from the QW into adjacent InAlAs deep level donor states sets in. This initial charge migration process is linked to the intrinsic band tilting, generated by the ionized deep level donor states inside the InAlAs spacer. Electron transfer from these doping sites into the QW and towards the interface results in the formation of a trough-shaped InAlAs band profile, facilitating charge migration at sufficiently high  $V_{TG}$ . Completely removing the InGaAs cap layer by wet-chemical etching leads to an apparent decrease of interface energy states, which manifests itself in form of an extended saturation area in gating regime II before a significant transfer of electrons into the deep level donor states sets in. On the basis of our measurement sequences, no further information about the exact Fermi level pinning and thereby on the intrinsic band tilting can be drawn for the InAlAs terminated samples. To our knowledge, there is no comparable study of the gating response of InAlAs surface terminated heterostructures. We are aware of a report in literature [14], in which MT measurements on a gated InAs/ $\text{In}_{0.75}\text{Ga}_{0.25}\text{As}/\text{In}_{0.75}\text{Al}_{0.25}\text{As}$  heterostructure with an InAlAs surface termination are conducted. However, only a narrow density interval of the gating response up to a maximum electron density of  $n_{Hall}^{max} = 5 \cdot 10^{11}\text{cm}^{-2}$  is shown. Therefore, we cannot compare our experimental findings beyond gating area I to reports in literature for a better assessment of our results.

In a first attempt to fabricate QPCs on InAlAs surface-terminated samples, we find the deposited  $\text{Al}_2\text{O}_3$  layers on the etched InAlAs surface to be prone to leakage current for  $d_{\text{Al}_2\text{O}_3} < 30\text{nm}$ . Commonly, this can be interpreted as an indication of a low-quality oxide formation with a large density of parasitic defect states inside the oxide, as well as at the semiconductor/dielectric interface. However, we find a high quality of the ALD-deposited oxide on InGaAs capped samples, processed during the same time period. The saturation of the charge density at  $n_s^{peak}$  in gating regime II of sample *H* furthermore

indicates a reduction of the interface defect density. Thus, we assume the etching process to greatly enhance surface roughness, whereby a thicker dielectric layer is indispensable to guarantee a closed and thereby insulating layer of  $\text{Al}_2\text{O}_3$  on top. As a downside, however, a thicker dielectric layer leads to a less well-defined potential profile created by the SG-electrodes inside the 2D channel for QPC formation. We recommend further tests on MBE-grown heterostructures with an InAlAs surface termination to study the influence of surface roughness on charge instabilities in the heterostructure.

Here, we conclude this subsection with the acquired evidence that charge migration from the 2DEG is induced by the presence of available InAlAs deep level donor states. We were able to eradicate the parasitic conductive layer at the semiconductor/dielectric interface and to double the electrostatically controllable charge density range in the heterostructures. This led to a perceptible increase of reproducibility of the transport characteristics. The acquired understanding of the electrostatic gating response of the heterostructure and the thereby modified processing recipe form the foundation for elaborated 1D transport measurements on QPCs in our high intrinsic SOI material system.

In the following section - as we learned from our measurement series that we are able to actively influence the intrinsic band bending of the InAlAs spacer layer via a modification of the interface density of states - we test a further approach to auxiliary suppress charge migration from the 2DEG.

## 7.3 Post-deposition thermal annealing

Post-deposition thermal annealing (PDA) is often applied for the activation of dopants after implantation processes, as well as for defect state passivation or healing of the bulk crystal and its interface. Generally, this results in a reduction of the interface density of states and also of the density of defect states inside the dielectric material [159, 162, 169, 171, 185].

In order to reduce the interface density of states in the gate stacking and to test whether the gating interval, in which the charge density of the 2DEG increases linearly with the applied TG-voltage, may be further extended, we apply an additional PDA step in our fabrication process.

### 7.3.1 Gating responses of annealed samples I - L

#### Fabrication details

To study the influence of PDA on the gating response of the heterostructure, we fabricate top-gated Hall bar devices, for which an additional annealing step is implemented. As an ambient atmosphere, we choose forming gas ( $10\%\text{H}_2 + 90\%\text{N}_2$ ) under a pressure of  $900\text{mbar}$ . We rapidly heat our samples from ambient temperature to  $350^\circ\text{C}$  and hold this temperature for several minutes. To test the influence of the PDA process on the

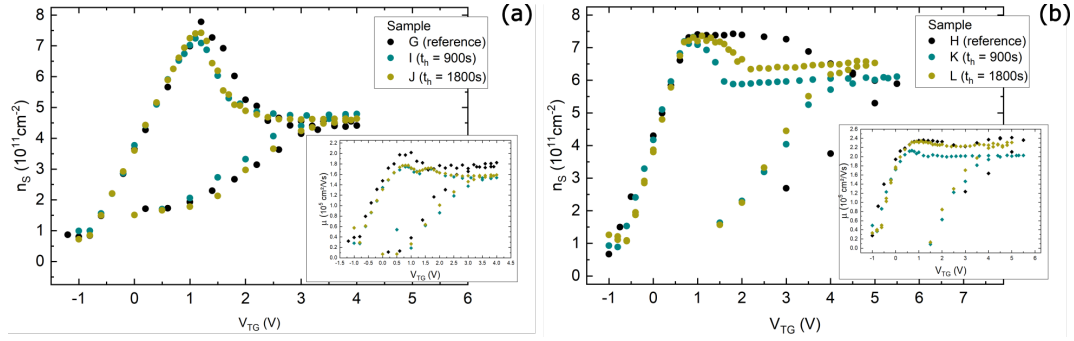


**Figure 7.14:** MT measurement sequences in the non-illuminated state for  $V_{CD} = 0\text{V}$  at  $T = 4.2\text{K}$ : **(a)** Gating response of the annealed samples *I* and *J* with an InGaAs surface termination, sample *G* for reference. The inset shows the corresponding mobility. **(b)** Gating response of the annealed samples *K* and *L* with an InAlAs surface termination, sample *H* for reference. The insets show the corresponding mobilities.

different surface terminations, we fabricate two InGaAs-capped Hall bar devices, labeled as samples *I* and *J*, from the same wafer as sample *G* (C160420B), and two further samples, labeled as samples *K* and *L*, from wafer C160428A, being equipped with an etched InAlAs surface. For samples *I* and *K* a hold time  $t_h = 900\text{s}$  at  $T_{PDA} = 350^\circ\text{C}$  is chosen, for samples *J* and *L* the hold time is extended to  $t_h = 1800\text{s}$ .

### Measurement sequences

Figure 7.14(a) shows the gating response of the InGaAs-capped samples *I* and *J*, together with the previously analysed measurement sequence of sample *G* as a reference. In figure 7.14(b), the measurement sequences of the InAlAs-terminated samples *K* and *L* are displayed, along with the measurement sequence of the already discussed sample *H* for reference. We find the gating curves of the annealed samples *I* and *J* to remarkably align with the measurement sequence of the non-annealed reference sample *G*: All curves can be divided into the previously defined characteristic gating areas I to VI, exhibiting approximately the same value for  $n_s^{peak} \approx 7.5 \cdot 10^{11} \text{ cm}^{-2}$  before a drop of the charge density in the 2DEG sets in (regime II and III). Furthermore, all three samples saturate at the same charge density of  $n_s^{sat} \approx 4.8 \cdot 10^{11} \text{ cm}^{-2}$  in gating regime V. When choosing the same  $V_{TG}^{max}$  for samples *G*, *I* and *J*, the strength of the hysteresis is also equal in magnitude. Hence, based on the gating response of the charge density, we cannot identify any difference between the InGaAs-capped samples with and without the additional implemented annealing step. Yet, the corresponding mobility of the annealed samples *I* and *J* (see inset of figure 7.14(a)) is lowered by about 10% as compared to the non-annealed reference sample *G*.

In contrast, the gating responses of the annealed InAlAs-terminated samples *K* and *L* differ from the response of the reference sample *H* (figure 7.14(b)). For all three



samples, we determine the same value of  $n_s^{peak}$  of around  $7.4 \cdot 10^{11} \text{ cm}^{-2}$ . However, whereas sample *H* saturates at this density value in regime II, the electron densities of the annealed samples *K* and *L* rapidly decrease and evolve into a gating regime similar to the characteristic gating area V presented for sample *G* in subsection 7.2.3: Here, an increase of  $V_{TG}$  only leads to a small increase in  $n_s$ . For sample *K* with  $t_h = 900\text{s}$  this saturation already sets in at  $V_{TG} = +1.8\text{V}$  at  $n_s = 5.9 \cdot 10^{11} \text{ cm}^{-2}$ , and smoothly evolves towards  $n_s = 6.1 \cdot 10^{11} \text{ cm}^{-2}$  at  $V_{TG} = +5.5\text{V}$ . Sample *L*, however, for which a longer annealing time of  $t_h = 1800\text{s}$  was applied, shows a less steep decrease of  $n_s$  in gating area II than sample *K*, and evolves into gating area V at  $V_{TG} = +2.2\text{V}$  with  $n_s = 6.3 \cdot 10^{11} \text{ cm}^{-2}$ , steadily increasing towards  $n_s = 6.5 \cdot 10^{11} \text{ cm}^{-2}$  at  $V_{TG} = +5.0\text{V}$ . This trend is in clear contrast to the non-annealed reference sample *H*, for which saturation does not emerge until  $V_{TG} > +5.5\text{V}$ . Remarkably, even though samples *K* and *L* saturate at  $V_{TG} = +1.8\text{V}$  and  $+2.2\text{V}$ , respectively, the capacitive coupling to the QW sets in almost immediately in the down-sweep of  $V_{TG}$  in gating area VI, in contrast to samples *G*, *I* and *J*. We are not able to comment on sample *H* in regard to this experimental finding, since the chosen  $V_{TG}^{max}$  is not located sufficiently far in regime V, where clear saturation effects would be observable. Furthermore, for all three InAlAs-terminated samples *H*, *K* and *L* (see inset in figure 7.14(b)), we observe a very similar  $V_{TG}$ -dependence of the mobility. The mobility of sample *K* with  $t_h$  of only 900s, however, is reduced by approximately 10% as compared to samples *H* and *L*.

## Discussion

We find the gating responses of the InGaAs-capped samples *I* and *J* to be unaffected by the PDA process. Thereby, we conclude that a heating of the semiconductor crystal to  $T_{PDA} = 350^\circ\text{C}$  has no measurable effect on the bulk crystal structure, as well as on the interface between InGaAs and  $\text{Al}_2\text{O}_3$ . For the InAlAs-terminated samples *K* and *L*, on the other hand, we find the gating behavior to be distinctly altered by the additional annealing step. In the framework of our charge transfer model (see subsection 7.2.3), the gating responses of samples *K* and *L* can be again divided into the previously defined gating areas I to VI. For both samples, we find a shortened gating regime II, that quickly evolves into gating area III. Therein, the charge density of the QW drops and fairly quickly reaches a saturation. We assign this shortening of gating areas II and III to a facilitated charge migration from the QW into upper lying defect states for InAlAs-terminated annealed samples. As the intrinsic band bending determines the onset of the charge transfer towards the interface, i.e. the onset of regime II, we conclude that a higher density of energy states at the InAlAs/ $\text{Al}_2\text{O}_3$  interface is likely to be present after annealing. The enhanced interface state density leads to an amplified charge transfer from the electron-providing deep level donor states inside the InAlAs spacer towards these interface states during cool-down. As a consequence, the trough-shaped InAlAs band profile (see figure 7.10) is more pronounced in the non-annealed case. In turn, this results in a narrowing of the tunneling potential at the upper InGaAs QW interface, making the barrier more transparent and creating a metastable state that provokes the earlier onset of

## 7 Gating response of various III-V heterostructures

---

charge transfer.

A second remarkable observation in the gating response of the InAlAs-terminated samples *K* and *L* is the early saturation-like behavior in gating area V, i.e.  $V_{TG} > +1.8V$  and  $V_{TG} > +2.2V$ , respectively. In these gating areas, we still have capacitive coupling to the QW, as can be seen from the immediate onset of the decrease of  $n_s$  in the down-sweep of  $V_{TG}$  (gating regime VI). We attribute this notable gating response in regime V to an equilibrated state of our system: An increase in  $V_{TG}$  leads to a charge transfer towards the interface, thereby balancing the increase of the external TG-field. Yet, we find no parallel conducting layer at the interface as in other samples, which indicates an increased surface roughness since with an electron transfer of more than  $\Delta n_{II \rightarrow V} > 18 \cdot 10^{11} cm^{-2}$  we still find the interface electron density to be smaller than the critical charge density  $n_c$ . The exact charge configuration and interface density of states in our devices is not directly accessible experimentally and we rely on probing it indirectly via measuring the gating response of our heterostructure in transport measurements. At the same time, our interpretation is in line with theoretical findings in the literature: In the framework of DFT model calculations, Chagarov et al. [156] simulated the electronic and chemical structure of annealed and non-annealed  $Al_2O_3/InGaAs$  and  $Al_2O_3/InAlAs$  interfaces. They found no modification of the bonding order in the InGaAs case since no additional defect states due to, e.g., material intermixing, are created, leaving the Fermi level position near midgap after PDA. For InAlAs, on the other hand, additional acceptor states inside the bandgap are created. In their simulations they found that substrate Al-atoms are pulled towards the  $Al_2O_3$  dielectric layer. Thereby, In-Al metal-metal bonds are created, as well as energy states due to the generation of dangling bonds of the two As-atoms, which were bonded to the Al-atom prior to the annealing process. These newly created energy states lead to a higher charge transfer rate from the QW towards the interface for sufficiently strong band-tilting.

Furthermore, there are reports in literature, describing an out-diffusion of In during thermal annealing [171, 173, 185]. However, this process should be observable for both of our studied surface terminations, i.e. InGaAs and InAlAs. Hence, we assume that this mechanism does not dominate the experimentally observed modification in the gating response of the InAlAs-terminated samples after PDA.

The differences observed between sample *K* with  $t_h = 900s$  and sample *L* with  $t_h = 1800s$  are still under debate. More statistics would be required to appreciate the reproducibility of our observations for both  $t_h$  values and certainly a few more  $t_h$  values would be needed to clearly detect any  $t_h$ -induced trend.

## Conclusion

In order to reduce the interface density of states, we tested the effect of a post-deposition annealing step of  $Al_2O_3$  in forming gas on the gating response for samples with an InGaAs cap layer, as well as for samples with an InAlAs surface termination. Whereas we find no significant modification in the InGaAs case, the gating behavior of InAlAs-terminated samples is distinctly altered. The experimentally observed shortening of the gating

intervals II to IV, followed by an extended saturation regime V, in which capacitive coupling to the QW is still maintained, implies an increased density of interface states after the annealing process. This is likely to be caused by material intermixing at the InAlAs/Al<sub>2</sub>O<sub>3</sub> interface, creating additional energy states at the interface, in compliance with the also observed reduced mobility in the gating areas II to VI.

On the bottom line, in terms of gating ability, we find no improvement of the transport characteristics for both surface terminations via the application of an additional PDA process. Since an In out-diffusion and an intermixing of the interface materials cannot be excluded also for the InGaAs-capped samples, we decided to omit this additional annealing step in the fabrication process of our devices for the remainder of this thesis.

Given the clear role of defect states at the interface, an interesting test presents the variation of the utilised dielectric material. In the subsequent section, we test the effect of MBE-grown MgO as dielectric, as well as Al<sub>2</sub>O<sub>3</sub> in combination with HfO<sub>2</sub> as interlayer on newly fabricated top-gated Hall bar devices. As surface termination, we choose InAlAs since we concluded in subsection 7.2.5 that the extended gating areas II and III of sample *H* imply a reduced density of interface states.

## 7.4 Variation of the dielectric material

We test the gating response of our heterostructure with MBE-grown MgO and HfO<sub>2</sub> in combination with Al<sub>2</sub>O<sub>3</sub> as alternative dielectric materials. As we consider InAlAs surface-terminated samples to exhibit a reduced interface density of states as compared to heterostructures with a thin layer of InGaAs as capping, we fabricate two new top-gated Hall bar devices, samples M and N, from wafer C160429A (same as for sample *H*), for which the InGaAs cap layer is removed by wet-chemical etching.

### Fabrication details

For sample *M*, we choose a thin layer of ALD-grown HfO<sub>2</sub> as a physical separation barrier between the Al-containing semiconductor surface and Al<sub>2</sub>O<sub>3</sub> in an attempt to prohibit material intermixing through exchange of Al atoms and the generation of additional interface states. Furthermore, ALD-grown HfO<sub>2</sub> presents a promising high-*k* dielectric material, as it was found to reduce the charge defect formation at semiconductor/dielectric interfaces and additionally controls the fixed charge density and polarity inside a subsequent Al<sub>2</sub>O<sub>3</sub> layer [186]. In addition, a self-cleaning effect of ALD-grown HfO<sub>2</sub> is shown in literature, as native oxides are efficiently removed from III-V surfaces during the deposition process, leading to an unpinning of the Fermi level at the semiconductor surface [177, 187–189].

For the ALD deposition of HfO<sub>2</sub>, we use tetrakis-ethyl-methyl-amino-hafnium (TEMAH) as the precursor and H<sub>2</sub>O as the oxidation source. In contrast to Al<sub>2</sub>O<sub>3</sub>, the HfO<sub>2</sub> deposition process highly depends on the applied process temperature [189], as well as on the individual pulse times for TEMAH and H<sub>2</sub>O [190]. Thus, in order to guarantee

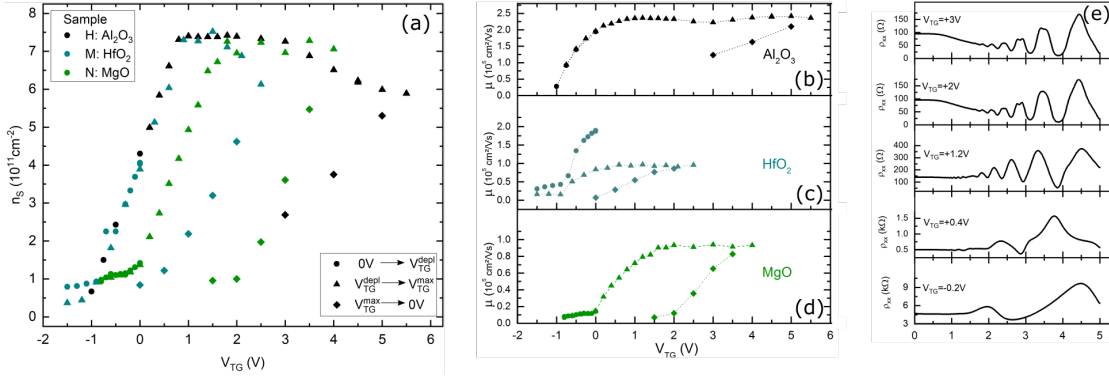


**Figure 7.15:** MT measurement sequences of sample *H* with Al<sub>2</sub>O<sub>3</sub>, sample *M* with HfO<sub>2</sub>/Al<sub>2</sub>O<sub>3</sub> and sample *N* with MgO/Al<sub>2</sub>O<sub>3</sub> (wafer C160429A) in the non-illuminated state for  $V_{CD} = 0\text{V}$  at  $T = 4.2\text{K}$ : **(a)** Charge density  $n_s$  as a function of  $V_{TG}$  of samples *H*, *M* and *N*. **(b - d)** Mobility responses of sample *H* (b), *M* (c) and *N* (d). The different symbols indicate the corresponding sweep directions of  $V_{TG}$ . **(e)** Exemplary MT measurements of sample *N*, displaying the longitudinal resistivity  $\rho_{xx}(B)$  for different  $V_{TG}$  ranging from  $-0.2\text{V}$  (undermost curve) to  $+3.0\text{V}$  (topmost curve).

electric insulation between the metal gate and the semiconducting layers, we additionally deposit several nanometers of Al<sub>2</sub>O<sub>3</sub> on top of HfO<sub>2</sub>. This is done in a single ALD process, whereby we thoroughly purge the reaction chamber with N<sub>2</sub> between the HfO<sub>2</sub> and Al<sub>2</sub>O<sub>3</sub> deposition to reduce any intermixing of these two dielectrics.

For sample *N*, we use MBE-grown MgO as the dielectric material, which presents itself as an attractive alternative to the ALD-deposited Al<sub>2</sub>O<sub>3</sub> and HfO<sub>2</sub>. The MBE growth process does not rely on iterative chemical reactions between two chemical compounds, which is often accompanied by the formation of detrimental by-products, as is the case for ALD. Instead, highly purified source materials are used in an UHV chamber, whereby, in principle, the formation of intrinsic defect states is greatly suppressed. An illustration for the superior quality of the bulk MgO crystal can be found in the application of MgO as a tunnel barrier in spin-injection experiments [191, 192], in which a high-purity barrier material is required. We choose a MgO layer thickness of  $50\text{nm}$ , followed by a thin layer of ALD-deposited Al<sub>2</sub>O<sub>3</sub>.

## Measurement sequences

Figure 7.15(a) shows the gating responses of samples *M* (HfO<sub>2</sub>/Al<sub>2</sub>O<sub>3</sub> as dielectric) and *N* (MgO/Al<sub>2</sub>O<sub>3</sub> as dielectric), together with the measurement sequence of sample *H* (Al<sub>2</sub>O<sub>3</sub> as dielectric) as a reference. For sample *M*, a  $V_{TG}^{\text{max}}$  of  $+2.0\text{V}$  is chosen; for sample *N*, we apply a  $V_{TG}^{\text{max}}$  of  $+4.0\text{V}$ . As supplementary information, positively biased cool-down MT measurement sequences of sample *H*, *M* and *N* are shown in the appendix in figure B.5. A positive  $V_{CD}$  shifts the gating curves of samples *M* and *N* horizontally into positive

$V_{TG}$ -direction as we also find for sample  $H$ . The gating responses of samples  $M$  and  $N$  in figure 7.15(a) resemble the measurement sequence of sample  $H$  and can be divided into the characteristic gating areas, defined in the charge transfer model in subsection 7.2.3. The gating curve of sample  $N$ , however, is shifted horizontally into positive  $V_{TG}$ -direction as compared to the gating responses of samples  $H$  and  $M$ . As can be deduced from the slope of the density curves in gating area I, all three samples exhibit a very similar capacitive coupling  $c = \frac{\partial n}{\partial V}$  to the 2DEG. Since for sample  $M$ , we only deposited a thin layer of  $\text{HfO}_2$  in addition to the much thicker dielectric layer of  $\text{Al}_2\text{O}_3$ , the  $\text{Al}_2\text{O}_3$  layer dominates the contribution of the dielectric layers to the capacitive coupling between the TG and the 2DEG. Thus, the gating response of sample  $M$  should indeed be equal to the density response of our reference sample  $H$  in gating area I. For sample  $N$ , we understand the similarity of the experimentally observed capacitive coupling to samples  $M$  and  $H$  by means of the equivalent permittivity  $\epsilon_{\text{MgO}}$  to  $\epsilon_{\text{Al}_2\text{O}_3}$  [193]. At the end of gating interval I, samples  $M$  and  $N$  both reach  $n_s^{\text{peak}} = 7.4 \cdot 10^{11} \text{ cm}^{-2}$  just as the reference sample  $H$ , and then evolve into gating regime II. For sample  $M$ , however, we find a shortened gating interval II and III, before the charge density saturates at  $n_s^{\text{sat}} \approx 6 \cdot 10^{11} \text{ cm}^{-2}$  (see also in the appendix B in figure B.5(b)). The charge density response of sample  $N$  follows the gating behavior of the reference sample  $H$ , exhibiting an extended gating area II and a comparable hysteresis between up- and down-sweep of  $V_{TG}$ . At the same time, the mobility responses of samples  $M$  and  $N$ , plotted in figure 7.15(b), (c) and (d), differ significantly from sample  $H$ . During the first down-sweep of  $V_{TG}$  from 0V into negative  $V_{TG}$ -direction after the cool-down, sample  $M$  exhibits a similar mobility as the reference sample  $H$ . In the following up-sweep of  $V_{TG}$ , however, we determine that the mobility is decreased by almost a factor of two as compared to sample  $H$ . The mobility of sample  $N$  is generally about half the value of the reference sample  $H$ .

### Discussion

In summary, for sample  $M$ , which is equipped with a thin interlayer of  $\text{HfO}_2$  between  $\text{InAlAs}$  and  $\text{Al}_2\text{O}_3$ , we determine an earlier onset of charge migration towards the interface compared to the reference sample  $H$ . Building on our charge transfer model, we assign this behavior to the presence of an enhanced charge density at the interface. The significant reduction of the electron mobility after the first down-sweep of  $V_{TG}$  can be attributed to a band tilting-induced reorganization of charge carriers in the gate stack, induced by the  $\text{HfO}_2$  interlayer. Owing to the  $\text{HfO}_2$  layer, Coulomb scattering centers are additionally introduced into the heterostructure, which increase the scattering rate of the conduction electrons. Yet, we want to note that this hysteresis in mobility does not manifest itself in the corresponding gating response of the charge density. For sample  $N$  with  $\text{MgO}$  as additional dielectric for the physical separation of the  $\text{Al}$ -containing semiconductor surface and  $\text{Al}_2\text{O}_3$ , we find the gating response to be equivalent to our reference sample  $H$ . In contrast to the density response, the mobility is significantly reduced as compared to sample  $H$ . This indicates a strongly increased large-angle backscattering with  $\text{MgO}$  as dielectric in contrast to  $\text{Al}_2\text{O}_3$ . The horizontal shift of the gating curve into positive voltage direction

implies an increased negative charge accumulation between the metal gate electrode and the QW, which effectively reduces the electric TG-field at the QW. Accordingly, the reduced mobility for device  $N$  can be assigned to increased Coulombic disorder due to the additional negative charge. This deduction, however, is rather inconsistent to auxiliary conducted biased cool-down measurements with sample  $N$  (see appendix B), with which a similar horizontal shift of the gating curve can be deliberately induced with an appropriate  $V_{CD}$ . This shift is also understood as accumulated charge above the QW. Yet, we observe no significant reduction in mobility in the respective measurement.

A peculiar experimental finding in the MT measurements of the longitudinal resistivity  $\rho_{xx}(B)$  of sample  $N$  is displayed in figure 7.15(e). Even for small values of  $n_{Hall}$ , we find a distinct knot in the Shubnikov-de Haas oscillations, for example at  $B = 1.5T$  at  $V_{TG} = +0.4V$ . Evaluating the FFT spectra of  $\rho_{xx}(B)$ , however, provides no further insight into the origin of the B-field-dependent magnetooscillation damping, owing to the limited number of available oscillations in  $\rho_{xx}(B)$ . Furthermore, with good reason, we can exclude the population of a second size-quantized subband to be the origin of our observed modulation of the Shubnikov-de Haas amplitude. Since we maintain the capacitive coupling between the TG and the 2DEG even for higher  $V_{TG}$ , we are able to also exclude a parasitic conductive layer in the system as the possible cause. The exact origin of this conspicuous effect is still unknown.

### Conclusion

In our test of MBE-grown MgO and of HfO<sub>2</sub> as interlayer dielectrics, we find both materials to exhibit adverse effects on the gating response of the heterostructure compared to reference samples with ALD-deposited Al<sub>2</sub>O<sub>3</sub>: We determine an enhanced charge migration and a significant reduction of the electron mobility for samples  $M$  and  $N$ . It is interesting to note that all of our tested dielectrics are based on oxidic-materials. Possible As-O bond formation creates midgap states at the semiconductor/dielectric interface [156], being likely responsible for enhanced charge migration towards the interface and for charge trapping. We therefore propose to test non-oxide based materials, e.g. h-BN, as dielectric materials.

## 7.5 Charge carrier mobility and scattering sources

In the course of this chapter, the mobility responses of samples  $A$  to  $N$  have been already displayed along with the corresponding gating responses of the charge density. In the following, in order to determine the dominating scattering sources in the heterostructure which limit the mobility and also affect the transport in our QPC devices, we evaluate the density-dependence of the electron mobility in the system. Furthermore, we examine the elastic mean free paths of the conduction electrons in the different heterostructures that we analysed in the course of this chapter, enabling us to determine the most suitable gate

stacking for QPC applications.

### 7.5.1 The charge carrier mobility

In a metal/dielectric/semiconductor heterostructure, there are several scattering mechanisms which may affect the resistivity of the system. The impact of an individual scattering source on the conduction electrons further depends on the charge density of the system since the screening ability of charged Coulomb disorder is linked to  $n_s$ . We can neglect scattering on acoustic and optical phonons in our mobility analysis owing to the cryogenic temperatures at which our measurements are conducted. Furthermore, since our semiconductor heterostructures are fabricated via MBE growth, various scattering mechanisms such as growth-related roughness at the QW interfaces are typically suppressed due to the utilisation of highly purified source material and the low residual ambient pressure in the UHV chamber during the epitaxial growth process. The long-range surface modulation due to cross hatching on the micrometer scale (see section 5.1) should play a minor part in our observed scattering events, given that the analysed 2DEGs are typically buried deeper than  $100\text{nm}$  below the sample surface. We therefore assume Coulombic scattering and alloy disorder to be the most prominent mechanisms in the studied InGaAs/InAlAs heterostructures, limiting the electron mobility in the 2DEG. Our assumption is further supported with findings in pertinent literature [37–39, 50, 181, 194]. To test our hypothesis, we experimentally determine the dominating mechanism in our heterostructure by analysing  $\mu$  as a function of  $n_s$ . Therefore, we assume the power law relation

$$\mu \propto n_s^\alpha, \quad (7.5)$$

whereby the density-scaling exponent  $\alpha$  is determined by the type of disorder, which controls the resistivity and thereby the mobility in the system [181]. Furthermore,  $\alpha$  depends on a dimensionless parameter  $q_S = q_{TF}/2k_F$ , with  $q_{TF}$  being the Thomas-Fermi wave vector and  $k_F$  being the Fermi wave vector.  $q_S$  characterises the screening regime of the studied system:  $q_S \gg (\ll) 1$  implies a strong (weak) screening regime. The transition between strong and weak screening can be expressed in terms of a charge carrier density  $n$ :

$$n \ll (\gg) \left( \frac{m^*}{m_e \epsilon} \right)^2 \cdot 1.14 \cdot 10^{16} \text{cm}^{-2} \quad (7.6)$$

$\epsilon$  is the background static lattice dielectric constant and  $m^*$  is the effective electron mass [181]. Employing the determined permittivity for InAlAs of  $\epsilon_{\text{InAlAs}} = 13.7$  from subsection 7.2.2 and the effective mass  $m^* = 0.041 \cdot m_0$  from our cyclotron measurements (section 5.2) yields a threshold value of  $n = 1.03 \cdot 10^{11} \text{cm}^{-2}$  according to the above equation (7.6). Accordingly, in our analysed density range of  $n > 1.5 \cdot 10^{11} \text{cm}^{-2}$ , we are in the strong screening regime. Following the model of Das Sarma et al. [181], depending on the dominating scattering source,  $\alpha$  takes the following values:

## 7 Gating response of various III-V heterostructures

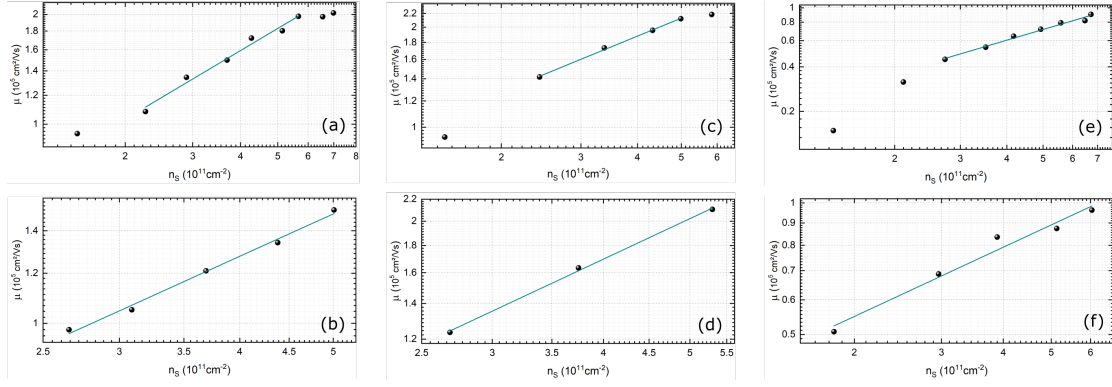


**Figure 7.16:** Log-log plot of  $\mu$  as function of  $n_s$  (dots) with linear fit (solid line) to determine the density scaling parameter  $\alpha$  for (a) sample G (up-sweep), (b) sample G (down-sweep), (c) sample H (up-sweep), (d) sample H (down-sweep), (e) sample M (up-sweep), (f) sample N (up-sweep).

$$\alpha \rightarrow 1/2 \quad \text{for scattering at unintentional background (3D) impurities} \quad (7.7)$$

$$\alpha \rightarrow 3/2 \quad \text{for scattering at remote (2D) impurities} \quad (7.8)$$

Figure 7.16 shows several log-log plots of  $\mu$  as a function of  $n_s$  of exemplary samples, analysed in the gating study in this chapter. In our evaluation, we are restricted to a density interval of approximately  $1.5 \cdot 10^{11} \text{ cm}^{-2} \leq n_s \leq 6.5 \cdot 10^{11} \text{ cm}^{-2}$  for the  $\alpha$ -fit (cyan solid curve) since for  $n_s > 6.5 \cdot 10^{11} \text{ cm}^{-2}$  charge migration towards the interface sets in, i.e. the end of the linear gating regime I, leading to a distinct modification of the Coulombic disorder in the system. Consequently, we determine the density-scaling exponent  $\alpha$  in the linear gating regimes I (up-sweep) and VI (down-sweep) of our MT measurement sequences.

The determined  $\alpha$ -values for samples A to N are listed in table 7.2. For some samples no meaningful value for  $\alpha$  could be determined in regime VI due to an early onset of the MIT. Evaluating regime I, we find  $0.5 < \alpha_{up} < 0.7$ . According to the relation (7.7), we identify scattering on 3D charged background impurities as the dominating mechanism in the gating area I. All of our analysed heterostructures are non-intentionally doped. The electron-providing InAlAs defect sites, which we assume to be evenly distributed in the InAlAs spacer layers, are partially ionized. Thus, we infer that these defect sites introduce the Coulombic disorder background potential in our studied material system. Evaluating the second linear gating regime in our MT measurement sequence, i.e. regime VI, we determine the density-scaling exponent  $\alpha_{down}$ . In comparison to  $\alpha_{up}$ , we find the values of  $\alpha_{down}$  to be increased to approximately 0.8. This clear trend of  $\alpha$  in all of our analysed samples implies a modification of the dominating scattering mechanisms in gating area VI as compared to area I. In our charge transfer model, we were able to clearly relate the measured charge density decrease in the 2DEG during gating areas II to V to



a substantial accumulation of electrons at the semiconductor/dielectric interface. This negatively charged 2D remote electron layer is likely to act on the conduction electrons in the QW as an additional scattering source. According to the model of Das Sarma et al. [181], this type of scattering mechanism corresponds to a  $\alpha$ -value of 1.5 (see relation (7.8)). Thus, we infer that the distinct increase of  $\alpha_{down}$  in regime VI as compared to  $\alpha_{up}$  in I reflects the effect of electron migration in gating areas II to V. Thereby, the contribution of 2D remote scattering to 3D impurity scattering is enhanced in our samples and the  $\alpha$ -values shift from 0.5 towards higher values. This further consolidates our developed charge transfer model.

sample	surface	$\alpha_{up}$	$\alpha_{down}$	$l_{mfp}^{max}$ ( $\mu m$ )	$n_{l_{mfp}^{max}}$ ( $10^{11} cm^{-2}$ )
A	InGaAs	0.6	(2.2)	2.0	3.8
B	InGaAs	0.6	0.8	1.7	4.3
C	InGaAs	0.9	/	1.7	5.2
D	InGaAs	0.6	/	2.0	5.4
E	InGaAs	0.6	0.6	2.5	6.9
F	InGaAs	0.5	0.8	2.5	6.9
G	InGaAs	0.7	0.8	2.7	7.0
H	InAlAs	0.7	0.8	3.4	7.4
I	InGaAs	0.7	0.8	2.4	6.7
J	InGaAs	0.7	1.0	2.4	6.9
K	InAlAs	0.5	0.7	2.9	7.0
L	InAlAs	0.7	0.8	3.3	7.4
M	InAlAs	0.5	/	2.0	4.0
N	InAlAs	0.7	/	1.3	7.0

**Table 7.2:** Density scaling exponent  $\alpha_{up}$ , determined in gating interval I, and  $\alpha_{down}$ , determined in gating interval VI, together with  $l_{mfp}^{max}$  and the corresponding  $n_{l_{mfp}^{max}}$  of samples A to N.

Our interpretation of the experimental findings with the  $\alpha$ -analysis is consistent with reports in literature: Shabani et al. [14] determined in their InAs/InGaAs/InAlAs heterostructure, in which a parasitic conductive layer at the semiconductor surface is present, an enlarged  $\alpha$ -parameter of 0.8 as compared to an equivalent heterostructure of Hatke et al. [108], for which the parasitic interface channel has been eliminated. There, the  $\alpha$ -value was found to be reduced to 0.5. They also attribute the enhancement of  $\alpha$  in [14] to the scattering at the remote surface channel, equivalently to our assignments of  $\alpha$ . Remarkably, we find no significant difference of the  $\alpha$ -parameter for InGaAs- and InAlAs-capped samples. Moreover, the variation of the dielectric material does not manifest itself in an alteration of the dominating scattering mechanism in gating area I, even though, we inferred in section 7.4 that the interface density of states, and thus the density of

## 7 Gating response of various III-V heterostructures

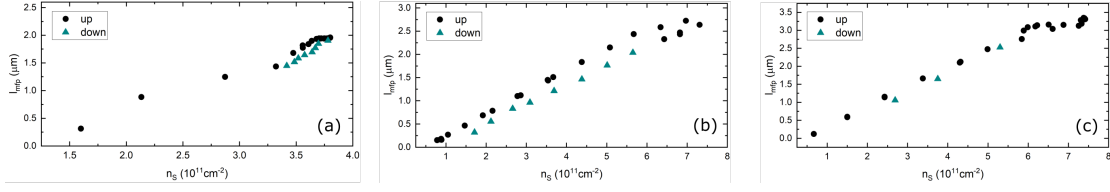


**Figure 7.17:** Elastic mean free path  $l_{mfp}$  as a function of charge carrier density  $n_s$ , determined from the gating sequences of (a) sample A (b) sample G (c) sample H. The dots indicate the determined  $n_s$  during the up-sweep of  $V_{TG}$  in gating area I and II, the triangle symbol indicate that the values of  $l_{mfp}$  are determined in gating area VI.

charged remote 2D scattering centers, is enlarged for samples *M* and *N* as compared to the reference sample *H* with  $\text{Al}_2\text{O}_3$  as dielectric.

We want to note that we were not able to determine a meaningful  $\alpha_{down}$ -parameter for two out of three InGaAs-capped samples without a chemical cleaning of the surface, i.e. sample *C* and *D*, as well as for sample *M* and *N*, being equipped with  $\text{HfO}_2/\text{Al}_2\text{O}_3$  and  $\text{MgO}/\text{Al}_2\text{O}_3$  as dielectric, respectively, since the curves could not be fitted with a single density-scaling exponent  $\alpha$ . This reflects the experimentally detected uncontrollability of the transport properties in these devices (therefore see sections 7.4 and 7.2).

### 7.5.2 The elastic mean free path

The physical quantity which marks the limits of our ballistic mesoscopic system is the elastic mean free path  $l_{mfp}$ . This quantity defines the length scale for elastic impurity scattering, evaluated at the Fermi energy:

$$l_{mfp} = v_F \tau_{tr} = \mu \cdot \sqrt{2\pi n_s} \cdot \frac{\hbar}{e}.$$

The determined values for the maximum mean free paths  $l_{mfp}^{max}$ , together with the corresponding charge density  $n_{l_{mfp}}^{max}$  for the samples *A* to *N* are listed in table 7.2. Furthermore, figure 7.17 shows  $l_{mfp}$  as a function of  $n_s$  for three exemplary samples *A*, *G* and *H*. Generally, we find  $l_{mfp}$  to increase with  $n_s$ . This can be attributed to an increased screening ability of the system with a rising charge density. Before the onset of the gating area II in the charge density response, we find the curve of  $l_{mfp}$  to flatten. We assign this behavior to the saturation in mobility in the corresponding density range, which we interpret as commencing scattering into the second size-quantized subband. This interpretation is further supported by the shift of the fully resolved Zeeman spin-splitting Landau levels towards higher B-field values, indicating a reduced quantum lifetime and thus an increase in scattering of the conduction electrons. However, before a significant second subband population sets in, charge migration towards the interface starts to take place, impeding a meaningful mobility analysis in gating areas II to V. A

further remarkable observation in the plots in figure 7.17 is the only marginal reduction of  $l_{mfp}$  in the down-sweep of  $V_{TG}$  in gating area VI as compared to the up-sweep in I. This is astonishing given that we were not able to conduct a MT measurement below  $n_s < 2 \cdot 10^{11} \text{cm}^{-2}$  due to an earlier onset of MIT, i.e. an increase of the critical density  $n_c$ . We interpret the increase of  $n_c$  in gating regime VI as follows: Electrons, which were initially transferred towards the interface in gating intervals II to V, partially stay as fixed additional negative charge at trap sites at or near the interface and in InAlAs defect states inside the spacer layer (see figure 7.10). This electron distribution, residing above the QW, effectively reduces the quantum lifetime  $\tau_q$  of the conduction electrons, thereby obscuring the Landau level oscillation in our MT measurement (figures 7.8 and 7.13). Since the mobility  $\mu$  in the gating response in regime VI is solely marginally reduced as compared to gating area I at the same charge density, we conclude that we obtain a similar large-angle back-scattering rate in areas I and VI. Yet, the total scattering rate, including small-angle scattering is enlarged in gating area VI, which thus influences  $\tau_q$ . A maximum mean free path  $l_{mfp}^{max} = 3.4 \mu\text{m}$  is determined for the InAlAs-terminated sample *H* at a charge density of  $7.4 \cdot 10^{11} \text{cm}^{-2}$ . The values of  $l_{mfp}^{max}$  of the other analysed InAlAs-terminated samples differ with respect to each other. For InGaAs-capped samples, for which residual native oxides are removed by wet-chemical etching prior to the ALD process, the values of  $l_{mfp}^{max}$  are consistently determined to be  $\approx 2.5 \mu\text{m}$  at a charge density of approximately  $7 \cdot 10^{11} \text{cm}^{-2}$ . This behavior reflects the high reproducibility of InGaAs-capped samples in contrast to samples with an InAlAs-etched surface. A MBE-grown InAlAs surface termination presents itself as interesting candidate to achieve large values of  $l_{mfp}^{max}$ .

## Conclusion

By studying the mobility response of our system, we find indications for the dominating scattering mechanism to be generated by charged background impurities inside the heterostructure. We ascribe the main contribution to this background Coulombic disorder to be generated by the InAlAs deep level donor states inside the barrier layers with a density of about  $3 \cdot 10^{16} \text{cm}^{-3}$ . Depending on the density of available interface states, which can be controlled by the application of an external electric field, scattering due to remote 2D Coulombic disorder comes into play. This can be nicely seen as a shift of the density-scaling exponent  $\alpha$  towards higher values, determined in the gating interval VI. The elastic mean free path in the systems is determined to be several times larger than the dimensions of our finger-gate defined QPC constrictions. This is an essential prerequisite to attain well-defined conductance steps in 1D transport measurements [18]. However, in addition to the limitation of the mobility in our system, the background impurity-induced disorder potential is still likely to impede the formation of a smooth saddle potential with the SG-electrodes in the 2DEG. Thus, as a next step, we attempt to reduce the MBE growth-related density of charged background impurities in our heterostructures, i.e. the InAlAs deep level donor states.

## 7.6 Towards the reduction of InAlAs deep level donor states

As described at the beginning of chapter 5, the electron-providing InAlAs deep level donor states are assigned to As-related antisite defects in the InAlAs barrier layers. In order to reduce the background Coulombic disorder potential in the system, we aim to decrease the density of these MBE growth-related defect states. Thus, we follow an experimental approach by Campion et al. [195], who reported a significant reduction of As-related antisite defects by employing  $\text{As}_2$  instead of  $\text{As}_4$  at low substrate temperatures for the epitaxial growth process of their GaMnAs layer films. Equivalently to a MBE growth study of Chen et al. [38], we transfer these modified growth parameters from Campion et al. [195] to the epitaxy of our  $\text{In}_{0.75}\text{Ga}_{0.25}\text{As}/\text{In}_{0.75}\text{Al}_{0.25}\text{As}$  layer systems. By supplying  $\text{As}_2$  instead of  $\text{As}_4$  as group-V material during the MBE growth process, we fabricate two new wafer structures. The BEP of  $\text{As}_2$  is kept at  $8 \cdot 10^{-6} \text{ Torr}$ . We furthermore modify the substrate temperature  $T_{act}$  of the active layer to stress the influence of  $T_{act}$  on the InAlAs defect state formation: For wafer C170731A, we choose  $T_{act} = 430^\circ\text{C}$ , being similar to  $T_{act}$  of our previously analysed heterostructures during the course of this thesis. For wafer C170731B, we apply a reduced temperature of  $T_{act} = 330^\circ\text{C}$ . For better comparison with literature, we monitor and control the substrate temperature via a BandiT system in addition to the standardly used optical pyrometer.

wafer	$n_{vdP}^{dark} (\cdot 10^{11} \text{ cm}^{-2})$	$\mu_{vdP}^{dark} (\text{cm}^2/\text{Vs})$	$n_{vdP}^{ill} (\cdot 10^{11} \text{ cm}^{-2})$	$\mu_{vdP}^{ill} (\text{cm}^2/\text{Vs})$
C170731A	/	/	3.0	3000
C170731B	/	/	2.1	3000

**Table 7.3:** Transport properties determined via vdP measurements at  $T = 4.2\text{K}$ .

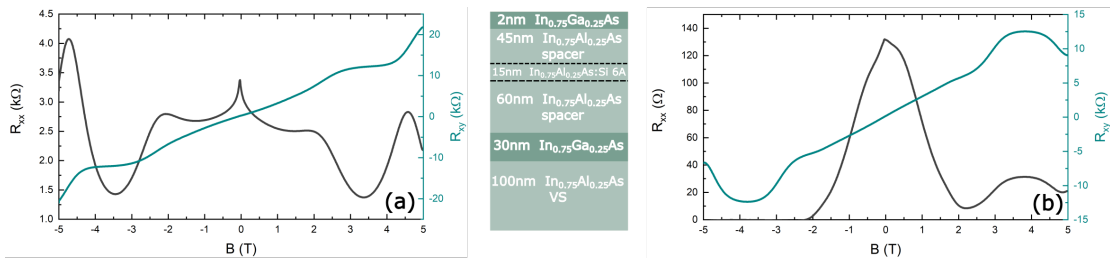


**Figure 7.18:** VdP Hall measurements of wafer (a) C170731A (b) C170731B in the illuminated state at  $T = 1.5\text{K}$ .

Figure 7.18 depicts a sketch of the newly grown heterostructure of wafers C170731A and C170731B. Since we expect the intrinsic doping density to be reduced by means of the adjusted growth-parameters, we introduce a  $15\text{nm}$  Si modulation doping layer

above the QW, whereby dopant segregation into the InGaAs QW is circumvented. The introduced Si doping density is  $n_{dop} \approx 2 \cdot 10^{11} \text{ cm}^{-2}$ . For rapid transport characterisation, we fabricate vdP samples. The corresponding Hall measurements in the illuminated state are shown figure 7.18(a) and (b). The determined electric transport properties are listed in table 7.3. As indicated by the backslash in the table 7.3, we are not able to drive a current through the vdP samples of both wafers in the non-illuminated state. Only after illumination, the samples become conducting, yet, we determine an exceptionally low mobility of only  $\mu_{vdP}^{ill} = 3000 \text{ cm}^2/\text{Vs}$  for both samples. Remarkably, however, for sample C170731A the determined electron density  $n_{vdP}^{ill}$  after illumination is only slightly higher than the introduced Si modulation doping density  $n_{dop}$ , for sample C170731B we even find  $n_{vdP}^{ill}$  to perfectly match  $n_{dop}$ . This is a clear indication of a tremendous reduction of the As-related antisite defects inside the heterostructure via utilisation of  $\text{As}_2$  instead of  $\text{As}_4$ .

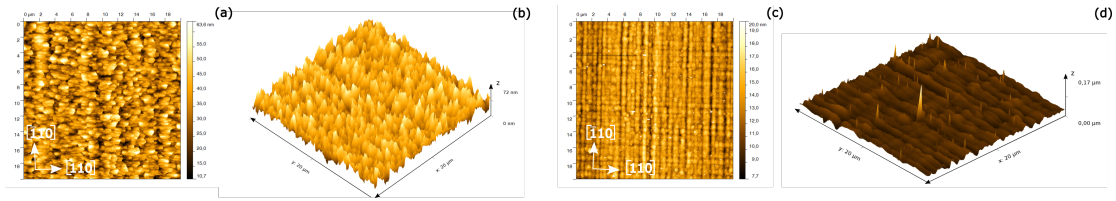


**Figure 7.19:** (a)  $20 \times 20 \mu\text{m}$  plan view AFM image of wafer C170731A (b) 3D plot of profile of wafer C170731A (c)  $20 \times 20 \mu\text{m}$  plan view AFM image of wafer C170731B (d) 3D plot of profile of wafer C170731B.

To comment on the tremendous mobility reduction in these heterostructures, we analyse the wafer surface via AFM as displayed in figure 7.19. Wafer C170731A with  $T_{act} = 430^\circ\text{C}$  exhibits a rough morphology in form of 3D islands instead of the typical cross hatching pattern, whereas wafer C170731B with  $T_{act} = 330^\circ\text{C}$  shows a very close meshed cross hatching surface texture. The transition from 2D layer-by-layer growth to 3D island formation is ascribed to elastic strain relaxation at the edges of the formed islands, whereby the crystal energy is minimized. A lowering of the substrate temperature, as in the case for wafer C170731B, extends the 2D layer-by-layer growth regime since the surface diffusion length of our growth material atoms is reduced, preventing the system from reaching thermal equilibrium [38, 109, 196]. Accordingly, we assign the reduced mobility to altered growth kinematics with  $\text{As}_2$  as compared to  $\text{As}_4$ .

Nevertheless, this experiment clearly shows an enormous reduction of InAlAs deep level donor states by applying  $\text{As}_2$  as group-V material together with an additionally lowered substrate temperature  $T_{act}$  during the active layer growth.

## 7.7 Conclusion

In this chapter, we evaluated the response of  $\text{In}_{0.75}\text{Ga}_{0.25}\text{As}/\text{In}_{0.75}\text{Al}_{0.25}\text{As}$  heterostructures under gate operation, since the 1D transport behavior in the therein defined QPCs suffered

from intrinsic charge reconfigurations. In order to gain a better understanding of the electrostatic response of the system, we conducted a series of measurements on top-gated Hall bar samples, in which we focused on the aspect of surface termination of the semiconductor layer system in particular.

For gate stackings, as the ones used in chapter 6 for our QPC devices, we find a parasitic conductive layer already to be present at the interface of the  $5\text{nm}$  InGaAs capping layer and the  $\text{Al}_2\text{O}_3$  dielectric for a TG-voltage of  $V_{TG} = 0\text{V}$ . To restore capacitive coupling to the 2DEG, this interface layer has to be depleted via the application of a negative TG-voltage. Furthermore, biased cool-down measurements on this heterostructure revealed the presence of additional parasitic energy states above the InGaAs /  $\text{Al}_2\text{O}_3$  interface. We expect these defect states to be located inside the dielectric layer in the form of deep trap states. A reduction of the InGaAs cap thickness to  $2.5\text{nm}$  in combination with a chemical removal of residual native oxides leads to a significant enlargement of the accessible and non-hysteretic density range in the heterostructure. For  $n_s \gtrsim 7 \cdot 10^{11} \text{cm}^{-2}$  charge migration from the QW towards the interface still sets in, which manifests itself in form of a two-stage charge transfer process, described in detail in our phenomenological charge transfer model. We infer that the InAlAs deep level donor states inside the spacer layer, as well as the interface density of states play a key role in the process of charge migration. A high interface density of states, which can be effectively populated with free electrons from the InAlAs deep level donor states, leads to the formation of a trough-shaped InAlAs spacer band profile. During charge migration, electrons become effectively localized in this potential dip, such that a metastable state inside the system is generated. This process is characterised by a robustly adjustable decrease of the charge density inside the QW when  $V_{TG}$  is further increased, whereby capacitive coupling to the QW is still maintained. For increasing positive TG-voltages, electrons are then transferred to the interface and a parasitic conductive layer is created.

In an attempt to reduce the interface states of the heterostructure, we remove the low band gap InGaAs capping by wet-chemical etching, whereby we create an InAlAs surface termination. For these samples, the charge transfer rate from the QW towards the interface during gating is effectively reduced as compared to InGaAs-terminated samples. Yet, the maximum achievable electron density, marking the end of the linear gating regime according to the field-effect, of InAlAs-terminated samples is equivalent in magnitude as for the InGaAs case. Increased interface roughness due to the etching process increases the probability of gate leakage in these InAlAs devices. This problem may be circumvented for samples with MBE-grown InAlAs surface terminations.

We tested the possibility to reduce the defect density inside our gate stacking via rapid thermal annealing in a forming gas atmosphere. For InGaAs-capped samples, we determined no significant modification of the gating response after annealing. For InAlAs-terminated samples, however, we found clear indications for a substantial material intermixing at the interface.

In addition, we examined alternative dielectric materials, MBE-grown  $\text{MgO}$  and  $\text{HfO}_2$  in combination to  $\text{Al}_2\text{O}_3$ , in our samples. These devices exhibited a similar gating response as samples with ALD- $\text{Al}_2\text{O}_3$ , yet with a reduced mobility. Furthermore, we

found indications for an increased density of interface states. We want to point out to the fact that all of our tested dielectrics contain oxygen, presumably leading to the creation of oxygen-metal-bonds at the interface. Non-oxide based dielectrics present themselves as interesting alternatives for further tests.

By means of analysing the electron mobility in regard to the corresponding charge density, we were able to identify the dominating scattering mechanism in the heterostructure to be formed by scattering on 3D charged impurity sites. Charge migration towards the interface introduces a remote 2D Coulombic disorder potential, which then effectively contributes to the scattering in the 2DEG.

On the basis of the analysis in this chapter, we understand the determined 1D conduction properties of our QPCs in chapter 6: The negative applied SG-voltage lifts the charged interface states of the 5nm InGaAs-capped samples above the Fermi level. This imbalance leads to charge transfer from electrons underneath the SG-electrodes towards surrounding energy states at the interface. In our 1D transport measurements, this charge migration then manifests itself in form of a hysteresis between the depletion and the opening of the QPC, as well as in the experimentally observed time instability of the 1D conductance near depletion. This behavior should be efficiently reduced by the elimination of interface states in form of a reduced InGaAs cap thickness in combination with wet-chemical oxide removal, or, alternatively, with InAlAs-terminated samples. We expect an equivalent 1D transport behavior for both types of interface terminations.

As comprehended in our charge transfer model, we ascribe both, the limitation of the linear gating area following the classical field-effect, as well as the hampered ballistic transport in our finger-gate-defined 1D constrictions, to the InAlAs deep level donor sites. Their effect in 2D measurements is well described in subsection 7.2.3; in 1D, the Coulombic disorder potential leads to the generation of localized states in the QPC channel and to less well-defined conduction steps due to enhanced energy broadening and conductance oscillations at low temperatures.

By modifying the MBE growth parameters, we were able to tremendously reduce the As-related antisite InAlAs defect states. We currently optimize the epitaxy process of (InAs/)  $\text{In}_x\text{Ga}_{1-x}\text{As}/\text{In}_x\text{Al}_{1-x}\text{As}$  in the framework of a doctoral thesis with a view to mobility enhancement and the controllability of SOI [126].

In the next chapter, new QPC devices are fabricated on InAlAs-terminated heterostructures, as well as on structures with a thin InGaAs capping layer, to test the effect of the reduced parasitic interface density of states in our QPC measurements. Since we found the reproducibility of the 2D transport characteristics for InGaAs-capped samples to be increased as compared to their InAlAs counterparts, we start the 1D transport measurements with QPC samples of wafer C160420B, being equipped with a 2.5nm InGaAs capping layer. Thereby, the risk of gate leakage for InAlAs-terminated samples due to surface roughness is circumvented.





# 8

## Ballistic conductance in InGaAs/InAlAs-based systems

In chapter 6, in which we thoroughly tested the 1D transport characteristics of our finger-gate defined QPCs in highly mobile  $\text{In}_{0.75}\text{Ga}_{0.25}\text{As}/\text{In}_{0.75}\text{Al}_{0.25}\text{As}$  heterostructures, we found the ballistics and electric stability of the devices severely deteriorated: A hysteresis between the depletion and the opening of the QPCs develops, which scales in magnitude with the dwell time in or near pinch-off, as well as with the chosen  $V_{SG}^{final}$ , i.e. the minimum SG-voltage applied in pinch-off. Thus, no stable working point on the conductance curve in the pinch-off area could be adjusted. In addition, ballistic conductance was significantly diminished when the QPCs were reopened after pinch-off. In a charge transfer model, which we developed in chapter 7, the electric instabilities of the 1D devices were discussed and unveiled: Parasitic energy states at the InGaAs/ $\text{Al}_2\text{O}_3$  interface, together with deep level donor states inside the InAlAs spacer layer are responsible for the observed adverse charge reconfigurations inside the layer system under gate operation. By means of a complete removal, respectively a sufficient reduction of the InGaAs cap thickness, combined with a chemical elimination of residual III-V-based oxides at the semiconductor surface, we could demonstrate electric stability of our gate stacking over a wide bias (and thus electron density) range in MT measurements on top-gated Hall bar devices.

In this chapter, our newly gained insight into the  $(\text{InAs})/\text{In}_{0.75}\text{Ga}_{0.25}\text{As}/\text{In}_{0.75}\text{Al}_{0.25}\text{As}$ -based material system allows us to implement another step towards the realization of reliable 1D transport in these heterostructures.

## 8.1 Realization of robust ballistic 1D conductance

Building on our experimental results of chapter 7, we choose a heterostructure with the same active layer system as sample  $G^1$  on which we fabricate triple-gated QPCs. Thereby, we employ the refined processing recipe for device fabrication with which we were able to achieve a robust and reproducible gating response of the 2DEG in top-gated Hall bar measurements. These newly fabricated TrG devices present an auspicious testing platform to accomplish electric stability of our QPCs under gate operation.

All experiments in this chapter are conducted at  $T = 1.5\text{ K}$  in the non-illuminated state since we determined that illumination generally increases uncontrollable charge redistribution processes in our devices. The samples are cooled down to cryogenic temperatures with the ohmic contacts set to the laboratory ground potential and the finger-gate electrodes, i.e. the SG-electrodes and the CG-electrode, fixed at  $V_{SG} = V_{CG} = 0\text{ V}$ . Some of the samples are furthermore equipped with a global TG with which we are able to control the electron density of the 2DEG. For these samples we apply a TG-voltage of  $V_{TG} = 0\text{ V}$  during cool-down. Unless otherwise specified, the TG-voltage is held constant at  $V_{TG} = 0\text{ V}$  during a 1D conductance measurement. For most measurements a sweep rate of  $5 - 10\text{ mV/s}$  is applied.

### 8.1.1 Reproducibility

Figure 8.1(a) shows five subsequent conductance curves of a triple-gated QPC. The conductance  $G$  is plotted as a function of the symmetrically applied SG-voltage  $V_{SG}$  in multiples of  $2e^2/h$ , whereby the CG-voltage is held constant at  $V_{CG} = +0.3\text{ V}$ . No serial channel resistance  $R_{ch}$  is subtracted. All conductance curves exhibit two clear SG-voltage regimes, i.e. area (I) and (II), which are characteristic for finger-gate-defined 1D constrictions: In regime (I), the area underneath the SG-electrodes is depleted, in regime (II) the 1D channel is laterally pinched off wherein quantized conductance features arise. The presence of only two regimes in the total conductance curve here presents a significant difference in the transport characteristics of the QPC under gate operation as compared to the triple-gated devices, which we analysed in the preceding 1D transport study in chapter 6. Therein, TrG-defined QPCs all exhibited a third gating area in-between the here observed areas (I) and (II). We assigned the emergence of this third gating regime to a charge accumulation underneath the positively biased CG-electrode: Negative charge carriers, that were fixed at parasitic trap states at the semiconductor/dielectric interface underneath the CG, had to be removed in these samples, whereby a more negative SG-voltage was required as compared to solely SG-defined QPCs. The lack of this third depletion regime for the newly fabricated QPC device demonstrates that we have effectively and efficiently removed detrimental defect sites from the semiconductor/dielectric interface in

<sup>1</sup>Sample  $G$  from wafer C160420B (studied in subsection 7.2.2):  $20\text{ nm}$  InGaAs QW with  $130\text{ nm}$  InAlAs spacer and  $2.5\text{ nm}$  InGaAs cap; chemical removal of residual oxides with HCl prior to  $\text{Al}_2\text{O}_3$  deposition.

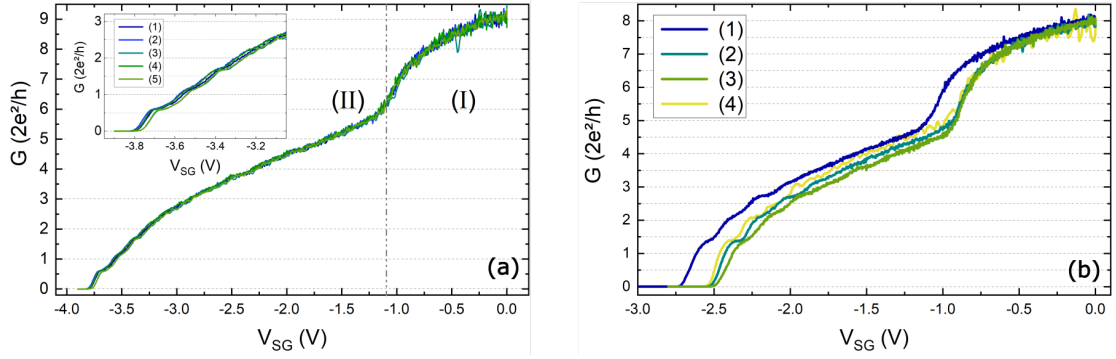


**Figure 8.1:** Conductance measurements at  $T = 1.5K$  in the non-illuminated state with no  $R_{ch}$  subtracted,  $V_{CD} = 0V$ . **(a)** Sample C160420B3 TrG1 with  $V_{CG} = +0.3V$ : Five subsequent conductance measurements with characteristic gating areas (I) and (II). Odd numbers depict the depletion curves of the QPC, even numbers mark the corresponding up-sweeps of  $V_{SG}$ . The inset presents a zoom into the area near pinch-off. **(b)** Sample C160420B2 TrG1 with  $V_{CG} = 0$ : Four subsequent depletion curves (chronologically numbered), being thermally recycled after each measurement with  $V_{CD} = 0V$ .

the heterostructure. Furthermore, a significant achievement presents the elimination of the formerly present hysteresis between the down-swept conductance measurements (odd numbered curves) and the subsequent up-sweep measurements (even numbered curves). The inset in figure 8.1(a) presents a zoom into the conductance area near pinch-off. Three clear steps in  $G$  can be identified, the lowest step being most pronounced. We want to note that the conductance steps do not match integer multiples of  $2e^2/h$  since no channel resistance is subtracted here. We find that the conductance curves of all SG-sweeps are fully congruent. This clearly shows that we gained electric stability in our samples by means of the ameliorated device fabrication method.

Figure 8.1(b) displays four depletion curves between which the device is warmed up to RT and then cooled down again with  $V_{CD} = 0V$ . We find that all curves except measurement (1), which is slightly shifted into the negative  $V_{SG}$ -direction as compared to measurements (2) to (4), are fully congruent. Generally, we obtain a good reproducibility of the 1D transport properties in successive biased cool-downs for all of our newly fabricated devices. This proves that we can efficiently preset the electronic configuration inside the heterostructure. Furthermore, we find that the height of the individual conductance steps after each cool-down is also well reproducible, meaning that the transmission coefficient of a particular 1D mode is identical after each cool-down, which further confirms that we have created the same electric potential environment in the QPC.

Accordingly, we are able to demonstrate reproducible and non-hysteretic 1D conductance in our TrG-defined QPC devices by means of the refined device fabrication process.

A second key element towards the realization of robust, ballistic 1D transport in a QPC

device is the attainment of reliable persistence of the conductance over time. This will be analysed in the following.

### 8.1.2 Time stability

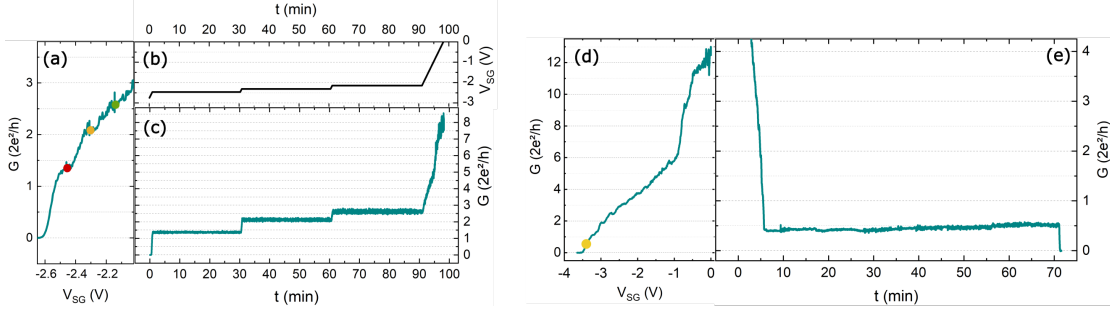


**Figure 8.2:** Time stability of the conductance through TrG devices at  $T = 1.5K$  in the non-illuminated state with no  $R_{ch}$  subtracted and  $V_{CD} = 0V$ . (a) - (c) Sample C160420B2 TrG1 with  $V_{CG} = +0.05V$ : (a)  $G$  as function of  $V_{SG}$ , colored dots mark the measurement points, at which the persistence of  $G$  over time  $t$  is tested. (b)  $V_{SG}$  over time  $t$ . (c)  $G$  as a function of time  $t$ . (d) - (e) Sample C160420A1 TrG1 with  $V_{CG} = +0.1V$ : (d)  $G$  as function of  $V_{SG}$ , the colored dot marks the measuring point. (e)  $G$  as a function of time  $t$ .

Figure 8.2(a) displays a section of the conductance curve near depletion of a triple-gated QPC (same as in figure 8.1(b)). The colored dots mark the positions along the conductance curve at which we test the time stability of the conductance through the QPC. For this experiment, we choose the first three conductance steps as measuring points. At these points, we keep  $V_{SG}$  fixed for a dwell time of 30 minutes before we sweep  $V_{SG}$  to the next testing point. Figure 8.2(b) displays the applied  $V_{SG}$  as a function of time  $t$ . The obtained conductance  $G$  over time  $t$  is shown in figure 8.2(c). We find  $G$  to be remarkably stable over the whole dwell time. This indicates that charge redistribution in the vicinity of the 1D channel is efficiently suppressed when the Fermi level lies in-between two subsequent 1D subbands. The noise on the signal slightly increases with increasing  $G$ , implying an increase of charge fluctuations as the width of the channel increases and the subband distance reduces.

Figure 8.2(d) and (e) show the time stability measurement of an InAlAs-terminated QPC device, with an additional InAs inset in the InGaAs QW. The corresponding heterostructure is sketched in figure 8.6. For this device, we adjust the measuring points right before the onset of the first conductance step (see figure 8.2(d)). The flank of a conductance step presents the most sensitive measuring point on the transport curve. Here, a dwell time of 70 minutes is applied. The time stability of the conductance is shown in figure 8.2(e). We find  $G$  to be reasonably stable during the whole dwell time. There is only a slight increase of  $G$ , which occurs rather stepwise. We attribute this behavior to small

but abrupt recharging processes in the spatial area of the 1D constriction, modifying the transmission probability of the 1D channel modes.

### 8.1.3 Conclusion

In summary, for both surface terminations, InGaAs and InAlAs, we find that the conductance through triple-gated QPCs is persistent over time. The conductance near depletion is stable at least on the timescale of half an hour at  $T = 1.5K$ . Furthermore, the 1D transport properties of our tested QPCs are non-hysteretic and reproducible as we confirm by means of successive up- and down-sweeps of  $V_{SG}$  as well as with conductance measurements after several cool-downs of the device.

Accordingly, we successfully demonstrated the realization of robust and ballistic 1D conductance in triple-gated devices for samples with an InAlAs spacer thickness in the range of 100 – 130nm.

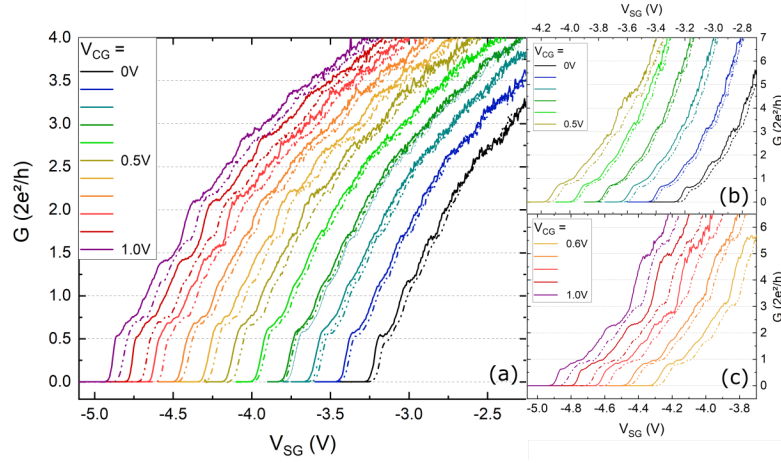
## 8.2 Tuning the ballistic conductance

Until now, we have employed only small CG-voltages in order to facilitate ballistic conductance through the 1D constrictions. Moreover, the SG-electrodes were mainly biased symmetrically.

In this section, we analyse our ability to further tune the ballistic 1D transport properties in the QPCs by the application of a more positive  $V_{CG}$  with which we enlarge the 1D subband spacing and thereby intend to reduce the effect of impurity scattering inside the 1D constriction [8, 18]. In addition, as a further tuning knob of ballisticity in the 1D channel, we shift the QPC laterally in space by biasing the SG-electrodes asymmetrically, i.e.  $V_{SG1} \neq V_{SG2}$  [144].

### 8.2.1 Variation of $V_{CG}$

In the preceding 1D transport characterisation of our QPC devices in chapter 6 a positive CG-voltage led to a pronounced hysteresis of the conductance between up- and down-sweep measurements, as well as to a severe deterioration of the 1D conductance features in the opening curve of the QPC. Building on the 2D gating study of chapter 7, we understand the emergence of the hysteretic behavior for positive  $V_{CG}$  in these devices as follows: The difference in the applied bias of several volts between CG-electrode and SG-electrodes, in particular near channel depletion, constitutes a significant spatial potential imbalance in the QPC devices. This potential difference provokes charge transfer between parasitic energy sites at the semiconductor/dielectric interface, which we identified to be present with a high surface and interface defect density for samples with an InGaAs cap thickness of 5nm, at which residual native oxides are still present. Here, we test the effect of the refined device fabrication process on the transport in QPC devices in the case of large positive  $V_{CG}$ .



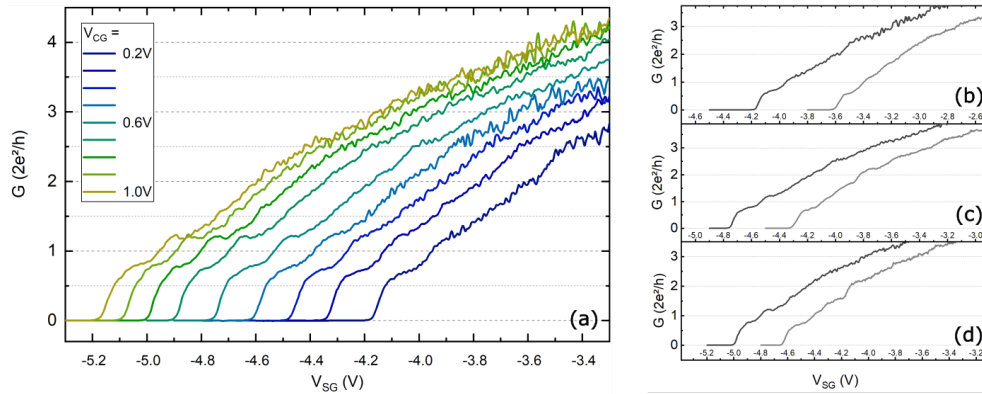
**Figure 8.3:** Conductance curves of sample C160420B3 TrG1 at  $T = 1.5K$ : (a)  $G$  as a function of  $V_{SG}$  for various  $V_{CG}$ , no channel resistance is subtracted. Figures (b) and (c) present zooms into the gating area near depletion for (b):  $0V \leq V_{CG} \leq +0.5V$ , (c):  $+0.6V \leq V_{CG} \leq +1.0V$ , with  $R_{ch} = 3.5k\Omega$  subtracted. The down-sweeps of  $V_{SG}$  are marked with solid lines, the subsequent up-sweeps with dashed lines.

Figure 8.3(a) shows the conductance of a TrG device for various CG-voltages.  $V_{CG}$  is increased from  $0V$  towards  $+1.0V$  in  $0.1V$ -steps. No channel resistance  $R_{ch}$  is subtracted. Increasing  $V_{CG}$  leads to a shift of the pinch-off voltage  $V_p$  into the negative  $V_{SG}$ -direction since the positive CG-voltage has to be compensated by a more negative  $V_{SG}$  to attain channel depletion. Even though a  $V_{CG}$  of up to  $+1.0V$  is applied, we determine only a little mismatch between the downwards (solid lines) and upwards (dashed lines) sweeps. In the case of  $V_{CG} < +0.5V$ , the depletion and opening curves of the QPC are almost fully congruent. We consider the elimination of the hysteretic behavior of the conductance even for large positive  $V_{CG}$  as a further proof of the effective removal of interfacial defect states in the heterostructures. Furthermore, we find that the higher the applied  $V_{CG}$ , the more the first conductance plateau approaches  $G = 2e^2/h$ . This clearly shows that we are able to efficiently improve the ballistic conductance in the 1D channel by increasing the applied CG-voltage: Increasing  $V_{CG}$  distinctly reduces intersubband scattering inside the QPC channel, pushing the 1D mode transmission coefficients towards 1. Figures 8.3(b) and (c), which display the measured conductance curves for  $0V \leq V_{CG} \leq +0.5V$  and for  $+0.6V \leq V_{CG} \leq +1.0V$ , respectively, present a zoom-in on the area near pinch-off. A serial channel resistance<sup>2</sup> of  $R_{ch} = 3.5k\Omega$  is subtracted to match the first conductance plateaus to values of approximately  $2e^2/h$ . For all  $V_{CG}$ , we find three to four clear steps in the conductance curve. However, for measurements around  $V_{CG} \approx +0.5V$ , the second plateau is only poorly developed, whereas higher conductance modes are again more

<sup>2</sup>Generally, the channel resistance of our devices is highly dependent on  $V_{SG}$  in a non-linear fashion. The high channel resistance near depletion quickly decreases with increasing  $V_{SG}$ .

pronounced. For higher  $V_{CG}$ , we find the second step to re-emerge. Since this phenomenon scales with the applied CG-voltage, and thus with the confining potential of the channel, we attribute this behavior to a mode-dependent scattering at impurity disorder potentials. Additionally, a fine structure of  $G$  develops for  $V_{CG} > +0.9V$ : A kink right under the first conductance plateau evolves, together with superimposed conductance oscillations on the first conductance plateaus. Since the channel resistance strongly depends on  $G$ , it is rather intricate to clearly relate the kink in our measurement to the 0.7-anomaly [7, 137, 138]. We attribute such features in the sublevel spectrum, which we already observed in the 1D transport study in chapter 6, to arise due to the presence of quasi-bound states inside the 1D constriction. Consequently, this leads to an energy-dependent transmission coefficient [144, 145, 148–150].

### 8.2.2 Asymmetric biasing $V_{SG1} \neq V_{SG2}$



**Figure 8.4:** Conductance curves of sample C160420B3 TrG1 at  $T = 1.5K$  in non-illuminated state,  $V_{CD} = 0V$ . **(a)**  $G$  as function of  $V_{SG}$  for various  $V_{CG}$ , increased in  $0.1V$ -steps with an offset bias of  $|\Delta V| = 1V$  applied between the two SG-electrodes. **(b) - (d):** Comparison of symmetric (light grey curves), i.e.  $|\Delta V| = 0V$ , and asymmetric (dark grey curves), i.e.  $|\Delta V| = 1V$ , SG-sweeps for (b)  $V_{CG} = +0.2V$ , (c)  $V_{CG} = +0.6V$ , (d)  $V_{CG} = +0.8V$ .

In a next step, we start to shift the QPCs laterally in space. This is done by asymmetrically biasing the two SG-electrodes: An offset voltage  $\Delta V$  is applied between SG1 and SG2 so that  $V_{SG1} \neq V_{SG2}$ . The SG-electrodes are then parallelly swept into negative direction towards channel depletion. Due to the applied  $\Delta V$ , the QPC channel is laterally displaced in space as compared to the symmetrically biased case. Accordingly, the electric environment of the 1D constriction is altered since the respective impurity arrangement is different as the position of the QPC in the 2DEG changes [144]. By utilising this method, we are able to circumvent individual scattering centers, which act upon the QPC.

Figure 8.4(a) shows several depletion curves for different CG-voltages of the same device as analysed in the preceding subsection 8.2.1. Here, an offset voltage of  $|\Delta V| = 1V$  is applied



between SG1 and SG2. For clarity, solely one sweep-direction of  $V_{SG}$  is displayed since the opening and depletion curves coincide. As for the symmetrically biased case, with increasing  $V_{CG}$  the conductance plateaus shift towards integer multiples of  $2e^2/h$ . The first two conductance steps are much more pronounced than for the previous symmetric SG-sweeps with  $|\Delta V| = 0V$ , which have been shown in figure 8.3. This phenomenon is most pronounced in the second conductance step. Higher-order conductance steps, however, are hardly distinguishable. By means of three exemplary conductance measurements with different  $V_{CG}$ , we compare the conductance features of the asymmetrically and the symmetrically biased transport measurements of QPC C160420B3 TrG1: Figure 8.4(b) displays the symmetrically biased conductance measurement together with the asymmetrically biased curve for a CG-voltage of  $V_{CG} = +0.2V$ , figure 8.4(c) shows the two conductance curves for  $V_{CG} = +0.6V$  and figure 8.4(d) displays the measurements at  $V_{CG} = +0.8V$ . These two sets of measurements are representative for the majority of the conductance curves that we obtain with our devices. The horizontal offset between the two conductance curves is due to the offset voltage  $|\Delta V|$  in the asymmetrically biased case. We find the height, as well as the width of the conductance steps of the two measurements to differ from each other for all three  $V_{CG}$ . This clearly demonstrates that we face unique scattering situations in all of the six different potential configurations, which we adjust by  $V_{CG}$  and  $|\Delta V|$ . Consequently, we conclude that impurity disorder in the vicinity of the QPCs strongly influences the 1D transport properties in the devices.

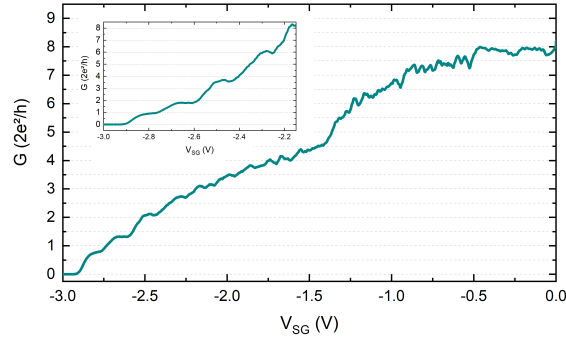


**Figure 8.5:** Conductance curves of sample C160420B2 TrG1 at  $T = 1.5K$  in the non-illuminated state with an offset bias of  $|\Delta V| = 50mV$ . The inset displays a zoom into the area near depletion with  $R_{ch} = 2.8k\Omega$  taken into account.

Figure 8.5 displays a particularly well-resolved conductance curve measured with one of the InGaAs/InAlAs QPCs. Hereby, a CG-voltage of  $0V$  and an offset bias of  $|\Delta V| = 50mV$  are applied. Four very robust and well-defined plateaus are clearly visible. Subtracting a channel resistance of  $R_{ch} = 2.8k\Omega$  matches the first two conductance steps well to  $2e^2/h$  and  $4e^2/h$ . For higher-order steps, this value of  $R_{ch}$  does not result in even order of  $G$ . As the effective width of the channel increases for those modes, the actual channel resistance decreases and thus deviates more and more from this value of  $R_{ch}$ .



### 8.2.3 Conclusion

Generally, we are able to effectively tune the conductance in our TrG-defined QPC constrictions via the CG-electrode. Furthermore, the asymmetrical biasing of the SG-electrodes presents a further control knob for the ballisticity in the system. Thereby, a device-dependent optimum of ballistic conductance can be adjusted. For the application of the QPC as, e.g., a charge sensor in a qubit device, a fine-tuning of the conductance characteristics by moving the QPC in space is commonly used. For the all-electrical spin-FET device, however, this tuning knob is not well-suited: The device concept is based on two QPCs, which have to be perfectly aligned in the transport direction (see section 3.3). Consequently, a lateral shift of one QPC with respect to the other leads to enhanced backscattering, which would deteriorate the ballisticity and hence the spin signal. Thus, for more complex device applications, we suggest to improve the ballistic conductance in the heterostructure by eliminating the mobility-limiting scattering mechanisms which impair the ballisticity in the 1D channels. In our 2D transport study in chapter 7, we identified the InAlAs deep level donor states as the dominating scattering source in the material system. A reduction of the density of these defect states presents itself as pivotal for the realization of multi-component mesoscopic devices.

## 8.3 1D conductance in alternative heterostructures

The spin-FET device, presented in section 3.3, consists of two serial QPCs, which exploit Rashba-type SOI in 1D constrictions whereby a highly spin-polarized current is created. The spin-polarization direction of the current is modulated by a middle-gate, which modifies the structural inversion asymmetry of the 2DEG via the applied gate electric field. Accordingly, more intricate InGaAs/InAlAs-based heterostructures are interesting substrate materials for this device application: An  $\text{In}_{0.75}\text{Ga}_{0.25}\text{As}$  QW with an additional InAs inset offers a larger intrinsic SOI than a pure  $\text{In}_{0.75}\text{Ga}_{0.25}\text{As}$  QW [55]. In addition, 2D electron systems, which are closer to the semiconductor surface - and thus to the QPC-defining finger-gate electrodes - would be beneficial in the above described device application, since the electric field of the gate electrodes is more well-defined as compared to heterostructures with a larger InAlAs barrier thickness. Thus, we conduct further experiments with alternative active layer systems in addition to the so far utilised heterostructure, which is composed of a 130nm InAlAs spacer and a 20nm InGaAs QW. Figure 8.6 displays a sketch of the gate stacking of a newly fabricated QPC device (sample C160420A1 TrG5<sup>3</sup>). The QW is composed of 16nm  $\text{In}_{0.75}\text{Ga}_{0.25}\text{As}$  with a 4nm InAs inset. This two-step QW is separated from the dielectric layer by an  $\text{In}_{0.75}\text{Al}_{0.25}\text{As}$  spacer layer with a thickness of approximately 90nm.

<sup>3</sup>The time stability of the conductance of this device has been already analysed in subsection 8.1.2.

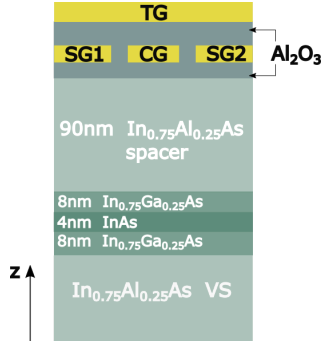


**Figure 8.6:** Sketch of layer structure of sample C160420A.

Figure 8.7(a) shows the conductance through the TrG-defined constriction for various  $V_{CG}$ . The SG-electrodes are biased symmetrically. For clarity, only depletion curves are plotted here, since we find the downwards- and upwards-swept curves to coincide. The conductance measurements show the expected gating response to an increase of  $V_{CG}$ : The pinch-off point  $V_p$  of the conductance shifts towards more negative values of  $V_{SG}$ . Furthermore, we find that the higher  $V_{CG}$  is chosen, the better the quality of the conductance steps. For all applied  $V_{CG}$ , three to four conductance steps clearly develop. In contrast to the samples discussed in the preceding sections, however, we find the quantization steps to be less uniform. The step height of the individual plateaus differ strongly, which indicates a particular mode-dependency of the

transmission coefficients. Furthermore, some of the conductance steps, e.g., the first step of the measurements with  $V_{CG} = 0V$  and  $V_{CG} = 0.2V$ , are hardly visible, yet re-emerge for higher CG-voltages. These observations point towards an increase of the disorder potential inside the heterostructure, affecting the transport through the QPC. Since we have applied the same MBE growth conditions as for the previously studied samples, we attribute the enlarged potential disorder primarily to the etching process (which was employed in order to obtain the InAlAs surface termination) of the semiconductor surface. We suppose that this process generates additional interface roughness. The reduction of the InAlAs spacer thickness from  $130nm$  to  $90nm$  further enhances the impact of the interfacial disorder potential on the 1D channel. To support this hypothesis, investigating a greater number of samples is required to eliminate a misinterpretation based on the limited statistics.

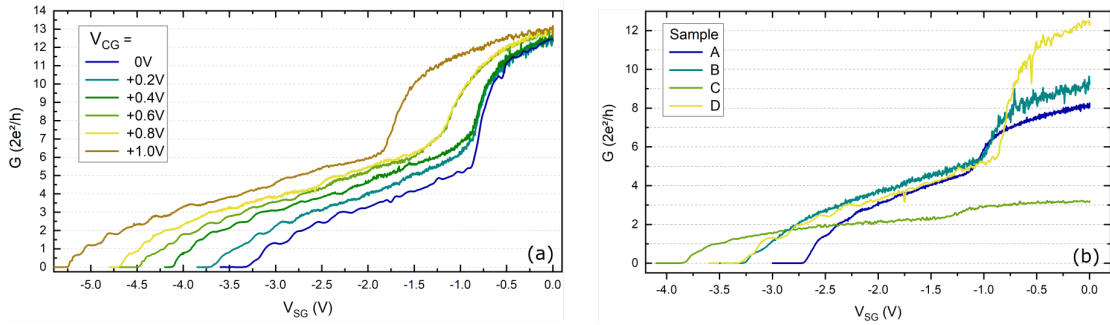


**Figure 8.7:** Conductance curves at  $T = 1.5K$  in non-illuminated state with  $R_{ch} = 0k\Omega$ ,  $V_{CD} = 0V$  and  $|dV| = 0V$  (a) Sample C160420A1 TrG5 :  $G$  as function of  $V_{SG}$  for various  $V_{CG}$ . (b)  $G$  as function of  $V_{SG}$  of four different samples: sample A: C160420B2 TrG1, sample B: C160420B3 TrG1, sample C: C160406B1 TrG1, sample D: C160420A1 TrG5.

Figure 8.7(b) depicts four conductance curves of different triple-gated QPC-devices,

labeled as samples A to D, at a CG-voltage of 0V. Samples A and B, which we already analysed in the previous sections in this chapter, stem from different positions of the same wafer, i.e. wafer C160420B. The newly analysed sample C is composed of a  $2.5\text{nm}$   $\text{In}_{0.75}\text{Ga}_{0.25}\text{As}$  capping layer, a  $35\text{nm}$   $\text{In}_{0.75}\text{Al}_{0.25}\text{As}$  spacer and a  $20\text{nm}$   $\text{In}_{0.75}\text{Ga}_{0.25}\text{As}$  QW. Thus, the distance between the QW and the semiconductor/dielectric interface is significantly smaller than for all other tested devices so far. Sample D is the above discussed QPC device C160420A1 (see figure 8.7(a)), whose conductance response is plotted here for comparison. All four samples exhibit the SG-characteristic depletion-form of the conductance curve. The 1D transport quality and behavior of sample A is equivalent to the conductance in sample B: Although the depletion curves are horizontally shifted with respect to each other, the conductance steps are well resolved in both measurements. Hence, we conclude that the 1D transport properties in different QPC devices, which are identical in composition, are well reproducible. Sample C, however, shows a quite different transport behavior: Even for  $V_{SG} = 0\text{V}$ , we determine a high channel resistance, whereby the conductance is reduced to around  $6e^2/h$  (no serial resistance  $R_{ch}$  is subtracted). Furthermore, we find the ballisticity in this device to be severely impaired since no clear conductance steps develop, even when we increase  $V_{CG}$  up to  $+2\text{V}$ . Also a variation of  $V_{TG}$  does not improve the ballistic conductance in this device. Adversely, a hysteresis develops for all applied  $V_{CG}$ -values as shown in figure B.4 in the appendix. We attribute this hysteretic behavior to charge migration between defect states at the  $\text{In}_{0.75}\text{Ga}_{0.25}\text{As}/\text{Al}_2\text{O}_3$  interface and the QW. Our experimental findings with sample C point to a markedly enhanced influence of potential disorder on the 1D transport in surface-near devices. Analysing the 2D gating response of this top-gated Hall bar sample while  $V_{SG} = V_{CG} = 0\text{V}$  is applied reveals a saturation of  $n_s$  for  $V_{TG} > 0\text{V}$ . The corresponding MT measurement sequence is shown in figure B.2 in the appendix. This early onset of the charge density saturation resembles our experimental findings in chapter 7 of sample A<sup>4</sup> and of samples B to D<sup>5</sup>. For these devices, we determined a large density of parasitic energy states inside the dielectric and at the semiconductor/dielectric interface. However, for sample C here, we employed the ameliorated device fabrication process, whereby the detrimental interfacial density of states is expected to be significantly reduced. We interpret the recurrence of the hysteretic gating response, as well as the formation of the parasitic conductive interface layer even at small  $V_{TG}$  to a charge transfer from the QW towards the interface, mediated by the deep level InAlAs donor states owing to the reduced InAlAs spacer layer thickness of  $35\text{nm}$ .

We summarize that the heterostructure/dielectric interface clearly affects the robustness of the QPCs in two ways: For etched heterostructure surfaces with a reduced spacer thickness, the disorder potential in the constriction is increased, whereby our ability to control the formation of conductance steps is limited. For surface-near samples a

<sup>4</sup>Sample A (wafer C160429A): Hall bar sample of a deeply buried and undoped  $\text{In}_{0.75}\text{Ga}_{0.25}\text{As}/\text{In}_{0.75}\text{Al}_{0.25}\text{As}$  QW with  $5\text{nm}$  InGaAs cap and no chemical removal of residual oxides.

<sup>5</sup>Sample B to D (wafer C160420B): Hall bar samples of a deeply buried and undoped  $\text{In}_{0.75}\text{Ga}_{0.25}\text{As}/\text{In}_{0.75}\text{Al}_{0.25}\text{As}$  QW with  $2.5\text{nm}$  InGaAs cap and no chemical removal of residual oxides at the interface.

hysteresis develops between up- and down-sweeps due to an increase in charge migration between QW and interface.

### 8.4 Conclusion

In this chapter, we demonstrated robust ballistic transport through our triple-gated QPC devices, defined in (InAs/) $\text{In}_{0.75}\text{Ga}_{0.25}\text{As}/\text{In}_{0.75}\text{Al}_{0.25}\text{As}$  deeply buried 2DEGs. In these samples, conductance characteristics of depletion and opening curves coincide and are highly reproducible. Furthermore, we are able to adjust electrically stable working points on the conductance curves even near channel depletion which is a clear proof of the efficient reduction of interface states in the heterostructures. In addition, the ballistic conductance can be essentially improved with the application of a positive CG-voltage, whereby the lateral confining potential is narrowed and deepened. This leads to a perceptible increase of the 1D subband spacing, which suppresses disorder-induced intersubband scattering and inhibits the creation of quasi-bound states. By shifting the QPC laterally in space via asymmetrically biasing the SG-electrodes, we are able to circumvent single scattering centers. Consequently, ballistic transport in the 1D channel can be further facilitated. For heterostructures, being equipped with an InAs inset inside the InGaAs QW and an InAlAs-terminated semiconductor surface, we determined the conductance steps to be less uniform than for InGaAs-terminated samples with a 20nm InGaAs QW. Increased interface roughness due to the etching process and the reduced InAlAs spacer thickness are likely to generate an enhanced disorder potential, which adversely affects the 1D sublevel spectrum.

Although, we could eliminate the hysteretic behavior for deeply buried QW samples for both surface terminations, InGaAs and InAlAs, we find a pronounced shift of the pinch-off point between the depletion and the opening curve of the 1D channel for near surface QW samples. The charge redistribution during the pinch-off of the QPC confirms our model in which charge transfer from the 2DEG towards the interface is mediated by the InAlAs defect states. In addition, for highly conducting channels near the surface the conductance steps are obscured in comparison to samples with a deeper buried 2DEG. We attribute this observation to a more strongly disordered potential inside the QPC channel, owing to increased interface roughness. However, we want to point out that our experimental findings for samples C and D, studied in section 8.3, need yet to be substantiated by a relevant number of devices to gain statistical significance.

In conclusion, for the realization of robust 1D transport, we recommend to further optimize the MBE growth process in order to reduce the amount of deep level donor states inside the InAlAs spacer layers. This would be beneficial in two different ways: First of all, the potential fluctuations, introduced by the InAlAs defect states, would be minimized, whereby quasi-bound states inside the 1D channel could be reduced. This would lead to a general improvement of ballistic conductance. Secondly, band bending-induced charge transfer should be diminished, which would yield a more robust 1D transport in QPC devices.

# Signatures of Rashba-type spin-orbit interaction

In this chapter, the peculiar gating response of the heterostructure in gating areas II, III and IV, as introduced in chapter 7, is discussed. These gating regimes are characterised by a decrease of the measured 2D charge carrier density when the TG-voltage is increased. The physical origin of this behavior is well described by the charge transfer model, which we developed in the course of our 2D gating study in chapter 7. What we have left unaddressed so far are the observed undulations in the magnetooscillations in these particular gating areas, giving rise to a second frequency in the corresponding FFT spectra. This chapter serves to give a comprehensive discussion of this experimental finding. Furthermore, we give an estimation of the strength of Rashba-type SOI in the heterostructure via a self-consistent calculation of the band structure with a Schrödinger-Poisson solver in conjunction with calculations employing the envelope function approximation within the  $\mathbf{k} \cdot \mathbf{p}$ -method.

## 9.1 Gating response of undoped InGaAs/InAlAs heterostructure

In the following, we want to briefly recapitulate the underlying processes during the gating of the non-intentionally doped  $\text{In}_{0.75}\text{Ga}_{0.25}\text{As}/\text{In}_{0.75}\text{Al}_{0.25}\text{As}$  heterostructures, which were analysed in detail in chapter 7. To this end, we review the MT measurement sequence of an exemplary top-gated Hall bar sample, sample  $H^1$ , of our preceding gating study. Figure 9.1(a) shows the corresponding measurement sequence of this sample, which has been already discussed in section 7.2.4. Figure 9.1(b) displays exemplary measurement curves of the magnetoresistivity  $\rho_{xx}$  in gating areas II and III. The individual measurement points are marked with colored dots in the gating curve in figure 9.1(a). After a linear increase of  $n_s$  along with  $V_{TG}$  in gating area I, we find the charge density to saturate at

<sup>1</sup>InAlAs surface termination with  $\text{Al}_2\text{O}_3$  as dielectric

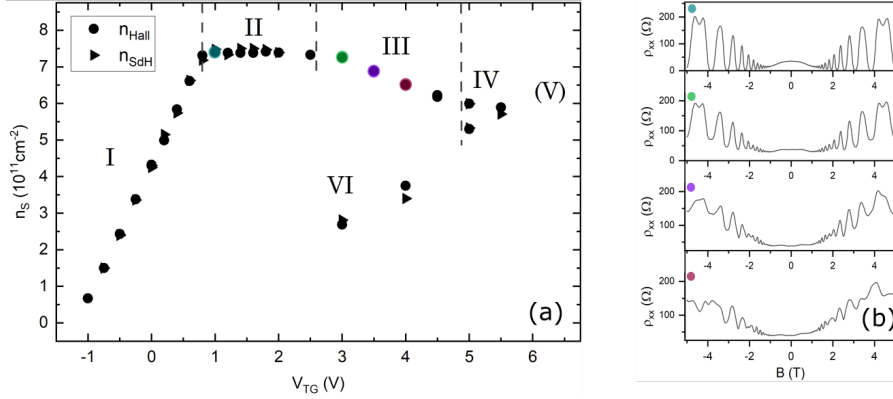


**Figure 9.1:** (a) MT measurement sequence of sample *H*. Roman numerals I to VI denote the constituent gating areas. (b) Exemplary measurements of  $\rho_{xx}(B)$  in gating areas II and III as is indicated by the colored dots in (a).

$n_s^{peak} = 7.5 \cdot 10^{11} \text{ cm}^{-2}$  in the gate interval II, i.e.  $+0.8 \text{ V} < V_{TG} < +2.6 \text{ V}$ , after which  $n_s$  starts to decrease with increasing  $V_{TG}$  (gating area III), until saturation starts to set in for  $+4.5 \text{ V} < V_{TG} < +5.5 \text{ V}$  (regime IV). This transport behavior can be described by means of our developed charge transfer model (see subsection 7.2.3). In gating area III, we obtain a pronounced modulation of the magnetooscillations, which is shown in figure 9.1(b). These modulations in  $\rho_{xx}(B)$  resemble a superimposed long-wave envelope, generating a recurrent compression of the oscillation amplitude of the Shubnikov-de Haas oscillations in form of distinct nodes. Determining the charge density of the 2DEG from the minima of the Shubnikov-de Haas oscillations does not yield a single value for  $n_{SdH}$ . Hence, figure 9.1(a) solely displays the measured value of  $n_{Hall}$  in regime III. Furthermore, the undulations of the Shubnikov-de Haas oscillations are accompanied by a parabolic background in  $\rho_{xx}(B)$ . This beating effect and the parabolic background in  $\rho_{xx}(B)$  vanish as soon as  $n_s$  starts to saturate in gating area IV and V (see figure 7.13). Thus, we find these peculiar features in  $\rho_{xx}(B)$  to be limited to gating area III, which we interestingly found to be characterised by the charge migration from the QW via deep level donor states inside the InAlAs spacer towards the interface.

In a next step, to gain further information on the magnetooscillatory behavior, we spectrally decompose and analyse the longitudinal resistivity measurement signals of this MT measurement sequence.

## 9.2 FFT of magnetooscillations

The longitudinal resistivity  $\rho_{xx}(B)$  as a function of  $1/B$  is transformed into its constituting frequency spectrum via a FFT. This yields the individual signals, which contribute to the measured  $\rho_{xx}(B)$  and exhibit a  $1/B$ -periodicity such as for example the Landau level DOS.

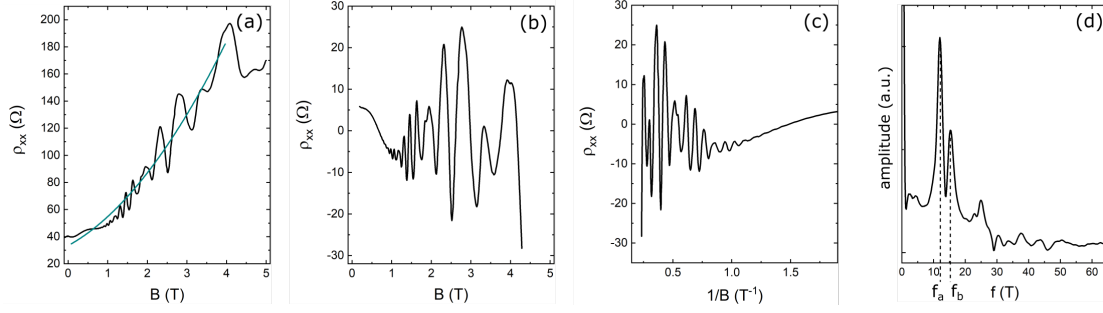


**Figure 9.2:** Exemplary FFT routine of  $\rho_{xx}(B)$  of a MT measurement of sample  $H$  at  $V_{TG} = +4.0V$ ,  $T = 4.2K$ : **(a)** Raw-data of  $\rho_{xx}$  over  $B$  (black line) with a polynomial fit (cyan line). **(b)** Residual resistivity after subtraction of the polynomial fit in (a). **(c)** Residual resistivity of (b) as a function of  $1/B$ . **(d)** FFT spectrum of signal in (c) with a double-peak structure  $f_a = 12.06T$  and  $f_b = 15.41T$ .

### 9.2.1 Exemplary FFT in gating regime III

Figure 9.2 illustrates, step-by-step, the FFT process of an exemplary magnetoresistivity measurement in gating area III of sample  $H$ . The thereby employed raw-data of  $\rho_{xx}(B)$  for  $V_{TG} = +4.0V$  is shown in figure 9.2(a). The superimposed background is fitted with a polynomial curve (cyan curve) and subsequently subtracted. This yields the residual resistivity of  $\rho_{xx}(B)$ , plotted in figure 9.1(b), in which we find the modulation of the oscillation amplitude to be better resolved. Given the periodicity of the Shubnikov-de Haas oscillations over  $1/B$ , the residual resistivity is then plotted as a function of the inverse magnetic field as displayed in figure 9.2(c). For the FFT a rectangular window function is applied to avoid a weighting of particular data-points. The Fourier transform of the signal in (c) is plotted in figure 9.2(d), displaying its spectral composition. The spectrum yields a clear double-peak structure with the amplitude maxima located at  $f_a = 12.06T$  and  $f_b = 15.41T$ . These frequencies are converted into the corresponding electron densities  $n_s$  via

$$f^{-1} = \Delta(1/B) = 2 \cdot \frac{e}{n_s h}, \quad (9.1)$$

where  $h$  is Planck's constant. For a spin-degenerate system, the factor two must be included. With equation (9.1), we determine  $f_a$  and  $f_b$  to correspond to a charge carrier density of  $n_a = 5.8 \cdot 10^{11} cm^{-2}$  and  $n_b = 7.5 \cdot 10^{11} cm^{-2}$ , respectively. Generally, if more than just one 2D channel contributes to the transport in a system, e.g., if multiple size-quantized subbands of a QW are populated, the individual charge densities of the participating subbands are summed up in the measured Hall density  $n_{Hall}$  as long as no additional bulk conductance is present. For the here considered measurement, however, we determine  $n_{\Sigma} = n_1 + n_2 = 13.3 \cdot 10^{11} cm^{-2}$ , which is exactly twice the measured Hall density  $n_{Hall} = 6.5 \cdot 10^{11} cm^{-2}$ . Thus, it seems unlikely, at first sight, that two parallel

2D systems are active here. We will discuss the assignment of these two frequencies in the remainder of this chapter.

In literature, such a modulation of  $\rho_{xx}(B)$  is often interpreted as a sign of SOI, which is very interesting in the context of our employed high SOC material system. However, there are several microscopic effects, which may impose similar features on the Shubnikov-de Haas oscillations. These should be carefully considered before analysing possible signatures of SOI. In the following, we will thus in particular discuss features in  $\rho_{xx}(B)$  related to our applied evaluation method, as well as features in the magnetooscillations, originating from size-quantization effects and which are worth to be considered in our field-effect analysis.

### 9.2.2 Large magnetic field limit

Usually, in the literature, the FFT of the Shubnikov-de Haas oscillations is restricted to small magnetic fields. This limitation is mainly motivated by two effects: The Zeeman spin-splitting, as well as the breakdown of the semi-classical model description of the Landau level DOS as a sinusoidal function of  $1/B$  both lead to a modification of the frequency spectrum of the longitudinal resistivity at sufficiently high magnetic fields. These two mechanisms are discussed in the following.

#### Limits of the semi-classical description

As introduced in subsection 2.1.2, we can describe the magnetoresistivity of a 2DEG in the limit of small magnetic fields by means of a semi-classical formula:

$$\Delta\rho_{xx} = \rho_0 + 4 \cdot \frac{2\pi k_B T m^*}{\hbar e B} \cdot \frac{1}{\sinh \frac{2\pi k_B T m^*}{\hbar e B}} \cdot \exp\left(-\frac{\pi m^*}{e\tau_q} \cdot \frac{1}{B}\right) \cdot \cos\left(\frac{2\pi \mathcal{E} m^*}{\hbar e} \cdot \frac{1}{B} - \pi\right), \quad (9.2)$$

with  $\mathcal{E} = E_F - E_n$ , where  $E_n$  is the energy of the  $n$ th subband and  $\tau_q$  is the quantum lifetime [48]. This semi-classical description of  $\rho_{xx}(B)$  is roughly valid for magnetic fields for which  $\omega_c \tau_q \leq 1$  still holds. For larger magnetic fields, however, the magnetoresistivity starts to deviate from this behavior as  $\rho_{xx}(B)$  vanishes over finite magnetic field intervals. This effect, referred to as quantized Hall effect [53, 54], sets in when the Fermi level lies in between two consecutive Landau levels and only negligible scattering of charge carriers into neighboring extended Landau states takes place. We can determine  $\tau_q$  by means of equation (9.2) from the linear slope of a Dingle plot, in which the exponential decay of the Shubnikov-de Haas oscillation amplitude as a function of  $1/B$  is evaluated, as long as further modulations of the oscillation amplitude in  $\rho_{xx}(B)$  are not present. Accordingly, we cannot give an estimation of  $\tau_q$  in gating area III since therein the magnetooscillation amplitude is modulated by the additional envelope function (see figure 9.1(b)). To this end, we evaluate the amplitude decay of the Shubnikov-de Haas oscillations in gating area I. This yields an upper limit for  $\tau_q$  in our samples, as the charge migration in gating areas



II and III will tend to reduce the electron mobility in the heterostructures (see section 7.5.1). Based on this evaluation method of  $\rho_{xx}(B)$ , we find  $\tau_q$  to decrease with increasing  $V_{TG}$  at the end of gating area I and in gating area II. This is shown in the appendix B.2. At  $V_{TG} = +1.4V$ ,  $\tau_q$  is as low as  $1.3 \cdot 10^{-13}s$ , which is about 30-times smaller than the corresponding transport scattering time  $\tau_{tr}$ , pointing towards long-range scattering potentials [43]. This value of  $\tau_q$  limits the legitimized FFT interval to  $B \leq 2T$ . Since we assume a further drop of  $\tau_q$  in gating interval III due to effects from charge migration, we do not consider the above determined boundary value to be a hard limit.

### Zeeman spin-splitting

An external magnetic field, breaking the time reversal symmetry, lifts the spin degeneracy. For bulk semiconductors, in first order, the Zeeman spin-splitting  $\Delta E_Z$  is isotropic in space and can be described with

$$\Delta E_Z = g^* \mu_B B, \quad (9.3)$$

where  $g^*$  is the effective Landé g-factor and  $\mu_B$  is the Bohr magneton. Thus, the spin-splitting strength is not only proportional to the applied magnetic field  $B$  but also to the prefactor  $g^*$ . Including the Zeeman spin-splitting from equation (9.3) into the description of the Landau level eigenstates of equation (2.18) simply yields

$$E_{n_{xy}} = \hbar\omega_c \left( n_{xy} + \frac{1}{2} \right) \pm \frac{1}{2} g^* \mu_B B \quad (9.4)$$

in the case of  $\mathbf{B} \parallel \mathbf{z}$ , with  $\mathbf{z}$  being the growth direction. This energy spin-splitting enters the description of the corresponding DOS of the Landau levels, provoking a modification of the periodicity of the Shubnikov-de Haas oscillations at sufficiently strong magnetic fields. Since the factor of two in equation (9.1) is not included anymore in the spin-split case, a transition of the  $1/B$ -periodicity of the magnetoresistivity at a frequency  $f$  to a harmonic at  $2f$  in the spectrum takes place if the Zeeman splitting is fully resolved [197]. Winkler [55] pointed out that Zeeman spin-splitting does not affect the determined frequency  $f$  of the spin-degenerate oscillations in the Fourier power spectrum of  $\rho_{xx}$ . Yet, it alters the amplitude and phase of the Shubnikov-de Haas oscillations. Consequently, for our experiments, we conclude from these considerations that while Zeeman spin-splitting will induce a modification of the FFT of the magnetooscillations, yet it cannot be responsible for the observed double-peak structure in the Fourier transformed power spectra in gating area III. Moreover, Zeeman splitting is not resolved in our MT measurements for  $B < 3.5T$ . Correspondingly, we expect Zeeman spin-splitting-induced features in the magnetooscillations to be less prominent as compared to samples, for which Zeeman-type spin-splitting is already resolved at low magnetic field values.

In the following, in order to test the dependence of the FFT spectra on the utilised B-field interval, we contrast the Fourier transformed spectra for two different upper magnetic field limits.

**Comparison of B-field intervals for FFT analysis** Figure 9.3 displays two FFT spectra of the magnetoresistivity measurement of sample *H* at  $V_{TG} = +4.0V$ , determined in different magnetic field intervals. The cyan curve displays a FFT spectrum, determined in the magnetic field interval  $B \leq 2T$ , legitimized by the semi-classical description in the framework of the QHE, for a corresponding quantum lifetime of  $\tau_q \approx 1.3 \cdot 10^{-13}s$ . In contrast, the grey curve displays the Fourier transformed magnetooscillations in an extended magnetic field range of  $B \leq 4T$ , which we transformed in the FFT process in figure 9.1. By comparing the Fourier transformed signals, we find both spectra to exhibit the equivalent spectral information. However, the double-peak structure is not fully resolved in the reduced magnetic field interval. Instead, the second peak appears as a shoulder at the right side of the main peak at  $f \approx 12T$ . We assign the undulated background, which arises in both spectra, to be caused by the finite amount of Fourier transformed oscillations in  $1/B$  and by the abrupt ending of the transformation interval, as well as by the residual background in  $\rho_{xx}$ , which has not been fully eliminated by the polynomial fit (see figures 9.1(a) and (b)). Mathematically, an interaction between the two transport channels, which correspond to the observed main frequencies  $f_a$  and  $f_b$ , is likely to generate sum- and difference-frequency peaks in the spectral decomposition of the signal. This will be further addressed in subsection 9.3.1.

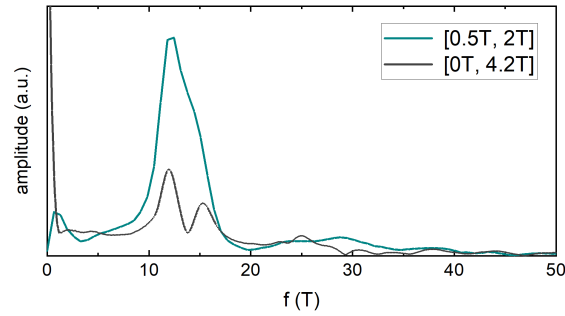


**Figure 9.3:** Comparison of two FFT spectra of the magnetoresistivity of sample *H* at  $V_{TG} = +4V$ , determined in different magnetic field intervals.

From the above analysis, we infer that using an extended Fourier transformed magnetic field interval (here up to  $4T$ ) is not responsible for the generation of the observed double-peak structure in our spectra. Restricting the applied FFT magnetic field interval to  $B \leq 2T$  solely deteriorates the spectral resolution of the transformation due to the reduced number of included magnetooscillations.

In the following, we thus deliberately employ an extended magnetic field range for our FFT analysis of the MT measurements in gating regime III to improve our analysis of the observed frequency components.

### 9.2.3 Semi-classical simulation of the magnetoresistivity

We can further test the accuracy of our determined FFT frequencies, i.e. the charge densities of the participating channels, by using the gained frequencies  $f_a$  and  $f_b$  to give

a description of  $\rho_{xx}(B)$  on the basis of the semi-classical formula (9.2).

### Mathematical description

To this end, we exemplarily simulate the measured longitudinal magnetoresistivity of sample *H* at  $V_{TG} = +4.0V$  (see figure 9.1(a)). We describe  $\rho_{xx}(B)$  as a superposition of two transport channels with the two charge densities  $n_a = 5.8 \cdot 10^{11} \text{cm}^{-2}$  and  $n_b = 7.5 \cdot 10^{11} \text{cm}^{-2}$ , deduced from our experiments through equation (9.1). The values of  $n_a$  and  $n_b$  are employed to calculate the energy intervals  $\mathcal{E}_i = E_F - E_i$ ,  $i = a, b$ , of the cosine-terms in equation (9.2). For the calculation of  $\mathcal{E}_i$ , we employ the 2D DOS  $\mathcal{D}_{2D}(E) = \frac{\partial N}{\partial E} = \frac{m^*}{\pi \hbar^2} = \frac{n_i}{\mathcal{E}_i}$ , using our experimentally determined value  $m^* = 0.041 \cdot m_0$  from chapter 5. Furthermore, we employ a quantum lifetime of  $\tau_q = 1.5 \cdot 10^{-13} \text{s}$  as determined from the Dingle plot analysis given in the appendix in B.2. We additionally include interaction between the two participating transport channels in the form of a modified Shubnikov-de Haas oscillation amplitude, together with a superimposed parabolic background in  $\rho_{xx}(B)$ . In this description of  $\rho_{xx}(B)$ , the Landau level spin-splitting due to the external magnetic field is not included. By comparing the experimentally obtained curve of  $\rho_{xx}(B)$  to our fit - besides the verification of our determined charge densities - we can expect to be able to identify Zeeman splitting-induced deviations from our assumed semi-classical model description of the Shubnikov-de Haas oscillations.

### Comparison of calculation and experiment

Figure 9.4(a) displays the experimentally determined longitudinal resistivity (solid line), together with the semi-classical simulation of  $\rho_{xx}(B)$  (dashed line) as described above for  $B < 4T$ . The two curves are vertically offset for clarity. We find the simulated curve of  $\rho_{xx}(B)$  to be in excellent agreement with the experiment since we are able to reproduce all important features of the measured magnetoresistivity, i.e. the extrema of the Shubnikov-de Haas oscillations and the node positions of the superimposed envelope of  $\rho_{xx}(B)$ . For  $B > 3.5T$ , however, we find the simulated curve to start to deviate from the experiment. We attribute this variance to the Zeeman effect.

The good reproducibility of the measured curve with a simulation based on equation (9.2) gives further weight to our input parameters: the estimated value of the quantum lifetime  $\tau_q$ , as well as the determined charge densities  $n_a$  and  $n_b$ , stemming from the FFT in the extended magnetic field range. Figures 9.4(b) to (e) display the step-by-step FFT method, presented in subsection 9.2.1, which we now apply on the simulated curve of  $\rho_{xx}$ . Hereby, we can test the influence of the mathematical FFT process on the obtained results. For the FFT of the fit signal, we receive two distinct frequencies  $f_a^{sim}$  and  $f_b^{sim}$ . Converting these frequencies into the corresponding spin-degenerate charge densities yields  $n_a^{sim}$  and  $n_b^{sim}$ , which are identical to the densities  $n_a$  and  $n_b$  that we used as input parameters to the simulation. Unlike in the FFT of the experimental curve, however, we find no significant background in the spectral decomposition of our simulated curve. Since we applied the same FFT window function for the simulated curve as for the experiment, we attribute

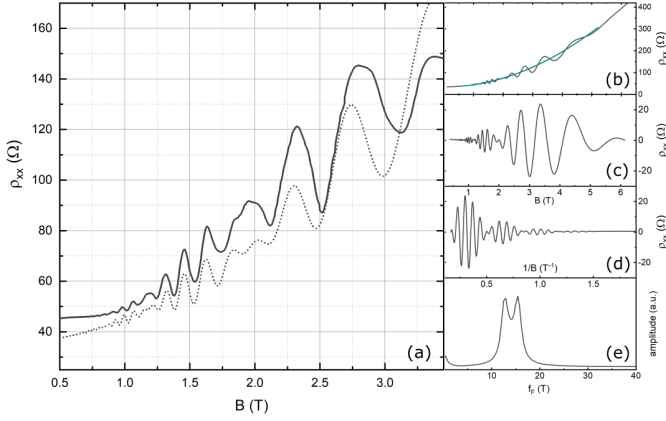


**Figure 9.4:** (a) Solid curve:  $\rho_{xx}$  of sample *H* at  $V_{TG} = +4.0V$ , dashed curve: semi-classical model description of  $\rho_{xx}(B)$  with  $n_a = 5.8 \cdot 10^{11} cm^{-2}$  and  $n_b = 7.5 \cdot 10^{11} cm^{-2}$  for a spin-degenerate system. (b) Polynomial fit (cyan) to calculate  $\rho_{xx}(B)$  from (a). (c) Residual resistivity as function of  $B$ . (d) Residual resistivity over  $1/B$ . (e) FFT of residual resistivity from (d).

this difference in the arising background to the Zeeman splitting (not contained in the simulation), as well as to interaction effects between the two participating channels. In conclusion, the comparison between the FFT of the simulation and of the experiment confirms our assumption that the FFT process itself does not significantly alter the charge densities determined from the experimental data.

### Determination of the $g^*$ factor

As introduced in subsection 9.2.2, the strength of the Zeeman spin-splitting  $\Delta E_Z$  and thus its experimental resolution in a MT measurement depends on the energy broadening of the Landau levels. There are two effects, which primarily determine the level broadening in our system: Firstly, the thermal energy  $\Delta E_{Th}$  blurs the sharpness of a Landau level, and, secondly, scattering processes inside the extended states of a Landau level lead to a level broadening  $\Gamma$ . By employing the experimentally determined resolution limit of the Zeeman spin-splitting, we are able to give an estimation for the value of the effective  $|g^*|$ -factor of the material system.

In the MT measurements in the linear field-effect regime I of sample *H*, we determine the Zeeman spin-splitting to be clearly resolved for  $B \geq 3.5T$ . When assuming that the Landau level broadening is dominated by the thermal energy at  $T = 4.2K$  of the system, we can write  $\Delta E_Z = \Delta E_{Th}$ , with  $\Delta E_{Th} = k_B T = 0.36 meV$  being the thermal energy and  $k_B$  the Boltzmann constant. Thus, considering only thermal broadening, the estimation of  $|g^*|$  yields:  $|g^*| \approx \frac{k_B T}{\mu_B B} = 1.8$ .

In the field-effect study in chapter 7, we found that the transport properties of the samples are strongly affected by elastic and inelastic scattering processes. Consequently, we now determine the value of the effective  $|g^*|$ -factor by assuming the resolution of Zeeman spin-splitting to be determined by the scattering-induced level broadening  $\Gamma$ . To this end, we parameterize  $\Gamma$  by means of the single particle lifetime  $\tau_q$ . For gating area I, we determined  $\tau_q \approx 1.3 - 1.9 \cdot 10^{-13} s$ . Thus, the Lorentzian-shaped energetical Landau level

broadening  $\Gamma$  is calculated as  $\Gamma = \frac{\hbar}{2\tau_q} \approx 2.5\text{meV}$  [48] from which we can deduce  $g^*$ .<sup>2</sup> With  $g^*\mu_B B = \Gamma$ , we determine  $|g^*| \approx 10$ . This is congruent with findings in literature: Holmes et al. [117] report an effective g-factor of  $|g^*| \approx 9$  in their nominally undoped  $\text{In}_{0.75}\text{Ga}_{0.25}\text{As}/\text{In}_{0.75}\text{Al}_{0.25}\text{As}$  heterostructure. By means of the coincidence method, Sato et al. [199] experimentally deduce  $g^*$  to lie within the range of -7 to -14. On account of the larger effect on the Landau level broadening, we conclude that the resolution of Zeeman spin-splitting is controlled by scattering-induced level broadening. Thus, we infer a  $|g^*|$ -factor of 10 in our system.

### 9.2.4 Gate voltage dependence of FFT spectra

After validation of our FFT evaluation method, we now discuss the Fourier transformed signal of the MT measurements of  $\rho_{xx}$  of sample *H* in gating areas II, III and IV, following the FFT procedure as we described in the preceding course of this section. The corresponding measurement curves are displayed in figure 9.5(a). We find the beating of the magnetooscillations to be most pronounced in the middle of gating regime III at  $V_{TG} \approx +3.5\text{V}$  and  $V_{TG} \approx +4.0\text{V}$ . With the onset of regime IV, i.e.  $V_{TG} \geq +4.5\text{V}$ , the beating in  $\rho_{xx}(B)$  starts to diminish. Figure 9.5(b) shows the spectral evolution of the Fourier-transformed magnetoresistivity in the TG-voltage interval  $+0.8\text{V} \leq V_{TG} \leq +5.0\text{V}$ . The individual curves are vertically offset for clarity.

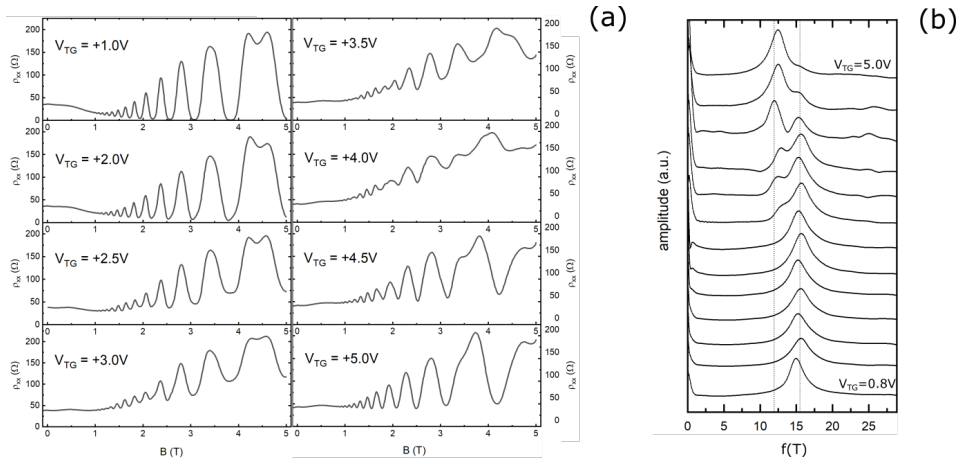


**Figure 9.5:** (a) MT measurements of  $\rho_{xx}(B)$  of sample *H* in gating area II, III and IV at  $T = 4.2\text{K}$ . (b) FFT spectra for  $V_{TG}$  interval from  $+0.8\text{V}$  to  $+5.0\text{V}$ , vertically offset for clarity.

During gating interval II, we solely find a single peak in the Fourier-transformed curves, centered at  $f \approx 15\text{T}$ , which corresponds to a charge density of  $n_{FFT} = 2\frac{e}{h}f \approx 7.3 \cdot 10^{11}\text{cm}^{-2}$ . In this gating interval II, we find  $n_{FFT} = n_{SDH} = n_{Hall}$ . With the onset of

<sup>2</sup>Note, that this is a rough estimate for  $\Gamma$  since we neglected a B-field dependence of  $\Gamma$ , i.e.  $\Gamma_B = \Gamma\sqrt{B}$  [198].

gating area III, i.e.  $V_{TG} > +2.0V$ , in which a significant electron transfer from the QW towards InAlAs defect states sets in, an additional peak develops as a shoulder to the main peak in the Fourier spectrum. For increasing  $V_{TG}$  the peaks become similar in height and slightly shift in horizontal direction. Yet, and notably, the substantial loss of electrons in the 2DEG in regime III does not manifest itself in a shift of the corresponding magnitude in the FFT signal. Calculating the Shubnikov-de Haas charge density  $n_{SDH}$ , we find that the double-frequency structure translates into a set of two different electron densities  $n_{SDH}^+$  and  $n_{SDH}^-$ , which do not coincide with the measured  $n_{Hall}$ . We determine  $n_{SDH}^+$  to be slightly larger than  $n_{Hall}$ , and  $n_{SDH}^-$  to be slightly smaller than  $n_{Hall}$ . With the onset of the saturation in  $n_{Hall}$  in gating area IV, one frequency starts to vanish, until a single peak at  $f \approx 12.3T$  is left, corresponding to a charge density of  $n_{FFT} \approx 6.0 \cdot 10^{11} cm^{-2} = n_{Hall}$ . In regime V, we find  $n_{FFT} = n_{SDH} = n_{Hall}$  to be valid again.

If we summarize at this point, we have excluded the double-frequency structure in regime III to be a result of our choice of data sets and of the data processing. Also, we find the evolution of this feature with gate voltage to be peculiar. Indeed, the mere decrease of  $n_s$  in regime III does not explain the occurrence of a double-peak signature and its gate-dependent evolution. In the following, we will thus discuss in more details possible physical mechanisms.

### 9.3 Double-peak generation in FFT

There are several relevant mechanisms in gated 2D systems, which can lead to the generation of multiple frequencies in the FFT spectrum of the magnetoresistivity. At high charge carrier densities, size-quantization effects need to be taken into account when analysing and interpreting MT measurements. Furthermore, the impact of SOI needs to be considered in our high intrinsic SOC material system. These two effects will be discussed in the following.

#### 9.3.1 Size-quantization effects

##### Influence of remote 2nd transport channel

One possible origin of the obtained modulation of magnetooscillations is the effect of a spatially separated remote transport channel inside the system. However, as we thoroughly discussed in chapter 7, we are able to exclude the participation of a second transport channel in gating areas I to IV. The parasitic conductive layer, which is not fully developed until area V, manifests itself only as a loss of capacitive coupling to the QW channel, yet not in the form of a frequency modulation of the Shubnikov-de Haas oscillations. Thus, we exclude a remote 2D transport channel to contribute to  $\rho_{xx}(B)$  in gating areas II to IV.

### Second subband population

A further possibility of the influence of size-quantization on the magnetooscillations is the participation of a second subband of the QW-2DEG to the transport. In subsection 2.1.1, we introduced the effect of parallel transport on the Drude conductivity, and thus on the obtained Hall density  $n_{Hall}$ . Therein, we determined  $n_{Hall}$  to be a function of the individual charge densities of the participating channels, weighted by the corresponding mobilities of the charge carriers. Considering two 2D subband channels to participate in transport with  $n_1$  and  $\mu_1$  characterising the ground subband and  $n_2$  and  $\mu_2$  characterising the second subband, we can write in the limit of  $\mu_2 \ll \mu_1$ , which will generally be true for a newly populated second subband

$$n_{Hall} = \frac{(n_1\mu_1 + n_2\mu_2)^2}{n_1\mu_1^2 + n_2\mu_2^2} \approx \frac{(n_1\mu_1 + n_2\mu_2)^2}{n_1\mu_1^2}. \quad (9.5)$$

After expansion, we get

$$n_{Hall} \approx n_1 + 2n_2 \cdot \frac{\mu_2}{\mu_1}. \quad (9.6)$$

From this relation we draw two main conclusions: Firstly, even in the case of a reduced mobility in the ground subband due to scattering into the second subband, the weighting of the density  $n_1$  with mobility  $\mu_1$  in equation (9.5) can be neglected. Thus,  $n_1$  does not decrease significantly when a second subband is newly populated. This implication is particularly interesting with regard to the density drop in gating areas II to IV. We thus find equation (9.6) to further confirm our developed charge transfer model from chapter 7, where we assigned the density drop beyond the linear gating regime I to charge migration towards the interface. Secondly, in the limit of a newly populated second subband, implying  $n_2 \ll n_1$  and  $\mu_2 \ll \mu_1$ , we find  $n_{Hall} \geq n_1$  clearly to be valid since  $n_{Hall}$  contains both subband contributions.

Moreover, the FFT peak of a newly populated subband should evolve from the low frequency side towards the main peak as soon as the subband becomes sufficiently mobile. Such an evolution is not observed for any of our analysed undoped Hall bar devices. In addition, self-consistent band structure calculations with a Schrödinger-Poisson solver yield a significant onset of second subband population to take place for charge densities of  $n_s \geq 8 \cdot 10^{11} \text{ cm}^{-2}$ , that is densities that are larger than the ones that we encounter in our samples.

Hence, we exclude the population of a second size-quantized subband to be responsible for the double-frequency generation in the FFT spectra.

### Magneto-intersubband scattering

As we introduced in subsection 2.1.2, there is a further effect how a second size-quantized subband can affect the magnetooscillations in a 2D system: The simultaneous Fermi level crossing of two sets of Landau levels, corresponding to two spatially non-separated

size-quantized subbands of the 2DEG, gives rise to the generation of additional terms in  $\rho_{xx}(B)$  due to subband interaction. This effect is commonly referred to as magneto-intersubband scattering (MIS). These terms contain the sum- and difference-frequencies of the participating subbands, i.e.  $f_1 + f_2$  and  $f_1 - f_2$  in equations (2.32) - (2.34) in subsection 2.1.2.  $f_1$  corresponds to the ground subband with a respective charge density  $n_1$  and  $f_2$  to the second subband with charge density  $n_2$ .

We now follow the hypothesis of MIS to be present in our system to discuss its effect on the transport properties. Since the mobility  $\mu_2$  and the density  $n_2$  of the second subband are generally distinctly smaller than  $\mu_1$  and  $n_1$ ,  $f_2$  can be solely resolved for a sufficiently strong second subband population. Thus, the second term in equation (2.32) can be neglected in our analysis, in accordance with our argumentation in subsection 9.3.1. Consequently, the two additional sidebands with frequencies  $f_1 + f_2$  and  $f_1 - f_2$  from equation (2.34) to  $f_1$  would be most likely to emerge in the FFT spectra in our heterostructures. With  $f_2 \ll f_1$ , the sum- and difference-frequency terms would give rise to nearby peaks to the fundamental frequency  $f_1$ , similar to the double-frequency peak in our FFTs in regime III. For higher temperatures, the sum-frequency-contribution to the total magnetoresistivity is strongly damped due to the  $D(2X)$ -factor in equation (2.34), whereas the difference-frequency contribution experiences no thermal damping at all. The latter contribution is therefore considered as the leading term in the limit of higher temperatures, since the Shubnikov-de Haas oscillations also attenuate with rising temperature. Correspondingly, we infer that the frequency contribution of the ground subband  $f_1$  together with the difference-frequency  $f_1 - f_2$  would be likely to dominate the FFT spectra of our MT measurements in the case of MIS. Following the evolution from the single peak FFT spectra in gating area I and II to the double-peak structure in gating area III (see figures 9.1 and 9.5), we assign the FFT peak at  $f_1 = 15.3T$  to the ground subband. Consequently, in the hypothesis of MIS, we would interpret the newly arising second peak in the FFT spectra in regime III as an MIS peak, expected at  $f_1 - f_2$ . This assignment would also fulfill the mandatory condition  $(f_1 - f_2) < f_1$ .

Taking the exemplary MT measurement at  $V_{TG} = +4.0V$ , we determine a second frequency  $f_1 - f_2 \approx 12T$ , indicating  $f_2 \approx 3.3T$ . Calculating the corresponding charge carrier densities via  $n = 2 \frac{e}{h} f$  yields  $n_1 = 7.3 \cdot 10^{11} cm^{-2}$  and  $n_2 = 1.6 \cdot 10^{11} cm^{-2}$ . Accordingly, the sum of the charge densities of the two participating transport channels is  $n_{\Sigma} = n_1 + n_2 = 8.9 \cdot 10^{11} cm^{-2}$ . The corresponding measured Hall density at  $V_{TG} = +4.0V$  is  $n_{Hall} = 6 \cdot 10^{11} cm^{-2}$ , whereby we find  $n_{Hall} < n_1 \ll n_{\Sigma}$ . This is in contradiction to formula (9.6), which implies  $n_{Hall} \geq n_1$ . Consequently, we have refuted our above made hypothesis and conclude that MIS is not responsible for the second frequency generation in our system.

A further, yet more hand-waving argument, which additionally disproves MIS to be present in our system, is given by following considerations: To ascribe the double-peak structure in regime III to the MIS would imply that intersubband scattering gets more pronounced as the QW density decreases and thus, the Fermi level descends. This reasoning leads the assumption of MIS to be present ad absurdum.

Thus, we are able to clearly exclude MIS to be responsible for the observed second



frequency in the MT measurement in gating regime III.

To summarize, we have carefully analysed the signatures that size-quantization would induce in the magnetooscillations of our system and we were able to exclude these effects to be responsible for the observed double-frequency generation in the FFT spectra. Since we have also excluded evaluation artifacts to be accountable for the obtained second frequency in  $\rho_{xx}$ , we correspondingly conclude SOI to give rise to the modulation of the Shubnikov-de Haas oscillations in gating regime III. This assignment is rather surprising since the electric field at the QW in gating area III is decreasing due to the migrated electrons towards the interface and shall be discussed in more details in the remainder of this chapter.

### 9.3.2 SOI effect

Even without the application of an external magnetic field, spin degeneracy can be effectively lifted in non-centrosymmetric crystals. This relativistic effect couples the spin of the electron to its motion and results in a  $k$ -dependent effective magnetic field  $\mathbf{B}_{\text{eff}}$ , which acts on the spin. Generally, as we discussed in chapter 3, zero-field spin-splitting can arise due to a microscopic crystal potential (BIA), as well as due to a structure-induced inversion asymmetry (SIA), generated by a macroscopic potential. Both types of SOI lead to a modification of the dispersion relation of the 2D electron systems, consequently affecting the magnetooscillations.

In the following, we discuss the origin and strength of the experimentally observed SOI in our 2D electron system.

## 9.4 SOI in undoped InGaAs/InAlAs systems

### 9.4.1 SOI effects in magnetooscillations

In chapter 3, we deduced that Dresselhaus-type SOI can be neglected in our heterostructure as compared to the Rashba-type SOI. This conclusion is based on experimental and theoretical findings in literature. Furthermore, Winkler [55] showed in his calculations that at an external electric field of around  $40\text{ kV/cm}$  the SIA contribution clearly dominates over BIA in 2D systems. We can further exclude that our system is in a stable persistent spin helix (PSH) state, since we find no signs of spin-splitting in the measurement of the magnetoresistivity in the linear gating area I, in which the electric field at the QW interface is changed by more than  $70\text{ kV/cm}$ . An externally applied electric field modulates the Rashba spin-splitting, yet leaves SOI due to BIA unaltered. Correspondingly, we reason that even if the condition  $\beta = \pm\alpha$ , with  $\alpha$  being the SOC constant due to SIA and  $\beta$  being the SOC constant due to BIA, is fulfilled at a particular  $V_{TG}$ , the PSH state is clearly detuned in the course of the MT measurement sequence. Consequently, we attribute the amplitude modulation of the magnetooscillations to Rashba-induced SOI and neglect

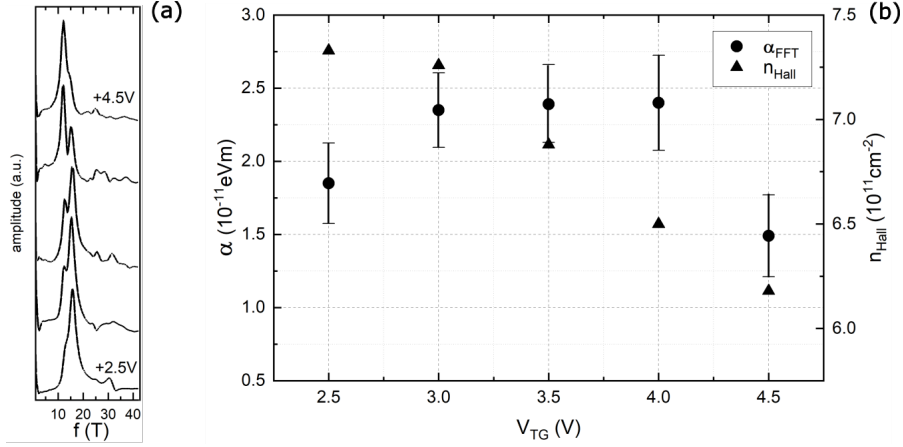


**Figure 9.6:** (a) FFT spectra of the MT measurements of  $\rho_{xx}$  in gating area III, vertically offset for clarity. (b)  $\alpha_{FFT}$  and  $n_{Hall}$  as a function of the applied  $V_{TG}$ . The solid vertical lines denote the particular error bar for the calculated value of  $\alpha_{FFT}$ .

Dresselhaus-type SOI in the following analysis of SOI strength in the heterostructure.

### 9.4.2 Evaluation of SOI strength

In subsection 3.2, we presented two evaluation methods with which the strength of Rashba-type SOI can be deduced by analysing the beating in the magnetooscillations in a MT measurement. These two methods are employed in the following to give an estimation of the strength of SOI in our heterostructure.

### 9.4.3 FFT analysis

The spectral analysis of the magnetooscillations via FFT provides one possibility to experimentally determine the strength of SOI in the system. When employing this method, one should recognize that Zeeman spin-splitting is included in this quantitative evaluation approach of spin-splitting.

We analyse the FFT spectra of sample *H* of gating area III, which are shown in figure 9.6(a). To this end, we convert the obtained two frequencies into the corresponding electron densities, now for the spin-split case, i.e.  $n = \frac{e}{h} f$ , whereby we gain the charge densities  $n_s^+$  and  $n_s^-$ . Following the evaluation approach we presented in section 3.2, we are able to calculate the Rashba parameter  $\alpha_{FFT}$  of the 2D electron system with equation (3.15). Figure 9.6(b) shows the thereby determined values of  $\alpha_{FFT}$  as a function of the applied  $V_{TG}$ , together with the corresponding Hall density  $n_{Hall}$ . The error bars indicate the uncertainty of  $\alpha_{FFT}$  when deduced from our MT measurements. The magnitude of the assumed error is composed as follows: Primarily, the resolution of the determined Rashba parameters is limited by the energetical Landau level broadening  $\Gamma$ , determined by

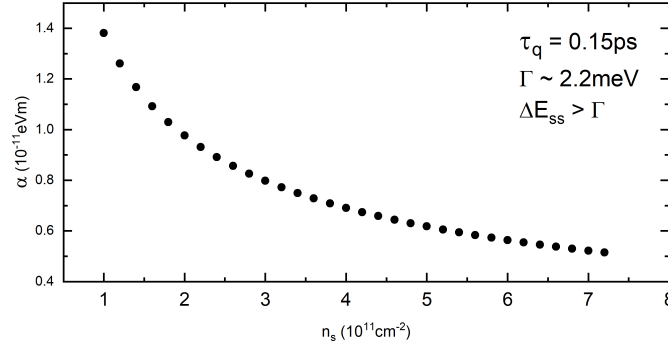


**Figure 9.7:** Resolution limit of  $\alpha_{FFT}$  under the condition of  $\Delta E_{ss} > \Gamma$  under the assumption of a constant  $\tau_q = 0.15ps$  during gating area I.

the quantum lifetime  $\tau_q$ , in our MT measurements. Furthermore, the finite temperature, the length of the Fourier-transformed magnetic field interval, as well as the charge carrier density, which is related to the number of Shubnikov-de Haas oscillations in the analysed magnetic field interval, affect the FFT resolution and thus the accuracy of the calculated value of  $\alpha_{FFT}$ . With  $\Delta E_{ss} = 2\alpha k$ , we can convert the above determined Landau level broadening of  $\Gamma = \frac{\hbar}{2\tau_q} \approx 2.5meV$ , for which we assumed a constant value of  $\tau_q \approx 0.15ps$ , into the corresponding uncertainty of the determined value of  $\alpha_{FFT}$ . The thereby determined resolution limit of the Rashba coefficient  $\alpha_{FFT}$  as a function of the total charge density  $n_s$  is plotted in figure 9.7. At the end of gating area I at a charge density of  $n_s \approx 6 \cdot 10^{11} \text{cm}^{-2}$ , we find that Rashba-type SOI is not resolved in our MT measurements until  $\alpha_{FFT} > 0.56 \cdot 10^{-11} \text{eVm}$ . For a charge density of  $3 \cdot 10^{11} \text{cm}^{-2}$ , the SOI strength has to be as high as  $0.8 \cdot 10^{-11} \text{eVm}$  so that we are able to resolve spin-splitting via FFT of  $\rho_{xx}$  in the system. This demonstrates a rather poor and strongly  $\tau_q$ -dependent resolution of the SOI strength in the system. Correspondingly, we neglect uncertainties induced by the temperature and the finite number of analysed magnetooscillations in our evaluation of  $\alpha_{FFT}$ , since we expect them to be comparably small. Given that only one frequency in the FFT spectrum of  $\rho_{xx}$  is observed, we were not able to determine a value for  $\alpha_{FFT}$  in the gating areas I, II, IV, V and VI of our MT measurement sequence. A meaningful evaluation of SOI strength in these gating regimes is thus not possible owing to the poor resolution.

The determined values of the Rashba parameters via the FFT analysis are shown in figure 9.6(b) as a function of the applied TG-voltage. At the beginning of gating regime III at  $V_{TG} = +2.5V$ , we find a Rashba parameter of  $\alpha_{FFT} = 1.85 \cdot 10^{-11} \text{eVm}$ . The determined values of  $\alpha_{FFT}$  peak in the middle of gating area III, where the modulation of the magnetooscillations is also found to be most pronounced. The maximum value is as high as  $2.4 \cdot 10^{-11} \text{eVm}$ . To our knowledge, this is one of the highest Rashba parameters reported for nominally undoped top-gated  $\text{In}_{0.75}\text{Ga}_{0.25}\text{As}/\text{In}_{0.75}\text{Al}_{0.25}\text{As}$  heterostructures. To the end of gating regime III at  $V_{TG} = +4.5V$ , where we find the beating in  $\rho_{xx}$  (see figure 9.5(a)) to be less pronounced, we determine  $\alpha_{FFT} = 1.5 \cdot 10^{-11} \text{eVm}$ .

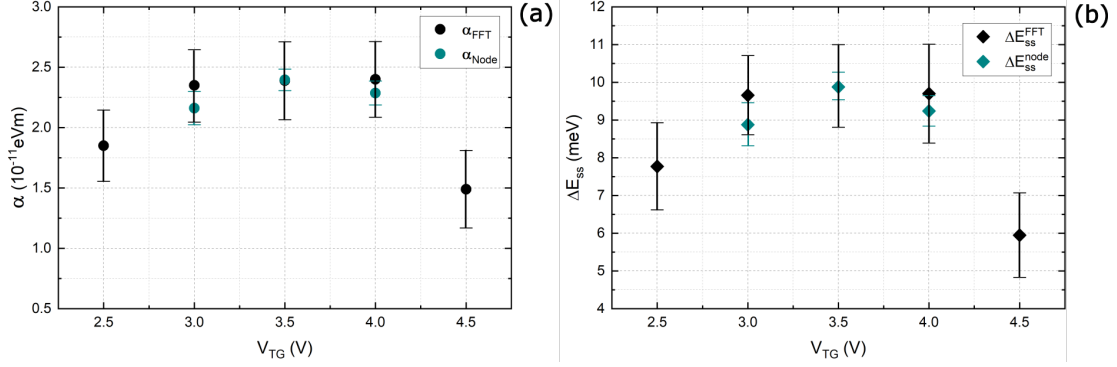


**Figure 9.8:** (a)  $\alpha_{node}$  and  $\alpha_{FFT}$  with (b) the corresponding spin-splitting energies  $\Delta E_{ss,node}$  and  $\Delta E_{ss,FFT}$  as a function of  $V_{TG}$ . The vertical lines indicate the respective error bars.

We determine the Rashba-type SOI strength for the top-gated samples *A* to *N* - when possible - analogously. Clear double-peak features always solely appear in gating regime III and yield maximal Rashba parameters  $\alpha_{FFT}$  in the range of  $1.7 - 2.7 \cdot 10^{-11} \text{ eV/m}$ . Generally, for InGaAs-capped samples a smaller number of Shubnikov-de Haas oscillations is resolved, which leads to a further degraded spin-splitting resolution in these samples. For sample *G*, for example, only one MT measurement exhibited a fully conclusive FFT spectrum with a clear double-peak structure with  $\alpha_{FFT} \approx 2.7 \cdot 10^{-11} \text{ eV/m}$ . Figure B.7 in the appendix B shows the FFT spectra and the determined SOI strength of an InAs/InGaAs/InAlAs heterostructure (not included in our 2D gating study in chapter 7).

### 9.4.4 Beating-node analysis

In the previous FFT evaluation method of the Rashba SOI, the influence of the Zeeman effect on the magnitude of the estimated spin-splitting has been neglected. Even though we argued in subsection 9.2.2 that Zeeman spin-splitting should play a minor role for spin-splitting in our samples for  $B < 3.5T$ , we assume the determined values of  $\alpha_{FFT}$  include a contribution to spin-splitting due to the Zeeman effect. As presented in chapter 3, there is a second evaluation method of SOI via the magnetooscillations. Therein, the beating-node position of the Shubnikov-de Haas oscillations is analysed.

We employ this evaluation procedure for the top-gated Hall bar samples *A* to *N* from chapter 7. A meaningful value of the Rashba coefficient by means of this evaluation method can only be determined for measurements where at least three clear nodes in  $\rho_{xx}(B)$  are identified, so that the determined node-position can be described with a linear fit. Figure 9.8(a) shows the determined values for  $\alpha_{node}$  for sample *H* in gating regime III, together with the determined values of  $\alpha_{FFT}$  for comparison. The error bars of  $\alpha_{node}$  are set by the linear fitting procedure. In the measurement of the magnetoresistivity of sample *H*, we find at least three distinct nodes at  $V_{TG} = +3.0V$ ,  $+3.5V$  and  $+4.0V$ . The values of  $\alpha_{node}$  lie within the estimated error range of the determined values of  $\alpha_{FFT}$  and thus

confirm the occurrence of this giant SOI in gating regime III. For all three measurements, we find  $\alpha_{node} \leq \alpha_{FFT}$ . This is consistent with the expected overestimation of the SOC strength with the FFT analysis due to the impact of Zeeman spin-splitting. Generally, as determined from the ratio  $\alpha_{FFT}/\alpha_{node}$ , we determine that the Zeeman contribution makes up 5 - 10% of the total spin-splitting. As in the evaluation of SOI via the FFT analysis, we find the beating-node position evaluation method to be less often applicable for InGaAs-capped samples since the node positions are less clear developed.

Figure 9.8(b) displays the corresponding  $k$ -dependent spin-splitting energies  $\Delta E_{ss}$  for the SOC parameters  $\alpha_{FFT}$ ,  $(\Delta E_{ss,FFT})$  and for  $\alpha_{node}$ ,  $(\Delta E_{ss,node})$ . A maximum spin-splitting of  $\Delta E_{ss}$  of almost  $10\text{meV}$  is obtained for sample  $H$  at a total 2D electron density of  $n = 6.5 \cdot 10^{11}\text{cm}^{-2}$ . With the determined value of  $|g^*| = 10$  in our samples, the Zeeman spin-splitting energy takes the value of  $\Delta E_z = 2\text{meV}$  at a magnetic field of  $B = 3.5\text{T}$ .<sup>3</sup> Comparing  $\Delta E_z$  to the SOI-induced spin-splitting energy  $\Delta E_{ss}$ , we find  $\Delta E_z \ll \Delta E_{ss}$  in the whole analysed B-field range via FFT. Thus, the overestimation of the Rashba parameter via our employed FFT analysis is small. This is also reflected in the rather good agreement of  $\alpha_{FFT}$  with  $\alpha_{node}$ , where Zeeman spin-splitting is not incorporated. In the next subsection, the microscopic origin of this peculiar gating-dependence of Rashba-type SOI is discussed.

### 9.4.5 Discussion

All analysed top-gated Hall bar samples  $A$  to  $N$  from chapter 7 exhibit an equivalent gating response as sample  $H$ , which we have discussed in more detail: After the linear gating response of the charge carrier density  $n_s$  in regime I,  $n_s$  decreases with increasing TG-voltage (regime II, III and IV). The density decrease in gating areas II, III and IV is attributed to a pronounced charge migration from the QW towards the semiconductor/dielectric interface via the deep level donor states inside the InAlAs spacer layer according to our charge transfer model. In gating area III, we find clear evidence of a large Rashba-type SOI in our MT measurements in the form of a beating in the longitudinal resistivity  $\rho_{xx}(B)$ . These undulations of the Shubnikov-de Haas oscillation amplitude vanish when we enter the transitional regime IV ( $V_{TG} > +4.5\text{V}$ ) to the saturation regime V, in which we have no longer capacitive coupling to the 2DEG due to the formed parasitic conductive layer at the semiconductor/dielectric interface. The assignment of our experimental observations in  $\rho_{xx}(B)$  to SIA-induced SOI is not evident at first sight since the total electric field at the QW is a superposition of the positive applied TG-voltage and the electric field, which is generated by the migrated electrons. Additionally, the ionized impurity potential of the InAlAs defect sites acts on the 2DEG. From this simple view, one would expect the electric field acting on the conduction electrons and thus the Rashba-type SOI to be reduced in regime III as compared to the end of the linear regime

<sup>3</sup>As described in 3.2.2, via the node analysis we acquire values for the  $g^*$ -factor from the linear fitting of the node-positions. However, these values scatter strongly. They accumulate around values of  $g^* = -15$ , yet exhibiting an error bar almost equal in size.

I (in which no beating in  $\rho_{xx}(B)$  is present).

A key observation in our experiments is that measurable SOI effects in our heterostructures solely arise in gating area III in which charge migration from the QW towards the interface takes place and a significant amount of electrons is located at InAlAs defect sites in the upper barrier layer. To visualize this situation, we self-consistently calculate the band structure of our gate stacking with a Schrödinger-Poisson solver [119–122]. In our simulations, we compare three exemplary electrostatic situations in the heterostructure, which are assigned to different gating areas in our MT measurement sequence. These band structure simulations are further evaluated by calculations in the envelope function approximation within the  $\mathbf{k} \cdot \mathbf{p}$ -method, in which we use the total electric potential, calculated with the Schrödinger-Poisson solver, as input parameter. Performing a general folding-down procedure, the Rashba SOC parameter is calculated [55, 79, 200, 201].<sup>4</sup> We want to emphasize that we do not intend to give an exact value of the Rashba coefficient with these calculations since we are aware that we lack an exact knowledge of the complex electrostatics in our gate stacking, i.e. the distribution and ionization of the deep level donor states inside the InAlAs barrier layers, as well as of the electron population of semiconductor/dielectric interface states. Instead, we aim to analyse the experimentally observed trend of the evolution of the Rashba-induced SOI strength in our heterostructure during gating. To this end, we employ simplified model assumptions of the density and ionization state of the InAlAs deep level donor states in the Schrödinger-Poisson simulations.

A sketch of the utilised layer system is shown in figure 7.1(a). The metal gate electrode is separated by a layer of 50nm  $\text{Al}_2\text{O}_3$  from the underlying semiconducting layers: a 2.5nm InGaAs capping, a 130nm InAlAs spacer and the 20nm InGaAs QW. The electron accumulation at the semiconductor/dielectric interface, arising due to residual energy states at the interface (see chapter 7) is accounted for as a thin negatively charged layer in these simulations. Since we want to give a qualitative picture, we choose an InAlAs deep level donor density of  $n_{D,1} = n_{D,2} = 3 \cdot 10^{16} \text{cm}^{-3}$ , which is rather large compared to literature, being evenly distributed inside the InAlAs layers, for the calculations. The TG electric field inside the heterostructure is modeled by the applied bias at the metal gate electrode. Figure 9.9(a) displays the conduction band profile  $E_{CB}$  at the  $\Gamma$ -point (black solid line) as a function of the growth-direction  $z$  for which the applied TG-voltage  $V_{TG}$  is set to 0V. The heterostructure is arranged in such a way that the InGaAs cap ends at  $z = 0$ . Thus, the top InGaAs-QW interface is positioned at  $z = 132.5\text{nm}$ , the bottom QW interface at  $z = 152.5$ . In negative  $z$ -direction, we find the high-band gap insulator, followed by the metal gate electrode. The blue dashed line indicates the InAlAs deep level donor density in the heterostructure, the black dashed lines indicate the density of the ionized InAlAs deep level donor states. The negatively charged interface layer and the asymmetric ionization of InAlAs defect states above and beneath the QW lead to an asymmetric conduction band profile even in the zero-biased case. A zoom into the

---

<sup>4</sup>The calculations were performed by Dr. Paulo E. de Faria Junior from the group of Prof. Dr. Jaroslav Fabian.

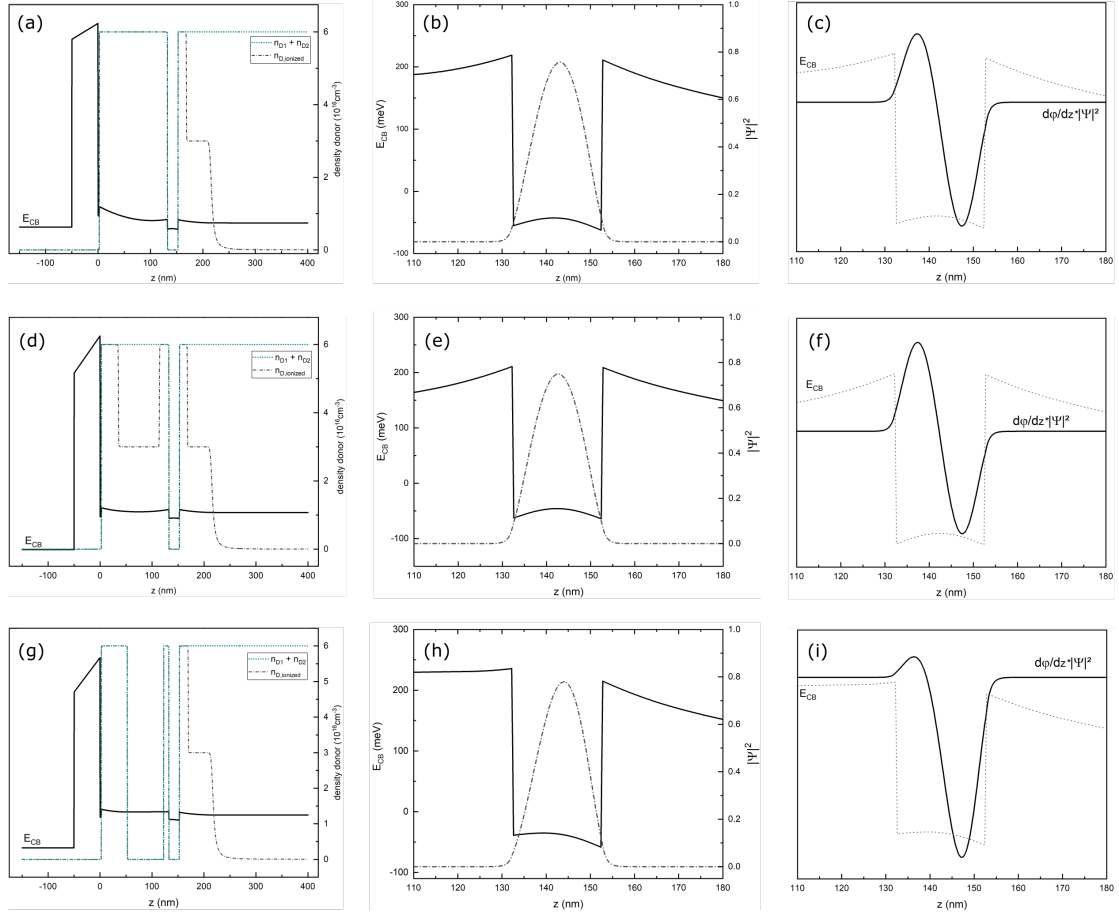


**Figure 9.9:** (a)–(c): Band structure simulation, corresponding to regime I, with  $V_{TG} = 0V$ ,  $n_{D1} = n_{D2} = 3 \cdot 10^{11} \text{cm}^{-2}$  evenly distributed in the InAlAs spacer layers. (d)–(f): Band structure simulation, corresponding to the end of regime I, with  $V_{TG} = +1V$ ,  $n_{D1} = n_{D2} = 3 \cdot 10^{11} \text{cm}^{-2}$  evenly distributed in the InAlAs spacer layers. (g)–(i): Band structure simulation, corresponding to regime II, III and IV, with  $V_{TG} = +1V$ ,  $n_{D1} = n_{D2} = 3 \cdot 10^{11} \text{cm}^{-2}$  evenly distributed in the InAlAs spacer layers and artificially deionized in the  $z$ -interval [50nm, 120nm]. The plots (a), (d) and (g) display the conduction band edge  $E_{CB}$  at the  $\Gamma$ -point as solid line (a.u.) with the total density of the InAlAs defect states (cyan dotted line) and the ionized density of the InAlAs defect states (black dotted line). Figures (b), (e) and (h) show the conduction band edge (solid line) with the wave function probability  $|\Psi|^2$  (dotted line). Figures (c), (f) and (i) present the conduction band edge (dotted line) with the derivative of the potential weighted by the wave function probability, i.e  $d\phi/dz \cdot |\Psi|^2$  (solid line).

band profile in the vicinity of the QW, shown in figure 9.9(b), displays an asymmetric tilting of the QW towards the bottom QW interface. The wave function probability  $|\Psi(z)|^2$  is indicated as dotted line. Figure 9.9(c) shows a plot of the electric field in the heterostructure, i.e.  $d\varphi(z)/dz$ , weighted by  $|\Psi(z)|^2$ . According to equation (3.9), the barrier contribution to the Rashba coefficient scales with the band offsets weighted by  $|\Psi(z)|^2$  at the bottom and top barrier QW interfaces [80–82, 84]. For the electrostatic situation shown here in figures 9.9(a) to (c), we find the contributions of the top and bottom QW interfaces to almost cancel each other. Furthermore, the strength of the electric field inside the QW, giving rise to a non-interfacial contribution to the Rashba coefficient, is small. We thus may expect the Rashba-induced SOI in the case of  $V_{TG} = 0V$  to be below our limit of detection with MT measurements. From the calculations of the strength of SOI by means of the band structure simulations, we find a Rashba coefficient of  $\alpha = -0.1 \cdot 10^{-12} eVm$ . This value is far below the resolution limit in our MT measurements. The calculation also tells us that the interface and the non-interface contribution terms (see section 3.2) are comparable in magnitude. Both, the value and the comparable small contributions of interface and non-interface, are consistent with the observed absence of SOI effects in the longitudinal resistance in gating regime I.

Figure 9.9(d) displays an electrostatic situation that corresponds to the end of the linear gating area I of our MT measurements, for which  $V_{TG} = +1.0V$  is applied. As compared to figure 9.9(a) with  $V_{TG} = 0V$ , we find the conduction band profile to be tilted downwards here. Figure 9.9(e) displays a zoom into the conduction band profile in the vicinity of the QW, for which the corresponding wave function probability is plotted as a dotted line. This configuration presents itself as more symmetric than the band profile in the zero-bias case. We assign this development to a compensation of internal electric fields and the external TG-field. As illustrated in figure 9.9(f), the symmetric arrangement of the wave function probability inside the QW manifests itself in an almost total balancing of the interface contributions to Rashba-type SOI. Consistently, the calculation of the Rashba coefficient shows a decrease of  $\alpha$  by a factor of four to  $\alpha = -0.024 \cdot 10^{-12} eVm$ . The simulated situation in figures 9.9(d) - (f) corresponds to the end of gating regime I in our MT measurement sequence, in which we find no indications of SOI in the magnetooscillations in our experiments. This is in line with the calculations of  $\alpha$ .

Figure 9.9(g) displays the conduction band profile for  $V_{TG} = +1.0V$ , for which we artificially deionize the deep level donor states inside the upper InAlAs barrier layer in the  $z$ -interval between  $50nm$  and  $120nm$ . This corresponds to the electrostatic situation in gating areas II, III and IV in our MT measurement sequence, in which significant charge migration from the QW via InAlAs deep level donor states takes place. Evaluating the gained electron density in the QW in this situation yields an equivalent charge density as for the case depicted in figure 9.9(a) with  $V_{TG} = 0V$ . A zoom into the band profile in the vicinity of the QW in figure 9.9(h) reveals a pronounced structural asymmetry. The band profile is tilted towards the bottom QW interface, which leads to an equivalent shift of the wave function probability. Figure 9.9(i) depicts the wave function probability weighted with the electric field. The plot clearly shows the modification of the spatial symmetry due to charge transfer from the QW into the top InAlAs barrier. This leads to a



significant change in the strength of the SOC. The calculations of the Rashba coefficient yield an increase of  $\alpha$  by around a factor of 12, as compared to the situation in figure 9.9(d) with  $V_{TG} = +1.0V$  without the artificial deionization of InAlAs defect states. This is in line with our experimental observation of a significant increase of the Rashba-type SOI, as we experimentally find it to rise above our experimental resolution limit (see figure 9.7) in gating area III. Even though, our calculated values of  $\alpha$  do not coincide with the experimentally determined values, the above band structure simulations together with the corresponding calculations of  $\alpha$  clearly reflect the evolution of the SOI strength in our heterostructure and underline the central role of intrinsic electric fields on the structural inversion asymmetry in the layer system.

### 9.4.6 Comparison to literature

Due to the complex electrostatic situation in the heterostructure, it is rather difficult to give a meaningful assignment of the individual contributions to SOI, i.e. interface and non-interface contribution, in the system. According to our calculations of  $\alpha$ , we find no clear predominance of one contribution over the other. Surprisingly large Rashba parameters have been reported previously. However, the results and interpretations are very contradictory and differ from our analysis:

Studying the oscillatory behavior of the magnetoresistance in a non-intentionally doped  $\text{In}_{0.75}\text{Ga}_{0.25}\text{As}/\text{In}_{0.75}\text{Al}_{0.25}\text{As}$  heterostructure with an upper InAlAs barrier thickness of  $120\text{nm}$  as in our samples, Holmes et al. [117] determined a Rashba coefficient of  $\alpha = 1 \cdot 10^{-11} \text{eV}$  at an electron density of  $n_s = 1.45 \cdot 10^{11} \text{cm}^{-2}$  in an ungated Hall bar sample. They attribute this large Rashba coefficient at this particularly low electron density to a pronounced structural inversion asymmetry, which they claim is created by built-in electric fields due to the Fermi level pinning and an asymmetric background impurity density in their heterostructure. By external gating of their devices, they claim to exclude the interface contribution to the Rashba parameter to be the dominating origin of Rashba-type SOI in their devices.

This assignment of the SOI strength is in contrast to a study from Sato et al. [199]. Analysing the magnetoresistivity of modulation doped  $\text{In}_x\text{Ga}_{1-x}\text{As}/\text{In}_x\text{Al}_{1-x}\text{As}$  heterostructures, they found a Rashba coefficient as large as  $\alpha = -3 \cdot 10^{-11} \text{eV}$  for  $x = 0.75$  and a QW-width of  $30\text{nm}$ . They assign their exceptionally large SOI strength to a pronounced difference of the wave function probability at the top and bottom QW interfaces. They test this hypothesis by means of MT measurements on the same heterostructure, yet with the QW width being reduced to  $10\text{nm}$ . Thereby, they find no indications of SOI in the magnetoresistance.

The Landau level broadening of the magnetooscillations prevents a study of certainly present SOI in the linear gating area I. This impedes a comparison of the giant SOI in the rather complex gating area III to the evolution of SOI strength with the TG electric field in gating area I, where there is no contribution of the migrated electrons to the potential landscape of the QW. Reducing the InAlAs deep level donor density, which leads to a small quantum lifetime in our heterostructures, presents itself as vital for the study of SOI

effects via MT measurements in our devices.

### 9.5 Conclusion

In this chapter, we explored the physical origin of the second frequency generation in the FFT of the longitudinal resistivity in gating area III of our MT measurement sequences with top-gated Hall bar samples. After carefully excluding evaluation and measurement artifacts, as well as size-quantization related effects, we conclude that we are in the presence of a giant SOI. Through a qualitative Schrödinger-Poisson based picture, we suggest that this giant SOI is directly related to the charge migration processes in gating areas II, III and IV. We deduced that Rashba-type SOI gives rise to the experimentally observed beating in  $\rho_{xx}(B)$ . By evaluating the FFT spectra of the MT measurements, we determined the Rashba coefficient in gating area III to be as high as  $\alpha_{FFT} \approx 2.4 \cdot 10^{11} \text{cm}^{-2}$ , which corresponds to a spin-splitting energy of  $\Delta E_{ss}^{FFT} \approx 10 \text{meV}$ . Employing a second evaluation method, i.e. the analysis of the node position in the oscillations of the magnetoresistance, we are able to determine the Rashba coefficient without incorporation of the Zeeman effect. By means of the beating-node analysis, we find a slightly smaller SOI strength, yielding an overestimation of 5 - 10% of the Rashba coefficient via the FFT analysis. Yet, the determination of  $\alpha$  on the basis of the node position is less often applicable in our MT measurements, since in the majority of magnetooscillation measurements less than three distinct nodes can be identified.

In order to gain comprehension about the microscopic origin leading to this significant increase in SOI strength in gating area III, we performed self-consistent band structure simulations with a Schrödinger-Poisson solver for different electrostatic situations during our MT measurement sequence. The Rashba coefficient is obtained via calculations in the envelope function approximation within the  $\mathbf{k} \cdot \mathbf{p}$ -method. To emulate the charge migration processes in gating areas II to IV, in which a substantial amount of charge carriers is located in InAlAs deep level donor states, we artificially deionize these defect states in between 50nm and 120nm in the upper barrier layer to analyse the effect on SOI. We determine an increase of SOI strength by a factor of 12 as compared to the ionized case of InAlAs deep level donor states. Our calculations clearly mimic the observed evolution of SOI strength in our MT measurement sequence, even though we are not able to calculate meaningful values of  $\alpha$ , since we lack an exact knowledge of the complex electrostatic situation in the heterostructure.

Note that besides the giant SOI occurring in the gating regime III, we are not able to analyse certainly present SOI in the linear gating area I due to the poor resolution limit of  $\alpha$  by evaluating the magnetooscillations, which we employ as sensing probe for SOI. To gain a better resolution of the frequency modulation in the magnetooscillations, it seems crucial to reduce the density of background impurities in the heterostructure.

## Conclusion and outlook

In this thesis, we evaluated the different aspects, which are critical for the realization of reliable 1D spinorbitronic devices from a materials perspective. For this purpose, we studied the electric transport behavior in one and two dimensions in the InGaAs/InAlAs-based material system, which offers high electron mobility and in principle gives access to high spin-orbit interaction. In our initial 1D transport measurements with electrically defined quantum point contacts, we found severe conductance instabilities near depletion of the 1D channel, which furthermore led to a significant hysteretic behavior with impeded ballisticity. In a systematic study of the electric transport in different InGaAs/InAlAs layouts, we identified energy states at the InGaAs surface, together with ionized deep level donor states inside the InAlAs barrier layers to limit the field-effect control of the transport properties in one and two dimensions. On the basis of the obtained results - all merging in a conclusive charge transfer model which we developed in the course of this thesis - we eventually achieved reliable control of the electric transport characteristics and accomplished to significantly enlarge the charge density range in the 2DEG accessible via external gating. In the course of this evaluation, we reveal a top-gate voltage field regime, in which we create a metastable charge configuration state in the system that yielded a giant and surprising magnification of Rashba-type spin-orbit interaction. We provide an interpretation for the origin of this effect by means of self-consistent band structure calculations.

In the beginning of this thesis, we explored different active layer designs of InAs/InGaAs/ InAlAs systems. Building on the state of the art at that time, we explored their applicability for spinorbitronic devices. In our analysis, we compared modulation doped and non-intentionally doped heterostructures (also denoted as undoped heterostructures in this thesis). In these latter structures, we exploited the peculiar and unavoidable, crystal impurity-driven intrinsic doping property observed in InAlAs to implement 2DEGs. By means of self-consistent Schrödinger-Poisson simulations of these heterostructures, we were able to determine an ionized background impurity density of  $N_D^{total} = 3 \cdot 10^{16} \text{cm}^{-3}$

in our system, which is in line with findings in literature [37, 38, 108].

Given the high mobilities at moderately low densities we achieved in undoped layer systems and by relying on the possibility to tune the Rashba spin-orbit interaction strength in the system with an external gate electric field, we chose non-intentionally doped InGaAs/InAlAs heterostructures as the initial testing platform for the realization and evaluation of 1D conductance in this ternary alloy system.

Our analysis of 1D transport in electrically defined quantum point contacts, which were formed via different finger-gate layouts, provided important insights into the inherent limitations of ballisticity in the employed material system. We identified electrostatic disorder to induce localized states inside the 1D transport channel, giving rise to a particular energy-dependence of the transmission coefficient. At low temperatures of  $T \approx 370\text{mK}$  the disorder potential manifested itself in form of conductance oscillations, imposed on the integer conductance steps.

By introducing a center-gate electrode in between the two split-gates, we achieved to significantly improve quantized conductance inside the 1D channel, using the center-gate as an additional knob to tune the lateral confinement potential. The positively biased center-gate allows to steepen the potential inside the constriction and thus to enlarge the 1D subband spacing. Engendered by the positive center-gate voltage, a more negative split-gate voltage was required to drive the quantum point contact into depletion. The corresponding enlarged band tilting in real space led to the emergence of a substantial bias history dependence of the 1D transport properties in form of a hysteresis in the conductance curves, as well as to unstable conductance properties.

In order to gain deeper insight into the material-related origins of the electrostatic response of the system, we systematically evaluated the field-effect tunability of the transport properties in 2DEGs in our heterostructure. For this purpose, we use the sheet carrier density and mobility as sensing probes, which we determined from magnetotransport measurements on top-gated Hall bar samples. In the first step of our detailed study, we identified a large density of energy states to be present within  $5\text{nm}$ -thin InGaAs surface layers used as protection from oxidation of the heterostructure, as well as energy states inside the subsequently deposited gate-dielectric insulating material  $\text{Al}_2\text{O}_3$ . Both types of defect energy states clearly limit the field-effect control of the transport properties in the system. We revealed that these interfacial energy states will easily induce the generation of a parasitic conductive layer at the semiconductor surface, which induces a loss of capacitive coupling to the quantum well. It is interesting to note, that the conductivity of this parasitic conductive interface layer was so low that its presence could not be experimentally detected from its contributions to the conductivity of the samples. Instead, its existence had to be deduced indirectly. With our model, we are able to explain the experimentally similar observations, but so far incomprehensible results reported in [14], in which an incapacity to control the electron density in top-gated InAs/ InGaAs/ InAlAs heterostructure was observed in a large bias range for samples with a  $10\text{nm}$  InGaAs surface layer.

Based on the results of our 2D transport study, we identified that local variations of the real space band profile, which are generated during a 1D conductance measurement,

---

provoke charge reconfigurations within the constriction area at the surface. These occurred on the timescale of minutes, consequently being the origin of the previously observed experimental instability of the conductance in our QPC experiments. Additionally, the migrated charges lead to an impaired confinement potential, resulting in a deterioration of quantized conductance features.

Building on these materials-related insights, we were able to greatly reduce the density of surface states in our hybrid dielectric/heterostructure system. We found a new wet-chemical cleaning step of the heterostructure surface to be pivotal in the sample fabrication process. Therein, residual native oxides at the semiconductor surface, which were previously only insufficiently annihilated during the self-cleaning atomic-layer deposition process of the  $\text{Al}_2\text{O}_3$  dielectric layer and thus introduced parasitic energy states at the semiconductor/dielectric interface, are effectively removed by the etchant.

By further reduction of the InGaAs cap thickness ( $2.5\text{nm}$  instead of previous  $5\text{nm}$ ) in combination with the additional wet-chemical cleaning step, we achieved a very significant and reproducible expansion of the charge density range in 2DEGs, which we are able to reliably induce via the linear electric field-effect. We further analysed the compound InAlAs as the semiconductor heterostructure surface termination, whereby we determined a similar field-effect control as for the InGaAs-capped devices when  $\text{Al}_2\text{O}_3$  was applied as dielectric.

Using these newly developed fabrication processes to inhibit interface state formation allowed us to demonstrate robust and non-hysteretic 1D conductance in triple-gate defined quantum point contacts. The devices exhibit well-pronounced quantization steps even at  $T = 1.5\text{K}$ . Remarkably, this significant progress was achieved in all studied types of heterostructures: in InGaAs- and InAlAs-terminated samples, as well as in heterostructures with an InAs inset inside the InGaAs quantum well.

At this point of the conclusion, let us point out the pivotal role of the analysis of a second step in our detailed study of 2D systems - the top-gate voltage regime beyond the linear capacitor behavior - for our microscopic understanding of the material system. In particular, it was this analysis which delivered important hints, from which we deduced the above mentioned significant amelioration of the operation of 2D and 1D devices.

Indeed, our comprehensive study in 2DEGs conducted over a larger than usual range of top-gate voltages, allowed us to develop a novel consistent microscopic model, explaining many peculiarities of gated InGaAs/InAlAs heterostructures, reported in this thesis and in the literature. Our model is qualitatively consistent with all the major experimental signatures observed in 2D and 1D devices in this thesis. While being phenomenological, the model is also consistent with quantitative verifications that we could access in this impurity-governed system.

A main element of our model – which at the same time identifies the key challenge in the engineering of such InAlAs-based heterostructures – is the uncovering of the major role played by the impurity-based deep level donor states in the gate operation - a point which has been overlooked in many literature reports up to now. The gate operation

inevitably results in electron migration from the quantum well into ionized deep level donor states inside the InAlAs spacer layer above a certain threshold gate voltage. This induces the formation of a metastable state in the system, introducing a pronounced structural asymmetry into the heterostructure.

These implications of our model are supported by the analysis of the functional dependence of the electron mobility in our 2DEGs to the corresponding electron density. Indeed, we identified scattering at 3D Coulombic disorder potential, i.e. ionized deep level donor states inside the InAlAs barrier layers, to be the limiting scattering mechanism in the system. With increasing top-gate voltages, we found that scattering at 2D remote Coulomb potentials arises from the negative charges transferred towards the interface. This process increasingly contributes to the total scattering in the system, which is consistent with our charge transfer model.

Our newly developed model also allowed us to develop an understanding of Rashba spin-orbit coupling in our 2D systems and to interpret experimental signatures which were surprising at first sight. In the above mentioned metastable regime, we experimentally encountered giant values of the Rashba coefficient from evaluating the magnetooscillations of the resistivity. The value of approximately  $\alpha \approx 2 \cdot 10^{-11} \text{ eVm}$  in our quantum well at a charge density of  $n_s \approx 6 \cdot 10^{11} \text{ cm}^{-2}$  is among the highest values reported in literature for an undoped InGaAs-based heterostructure so far. Similar values have only been reported in two instances in the literature [117, 199], but had so far been inconsistently interpreted. In this thesis, we present self-consistent Schrödinger-Poisson simulations in combination with calculations, employing the envelope function approximation within the  $\mathbf{k} \cdot \mathbf{p}$ -method, which reproduce the observed phenomenology, and in particular the occurrence of giant Rashba coefficients, extremely well. Again, the ionized deep level donor states, which are partly neutralized under gate operation, play a central role in the understanding of the origin of this phenomenon.

Note that the analysis of the magnetooscillations allowed us to estimate the resolution limit of the SOI via magnetotransport measurements. We found this experimental method of sensing the SOI strength to be strongly limited by the small quantum lifetime  $\tau_q$  of the conduction electrons in the system. We inferred that the absence of certainly present SOI effects in the linear field-effect regime of our top-gated samples (denoted as gating regime I in the thesis) is owed to this poor resolution via analysing the magnetooscillations.

Actually, the short  $\tau_q$  again points out the major role of the deep level impurities in the InAlAs barrier. The  $\tau_q$  value indicates that scattering at potential fluctuations of the conduction electrons causes a significant Landau level broadening in our system [43, 50, 51]. Additionally, the ratio  $\tau_{tr}/\tau_q > 10$ , where  $\tau_{tr}$  is the mean scattering time deduced from the electron mobility  $\mu$ , indicates that long-range scattering potentials dominate the transport in our system. Typically, these can be expected to be predominantly of Coulombic nature in our material system. Given their presence in the direct vicinity of the quantum well and their high concentration of the order of  $> 10^{16} \text{ cm}^{-3}$ , we conclude the random arrangement of the ionized deep level donor states inside the InAlAs to be the origin of these long-range scattering potentials. This 3D Coulombic disorder,

---

resulting from impurity-induced deep level donor states, on the one hand limits the conductivity in the 2D electron system, while, on the other hand, it dominates the density of states-broadening of the Landau levels.

Summarizing, one key conclusion of this thesis is the importance to realize the omnipresence of the deep level donor states inside the InAlAs layer in the gate operation of 1D and 2D devices in InGaAs/InAlAs-based systems. More precisely, we attribute the experimentally observed impeded ballisticity in our 1D devices to the introduced potential disorder in the 1D channel, as well as the poor resolution of SOI effects owing to mobility limitations in the system to the InAlAs defect states. Furthermore, they play a major role in the charge migration processes under gate operation. These points illustratively demonstrate the broad and diverse influence of InAlAs deep level donor states on the (magneto)transport in one and two dimensions.

In this work, we have developed a significant level of control, which allowed reproducible and stable operation of 1D quantum point contact devices in heterostructures where the 2DEG is buried  $130\text{nm}$  below the surface. At the same time, we note that first measurements on near-surface QW devices indicated that, even when employing our improved device fabrication recipe, 1D transport through quantum point contacts is prone to instabilities due to charge migration processes inside the heterostructure, still mediated by InAlAs deep level donor states. Thus, looking into future developments of this material system for spinorbitronic devices, our experimental results and the interpretation strongly point out the need that finding strategies to significantly decrease the density of deep level donor impurities in the InAlAs will represent a major advancement in the use of InAlAs-based heterostructures for spinorbitronic applications. In the preliminary growth study presented in this thesis, we achieved to substantially reduce the doping-providing, arsenic-related InAlAs defect states. Yet, the electron mobility in these structures was still impaired, evidencing the necessity to further refine the epitaxial process for these heterostructures. This goal is currently pursued through a systematic MBE growth study in a dedicated Ph.D. project [126].

Given the significant charge transfer under gate operation, controlling the interface between the semiconductor heterostructure and the dielectric will certainly represent a second important factor to achieve robust device operation. In the present thesis, we point out that it may be useful to reconsider the role of oxygen at this interface. Indeed, studying the gate operation of devices with MgO and HfO<sub>2</sub> as dielectric materials led to similar results as for devices for which Al<sub>2</sub>O<sub>3</sub> is employed.





# IV

## Appendix

<b>A</b>	<b>Sample fabrication .....</b>	<b>177</b>
----------	---------------------------------	------------

<b>B</b>	<b>Supplementary measurements .....</b>	<b>181</b>
----------	---	------------

B.1	1D and 2D transport measurements .....	181
B.2	Estimation of the quantum lifetime.....	185
B.3	Determination of SOI strength .....	186

	<b>Bibliography .....</b>	<b>187</b>
--	---------------------------	------------

	Acknowledgments .....	203
--	-----------------------	-----





# Sample fabrication

## I. Wet etch process of Hall bar mesa

- Standard cleaning of sample in acetone (Ac) (60s in ultrasonic bath), acetone (2min), propanol (Prop) (2min)
- Spin resist S1813: 30s, 2000rpm/s, 8000rpm
- Softbake: 4min at 90°C
- Exposure in mask aligner, Hall bar mask, 80s at 275W
- Develop in AR300-26 :  $\text{H}_2\text{O} = 1 : 3$  for 45s, rinsing in deionized (DI) water
- Etching of mesa with  $\text{C}_6\text{H}_8\text{O}_7 : \text{H}_2\text{O} : \text{H}_2\text{O}_2(30\%) : \text{H}_3\text{PO}_4(98\%) = 22 : 88 : 2 : 1.2$ , rinsing in DI water
- Lift-off in Ac (60°C), Ac, Prop

## II. Processing of ohmic contacts

- Procedure I
- Standard cleaning: Ac, Ac, Prop 2min each
- Prebake 5min at 120°C
- Spin resist LOR 3A: 45s, 2000rpm/s, 2000rpm
- Softbake: 4min at 120°C
- Spin resist: S1813: 30s, 2000rpm/s, 8000rpm

## A Sample fabrication

---

- Softbake: 4min at 90°C
- Optical lithography: UV exposure in mask aligner, ohmic contact mask, 81s at 275W
- Develop in MF26A for 50s, rinsing in DI water
- Oxide removal with HCl-dip:  $\text{H}_2\text{O} : \text{HCl}(37\%) = 1 : 1$  for 60s, rinsing in DI water
- Evaporation of 240nm/60nm AuGe(88% / 12%)/Ni
- Lift-off in Remover PG (60°C), Remover PG, Prop, Prop
- Forming gas annealing at 10mbar: 350°C for 120s, 450°C for 75s

### III. Processing of top-gate on Hall bar

- Procedure I and II
- HCl-dip:  $\text{H}_2\text{O} : \text{HCl}(37\%) = 1 : 1$  for 60s, rinsing in DI water
- $\text{Al}_2\text{O}_3$  deposition with ALD: flow  $\text{N}_2$  20sccm, purge time 4s,  $T = 300^\circ\text{C}$
- Standard cleaning: Ac, Ac, Prop 2min each
- Spin resist: S1813: 30s, 2000rpm/s, 8000rpm
- Softbake: 4min at 90°C
- Optical lithography: UV exposure in mask aligner, top-gate mask, 81s at 275W
- Develop in AR300-26 :  $\text{H}_2\text{O} = 1 : 3$  for 45s, rinsing in deionized (DI) water
- Evaporation of 20nm/100nm Ti/Au
- Lift-off in Ac (60°C), Ac, Prop

### IV. Processing of split-gate electrodes on Hall bar mesa

- Procedure I and II
- HCl-dip:  $\text{H}_2\text{O} : \text{HCl}(37\%) = 1 : 1$  for 60s, rinsing in DI water
- $\text{Al}_2\text{O}_3$  deposition with ALD: flow  $\text{N}_2$  20sccm, purge time 4s,  $T = 300^\circ\text{C}$
- Standard cleaning: Ac (150°C), Ac, Prop 2min each
- Spin resist PMMA 950k 4.5%:
  - (1) 3s, 4000rpm/s, 800rpm

---

(2) 40s, 4000rpm/s, 6000rpm

- Softbake: 2min at 150°C
- Electron beam lithography: acceleration voltage 30kV, aperture 10μm
- Develop in AR500-56 for 1min30s, 10s Prop
- Evaporation of 5nm/35nm Ti/Au

## **V. Processing of contacts to split-gate electrodes on Hall bar mesa**

- Procedure I, II and IV
- Standard cleaning: Ac (150°C), Ac, Prop 2min each
- Spin resist PMMA 950k 4.5%:
  - (1) 3s, 4000rpm/s, 800rpm
  - (2) 40s, 4000rpm/s, 4000rpm
- Softbake: 2min at 150°C
- Electron beam lithography: acceleration voltage 5kV, aperture 30μm
- Develop in AR500-56 for 1min30s, 10s Prop
- Evaporation of 15nm/100nm Ti/Au

## **VI. Processing of split-gated Hall bar sample with global top-gate**

- Procedure I, II, IV and V
- Al<sub>2</sub>O<sub>3</sub> deposition with ALD: flow N<sub>2</sub> 20sccm, purge time 4s, T = 300°C
- Standard cleaning: Ac, Ac, Prop 2min each
- Spin resist: S1813: 30s, 2000rpm/s, 8000rpm
- Softbake: 4min at 90°C
- Optical lithography: UV exposure in mask aligner, top-gate mask, 81s at 275W
- Develop in AR300-26 : H<sub>2</sub>O = 1 : 3 for 45s, rinsing in deionized (DI) water
- Evaporation of 20nm/100nm Ti/Au
- Lift-off in Ac (60°C), Ac, Prop



# B

## Supplementary measurements

### B.1 1D and 2D transport measurements

wafer	$d_{spacer}$	$n_s^{dark}$	$\mu^{dark}$	$n_s^{ill}$	$\mu^{ill}$
C160406B	35	/	/	3.5	182000
C160406B/Al <sub>2</sub> O <sub>3</sub>	35	0.7	27000	3.5	200000
C160418A	50	/	/	3.5	192000
C160418A/Al <sub>2</sub> O <sub>3</sub>	50	0.7	28000	3.6	178000
C160418B	90	0.9	170000	3.4	120000
C160418B/Al <sub>2</sub> O <sub>3</sub>	90	1.2	260000	3.3	130000
C160429A/Al <sub>2</sub> O <sub>3</sub>	130	2.5	150000	3.5	190000

**Table B.1:** Test series of Hall bar samples with increasing InAlAs spacer thickness  $d_{spacer}$ , given in units of  $nm$ , and with and without Al<sub>2</sub>O<sub>3</sub> as dielectric deposited on the semiconductor surface. The charge densities  $n_s^{dark}$  and  $n_s^{ill}$  are given in units of  $10^{11} cm^{-2}$ , the mobilities  $\mu^{dark}$  and  $\mu^{ill}$  in units of  $cm^2/Vs$ .

## B Supplementary measurements

wafer	$n_s^{dark}$	$\mu^{dark}$	$n_s^{ill}$	$\mu^{ill}$
C160316B-vdP	2.1	61000	4.9	132000
C160316B-1/Al <sub>2</sub> O <sub>3</sub> +SG	2.2	61000	4.9	130000
C160316B-4/Al <sub>2</sub> O <sub>3</sub> +SG	3.0	101000	4.6	120000
C160316B-5/Al <sub>2</sub> O <sub>3</sub> +SG	5.0	137000	4.8	153000
C160316B-6/Al <sub>2</sub> O <sub>3</sub> +SG	3.1	95000	4.7	115000
C160316B-9/Al <sub>2</sub> O <sub>3</sub> +SG+TG	3.3	85000	4.9	123000
C160316B-10/Al <sub>2</sub> O <sub>3</sub> +SG+TG	n.a.	n.a.	4.6	131000
C160428A-1/Al <sub>2</sub> O <sub>3</sub> +SG	2.8	149000	3.5	181000
C160428A-2/Al <sub>2</sub> O <sub>3</sub> +TG	3.4	189000	3.5	181000
C160428B-vdP	1.8	110000	3.9	200000
C160428B-1/Al <sub>2</sub> O <sub>3</sub> +TG	4.1	178000	n.a.	n.a.
C160428B-3/Al <sub>2</sub> O <sub>3</sub> +TG	4.2	172000	n.a.	n.a.
C160428B-4/Al <sub>2</sub> O <sub>3</sub> +TG	4.2	188000	n.a.	n.a.
C160429A-vdP1	2.0	67000	3.4	180000
C160429A-vdP2	1.4	100000	3.5	100000
C160429A-vdP3	1.9	51000	3.4	160000
C160429A-1/Al <sub>2</sub> O <sub>3</sub> +SG	2.6	152000	3.3	190000
C160429A-1/Al <sub>2</sub> O <sub>3</sub> +TG	3.6	192000	n.a.	n.a.

**Table B.2:** Hall bar and vdP samples, equipped with different functional layers and gate electrodes. The charge densities  $n_s^{dark}$  and  $n_s^{ill}$  are given in units of  $10^{11} cm^{-2}$ , the mobilities  $\mu^{dark}$  and  $\mu^{ill}$  in units of  $cm^2/Vs$ .



## B.1 1D and 2D transport measurements

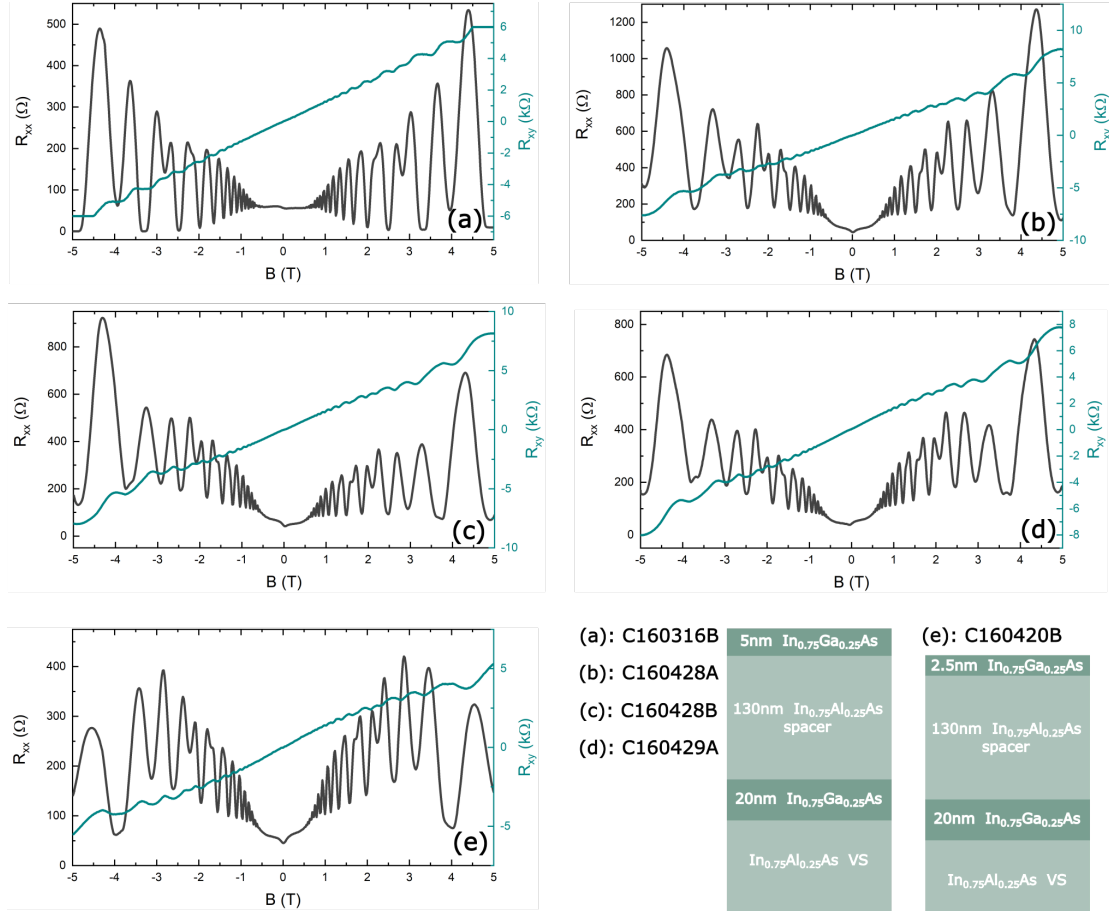


**Figure B.1:** VdP Hall measurements of wafer (a) C160316B (b) C160428A (c) C160428B (d) C160429A (e) C160420B in the illuminated state at  $T = 1.5K$  with sketches of the corresponding active layer structures.

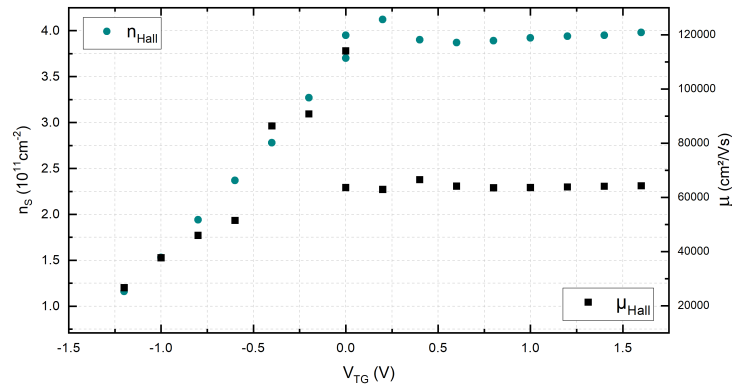


**Figure B.2:** Gating response of top-gated Hall bar sample C160406B1 at  $T = 1.5K$  in the non-illuminated state:  $n_s$  and  $\mu$  as a function of  $V_{TG}$ .

## B Supplementary measurements

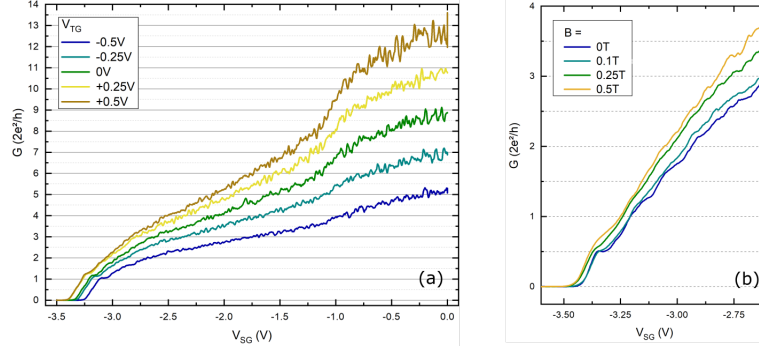


**Figure B.3:** Conductance curves of sample C160420B3 at  $T = 1.5K$  in the non-illuminated state with no channel resistance subtracted: **(a)**  $G$  of TrG1 as function of  $V_{SG}$  at  $V_{CG} = +0.3V$  for various  $V_{TG}$ . **(b)**  $G$  of TrG5 as function of  $V_{SG}$  at  $V_{CG} = +0.1V$  and  $V_{TG} = 0V$  for small perpendicular magnetic fields.

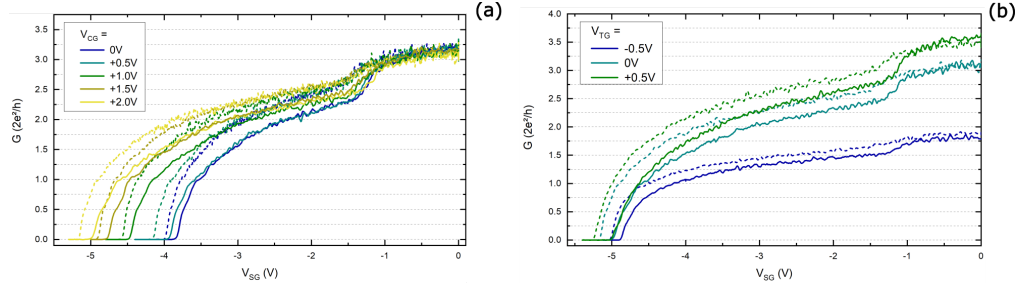


**Figure B.4:** Conductance curves of sample C160406B1 TrG1 at  $T = 1.5K$  in the non-illuminated state with no channel resistance subtracted: **(a)**  $G$  as function of  $V_{SG}$  at  $V_{TG} = 0V$  for various  $V_{CG}$ . **(b)**  $G$  as function of  $V_{SG}$  at  $V_{CG} = +0.2V$  for various  $V_{TG}$ . Down-sweeps of  $V_{SG}$  are indicated by solid lines, subsequent up-sweeps by dashed lines.

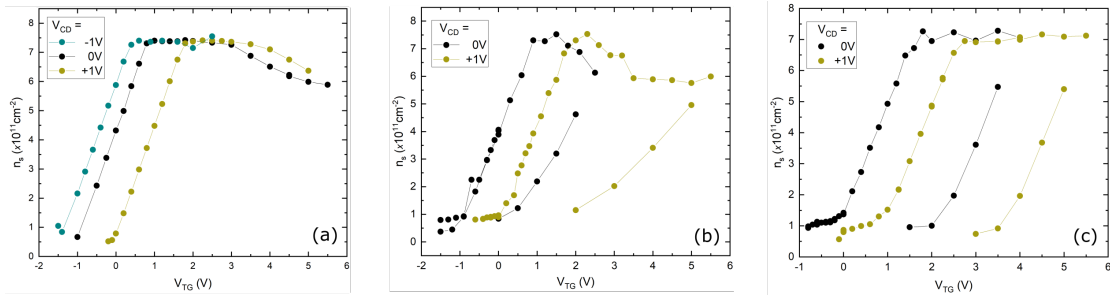


**Figure B.5:** MT measurement sequences of samples  $H$ ,  $M$  and  $N$  (wafer C160429A) in the non-illuminated state for various biased cool-down voltages  $V_{CD}$  at  $T = 4.2K$ : **(a)** Sample  $H$  with  $Al_2O_3$ , **(b)** sample  $M$  with  $HfO_2/Al_2O_3$ , **(c)** sample  $N$  with  $MgO/Al_2O_3$  as dielectric.

## B.2 Estimation of the quantum lifetime

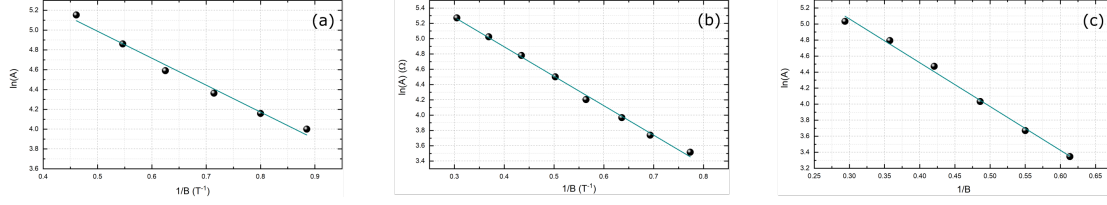


**Figure B.6:** Logarithmic plot of Shubnikov-de Haas oscillation amplitude  $A$  against inverse magnetic field  $1/B$  of sample  $H$  (wafer C160429A) (a) at  $V_{TG} = +0.4V$  in gating area I, (b) at  $V_{TG} = +0.8V$  in gating area I, (c) at  $V_{TG} = +1.4V$  in gating area II.

The magnetoresistivity  $\rho_{xx}(B)$  of a 2DEG can be described by the semi-classical expression given in equation (9.2). The oscillation amplitude of  $\rho_{xx}(B)$  decays exponentially with increasing  $1/B$ . Calculating the logarithm of the amplitude of the Shubnikov-de Haas oscillations in  $\rho_{xx}(B)$  yields a linear dependence on  $1/B$ , solely originating from the exponential factor in formula (9.2):

$$\ln(A) \propto \frac{\pi m^*}{e\tau_q} \cdot \frac{1}{B}.$$

The slope of the linear fit of  $\ln(A)$  over  $1/B$  gives an estimate for the quantum lifetime:

$$\tau_q \approx \frac{\pi m^*}{\text{slope} \cdot e}.$$

Figures B.6(a) to (c) show the Shubnikov-de Haas amplitude  $A$  of sample  $H$  on a logarithmic scale as a function of  $1/B$  at different TG-voltages. Following the above described evaluation method yields for the quantum lifetime  $\tau_q$ :


$$\begin{aligned} \tau_q &\approx 2.7 \cdot 10^{-13} s \quad \text{for } V_{TG} = +0.4V \\ \tau_q &\approx 1.9 \cdot 10^{-13} s \quad \text{for } V_{TG} = +0.8V \\ \tau_q &\approx 1.3 \cdot 10^{-13} s \quad \text{for } V_{TG} = +1.4V. \end{aligned}$$

### B.3 Determination of SOI strength

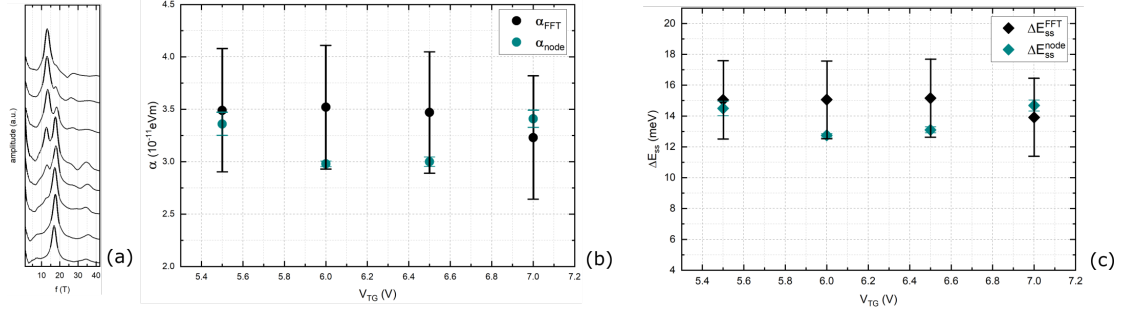


**Figure B.7:** Sample C160420A1: **(a)** FFT of the magnetooscillations in gating areas II, III and IV, vertically offset for clarity. The bottom curve corresponds to  $V_{TG} = +4.0V$ , the top-most curve to  $V_{TG} = +7.5V$ . **(b)** Rashba parameters  $\alpha_{FFT}$  and  $\alpha_{node}$  extracted from FFT and node analysis as a function of  $V_{TG}$ . **(c)** Rashba spin-splitting energies  $\Delta E_{ss}^{FFT}$  and  $\Delta E_{ss}^{node}$ , calculated with  $\alpha_{FFT}$  and  $\alpha_{node}$  from (b).

# Bibliography

- 
- [1] B. Van Wees, H. Van Houten, C. Beenakker, J. G. Williamson, L. Kouwenhoven, D. Van der Marel, and C. Foxon, *Quantized conductance of point contacts in a two-dimensional electron gas*, Physical Review Letters **60**, 848 (1988).
  - [2] D. Wharam, T. J. Thornton, R. Newbury, M. Pepper, H. Ahmed, J. Frost, D. Hasko, D. Peacock, D. Ritchie, and G. Jones, *One-dimensional transport and the quantisation of the ballistic resistance*, Journal of Physics C: Solid State Physics **21**, L209 (1988).
  - [3] R. Landauer, *Spatial variation of currents and fields due to localized scatterers in metallic conduction*, IBM Journal of Research and Development **1**, 223–231 (1957).
  - [4] M. Büttiker, *Absence of backscattering in the quantum Hall effect in multiprobe conductors*, Physical Review B **38**, 9375 (1988).
  - [5] B. J. van Wees, L. Kouwenhoven, E. Willems, C. Harmans, J. Mooij, H. Van Houten, C. Beenakker, J. Williamson, and C. Foxon, *Quantum ballistic and adiabatic electron transport studied with quantum point contacts*, Physical Review B **43**, 12431 (1991).
  - [6] M. Büttiker, *Quantized transmission of a saddle-point constriction*, Physical Review B **41**, 7906 (1990).
  - [7] L. W. Smith, H. Al-Taie, F. Sfigakis, P. See, A. Lesage, B. Xu, J. Griffiths, H. E. Beere, G. Jones, D. A. Ritchie, et al., *Statistical study of conductance properties in one-dimensional quantum wires focusing on the 0.7 anomaly*, Physical Review B **90**, 045426 (2014).
  - [8] H.-M. Lee, K. Muraki, E. Y. Chang, and Y. Hirayama, *Electronic transport characteristics in a one-dimensional constriction defined by a triple-gate structure*, Journal of Applied Physics **100**, 043701 (2006).

- [9] L. Kouwenhoven, B. Van Wees, C. Harmans, J. Williamson, H. Van Houten, C. Beenakker, C. Foxon, and J. Harris, *Nonlinear conductance of quantum point contacts*, Physical Review B **39**, 8040 (1989).
- [10] H. Chou, S. Lüscher, D. Goldhaber-Gordon, M. Manfra, A. Sergent, K. West, and R. Molnar, *High-quality quantum point contacts in GaN/AlGaN heterostructures*, Applied Physics Letters **86**, 073108 (2005).
- [11] O. Gunawan, B. Habib, E. De Poortere, and M. Shayegan, *Quantized conductance in an AlAs two-dimensional electron system quantum point contact*, Physical Review B **74**, 155436 (2006).
- [12] P. Ramvall, N. Carlsson, I. Maximov, P. Omling, L. Samuelson, W. Seifert, Q. Wang, and S. Lourdudoss, *Quantized conductance in a heterostructurally defined Ga<sub>0.25</sub>In<sub>0.75</sub>As/InP quantum wire*, Applied Physics Letters **71**, 918–920 (1997).
- [13] P. Chuang, S.-C. Ho, L. W. Smith, F. Sfigakis, M. Pepper, C.-H. Chen, J.-C. Fan, J. Griffiths, I. Farrer, H. E. Beere, et al., *All-electric all-semiconductor spin field-effect transistors*, Nature Nanotechnology **10**, 35–39 (2015).
- [14] J. Shabani, A. McFadden, B. Shojaei, and C. Palmstrøm, *Gating of high-mobility InAs metamorphic heterostructures*, Applied Physics Letters **105**, 262105 (2014).
- [15] S.-T. Lo, C.-H. Chen, J.-C. Fan, L. Smith, G. Creeth, C.-W. Chang, M. Pepper, J. Griffiths, I. Farrer, H. Beere, et al., *Controlled spatial separation of spins and coherent dynamics in spin-orbit-coupled nanostructures*, Nature Communications **8**, 1–7 (2017).
- [16] M. Kohda, T. Okayasu, and J. Nitta, *Spin-momentum locked spin manipulation in a two-dimensional Rashba system*, Scientific Reports **9**, 1–9 (2019).
- [17] S. Koester, C. Bolognesi, M. Rooks, E. Hu, and H. Kroemer, *Quantized conductance of ballistic constrictions in InAs/AlSb quantum wells*, Applied Physics Letters **62**, 1373–1375 (1993).
- [18] S. Koester, B. Brar, C. Bolognesi, E. Caine, A. Patlach, E. Hu, H. Kroemer, and M. Rooks, *Length dependence of quantized conductance in ballistic constrictions fabricated on InAs/AlSb quantum wells*, Physical Review B **53**, 13063 (1996).
- [19] P. Debray, S. Rahman, J. Wan, R. Newrock, M. Cahay, A. Ngo, S. Ulloa, S. Herbert, M. Muhammad, and M. Johnson, *All-electric quantum point contact spin-polarizer*, Nature Nanotechnology **4**, 759 (2009).
- [20] C. Mittag, M. Karalic, Z. Lei, C. Thomas, A. Tuaz, A. T. Hatke, G. C. Gardner, M. J. Manfra, T. Ihn, and K. Ensslin, *Gate-defined quantum point contact in an InAs two-dimensional electron gas*, Physical Review B **100**, 075422 (2019).
- [21] N. Goel, J. Graham, J. Keay, K. Suzuki, S. Miyashita, M. Santos, and Y. Hirayama, *Ballistic transport in InSb mesoscopic structures*, Physica E: Low-dimensional Systems and Nanostructures **26**, 455–459 (2005).

- 
- [22] D. Tobben, D. Wharam, G. Abstreiter, J. Kolthaus, and F. Schaffler, *Ballistic electron transport through a quantum point contact defined in a Si/Si<sub>0.7</sub>Ge<sub>0.3</sub> heterostructure*, Semiconductor Science and Technology **10**, 711 (1995).
  - [23] U. Wieser, U. Kunze, K. Ismail, and J. Chu, *Quantum-ballistic transport in an etch-defined Si/SiGe quantum point contact*, Applied Physics Letters **81**, 1726–1728 (2002).
  - [24] W. Lu, J. Xiang, B. P. Timko, Y. Wu, and C. M. Lieber, *One-dimensional hole gas in germanium/silicon nanowire heterostructures*, Proceedings of the National Academy of Sciences **102**, 10046–10051 (2005).
  - [25] A. Y. Kitaev, *Unpaired Majorana fermions in quantum wires*, Physics-Uspekhi **44**, 131 (2001).
  - [26] A. Y. Kitaev, *Fault-tolerant quantum computation by anyons*, Annals of Physics **303**, 2–30 (2003).
  - [27] Y. Oreg, G. Refael, and F. Von Oppen, *Helical liquids and Majorana bound states in quantum wires*, Physical Review Letters **105**, 177002 (2010).
  - [28] R. M. Lutchyn, J. D. Sau, and S. D. Sarma, *Majorana fermions and a topological phase transition in semiconductor-superconductor heterostructures*, Physical Review Letters **105**, 077001 (2010).
  - [29] R. t. Lutchyn, E. Bakkers, L. P. Kouwenhoven, P. Krogstrup, C. Marcus, and Y. Oreg, *Majorana zero modes in superconductor-semiconductor heterostructures*, Nature Reviews Materials **3**, 52–68 (2018).
  - [30] M. Kjaergaard, F. Nichele, H. J. Suominen, M. Nowak, M. Wimmer, A. Akhmerov, J. Folk, K. Flensberg, J. Shabani, w. C. Palmstrøm, et al., *Quantized conductance doubling and hard gap in a two-dimensional semiconductor-superconductor heterostructure*, Nature Communications **7**, 1–6 (2016).
  - [31] H. J. Suominen, M. Kjaergaard, A. R. Hamilton, J. Shabani, C. J. Palmstrøm, C. M. Marcus, and F. Nichele, *Zero-energy modes from coalescing Andreev states in a two-dimensional semiconductor-superconductor hybrid platform*, Physical Review Letters **119**, 176805 (2017).
  - [32] T.-M. Chen, M. Pepper, I. Farrer, G. Jones, and D. Ritchie, *All-electrical injection and detection of a spin-polarized current using 1D conductors*, Physical Review Letters **109**, 177202 (2012).
  - [33] M. Nowak and B. Szafran, *Spin current source based on a quantum point contact with local spin-orbit interaction*, Applied Physics Letters **103**, 202404 (2013).
  - [34] A. Manchon, H. C. Koo, J. Nitta, S. Frolov, and R. Duine, *New perspectives for Rashba spin-orbit coupling*, Nature Materials **14**, 871–882 (2015).
  - [35] K. Inoue, J. Harmand, and T. Matsuno, *High-quality In<sub>x</sub>Ga<sub>1-x</sub>As/InAlAs modulation-doped heterostructures grown lattice-mismatched on GaAs substrates*, Journal of Crystal Growth **111**, 313–317 (1991).

- [36] S.-I. Gozu, T. Kita, Y. Sato, S. Yamada, and M. Tomizawa, *Characterization of high indium content metamorphic InGaAs/InAlAs modulation-doped heterostructures*, Journal of Crystal Growth **227**, 155–160 (2001).
- [37] F. Capotondi, G. Biasiol, I. Vobornik, L. Sorba, F. Giazotto, A. Cavallini, and B. Fraboni, *Two-dimensional electron gas formation in undoped In<sub>0.75</sub>Ga<sub>0.25</sub>As/In<sub>0.75</sub>Al<sub>0.25</sub>As quantum wells*, Journal of Vacuum Science & Technology B: Microelectronics and Nanometer Structures Processing, Measurement, and Phenomena **22**, 702–706 (2004).
- [38] C. Chen, I. Farrer, S. N. Holmes, F. Sfigakis, M. P. Fletcher, H. E. Beere, and D. A. Ritchie, *Growth variations and scattering mechanisms in metamorphic In<sub>0.75</sub>Ga<sub>0.25</sub>As/In<sub>0.75</sub>Al<sub>0.25</sub>As quantum wells grown by molecular beam epitaxy*, Journal of Crystal Growth **425**, 70–75 (2015).
- [39] P. Brounkov, T. Benyattou, G. Guillot, and S. Clark, *Admittance spectroscopy of InAlAs/InGaAs single-quantum-well structure with high concentration of electron traps in InAlAs layers*, Journal of applied physics **77**, 240–243 (1995).
- [40] J. A. Del Alamo, *Nanometre-scale electronics with III-V compound semiconductors*, Nature **479**, 317 (2011).
- [41] R. M. Wallace, P. C. McIntyre, J. Kim, and Y. Nishi, *Atomic Layer Deposition of Dielectrics on Ge and III–V Materials for Ultrahigh Performance Transistors*, MRS Bulletin **34**, 493–503 (2009).
- [42] P. Drude, *Zur Elektronentheorie der Metalle*, Annalen der Physik **306**, 566–613 (1900).
- [43] T. Ihn, *Semiconductor Nanostructures: Quantum states and electronic transport* (Oxford University Press, 2010).
- [44] M. Kane, N. Apsley, D. Anderson, L. Taylor, and T. Kerr, *Parallel conduction in GaAs/Al<sub>x</sub>Ga<sub>1-x</sub>As modulation doped heterojunctions*, Journal of Physics C: Solid State Physics **18**, 5629 (1985).
- [45] M. Reed, W. Kirk, and P. Kobiela, *Investigation of parallel conduction in GaAs/Al<sub>x</sub>Ga<sub>1-x</sub>As modulation-doped structures in the quantum limit*, IEEE Journal of Quantum Electronics **22**, 1753–1759 (1986).
- [46] H. Störmer, A. Gossard, and W. Wiegmann, *Observation of intersubband scattering in a 2-dimensional electron system*, Solid State Communications **41**, 707–709 (1982).
- [47] L. Landau, *Diamagnetismus der Metalle*, Zeitschrift für Physik **64**, 629–637 (1930).
- [48] P. Coleridge, R. Stoner, and R. Fletcher, *Low-field transport coefficients in GaAs/Ga<sub>1-x</sub>Al<sub>x</sub>As heterostructures*, Physical Review B **39**, 1120 (1989).
- [49] S. D. Sarma and F. Stern, *Single-particle relaxation time versus scattering time in an impure electron gas*, Physical Review B **32**, 8442 (1985).



- 
- [50] A. Gold, *Scattering time and single-particle relaxation time in a disordered two-dimensional electron gas*, Physical Review B **38**, 10798 (1988).
  - [51] U. Rössler, *Solid state theory: an introduction* (Springer Science & Business Media, 2009).
  - [52] P. Coleridge, *Small-angle scattering in two-dimensional electron gases*, Physical Review B **44**, 3793 (1991).
  - [53] K. v. Klitzing, G. Dorda, and M. Pepper, *New method for high-accuracy determination of the fine-structure constant based on quantized Hall resistance*, Physical Review Letters **45**, 494 (1980).
  - [54] R. Prange, *Quantized Hall resistance and the measurement of the fine-structure constant*, Physical Review B **23**, 4802 (1981).
  - [55] R. Winkler, *Spin-orbit coupling effects in two-dimensional electron and hole systems* (Springer, 2003).
  - [56] M. Raikh and T. Shahbazyan, *Magnetointersubband oscillations of conductivity in a two-dimensional electronic system*, Physical Review B **49**, 5531 (1994).
  - [57] P. Coleridge, *Inter-subband scattering in a 2D electron gas*, Semiconductor Science and Technology **5**, 961 (1990).
  - [58] D. Leadley, R. Fletcher, R. Nicholas, F. Tao, C. Foxon, and J. Harris, *Intersubband resonant scattering in GaAs-Ga<sub>1-x</sub>Al<sub>x</sub>As heterojunctions*, Physical Review B **46**, 12439 (1992).
  - [59] A. Yacoby and Y. Imry, *Quantization of the conductance of ballistic point contacts beyond the adiabatic approximation*, Physical Review B **41**, 5341 (1990).
  - [60] R. S. G. Lesovik, D. Khmelnitskii, and R. Shekhter, *Reflectionless quantum transport and fundamental ballistic-resistance steps in microscopic constrictions*, Journal of Experimental and Theoretical Physics Letters **48**, 238–241 (1988).
  - [61] K.-F. Berggren, T. Thornton, D. Newson, and M. Pepper, *Magnetic depopulation of 1D subbands in a narrow 2D electron gas in a GaAs:AlGaAs heterojunction*, Physical Review Letters **57**, 1769 (1986).
  - [62] K.-F. Berggren, G. Roos, and H. Van Houten, *Characterization of very narrow quasi-one-dimensional quantum channels*, Physical Review B **37**, 10118 (1988).
  - [63] J. Knobbe and T. Schäpers, *Magnetosubbands of semiconductor quantum wires with Rashba spin-orbit coupling*, Physical Review B **71**, 035311 (2005).
  - [64] J. J. Sakurai, *Advanced quantum mechanics* (Pearson Education India, 1967).
  - [65] G. Dresselhaus, *Spin-orbit coupling effects in zinc blende structures*, Physical Review **100**, 580 (1955).
  - [66] S. D. Ganichev and L. E. Golub, *Interplay of Rashba/Dresselhaus spin splittings probed by photogalvanic spectroscopy - A review*, Physica Status Solidi (B) **251**, 1801–1823 (2014).

- [67] M. Cardona, N. Christensen, and G. Fasol, *Relativistic band structure and spin-orbit splitting of zinc-blende-type semiconductors*, Physical Review B **38**, 1806 (1988).
- [68] M. Kohda, V. Lechner, Y. Kunihashi, T. Dollinger, P. Olbrich, C. Schönhuber, I. Caspers, V. Bel'kov, L. Golub, D. Weiss, et al., *Gate-controlled persistent spin helix state in (In,Ga)As quantum wells*, Physical Review B **86**, 081306 (2012).
- [69] E. I. Rashba, *Properties of semiconductors with an extremum loop. I. Cyclotron and combinational resonance in a magnetic field perpendicular to the plane of the loop*, Soviet Physics, Solid State **2**, 1109–1122 (1960).
- [70] Y. A. Bychkov and E. I. Rashba, *Oscillatory effects and the magnetic susceptibility of carriers in inversion layers*, Journal of Physics C: Solid State Physics **17**, 6039 (1984).
- [71] J. Nitta, T. Akazaki, H. Takayanagi, and T. Enoki, *Gate Control of Spin-Orbit Interaction in an Inverted  $\text{In}_{0.53}\text{Ga}_{0.47}\text{As}/\text{In}_{0.52}\text{Al}_{0.48}\text{As}$  Heterostructure*, Physical Review Letters **78**, 1335 (1997).
- [72] E. A. de Andrada e Silva, *Conduction-subband anisotropic spin splitting in III–V semiconductor heterojunctions*, Physical Review B **46**, 1921 (1992).
- [73] N. Averkiev, L. Golub, and M. Willander, *Spin relaxation anisotropy in two-dimensional semiconductor systems*, Journal of Physics: Condensed Matter **14**, R271 (2002).
- [74] J. Schliemann, J. C. Egues, and D. Loss, *Nonballistic spin-field-effect transistor*, Physical Review Letters **90**, 146801 (2003).
- [75] B. A. Bernevig, J. Orenstein, and S.-C. Zhang, *Exact  $SU(2)$  symmetry and persistent spin helix in a spin-orbit coupled system*, Physical Review Letters **97**, 236601 (2006).
- [76] G. Lommer, F. Malcher, and U. Rossler, *Spin splitting in semiconductor heterostructures for  $B \rightarrow 0$* , Physical Review Letters **60**, 728 (1988).
- [77] J. Luo, H. Munekata, F. Fang, and P. Stiles, *Effects of inversion asymmetry on electron energy band structures in GaSb/InAs/GaSb quantum wells*, Physical Review B **41**, 7685 (1990).
- [78] S. Faniel, T. Matsuura, S. Mineshige, Y. Sekine, and T. Koga, *Determination of spin-orbit coefficients in semiconductor quantum wells*, Physical Review B **83**, 115309 (2011).
- [79] T. Schäpers, G. Engels, J. Lange, T. Klocke, M. Hollfelder, and H. Lüth, *Effect of the heterointerface on the spin splitting in modulation doped  $\text{In}_x\text{Ga}_{1-x}\text{As}/\text{InP}$  quantum wells for  $B \rightarrow 0$* , Journal of Applied Physics **83**, 4324–4333 (1998).
- [80] G. Engels, J. Lange, T. Schäpers, and H. Lüth, *Experimental and theoretical approach to spin splitting in modulation-doped  $\text{In}_x\text{Ga}_{1-x}\text{As}/\text{InP}$  quantum wells for  $B \rightarrow 0$* , Physical Review B **55**, R1958 (1997).

- 
- [81] P. Pfeffer, *Spin splitting of conduction energies in GaAs-Ga<sub>0.7</sub>Al<sub>0.3</sub>As heterojunctions at  $B=0$  and  $B\neq 0$  due to inversion asymmetry*, Physical Review B **55**, R7359 (1997).
  - [82] E. A. de Andrada e Silva, G. La Rocca, and F. Bassani, *Spin-orbit splitting of electronic states in semiconductor asymmetric quantum wells*, Physical Review B **55**, 16293 (1997).
  - [83] B. Das, D. Miller, S. Datta, R. Reifengerger, W. Hong, P. Bhattacharya, J. Singh, and M. Jaffe, *Evidence for spin splitting in  $\text{In}_x\text{Ga}_{1-x}\text{As}/\text{In}_{0.52}\text{Al}_{0.48}\text{As}$  heterostructures as  $B\rightarrow 0$* , Physical Review B **39**, 1411 (1989).
  - [84] D. Grundler, *Large Rashba splitting in InAs quantum wells due to electron wave function penetration into the barrier layers*, Physical Review Letters **84**, 6074 (2000).
  - [85] P. Pfeffer and W. Zawadzki, *Spin splitting of conduction subbands in GaAs-Ga<sub>0.7</sub>Al<sub>0.3</sub>As heterostructures*, Physical Review B **52**, R14332 (1995).
  - [86] J. Luo, H. Munekata, F. Fang, and P. Stiles, *Observation of the zero-field spin splitting of the ground electron subband in GaSb-InAs-GaSb quantum wells*, Physical Review B **38**, 10142 (1988).
  - [87] F. Herzog, *Spin-orbit interaction and confinement effects in low-dimensional electron-systems studied by torque magnetometry and anisotropic magnetotransport*, Dissertation (Technische Universität München, 2015).
  - [88] A. Moroz and C. Barnes, *Effect of the spin-orbit interaction on the band structure and conductance of quasi-one-dimensional systems*, Physical Review B **60**, 14272 (1999).
  - [89] F. Mireles and G. Kirczenow, *Ballistic spin-polarized transport and Rashba spin precession in semiconductor nanowires*, Physical Review B **64**, 024426 (2001).
  - [90] U. Wurstbauer, *Herstellung und Charakterisierung von Mangan dotierten III–V Halbleiterheterostrukturen*, Dissertation (Universität Regensburg, 2008).
  - [91] C. Gerl, *Hochbewegliche zweidimensionale Lochsysteme in GaAs/AlGaAs Heterostrukturen*, Dissertation (Universität Regensburg, 2009).
  - [92] M. Utz, *Epitaxie von (Ga,Mn)As*, Dissertation (Universität Regensburg, 2012).
  - [93] F. Aumeier, *Strukturelle Untersuchung an Graded-Buffer-Systemen mit dem Transmissionselektronenmikroskop*, Masterarbeit (Universität Regensburg, 2015).
  - [94] L. J. van der Pauw, *A method of measuring the resistivity and Hall coefficient on lamellae of arbitrary shape*, Philips Technical Review **20**, 220–224 (1958).
  - [95] M. Wieand, *Conductance Quantization in the High Spin–Orbit-Coupling Material InGaAs/InAlAs*, Masterarbeit (Universität Regensburg, 2018).
  - [96] M. Schmalzbauer, *Heterostructure design of Si/SiGe two-dimensional electron systems for field-effect devices*, Dissertation (Universität Regensburg, 2014).

- [97] J. Loher, *Two-dimensional hole systems in indium-based quantum well heterostructures*, Dissertation (Universität Regensburg, 2015).
- [98] C. Neumann, *Isotopically-enriched  $^{28}\text{Si}$  heterostructures for qubit devices*, Dissertation (Universität Regensburg, 2017).
- [99] A. Wild, *Development of a robust platform for spin qubits in SiGe heterostructures*, Dissertation (Universität Regensburg, 2013).
- [100] J. Nitta, T. Bergsten, Y. Kunihashi, and M. Kohda, *Electrical manipulation of spins in the Rashba two dimensional electron gas systems*, Journal of Applied Physics **105**, 122402 (2009).
- [101] I. Vurgaftman, J. á. Meyer, and L. á. Ram-Mohan, *Band parameters for III–V compound semiconductors and their alloys*, Journal of Applied Physics **89**, 5815–5875 (2001).
- [102] F. Romanato, E. Napolitani, A. Carnera, A. Drigo, L. Lazzarini, G. Salviati, C. Ferrari, A. Bosacchi, and S. Franchi, *Strain relaxation in graded composition  $\text{In}_x\text{Ga}_{1-x}\text{As}/\text{GaAs}$  buffer layers*, Journal of Applied Physics **86**, 4748–4755 (1999).
- [103] F. Capotondi, G. Biasiol, D. Ercolani, V. Grillo, E. Carlino, F. Romanato, and L. Sorba, *Strain induced effects on the transport properties of metamorphic  $\text{InAlAs}/\text{InGaAs}$  quantum wells*, Thin Solid Films **484**, 400–407 (2005).
- [104] F. Capotondi, G. Biasiol, D. Ercolani, and L. Sorba, *Scattering mechanisms in undoped  $\text{In}_{0.75}\text{Ga}_{0.25}\text{As}/\text{In}_{0.75}\text{Al}_{0.25}\text{As}$  two-dimensional electron gases*, Journal of Crystal Growth **278**, 538–543 (2005).
- [105] S. Löhr, S. Mendach, T. Vonau, C. Heyn, and W. Hansen, *Highly anisotropic electron transport in shallow  $\text{InGaAs}$  heterostructures*, Physical Review B **67**, 045309 (2003).
- [106] D. Ercolani, G. Biasiol, E. Cancellieri, M. Rosini, C. Jacoboni, F. Carillo, S. Heun, L. Sorba, and F. Nolting, *Transport anisotropy in  $\text{In}_{0.75}\text{Ga}_{0.25}\text{As}$  two-dimensional electron gases induced by indium concentration modulation*, Physical Review B **77**, 235307 (2008).
- [107] Z. Jiang, W. Wang, H. Gao, L. Liu, H. Chen, and J. Zhou, *Strain relaxation and surface morphology of high indium content  $\text{InAlAs}$  metamorphic buffers with reverse step*, Applied Surface Science **254**, 5241–5246 (2008).
- [108] A. Hatke, T. Wang, C. Thomas, G. Gardner, and M. Manfra, *Mobility in excess of  $10^6\text{cm}^2/\text{Vs}$  in  $\text{InAs}$  quantum wells grown on lattice mismatched  $\text{InP}$  substrates*, Applied Physics Letters **111**, 142106 (2017).
- [109] N. Grandjean and J. Massies, *Epitaxial growth of highly strained  $\text{In}_x\text{Ga}_{1-x}\text{As}$  on  $\text{GaAs}$  (001): the role of surface diffusion length*, Journal of Crystal Growth **134**, 51–62 (1993).

- 
- [110] M. Lutz, R. Feenstra, F. LeGoues, P. Mooney, and J. Chu, *Influence of misfit dislocations on the surface morphology of  $\text{Si}_{1-x}\text{Ge}_x$  films*, Applied Physics Letters **66**, 724–726 (1995).
  - [111] E. A. Fitzgerald, Y.-H. Xie, D. Monroe, P. Silverman, J. Kuo, A. Kortan, F. Thiel, and B. Weir, *Relaxed  $\text{Ge}_x\text{Si}_{1-x}$  structures for III–V integration with Si and high mobility two-dimensional electron gases in Si*, Journal of Vacuum Science & Technology B: Microelectronics and Nanometer Structures Processing, Measurement, and Phenomena **10**, 1807–1819 (1992).
  - [112] E. Fitzgerald, M. Currie, S. Samavedam, T. Langdo, G. Taraschi, V. Yang, C. Leitz, and M. Bulsara, *Dislocations in relaxed SiGe/Si heterostructures*, Physica Status Solidi (A) **171**, 227–238 (1999).
  - [113] C. Lavoie, T. Pinnington, E. Nodwell, T. Tiedje, R. Goldman, K. Kavanagh, and J. Hutter, *Relationship between surface morphology and strain relaxation during growth of InGaAs strained layers*, Applied Physics Letters **67**, 3744–3746 (1995).
  - [114] K. H. Chang, R. Gilbala, D. J. Srolovitz, P. K. Bhattacharya, and J. F. Mansfield, *Crosshatched surface morphology in strained III–V semiconductor films*, Journal of Applied Physics **67**, 4093–4098 (1990).
  - [115] S. Mendach, C. Hu, C. Heyn, S. Schnüll, H. Oepen, R. Anton, and W. Hansen, *Strain relaxation in high-mobility InAs inserted-channel heterostructures with metamorphic buffer*, Physica E: Low-dimensional Systems and Nanostructures **13**, 1204–1207 (2002).
  - [116] P. Simmonds, S. Holmes, H. Beere, I. Farrer, F. Sfigakis, D. Ritchie, and M. Pepper, *Molecular beam epitaxy of high mobility  $\text{In}_{0.75}\text{Ga}_{0.25}\text{As}$  for electron spin transport applications*, Journal of Vacuum Science & Technology B: Microelectronics and Nanometer Structures Processing, Measurement, and Phenomena **27**, 2066–2070 (2009).
  - [117] S. Holmes, P. Simmonds, H. Beere, F. Sfigakis, I. Farrer, D. Ritchie, and M. Pepper, *Bychkov–Rashba dominated band structure in an  $\text{In}_{0.75}\text{Ga}_{0.25}\text{As}$ – $\text{In}_{0.75}\text{Al}_{0.25}\text{As}$  device with spin-split carrier densities of  $<10^{11}\text{cm}^{-2}$* , Journal of Physics: Condensed Matter **20**, 472207 (2008).
  - [118] J. Shabani, S. D. Sarma, and C. Palmstrøm, *An apparent metal-insulator transition in high-mobility two-dimensional InAs heterostructures*, Physical Review B **90**, 161303 (2014).
  - [119] S. Hackenbuchner, *Elektronische Struktur von Halbleiter-Nanobaelementen im thermodynamischen Nichtgleichgewicht*, Vol. 48 (Walter Schottky Institut der Technischen Universität München, 2002).
  - [120] M. Sabathil, *Opto-electronic and quantum transport properties of semiconductor nanostructures*, Vol. 67 (Walter Schottky Institut der Technischen Universität München, 2004).

- [121] T. Zibold, *Semiconductor based quantum information devices*, Vol. 87 (Walter Schottky Institut der Technischen Universität München, 2007).
- [122] T. Andlauer, *Optoelectronic and spin-related properties of semiconductor nanostructures in magnetic fields*, Vol. 105 (Walter Schottky Institut der Technischen Universität München, 2009).
- [123] T. Akazaki, J. Nitta, H. Takayanagi, T. Enoki, and K. Arai, *Improving the mobility of an  $\text{In}_{0.52}\text{Al}_{0.48}\text{As}/\text{In}_{0.53}\text{Ga}_{0.47}\text{As}$  inverted modulation-doped structure by inserting a strained InAs quantum well*, Applied Physics Letters **65**, 1263–1265 (1994).
- [124] A. Richter, M. Koch, T. Matsuyama, C. Heyn, and U. Merkt, *Transport properties of modulation-doped InAs-inserted-channel  $\text{In}_{0.75}\text{Al}_{0.25}\text{As}/\text{In}_{0.75}\text{Ga}_{0.25}\text{As}$  As structures grown on GaAs substrates*, Applied Physics Letters **77**, 3227–3229 (2000).
- [125] W. Desrat, F. Giazotto, V. Pellegrini, F. Beltram, F. Capotondi, G. Biasiol, L. Sorba, and D. Maude, *Magnetotransport in high-g-factor low-density two-dimensional electron systems confined in  $\text{In}_{0.75}\text{Ga}_{0.25}\text{As}/\text{In}_{0.75}\text{Al}_{0.25}\text{As}$  quantum wells*, Physical Review B **69**, 245324 (2004).
- [126] M. Prager, *ongoing PHD project* (Universität Regensburg).
- [127] H. Kroemer, *The 6.1A family (InAs, GaSb, AlSb) and its heterostructures: a selective review*, Physica E: Low-dimensional Systems and Nanostructures **20**, 196–203 (2004).
- [128] S. Brosig, K. Ensslin, R. Warburton, C. Nguyen, B. Brar, M. Thomas, and H. Kroemer, *Zero-field spin splitting in InAs-AlSb quantum wells revisited*, Physical Review B **60**, R13989 (1999).
- [129] W. Himmeler, *Fabrication and characterisation of Sb-based III/V-semiconductor 2D electron devices*, Masterarbeit (Universität Regensburg, 2019).
- [130] C. Mittag, M. Karalic, S. Mueller, T. Tschirky, W. Wegscheider, O. Nazarenko, M. V. Kovalenko, T. Ihn, and K. Ensslin, *Passivation of edge states in etched InAs sidewalls*, Applied Physics Letters **111**, 082101 (2017).
- [131] C. Mittag, M. Karalic, Z. Lei, T. Tschirky, W. Wegscheider, T. Ihn, and K. Ensslin, *Edgeless and purely gate-defined nanostructures in InAs quantum wells*, Applied Physics Letters **113**, 262103 (2018).
- [132] T. Thornton, M. Pepper, H. Ahmed, D. Andrews, and G. Davies, *One-dimensional conduction in the 2D electron gas of a GaAs-AlGaAs heterojunction*, Physical Review Letters **56**, 1198 (1986).
- [133] H. Zheng, H. Wei, D. Tsui, and G. Weimann, *Gate-controlled transport in narrow GaAs/ $\text{Al}_x\text{Ga}_{1-x}\text{As}$  heterostructures*, Physical Review B **34**, 5635 (1986).
- [134] W. Spicer, I. Lindau, P. Skeath, and C. Su, *Unified defect model and beyond*, Journal of Vacuum Science and Technology **17**, 1019–1027 (1980).

- 
- [135] D. Colleoni, G. Miceli, and A. Pasquarello, *Origin of Fermi-level pinning at GaAs surfaces and interfaces*, Journal of Physics: Condensed Matter **26**, 492202 (2014).
  - [136] L. Lin and J. Robertson, *Defect states at III–V semiconductor oxide interfaces*, Applied Physics Letters **98**, 082903 (2011).
  - [137] K. Thomas, J. Nicholls, M. Simmons, M. Pepper, D. Mace, and D. Ritchie, *Possible spin polarization in a one-dimensional electron gas*, Physical Review Letters **77**, 135 (1996).
  - [138] A. Micolich, *What lurks below the last plateau: experimental studies of the  $0.7 \times 2e^2/h$  conductance anomaly in one-dimensional systems*, Journal of Physics: Condensed Matter **23**, 443201 (2011).
  - [139] F. Bauer, J. Heyder, E. Schubert, D. Borowsky, D. Taubert, B. Bruognolo, D. Schuh, W. Wegscheider, J. von Delft, and S. Ludwig, *Microscopic origin of the ‘0.7-anomaly’ in quantum point contacts*, Nature **501**, 73 (2013).
  - [140] C.-K. Wang and K.-F. Berggren, *Spin splitting of subbands in quasi-one-dimensional electron quantum channels*, Physical Review B **54**, R14257 (1996).
  - [141] M. Iqbal, R. Levy, E. Koop, J. Dekker, J. De Jong, J. van der Velde, D. Reuter, A. Wieck, R. Aguado, Y. Meir, et al., *Odd and even Kondo effects from emergent localization in quantum point contacts*, Nature **501**, 79 (2013).
  - [142] S. Cronenwett, H. Lynch, D. Goldhaber-Gordon, L. Kouwenhoven, C. Marcus, K. Hirose, N. S. Wingreen, and V. Umansky, *Low-temperature fate of the 0.7 structure in a point contact: A Kondo-like correlated state in an open system*, Physical Review Letters **88**, 226805 (2002).
  - [143] T. Rejec and Y. Meir, *Magnetic impurity formation in quantum point contacts*, Nature **442**, 900 (2006).
  - [144] L. W. Smith, K. J. Thomas, M. Pepper, D. A. Ritchie, I. Farrer, J. P. Griffiths, and G. A. C. Jones, *Disorder and Interaction Effects in Quantum Wires*, Journal of Physics: Conference Series **376**, 012018 (2012).
  - [145] I. I. Yakimenko and K.-F. Berggren, *Probing dopants in wide semiconductor quantum point contacts*, Journal of Physics: Condensed Matter **28**, 105801 (2016).
  - [146] D. K. Ferry, S. M. Goodnick, and J. Bird, *Transport in nanostructures* (Cambridge University Press, 2009).
  - [147] L. Smith, H. Al-Taie, A. Lesage, F. Sfigakis, P. See, J. Griffiths, H. Beere, G. Jones, D. Ritchie, A. Hamilton, et al., *Dependence of the 0.7 anomaly on the curvature of the potential barrier in quantum wires*, Physical Review B **91**, 235402 (2015).
  - [148] N. Aoki, C. R. Da Cunha, R. Akis, D. K. Ferry, and Y. Ochiai, *Scanning gate microscopy investigations on an InGaAs quantum point contact*, Applied Physics Letters **87**, 223501 (2005).

- [149] C. R. Da Cunha, N. Aoki, T. Morimoto, Y. Ochiai, R. Akis, and D. K. Ferry, *Imaging of quantum interference patterns within a quantum point contact*, Applied Physics Letters **89**, 242109 (2006).
- [150] A. See, A. Hamilton, A. Micolich, M. Aagesen, and P. E. Lindelof, *Using light and heat to controllably switch and reset disorder configuration in nanoscale devices*, Physical Review B **91**, 085417 (2015).
- [151] S. Maeda, S. Miyamoto, M. H. Fauzi, K. Nagase, K. Sato, and Y. Hirayama, *Fabry-Pérot interference in a triple-gated quantum point contact*, Applied Physics Letters **109**, 143509 (2016).
- [152] L. Smith, H. Al-Taie, A. Lesage, K. Thomas, F. Sfigakis, P. See, J. Griffiths, I. Farrer, G. Jones, D. Ritchie, et al., *Effect of Split Gate Size on the Electrostatic Potential and 0.7 Anomaly within Quantum Wires on a Modulation-Doped GaAs/AlGaAs Heterostructure*, Physical Review Applied **5**, 044015 (2016).
- [153] A. M. Zagoskin, S. Rashkeev, R. Shekhter, and G. Wendin, *Breakdown of conductance quantization in quantum point contacts with realistic impurity potentials*, Journal of Physics: Condensed Matter **7**, 6253 (1995).
- [154] C. Nguyen, B. Brar, H. Kroemer, and J. H. English, *Surface donor contribution to electron sheet concentrations in not-intentionally doped InAs-AlSb quantum wells*, Applied Physics Letters **60**, 1854–1856 (1992).
- [155] B. Brennan and G. Hughes, *Identification and thermal stability of the native oxides on InGaAs using synchrotron radiation based photoemission*, Journal of Applied Physics **108**, 053516 (2010).
- [156] E. A. Chagarov and A. C. Kummel, *Molecular dynamics simulation comparison of atomic scale intermixing at the amorphous Al<sub>2</sub>O<sub>3</sub>/semiconductor interface for  $\alpha$ -Al<sub>2</sub>O<sub>3</sub>/Ge,  $\alpha$ -Al<sub>2</sub>O<sub>3</sub>/InGaAs, and  $\alpha$ -Al<sub>2</sub>O<sub>3</sub>/InAlAs/InGaAs*, Surface Science **603**, 3191–3200 (2009).
- [157] R. Long, B. Shin, S. Monaghan, K. Cherkaoui, J. Cagnon, S. Stemmer, P. McIntyre, and P. Hurley, *Charged Defect Quantification in Pt/Al<sub>2</sub>O<sub>3</sub>/In<sub>0.53</sub>Ga<sub>0.47</sub>As/InP MOS Capacitors*, Journal of The Electrochemical Society **158**, G103–G107 (2011).
- [158] E. J. Kim, E. Chagarov, J. Cagnon, Y. Yuan, A. C. Kummel, P. M. Asbeck, S. Stemmer, K. C. Saraswat, and P. C. McIntyre, *Atomically abrupt and unpinned Al<sub>2</sub>O<sub>3</sub>/In<sub>0.53</sub>Ga<sub>0.47</sub>As interfaces: Experiment and simulation*, Journal of Applied Physics **106**, 124508 (2009).
- [159] M. Choi, A. Janotti, and C. G. Van de Walle, *Native point defects and dangling bonds in  $\alpha$ -Al<sub>2</sub>O<sub>3</sub>*, Journal of Applied Physics **113**, 044501 (2013).
- [160] Z. Guo, F. Ambrosio, and A. Pasquarello, *Oxygen defects in amorphous Al<sub>2</sub>O<sub>3</sub>: A hybrid functional study*, Applied Physics Letters **109**, 062903 (2016).



- 
- [161] T. Perevalov, O. Tereshenko, V. Gritsenko, V. Pustovarov, A. Yelisseyev, C. Park, J. H. Han, and C. Lee, *Oxygen deficiency defects in amorphous Al<sub>2</sub>O<sub>3</sub>*, Journal of Applied Physics **108**, 013501 (2010).
  - [162] B. Shin, J. R. Weber, R. D. Long, P. K. Hurley, C. G. Van de Walle, and P. C. McIntyre, *Origin and passivation of fixed charge in atomic layer deposited aluminum oxide gate insulators on chemically treated InGaAs substrates*, Applied Physics Letters **96**, 152908 (2010).
  - [163] M. Huang, Y. Chang, C. Chang, Y. Lee, P. Chang, J. Kwo, T. Wu, and M. Hong, *Surface passivation of III–V compound semiconductors using atomic-layer-deposition-grown Al<sub>2</sub>O<sub>3</sub>*, Applied Physics Letters **87**, 252104 (2005).
  - [164] R. Timm, A. Fian, M. Hjort, C. Thelander, E. Lind, J. N. Andersen, L.-E. Wernersson, and A. Mikkelsen, *Reduction of native oxides on InAs by atomic layer deposited Al<sub>2</sub>O<sub>3</sub> and HfO<sub>2</sub>*, Applied Physics Letters **97**, 132904 (2010).
  - [165] M. Milojevic, F. Aguirre-Tostado, C. Hinkle, H. Kim, E. Vogel, J. Kim, and R. Wallace, *Half-cycle atomic layer deposition reaction studies of Al<sub>2</sub>O<sub>3</sub> on In<sub>0.2</sub>Ga<sub>0.8</sub>As (100) surfaces*, Applied Physics Letters **93**, 202902 (2008).
  - [166] M.-S. Park, M. Razaei, K. Barnhart, C. L. Tan, and H. Mohseni, *Surface passivation and aging of InGaAs/InP heterojunction phototransistors*, Journal of Applied Physics **121**, 233105 (2017).
  - [167] H.-D. Trinh, E. Y. Chang, Y.-Y. Wong, C.-C. Yu, C.-Y. Chang, Y.-C. Lin, H.-Q. Nguyen, and B.-T. Tran, *Effects of wet chemical and trimethyl aluminum treatments on the interface properties in atomic layer deposition of Al<sub>2</sub>O<sub>3</sub> on InAs*, Japanese Journal of Applied Physics **49**, 111201 (2010).
  - [168] M. Prager, *Realisation of near-surface two-dimensional electron gases in InAs-based quantum wells*, Masterarbeit (Universität Regensburg, 2018).
  - [169] W. Cabrera, B. Brennan, H. Dong, T. P. O'Regan, I. M. Povey, S. Monaghan, É. O'Connor, P. K. Hurley, R. Wallace, and Y. Chabal, *Diffusion of In<sub>0.53</sub>Ga<sub>0.47</sub>As elements through hafnium oxide during post deposition annealing*, Applied Physics Letters **104**, 011601 (2014).
  - [170] P. Ye, G. Wilk, B. Yang, J. Kwo, H.-J. Gossmann, M. Hong, K. Ng, and J. Bude, *Depletion-mode InGaAs metal-oxide-semiconductor field-effect transistor with oxide gate dielectric grown by atomic-layer deposition*, Applied Physics Letters **84**, 434–436 (2004).
  - [171] I. Krylov, R. Winter, D. Ritter, and M. Eizenberg, *Indium out-diffusion in Al<sub>2</sub>O<sub>3</sub>/InGaAs stacks during anneal at different ambient conditions*, Applied Physics Letters **104**, 243504 (2014).
  - [172] R. Engel-Herbert, Y. Hwang, and S. Stemmer, *Comparison of methods to quantify interface trap densities at dielectric/III–V semiconductor interfaces*, Journal of Applied Physics **108**, 124101 (2010).

- [173] R. Winter, I. Krylov, C. Cytermann, K. Tang, J. Ahn, P. McIntyre, and M. Eizenberg, *Fermi level pinning in metal/Al<sub>2</sub>O<sub>3</sub>/InGaAs gate stack after post metallization annealing*, Journal of Applied Physics **118**, 055302 (2015).
- [174] S. Oktyabrsky, V. Tokranov, S. Koveshnikov, M. Yakimov, R. Kambhampati, H. Bakhru, R. Moore, and W. Tsai, *Interface properties of MBE-grown MOS structures with InGaAs/InAlAs buried channel and in-situ high-k oxide*, Journal of Crystal Growth **311**, 1950–1953 (2009).
- [175] F. Aguirre-Tostado, M. Milojevic, C. Hinkle, E. Vogel, R. Wallace, S. McDonnell, and G. Hughes, *Indium stability on InGaAs during atomic H surface cleaning*, Applied Physics Letters **92**, 171906 (2008).
- [176] R. Hussey, G. Sproule, J. McCaffrey, and M. Graham, *Characterization of Oxides Formed on InP, InGaAs, InAlAs, and InGaAs/InAlAs Heterostructures at 300–500° C*, Oxidation of Metals **57**, 427–447 (2002).
- [177] M. Kobayashi, P. Chen, Y. Sun, N. Goel, P. Majhi, M. Garner, W. Tsai, P. Pianetta, and Y. Nishi, *Synchrotron radiation photoemission spectroscopic study of band offsets and interface self-cleaning by atomic layer deposited HfO<sub>2</sub> on In<sub>0.53</sub>Ga<sub>0.47</sub>As and In<sub>0.52</sub>Al<sub>0.48</sub>As*, Applied Physics Letters **93**, 182103 (2008).
- [178] C. Chen, S. Holmes, I. Farrer, H. Beere, and D. Ritchie, *High mobility In<sub>0.75</sub>Ga<sub>0.25</sub>As quantum wells in an InAs phonon lattice*, Journal of Physics: Condensed Matter **30**, 105705 (2018).
- [179] D. Laroche, S.-H. Huang, E. Nielsen, Y. Chuang, J.-Y. Li, C.-W. Liu, and T.-M. Lu, *Scattering mechanisms in shallow undoped Si/SiGe quantum wells*, AIP Advances **5**, 107106 (2015).
- [180] C.-T. Huang, J.-Y. Li, K. S. Chou, and J. C. Sturm, *Screening of remote charge scattering sites from the oxide/silicon interface of strained Si two-dimensional electron gases by an intermediate tunable shielding electron layer*, Applied Physics Letters **104**, 243510 (2014).
- [181] S. D. Sarma and E. Hwang, *Universal density scaling of disorder-limited low-temperature conductivity in high-mobility two-dimensional systems*, Physical Review B **88**, 035439 (2013).
- [182] W.-Y. Chou, G. Chang, W. Hwang, and J. Hwang, *Analysis of Fermi level pinning and surface state distribution in InAlAs heterostructures*, Journal of Applied Physics **83**, 3690–3695 (1998).
- [183] L.-F. Wu, Y.-M. Zhang, H.-L. Lv, and Y.-M. Zhang, *Atomic-layer-deposited Al<sub>2</sub>O<sub>3</sub> and HfO<sub>2</sub> on InAlAs: A comparative study of interfacial and electrical characteristics*, Chinese Physics B **25**, 108101 (2016).
- [184] H. Guan and C. Jiang, *Study on the Physical and Leakage Current Characteristics of an Optimized High-k/InAlAs MOS Capacitor with a HfO<sub>2</sub>–Al<sub>2</sub>O<sub>3</sub> Laminated Dielectric*, Coatings **8**, 417 (2018).

- 
- [185] R. Winter, I. Krylov, J. Ahn, P. McIntyre, and M. Eizenberg, *The effect of post oxide deposition annealing on the effective work function in metal/Al<sub>2</sub>O<sub>3</sub>/InGaAs gate stack*, Applied Physics Letters **104**, 202103 (2014).
  - [186] D. K. Simon, P. M. Jordan, T. Mikolajick, and I. Dirnstorfer, *On the control of the fixed charge densities in Al<sub>2</sub>O<sub>3</sub>-based silicon surface passivation schemes*, ACS Applied Materials & Interfaces **7**, 28215–28222 (2015).
  - [187] C.-H. Chang, Y.-K. Chiou, Y.-C. Chang, K.-Y. Lee, T.-D. Lin, T.-B. Wu, M. Hong, and J. Kwo, *Interfacial self-cleaning in atomic layer deposition of HfO<sub>2</sub> gate dielectric on In<sub>0.15</sub>Ga<sub>0.85</sub>As*, Applied Physics Letters **89**, 242911 (2006).
  - [188] A. O'Mahony, S. Monaghan, G. Provenzano, I. M. Povey, M. Nolan, É. O'Connor, K. Cherkaoui, S. B. Newcomb, F. Crupi, P. K. Hurley, et al., *Structural and electrical analysis of the atomic layer deposition of HfO<sub>2</sub>/n-In<sub>0.53</sub>Ga<sub>0.47</sub>As capacitors with and without an Al<sub>2</sub>O<sub>3</sub> interface control layer*, Applied Physics Letters **97**, 052904 (2010).
  - [189] R. Suzuki, N. Taoka, M. Yokoyama, S.-H. Kim, T. Hoshii, T. Maeda, T. Yasuda, O. Ichikawa, N. Fukuhara, M. Hata, et al., *Impact of atomic layer deposition temperature on HfO<sub>2</sub>/InGaAs metal-oxide-semiconductor interface properties*, Journal of Applied Physics **112**, 084103 (2012).
  - [190] A. S. Sokolov, Y.-R. Jeon, S. Kim, B. Ku, D. Lim, H. Han, M. G. Chae, J. Lee, B. G. Ha, and C. Choi, *Influence of oxygen vacancies in ALD HfO<sub>2</sub> thin films on non-volatile resistive switching phenomena with a Ti/HfO<sub>2</sub>/Pt structure*, Applied Surface Science **434**, 822–830 (2018).
  - [191] T. Ishikura, L.-K. Liefeth, Z. Cui, K. Konishi, K. Yoh, and T. Uemura, *Electrical spin injection from ferromagnet into an InAs quantum well through a MgO tunnel barrier*, Applied Physics Express **7**, 073001 (2014).
  - [192] P. Barate, S. Liang, T. Zhang, J. Frougier, M. Vidal, P. Renucci, X. Devaux, B. Xu, H. Jaffrès, J. George, et al., *Electrical spin injection into InGaAs/GaAs quantum wells: A comparison between MgO tunnel barriers grown by sputtering and molecular beam epitaxy methods*, Applied Physics Letters **105**, 012404 (2014).
  - [193] J. Hornak, P. Trnka, P. Kadlec, O. Michal, V. Mentlík, P. Šutta, G. M. Csányi, and Z. Á. Tamus, *Magnesium oxide nanoparticles: dielectric properties, surface functionalization and improvement of epoxy-based composites insulating properties*, Nanomaterials **8**, 381 (2018).
  - [194] S. D. Sarma and E. Hwang, *The so-called two dimensional metal-insulator transition*, Solid State Communications **135**, 579–590 (2005).
  - [195] R. Campion, K. Edmonds, L. Zhao, K. Wang, C. Foxon, B. Gallagher, and C. Staddon, *The growth of GaMnAs films by molecular beam epitaxy using arsenic dimers*, Journal of Crystal Growth **251**, 311–316 (2003).

## Bibliography

---

- [196] D. Hurle, *A comprehensive thermodynamic analysis of native point defect and dopant solubilities in gallium arsenide*, Journal of Applied Physics **85**, 6957–7022 (1999).
- [197] P. Simmonds, S. Holmes, H. Beere, and D. Ritchie, *Spin-orbit coupling in an  $\text{In}_{0.52}\text{Ga}_{0.48}\text{As}$  quantum well with two populated subbands*, Journal of Applied Physics **103**, 124506 (2008).
- [198] E. A. de Andrada e Silva, G. La Rocca, and F. Bassani, *Spin-split subbands and magneto-oscillations in III–V asymmetric heterostructures*, Physical Review B **50**, 8523 (1994).
- [199] Y. Sato, T. Kita, S. Gozu, and S. Yamada, *Large spontaneous spin splitting in gate-controlled two-dimensional electron gases at normal  $\text{In}_{0.75}\text{Ga}_{0.25}\text{As}/\text{In}_{0.75}\text{Al}_{0.25}\text{As}$  heterojunctions*, Journal of Applied Physics **89**, 8017–8021 (2001).
- [200] R. S. Calsaverini, E. Bernardes, J. C. Egues, and D. Loss, *Intersubband-induced spin-orbit interaction in quantum wells*, Physical Review B **78**, 155313 (2008).
- [201] J. Fu and J. C. Egues, *Spin-orbit interaction in GaAs wells: From one to two subbands*, Physical Review B **91**, 075408 (2015).

# Danksagung



Ich möchte mich an dieser Stelle für die umfassende Unterstützung bedanken, die ich während meiner gesamten Studienzeit erhalten habe. Besonderer Dank gilt jenen, die wesentlich zur Bearbeitung meiner Dissertation in jeglicher Weise beigetragen haben.

Mein größter Dank dabei gilt **Prof. Dr. Dominique Bougeard** für die Möglichkeit, meine Dissertation in seiner Arbeitsgruppe durchführen zu können sowie für die exzellente Betreuung der Arbeit. Vielen Dank für die zahlreichen Diskussionen zu jeder Stunde und das ehrliche Interesse an jeglichen physikalischen Fragestellungen, die sich dabei ergeben haben.

Zudem möchte ich mich bei **Prof. Dr. Dieter Weiß** bedanken, der Zweitkorrektor dieser Arbeit ist. Vielen Dank auch für Diskussionen zu meinen Messergebnissen sowie die Nutzung des Reinraums zur Probenherstellung.

Außerdem möchte ich mich bei **Prof. Dr. Christian Schüller** für Diskussionen bedanken, die zum Verständnis von Spin-Bahn-Wechselwirkung beigetragen haben.

Mein besonderer Dank gilt **Dr. Matthias Kronseder** für die vielseitigen und spannenden Diskussionen über Physik sowie Gott und die Welt bei einem heißen Becher Chaitee. Vielen Dank auch für XPS-Messungen, MgO-Schichten und dein umfangreiches Epitaxie-Wissen.

Vielen Dank an **Dr. Paulo Eduardo de Faria Junior** für die von ihm durchgeführten Berechnungen für unser Projekt, aber vor allem für seine Geduld und die Zeit, die er mir und meinem Verständnis von Bandstruktur-Rechnungen und Spin-Bahn-Wechselwirkung gewidmet hat.

Auch möchte ich mich bei **Dr. Nicola Paradiso** für hilfreiche Gespräche und Tipps zum Thema 1D Transport bedanken.

Großer Dank gilt auch **Dr. Dieter Schuh** für sein umfassendes Wissen in Sachen Epitaxie und Messtechnik. Vielen Dank für die stetige Hilfe und Geduld, die du mir an der III-V MBE entgegengebracht hast.

**Prof. Dr. Josef Zweck** sowie **Felix Schwarzhuber** und **Elisabeth-Anna Zolnowski** möchte ich für diverse TEM-Messungen und deren Interpretation danken.

Bei **Imke Gronwald** möchte ich mich für ihre stetige und unentbehrliche Hilfe und Expertise, vor allem in Sachen Strukturierung, bedanken. Vielen Dank auch für die schönen und witzigen gemeinsamen Stunden am AFM.

Besonderer Dank gilt auch **Andreas Schützenmeier**, ohne dessen Unterstützung an diversen Setups oft wenig gegangen wäre.

Meinen ehemaligen Masterstudenten **Martin Wieand** und **Wolfgang Himmler** möchte ich für die schöne und spannende gemeinsame Zeit sowie ihren Beitrag an dieser Arbeit danken.

**Michael Prager** möchte ich vor allem für den gewinnbringenden Austausch über die jeweiligen Forschungsergebnisse danken sowie für Korrekturen und Anmerkungen zu meiner Arbeit.

Vielen Dank an **Dr. Florian Dirnberger** für das Korrekturlesen von Teilen dieser Arbeit.

**Dr. Juliane Laurer** möchte ich zudem für die Zurverfügungstellung dieser LaTeX-Vorlage danken.

Mein Dank gilt außerdem **Floyd Schauer**, **Viola Zeller**, **Andreas Schmidbauer**, **Maike Halbhuber**, **Thomas Mayer**, **Michael Prager**, **Dr. Christian Neumann**, **Dr. Juliane Laurer** und allen anderen, auch ehemaligen Mitgliedern, für die schöne gemeinsame Zeit, die ich mit ihnen während meiner Promotion verbringen durfte.

Besonderer Dank gilt außerdem **Dr. Florian Dirnberger** und **Dr. Andreas Bayer**, die weit über die Zeit an der Uni hinaus mein Leben mit ihrer Freundschaft bereichern.

Abschließend möchte ich mich bei meinen Eltern, **Dr. Walter Trottmann** und **Rosmarie Wimmer-Trottmann**, sowie **Mario Thoma** für die fortwährende und liebevolle Unterstützung in meinem Leben bedanken.